The structure of the proton and neutron, parameterized by moments of generalized parton distribution functions (GPDs), can be accessed from first principle through the computation of baryon three-point functions with lattice QCD. The numerical effort involved in such computations is sizable and thus an efficient algorithm that extracts most information at given cost is highly desirable.

In this work we demonstrate that stochastic estimation techniques can substantially increase the information/cost ratio. We examine the available results at $N_f = 2$ for the nucleon axial coupling g_A and iso-vector quark momentum fraction $\langle x \rangle_{u-d}$ from various collaborations and compare them to the experimental values. The tension between them is attributed to excited state contributions (ESCs).
We furthermore study the impact of ESCs in moments of GPDs through a model fit. This model also deals with the effects of the choice of parameters used in the computation, like the source-sink separation t_{sink}.
We demonstrate that the choice of t_{sink} by the Regensburg group in previous studies was reasonable and cannot account for discrepancies with the experiment.To reduce the excited state contributions in two-point functions, and consequently three-point functions, we suggest a non-Gaussian quark smearing. This is a linear combination of two Gaussian smearings with one free parameter, which can be tuned to an optimal choice with a fit.

Universitätsverlag Regensburg

ISBN 978-3-86845-109-2
gefördert von:
Alumni der physikalischen Fakultät der Universität Regensburg e.V.

Universität Regensburg

Johannes Siegfried Samir Najjar

39

Dissertationsreihe Physik

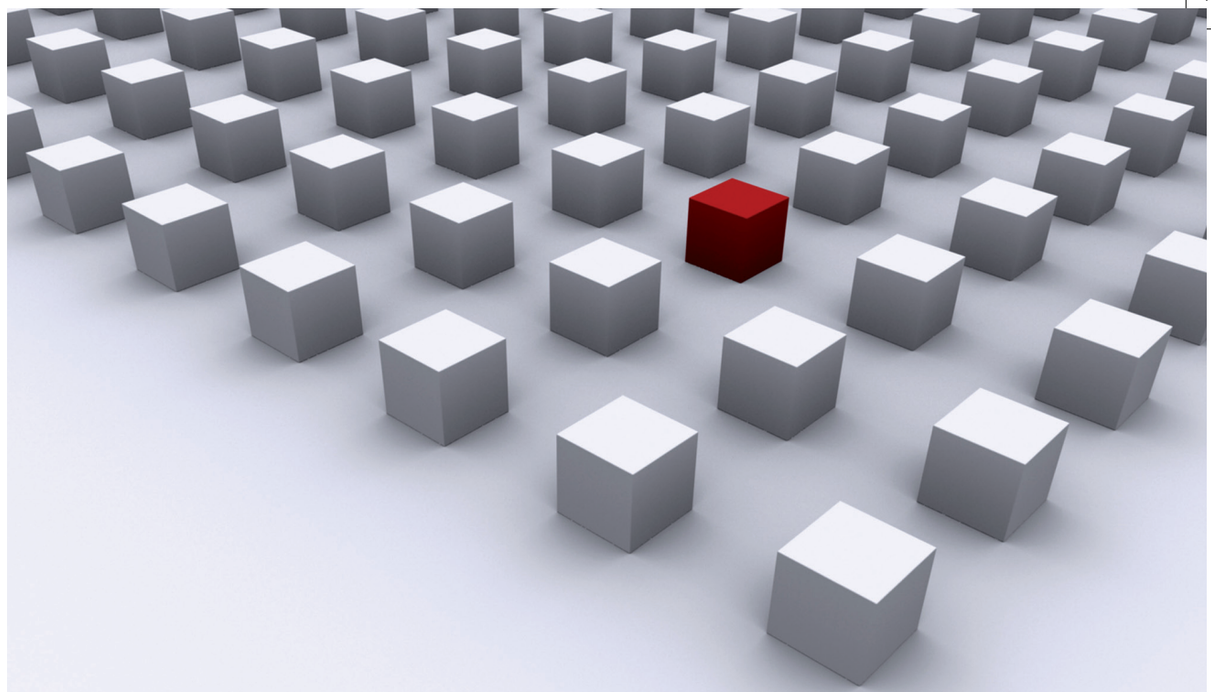

Johannes Siegfried
Samir Najjar

Nucleon structure from stochastic estimators

Universitätsverlag Regensburg

Dissertationsreihe Physik - Band 39

Johannes Siegfried Samir Najjar

Nucleon structure from stochastic estimators

Nucleon structure from stochastic estimators

Dissertation zur Erlangung des Doktorgrades der Naturwissenschaften (Dr. rer. nat.)
der naturwissenschaftlichen Fakultät II - Physik der Universität Regensburg
vorgelegt von

Johannes Siegfried Samir Najjar

aus Kelheim
im Jahr 2014

Die Arbeit wurde von Prof. Dr. G. Bali angeleitet.
Das Promotionsgesuch wurde am 18.11.2013 eingereicht.
Das Kolloquium fand am 06.05.2014 statt.

Prüfungsausschuss:	Vorsitzender:	Prof. Dr. C. Back
	1. Gutachter:	Prof. Dr. G. Bali
	2. Gutachter:	Prof. Dr. V. Braun
	weiterer Prüfer:	Prof. Dr. J. Fabian

Dissertationsreihe der Fakultät für Physik der Universität Regensburg, Band 39

Herausgegeben vom Präsidium des Alumnivereins der Physikalischen Fakultät:
Klaus Richter, Andreas Schäfer, Werner Wegscheider

Johannes Siegfried
Samir Najjar

Nucleon structure from stochastic estimators

Universitätsverlag Regensburg

Bibliografische Informationen der Deutschen Bibliothek.
Die Deutsche Bibliothek verzeichnet diese Publikation
in der Deutschen Nationalbibliografie. Detailierte bibliografische Daten
sind im Internet über http://dnb.ddb.de abrufbar.

1. Auflage 2014

Leibnizstraße 13, 93055 Regensburg

Konzeption: Thomas Geiger
Umschlagentwurf: Franz Stadler, Designcooperative Nittenau eG
Layout: Johannes Siegfried Samir Najjar
Druck: Docupoint, Magdeburg
ISBN: 978-3-86845-109-2

Weitere Informationen zum Verlagsprogramm erhalten Sie unter:
www.univerlag-regensburg.de

Contents

1 Introduction

1.1. Motivation

The Standard model of particle physics consists of the joint description of the electroweak [1] forces and the strong interaction [2, 3, 4]. Although it has some shortcomings, like the absence of gravity in the theory, it is very successful in describing the spectrum of observed particles and their interactions. The recent discovery of the Higgs boson [5] was long awaited and the search for it was the main goal of building the *Large Hadron Collider* (LHC). Mathematically speaking the Standard model is a quantum field theory of the groups $SU(2) \otimes U(1) \otimes SU(3)$, where the strong interaction is described by the color group $SU(3)$. Thus it is called *quantum chromodynamics* (QCD). Its gauge bosons are the *gluons* and their self interaction makes the theory non-linear. This complicates analytical computations at low energies, but as QCD displays *asymptotic freedom* [3] at higher energy scales perturbative expansions are possible.

For low energy properties of quark bound states, *hadrons* [6], non-perturbative methods are imperative. The approach chosen in this work is called *lattice QCD* (LQCD). Here we introduce a discrete spacetime lattice and perform Monte Carlo simulations to evaluate the path integral. The finite lattice spacing serves as an ultraviolet cut-off and the finite volume as an infrared regularization. Thus there are no divergences in the theory. The limit of infinite lattice size and vanishing lattice spacing is well defined and regularized continuum QCD is recovered [7].

LQCD has produced many convincing results[1]. A widely recognized achievement was the computation of the proton mass and the light hadron spectrum from first principles [8].

[1] There are many more results, also in different research areas like finite temperature LQCD, but we focus on hadron structure here.

1.2. Objectives

The objectives of this work lie in the improvement of the algorithms and parameter choices in the computation of nucleon masses and three-point functions[2], which are needed, e.g., to compute (generalized) form factors.
The primary goal was to find a method which performs well at high momentum transfers and utilizes as many different lattice momenta as possible. A natural candidate for this is the stochastic estimation of the –otherwise sequentially computed– propagator between the current insertion and the baryon sink.
Within the computation of three-point functions the baryon source sink distance in Euclidean time (t_{sink}) is fixed and this choice entails certain systematic effects. An estimation of these effects is necessary to enable judgment on how reliable the obtained data are.
The excited state contributions plague the extraction of ground state properties, and it is crucial to suppress these excitations as much as possible without compromising the signal-to-noise ratio. Therefore a new ansatz for quark smearing which fulfills these prerequisites is desirable.

1.3. Outline

This work focuses on technical aspects of the computation of nucleon properties. It contains several distinct topics and is structured in the following way. In Chapter 2 we will present an introduction to nucleon structure and the observables we use to parameterize it. The methods and techniques needed to compute these observables are presented in Chapter 3.
The lattice community has struggled to reach agreement on nucleon structure parameters with the experiment. With the progress in algorithms and computer power ever lighter pion masses and even some simulations at the physical point are possible. Still a tension between some lattice results and experimental observations persists, and one explanation for that is the presence of excited state contributions in the lattice data. This is illustrated for the examples of the nucleon axial coupling and the iso-vector quark momentum fraction in the nucleon in Chapter 4.
In Chapter 5 an excited state analysis is performed of data from one ensemble with multiple values for t_{sink}, and it is found that the choice made for t_{sink} on other ensembles is sufficient to suppress the excited state contributions when the quark smearing is sufficiently optimized.

[2] In lattice QCD one computes correlators between a hadron source at a spacetime point and a hadron sink. The energy of the hadron can then be extracted from this correlation function, and this is referred to as two-point function. The presence of a current insertion defines a third point and hence the name three-point function.

The computation of three-point functions on the lattice is conventionally done with the use of *sequential sources*. To compute such a sequential source one has to fix the sink momentum of the hadron. In Chapter 6 a new algorithm to compute these three-point functions with the help of stochastic estimator techniques is explained, and the benefits of having multiple sink momenta are shown in an exemplary computation of nucleon (generalized) form factors.
The quark level smearing discussed earlier is an essential ingredient in suppressing excited state contributions sufficiently to extract reliable ground state properties. The quality of the employed smearing and possible ways to improve it with a non-Gaussian gauge covariant smearing method is outlined in Chapter 7.
A summary is provided in Chapter 8.

2
Hadron structure in continuum QCD

The road that lead to the development of QCD was rather complex, but it has always been driven by the results of collider experiments and the so found non-trivial internal structure of hadrons. Some of the properties of the nucleon, like its charge radius, see Section 2.4.2, are not fully understood experimentally. For the charge radius a computation of it from first principles is highly desirable.
Another experiment with at the time surprising result was the measurement of the contribution of the quarks to the proton spin. In [9] the European Muon Collaboration (EMC) found that the quarks do not carry all the proton spin, contrary to naive expectations. This lead to the proton spin puzzle or spin crisis, see Section 2.4.3 for the individual hadron contrubutions to the proton spin.
In this section we classify the structure of the nucleon in a set of functions and show how they correspond to quantities which are accessible via lattice QCD computations.

2.1. Nucleon Structure

The parton model describes the nucleon at very high energy as a conglomeration of non-interacting quanta, i .e., its partons. A very extensive review about the structure of hadrons is given in [10] and we follow the derivations therein. These partons require a quantum mechanical treatment and thus they cannot be simply described by a probability to find one in a given state. Nevertheless it is possible to define analogs of Wigner distributions for them, and these are called generalized parton distributions (GPDs)[1]. Experimentally GPDs are accessible in, e.g., deeply virtual Compton scattering (DVCS) or deeply virtual meson production.
Compton scattering is an elastic scattering of an electron off a nucleon producing a photon. They exchange a virtual photon and if the energy of that photon is high enough (deeply virtual) it is sensitive to the inner structure of the nucleon, see Fig. 2.1. There is a process with the same initial and final state particles, the Bethe-Heitler process displayed in Fig. 2.2.

[1] The GPDs are also called off-forward parton distributions (OFPD) in [11].

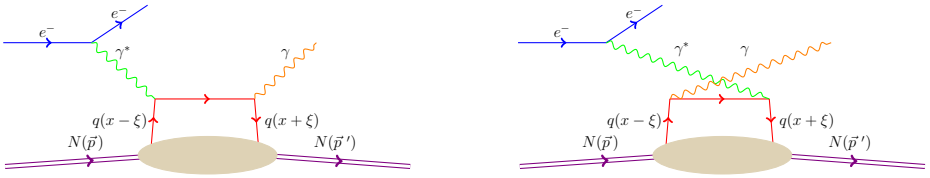

Figure 2.1.: Deeply virtual compton scattering, this is also sometimes referred to as the *handbag* diagram.

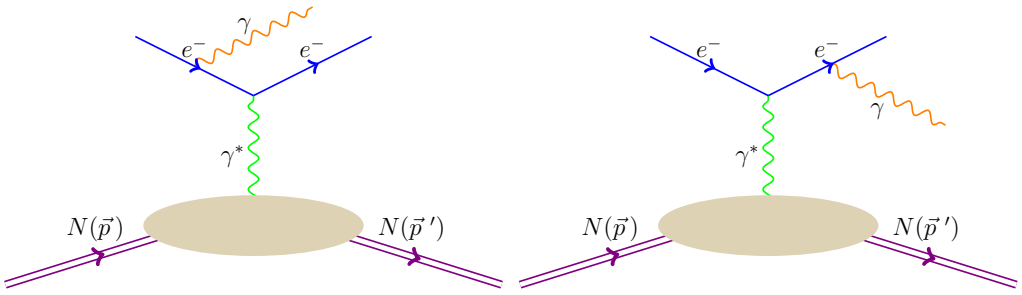

Figure 2.2.: Bethe-Heitler scattering.

In the total cross section of photon production in elastic electron nucleon scattering both processes and their interference terms enter. Since only DVCS depends on GPDs the interference terms depend on linear combination of GPDs and thus they can be measured directly [12].
To discuss the kinematical variables in this process we define the light-cone frame by two vectors $n^\mu, n^{*\mu}$ with $n^2 = n^{*2} = 0$ and $n^\mu n^*_\mu = 1$. Now we can decompose any four-vector as

$$k^\mu = k^+ n^\mu + k^- n^{*\mu} + k^\mu_\perp \tag{2.1}$$

into two components along the light cone axis and two components perpendicular (transverse) to it.
Let us choose a frame where the proton moves with "infinite" velocity in the z-direction, such that its constituents are non-interacting, and the vectors

$$n \equiv \frac{1}{\sqrt{2}}(1,0,0,-1)\,, \quad n^* \equiv \frac{1}{\sqrt{2}}(1,0,0,1)\,. \tag{2.2}$$

This is called the infinite momentum frame. When we additionally demand that the photon moves along the $x-y$ plane (thus q has zero z-component) we are in the so called Bjorken frame.

Then variables of such a process are often defined as follows in the literature

- The momentum of the proton prior/after the reaction : p^μ, p'^μ with respective energies E, E'
- The momentum of the quark before the interaction k^μ
- The space-like momentum of the transfered virtual photon q, so that $Q^2 = -q^2$ is positive
- The momentum transfer to the proton $\Delta = p' - p$
- The quark momentum fraction $x = \frac{k^+}{p^+} = \frac{k^0+k^z}{2E}$
- and the skewness parameter $\eta = 2\xi = \frac{\Delta^+}{p^+}$.

Additionally we define the Bjorken parameter $x_B = Q^2/2p \cdot q$ and the average momentum $2\overline{P} = p + p'$. In the Bjorken frame the three-momentum of the quark is $\vec{k} = (\mathbf{k}_\perp, xp^z)$, where $\mathbf{k}_\perp$ has two components.
In quantum mechanics, due to the Heisenberg uncertainty principle one cannot measure the position and momentum of a particle precisely at the same time. Wigner distributions are phase-space distributions and thus give quasi probabilities (which can be negative) to find the particle with a certain momentum at a given point. This concept can be extended to a field theoretical framework and the Wigner distribution of a quark in a proton would be $\mathcal{F}^q(x, \mathbf{k}_\perp; \eta, \Delta_\perp^2)$. In DVCS it turns out it is sufficient to know the generalized parton distributions (GPDs) of the quark to describe the cross section

$$F^q(x, \eta, \Delta_\perp^2) = \int d^2\mathbf{k}_\perp \mathcal{F}^q(x, \mathbf{k}_\perp; \eta, \Delta_\perp^2)\,, \tag{2.3}$$

so that we cannot measure the $\mathbf{k}_\perp$ dependence in this process.
To explain the theoretical computation of GPDs it is educational to step back to consider the forward scattering case of Compton scattering, which is connected to deep inelastic scattering (DIS), see Fig. 2.3, through the optical theorem. The techniques employed in this case are the same that one would have to use for GPDs in the general DVCS, but can be described without the additional degree of freedom of momentum transfer Δ.

2.2. Deep inelastic scattering

2.2.1. Definition

The scattering process involving a hadron with initial momentum p and mass M and a lepton with initial momentum k is mediated by a photon with momentum $q = k' - k$,

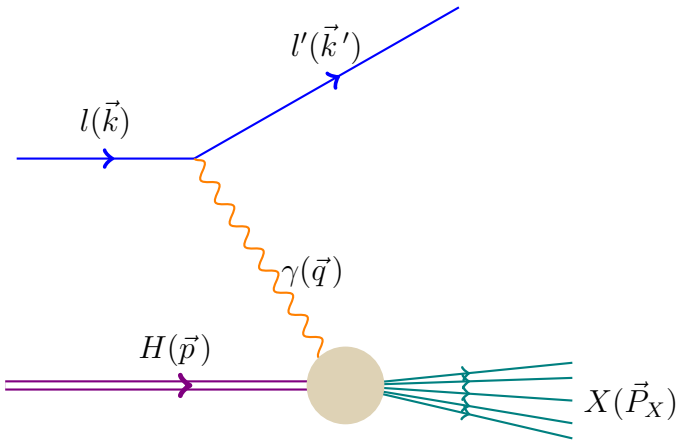

Figure 2.3.: Deep inelastic scattering.

where k' is the momentum of the outgoing lepton. We call this process deep inelastic scattering (DIS) in the limit $Q^2 \to \infty$ for fixed x_B.

DIS has been studied extensively and is the experiment that led to the discovery of quarks, for which the Nobel price 1990 was awarded to J. Friedman, H. W. Kendall and R. E. Taylor from the MIT-SLAC collaboration [13]. For a detailed theoretical discussion see [14]. We will only briefly state the most important formulae.

2.2.2. Decomposition of the cross section

The cross section can be split into a leptonic and a hadronic part:

$$d\sigma = \frac{e^4}{Q^4} \int \frac{d^3k'}{(2\pi)^3 2E(k')} \frac{4\pi l_{\mu\nu} W^{\mu\nu}}{2E(k) 2M \mid v_{rel} \mid} , \tag{2.4}$$

where v_{rel} is the velocity of the target relative to the beam.

The tensors contain products of electromagnetic currents, where we do not include the coupling e in their definitions. The leptonic tensor is

$$l^{\mu\nu} = \sum_{\text{final spin}} \langle k' \mid j_l^\nu(0) \mid k, s_l \rangle \langle k, s_l \mid j_l^\mu(0) \mid k' \rangle . \tag{2.5}$$

The hadronic tensor in DIS can be expressed as the forward scattering amplitude in

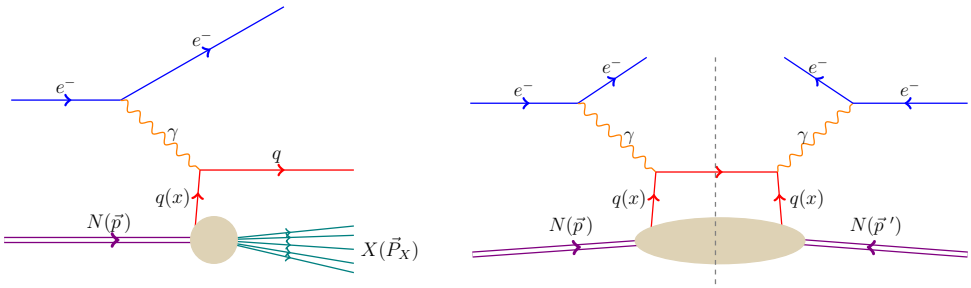

(a) DIS parton picture.

(b) Forward Compton scattering.

Figure 2.4.: Deep inelastic scattering in the parton picture to emphasize the similarity to DVCS. The left hand side squared after summing over all final states X corresponds to the right hand side. The dashed line means that particles are on-shell.

deeply virtual Compton scattering by means of the optical theorem:

$$W^{\mu\nu} = \frac{1}{2\pi}\,\mathrm{Im}\,T^{\mu\nu} \quad \text{where} \quad T^{\mu\nu} = \mathrm{i}\int d^4z \mathrm{e}^{\mathrm{i}q\cdot z}\langle H,\lambda' \mid \mathcal{T}\left\{\mathcal{J}^\mu(z)\mathcal{J}^\nu(0)\right\} \mid H,\lambda\rangle \tag{2.6}$$

and

$$W^{\mu\nu} = \frac{1}{4\pi}\int d^4z \mathrm{e}^{\mathrm{i}q\cdot z}\langle H(p),\lambda' \mid \mathcal{J}^\mu(z)\mathcal{J}^\nu(0) \mid H(p),\lambda\rangle \tag{2.7}$$

where the polarizations of the in and out going hadrons are given by λ and λ' respectively and $\mathcal{T}$ signifies a time ordered product. Note that we have summed over all possible reaction products X in this expression.

The leptonic tensor is known exactly, as the leptons are point-like fermions, and has a few noteworthy properties. First of all it is conserved so that

$$q_\mu l^{\mu\nu} = q_\nu l^{\mu\nu} = 0\,, \tag{2.8}$$

and under $\mu \leftrightarrow \nu$ the spin dependent part of $l_{\mu\nu}$ is antisymmetric, whereas the spin independent part is symmetric.

The general form of the spin $\frac{1}{2}$ hadronic tensor can be deduced by demanding time reversal and parity invariance and conserved currents, so that contractions with q_μ and

q_ν are zero [2]. We find

$$W_{\mu\nu} = -\left(g^{\mu\nu} - \frac{q^\mu q^\nu}{q^2}\right) F_1(x_B, Q^2) + \frac{F_2(x_B, Q^2)}{p\cdot q}\left(p^\mu - \frac{p\cdot q}{q^2}q^\mu\right)\left(p^\nu - \frac{p\cdot q}{q^2}q^\nu\right) - \frac{\mathrm{i}g_1(x_B, Q^2)}{p\cdot q}\varepsilon^{\mu\nu\lambda\sigma}q_\lambda s_{h,\sigma} - \frac{\mathrm{i}g_2(x_B, Q^2)}{(p\cdot q)^2}\varepsilon^{\mu\nu\lambda\sigma}q_\lambda\left(p\cdot q s_{h,\sigma} - s_h\cdot q p_\sigma\right) \quad (2.9)$$

where we denote the four-vector spin of the hadron as s_h. Now we have introduced the unpolarized structure functions F_1 and F_2 and the polarized structure functions g_1 and g_2.
Under $\mu \leftrightarrow \nu$ the antisymmetric part of $W_{\mu\nu}$ is spin dependent and the symmetric part is spin independent, in complete analogy to $l_{\mu\nu}$. Thus to measure F_1 and F_2 it is sufficient to use an unpolarized lepton beam and an unpolarized hadron target, and to also measure g_1 and g_2 both have to be polarized.

2.2.3. Operator product expansion and moments of structure functions

The product of currents in Eq. (2.7) is non-local. Furthermore Eq. (2.7) is dominated by the region near the light cone $z^2 \to 0$ [15].
With the help of the operator product expansion (OPE) one can split up the short-distance behavior, where perturbative QCD is applicable, and the long-range non-perturbative part. A general OPE for an arbitrary correlator $\mathcal{O}_i$ is given as

$$\lim_{z^2\to 0}\mathcal{O}_a(z)\mathcal{O}_b(0) = \sum_k c_{abk}(z)\mathcal{O}_k(0)\,. \quad (2.10)$$

This is generally divergent at the point $z^2 = 0$ and this divergence is encoded in the coefficient functions c_{abk}. All short-scale behavior has to be treated in the coefficient functions, and in QCD short scales allow for perturbative treatment.
A concise outline of the OPE in DIS can be found in [16]. Note that an operator $\mathcal{O}^{\mu_1\cdots\mu_n}$ has spin n if it is symmetrized in the μ_i and traces are subtracted. Then the contribution in the deep inelastic limit[3] to $l_{\mu\nu}W^{\mu\nu}$ of an operator with dimension d and spin s will be of order $\mathcal{O}(x_B^{-n}\left(\frac{Q^2}{m_N}\right)^{2+n-d})$, where m_N is the nucleon mass. In the exponent we have $n-d$ which is called the negative twist, so that

$$\text{twist} = \text{dimension} - \text{spin}\,. \quad (2.11)$$

The minimal twist is two and the operators of higher twist are suppressed at large Q^2.

[2] In addition to Eq. (2.8) that means we could drop all terms proportional to q_μ, q_ν in $W_{\mu\nu}$, or $l_{\mu\nu}$ but not in both, before we contract the hadronic and leptonic tensor.
[3] I.e., $p\cdot q$, $s\cdot q$, $p\cdot k$, and $p\cdot k'$ are all $\mathcal{O}(Q^2/m_N)$.

The matrix elements of the operators correspond to Mellin moments of the structure functions in the decomposition of the hadronic tensor $W_{\mu\nu}$ [17].
We define the n-th Mellin[4] moment of a function f as

$$f_n = \int_0^\infty \mathrm{d}x x^{n-1} f(x)\,. \tag{2.12}$$

There are different operators for the contributions of quarks and gluons to the structure functions. The latter will not be discussed here, but it is important to consider them as well when comparing to the experiment.
The tower of twist two operators for quarks that correspond to the structure functions which multiply Lorentz structures with the appropriate symmetries are

$$\begin{aligned}
\mathcal{O}_q^{\{\mu_1\mu_2\ldots\mu_n\}} &= \mathrm{i}^{n-1}\overline{q}\gamma^{\{\mu_1}\overleftrightarrow{D}^{\mu_2}\ldots\overleftrightarrow{D}^{\mu_n\}}q\,,\\
\mathcal{O}_{5q}^{\{\mu_1\mu_2\ldots\mu_n\}} &= \mathrm{i}^{n-1}\overline{q}\gamma^{\{\mu_1}\gamma_5\overleftrightarrow{D}^{\mu_2}\ldots\overleftrightarrow{D}^{\mu_n\}}q\,,\\
\mathcal{O}_{\sigma q}^{\nu\{\mu_1\ldots\mu_n\}} &= \mathrm{i}^{n-1}\overline{q}\sigma^{\nu\{\mu_1}\gamma_5\overleftrightarrow{D}^{\mu_2}\ldots\overleftrightarrow{D}^{\mu_n\}}q\,,
\end{aligned} \tag{2.13}$$

where

$$\overleftrightarrow{D}_\mu = \frac{1}{2}\left(\overrightarrow{D}_\mu - \overleftarrow{D}_\mu\right)\,, \tag{2.14}$$

$\sigma_{\mu\nu} = \mathrm{i}/2[\gamma_\mu,\gamma_\nu]$ and $\{\ldots\}$ means that indices are symmetrized and the traces subtracted.
Note that for each derivative in Eq. (2.13) both the spin and the dimension of the operator increase by one so that the twist is always two.
To compute the n-th Mellin moment of a structure function one needs an operator with spin n and the variable with respect to which we Mellin transform is the quark momentum fraction x.

2.2.4. Parton distribution functions in the nucleon

In the parton picture the scattering photon sees only one quark in the nucleon. The computation of the individual scattering amplitudes for each quark is very analogous to a QED calculation. To break down the total cross section into the individual contributions we need to define quark densities.
In a longitudinally polarized nucleon, i.e., nucleon spin and momentum are parallel, a quark with momentum fraction x and its spin aligned with the nucleon spin has the quark density $q_\uparrow(x,\mu^2)$ at the scale μ and $q_\downarrow(x,\mu^2)$ if its spin is opposite to the nucleon spin.

[4] In some sources the counting starts at zero, but we will stick to this convention.

Analogously, in a transversally polarized nucleon, i.e. nucleon spin and momentum are perpendicular, a quark with its spin aligned with the nucleon spin has the density $q_\perp(x,\mu^2)$ and $q_\top(x,\mu^2)$ if the quark spin points in the other direction.

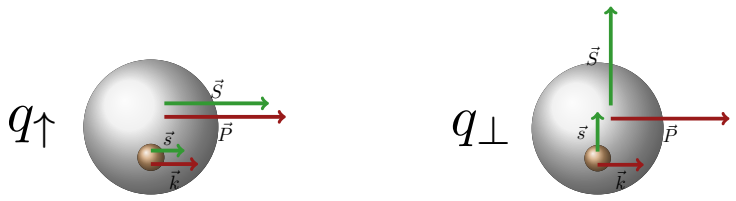

Figure 2.5.: Representation of quark densities, the momentum fraction of the quark is $x = k_+/P_+$. The picture should not imply that necessarily $\vec{k} \parallel \vec{P}$, in fact we integrate over all $\vec{k}$ with a given x to define the quark densities.

Then we define the generalized quark distribution functions[5] as

$$q(x,\mu^2) = q_\uparrow(x,\mu^2) + q_\downarrow(x,\mu^2)\,, \tag{2.15}$$
$$\Delta q(x,\mu^2) = q_\uparrow(x,\mu^2) - q_\downarrow(x,\mu^2)\,, \tag{2.16}$$
$$\delta q(x,\mu^2) = q_\perp(x,\mu^2) - q_\top(x,\mu^2)\,. \tag{2.17}$$

These functions are zero for $\mid x \mid > 1$, and for negative x they correspond to anti-quark distributions. We find[6] [18]

$$q(-x,\mu^2) = -\overline{q}(x,\mu^2) \tag{2.18}$$
$$\Delta q(-x,\mu^2) = +\Delta\overline{q}(x,\mu^2) \tag{2.19}$$
$$\delta q(-x,\mu^2) = -\delta\overline{q}(x,\mu^2)\,. \tag{2.20}$$

Using the above we can now define a compact notation for the n-th Mellin moment, that also incorporates anti-quark distributions and the constraint on x, so that we can write

$$\tilde{q}_n = \int_{-1}^{1} \mathrm{d}x x^{n-1} \tilde{q}(x)\,, \tag{2.21}$$

for $\tilde{q} \in \{q, \Delta q, \delta q\}$.
With these definitions we can re-express the structure functions by the individual con-

[5] Alternatively $f_1 \equiv q$, $g_1 \equiv \Delta q$, and $h_1 \equiv \delta q$ are found in the literature.
[6] This can be seen by using the charge conjugation properties of the corresponding quark bilinears defined in Eq. (2.24).

tributions of each quark flavor. In the unpolarized case one finds

$$F_1(x_B, Q^2) = \frac{1}{2x_B} F_2(x_B, Q^2) = \frac{1}{2} \sum_q c^2_{\text{el.},q} \left(q(x_B, Q^2) + \overline{q}(x_B, Q^2) \right) , \tag{2.22}$$

where the respective electrical charge of each quark flavor in units of the electron charge is denoted by $c_{\text{el.},q} \in \left\{ \frac{-1}{3}, \frac{2}{3} \right\}$ and it is customary to set the scale $\mu^2 = Q^2$ and to lowest order [7] $x = x_B$. The proportionality of F_1 and F_2 is a consequence of the quarks having spin $\frac{1}{2}$ and this was used to experimentally justify this picture. Bjorken scaling [19] is reached at high Q^2 when in Eq. (2.22) the F_i become independent of Q^2. It was a good description of the older DIS data and at the same time it was clear that such scaling would be violated. Mild scaling violations could only be explained in an asymptotically free theory.

In a manner similar to Eq. (2.22) the polarized structure function g_1 is

$$g_1(x_B, Q^2) = \frac{1}{2} \sum_q c^2_{\text{el.},q} \left(\Delta q(x_B, Q^2) + \Delta \overline{q}(x_B, Q^2) \right) . \tag{2.23}$$

Note that the transversal quark density δq does only appear in processes that have a helicity-flip [20], e.g., some channels in semi-inclusive DIS, and it is thus inherently more difficult to measure than the other two quark density combinations. See [21] for a recent review.

2.3. Moments of GPDs

In the previous section we have parameterized the time-ordered product of two electromagnetic currents in between two nucleon states by the structure functions and in the parton picture we have then broken them down to the parton distribution functions. To generalize this case to the non-forward scattering we need to replace the two currents by Fourier transformed bilocal operators, which depend on the momentum fraction of the quark x, of the form[8] [22]

$$O^q_\Gamma(x) = \int_{-\infty}^{\infty} \frac{d\alpha}{2\pi} e^{i\alpha x} \overline{q} \left(-\frac{\alpha}{2} n \right) \Gamma \, \mathcal{U}_{[-\frac{\alpha}{2}n, \frac{\alpha}{2}n]} q \left(\frac{\alpha}{2} n \right) , \tag{2.24}$$

[7] In Eq. (2.7) the exponent is an oscillating phase. The integrand contributes most if the longitudinally probed distance, also called Ioffe time, $z^- \approx (M x_B)^{-1}$. The momentum associated to this distance is the quark momentum fraction x, thus $x \approx x_B$. See Section 2.2.4 of [10] for a more thorough explanation.

[8] Note that in the conventions of [22] n is a light cone vector with $\overline{P} \cdot n = 1$.

where the Wilson line

$$\mathcal{U}_{[-\frac{\alpha}{2}n,\frac{\alpha}{2}n]} = \mathfrak{P} e^{ig\int_{\alpha/2}^{-\alpha/2} d\lambda\, n\cdot A(\lambda n)} \tag{2.25}$$

is a path ordered (denoted by $\mathfrak{P}$) exponential of gauge fields and it ensures gauge invariance.
The matrix elements of this bilocal operators are then decomposed into different Lorentz structures and the scalar prefactors are the GPDs. In the DIS discussion, Section 2.2, these prefactors of the Lorentz structures were the structure functions after we expressed them through the PDFs. The Lorentz structures depend on the Γ we use in Eq. (2.24). Possible independent twist two operators are O_V, O_A, and O_T where Γ was chosen as γ_μ, $\gamma_5\gamma_\mu$ and $i\sigma_{\mu\nu}$ respectively.
The GPDs depend on the momentum transfer $Q^2 = t$ and we have to renormalize them at a scale μ. In the DIS case we set $\mu^2 = Q^2$, a choice which is not suitable to study the Q^2-dependence of GPDs. To avoid confusion we will write them as functions of t and suppress the scale dependence for now. The list of GPDs [22] is

$$\langle N(p')|O_V^\mu(x)|N(p)\rangle = \overline{U}(p')\left\{\gamma^\mu H(x,\xi,t) + \frac{i\sigma^{\mu\nu}\Delta_\nu}{2m_N}E(x,\xi,t)\right\}U(p)\,, \tag{2.26}$$

$$\langle N(p')|O_A^\mu(x)|N(p)\rangle = \overline{U}(p')\left\{\gamma^\mu\gamma_5\widetilde{H}(x,\xi,t) + \frac{\gamma_5\Delta^\mu}{2m_N}\widetilde{E}(x,\xi,t)\right\}U(p)\,, \tag{2.27}$$

$$\begin{aligned}\langle N(p')|O_T^{\mu\nu}(x)|N(p)\rangle = \overline{U}(p')\Bigg\{&i\sigma^{\mu\nu}H_T(x,\xi,t) + \frac{\gamma^{[\mu}\Delta^{\nu]}}{2m_N}E_T(x,\xi,t)\\ &+ \frac{\overline{P}^{[\mu}\Delta^{\nu]}}{m_N^2}\widetilde{H}_T(x,\xi,t) + \frac{\gamma^{[\mu}\overline{P}^{\nu]}}{m_N}\widetilde{E}_T(x,\xi,t)\Bigg\}U(p)\,,\end{aligned} \tag{2.28}$$

where we omitted contributions of higher twist.
With the help of the OPE we can express these matrix elements of bilocal operators as expansionw in matrix elements of the local operators defined in Eq. (2.13), the moments of the GPDs of generalized form factors GFFs. A systematic expression of the moments of GPDs and the decomposition in the matrix elements can be found in [23]. In this work we only present the lowest moments and we will state them in Section 2.4.
The connection between the GPDs and the quark densities defined earlier is given by considering the forward case:

$$q(x) = H(x,0,0)\,, \tag{2.29}$$

$$\Delta q(x) = \widetilde{H}(x,0,0)\,, \tag{2.30}$$

$$\delta q(x) = H_T(x,0,0)\,. \tag{2.31}$$

To illustrate the GPDs we can consider impact parameter distributions like

$$H(x, \boldsymbol{b}) = \int \frac{\mathrm{d}^2\boldsymbol{\Delta}}{(2\pi)^2} e^{-\mathrm{i}\boldsymbol{b}\boldsymbol{\Delta}} H(x, 0, -\boldsymbol{\Delta}^2)\,, \tag{2.32}$$

at zero skewness. The transverse momentum transfer $\boldsymbol{\Delta}$ and impact parameter $\boldsymbol{b}$ live in the 2d-transverse plane[9]. Similar transformations can be done for the other GPDs. Doing this for a linear combination of Eq. (2.26) and Eq. (2.28) we obtain the density of quarks with transverse polarization[10]:

$$\begin{aligned}\frac{1}{2}\left[F + s^i F_T^i\right](x, \boldsymbol{b}) = \frac{1}{2}\Big[&H(x, \boldsymbol{b}) - b\sin\varphi \frac{1}{m_N}\frac{\partial}{\partial b^2} E(x, \boldsymbol{b}) \\ &-b\sin(\varphi - \chi)\frac{1}{m_N}\frac{\partial}{\partial b^2}\left(E_T(x, \boldsymbol{b}) + 2H_T(x, \boldsymbol{b})\right) \\ &+\cos\chi\left(H_T(x, \boldsymbol{b}) - \frac{1}{m_N^2}\frac{\partial}{\partial b^2}\left(b^2\frac{\partial}{\partial b^2}\tilde{H}_T(x, \boldsymbol{b})\right)\right) \\ &+b^2\cos(\chi - 2\varphi)\frac{1}{m_N^2}\left(\frac{\partial}{\partial b^2}\right)^2\left(\tilde{H}_T(x, \boldsymbol{b})\right)\Big]\end{aligned} \tag{2.33}$$

where we assume the nucleon spin $\boldsymbol{S} = (1, 0)$ and the quark spin $\boldsymbol{s} = (\cos\chi, \sin\chi)$, and we write $\boldsymbol{b} = b(\sin\varphi, \cos\varphi)$ with $b = \sqrt{\boldsymbol{b}^2}$. We can identify structures which break rotational symmetry and through them we can extract the angle of the quark spin χ to the nucleon spin. When additionally assuming a $\boldsymbol{b}^2$-dependence of the parton distributions as $\exp(-b^2/b_0^2)$ with $b_0 = 0.5$ fm these can then be plotted in the b_x-b_y plane, as shown in Fig. 2.6 or [24].

2.4. Lowest moments of GPDs, form factors and charges

In this section we will present the matrix elements of local operators that we can compute in lattice QCD and their physical significance. We use the abbreviation

$$\langle\langle O \rangle\rangle = \overline{U}(P', \sigma')\, O\, U(P, \sigma)\,, \tag{2.34}$$

in the following.
We present a subjective selection of the properties of the matrix elements and do not claim to present a complete review of these quantities. Gluonic contributions are matrix elements of field strength tensors with appropriate γ-matrices and derivatives [11]. We will focus on the contributions of quarks to the GPDs for most part.

[9] We will denote vectors in this plane by bold symbols.
[10] We use the notion of [24] and do not give the left hand side a new name.

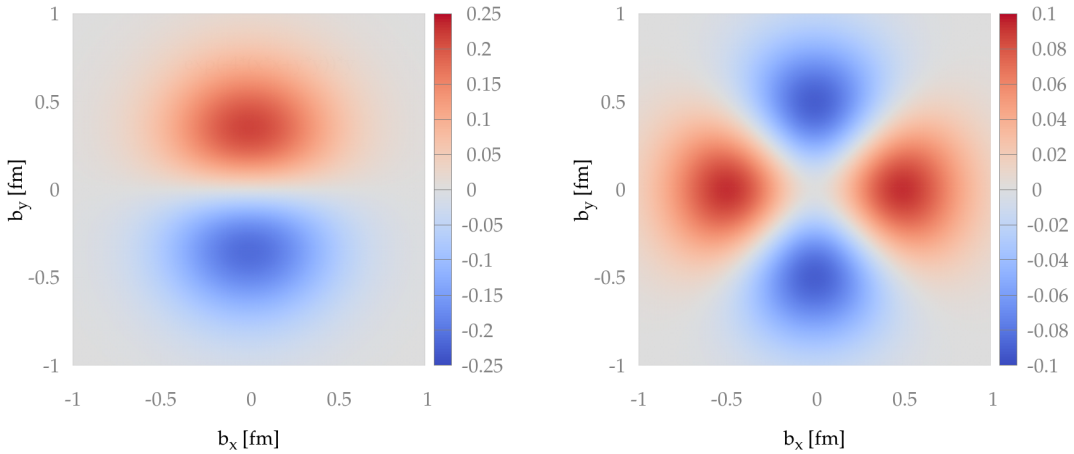

(a) $b\exp(-b^2/b_0^2)\sin(\varphi)$. (b) $b^2\exp(-b^2/b_0^2)\cos(2\varphi)$.

Figure 2.6.: Rotational invariance breaking contributions to the transverse quark density in the b_x-b_y plane. The color scale is arbitrary and the plot design is taken from [24].

2.4.1. Scalar form factor

The scalar form factor is actually a matrix element of a twist three operator. Thus it has no relation to our twist two GPDs, but is mentioned here for completeness because the techniques to compute it are the same as for the moments of GPDs.
The matrix element is

$$\langle P' \mid \overline{\Psi}_q \Psi_q \mid P\rangle = \langle\langle \mathbb{1} \rangle\rangle \, G_S(t)\,. \tag{2.35}$$

It signifies the coupling of the nucleon to scalar particles, like the Higgs-boson and it is relevant also in some extensions of the standard model [25].
At zero recoil ($p = p' = 0$) the scalar matrix element is related to the sigma terms

$$\sigma_q = m_q \langle N \mid \bar{q}q \mid N\rangle\,. \tag{2.36}$$

The pion nucleon sigma term $\sigma_{\pi N} = \sigma_u + \sigma_d$ plays an important role as a low energy constant for chiral perturbation theory.
As it is an iso-scalar quantity, disconnected contributions to the three-point function cannot be neglected. It contains a unit matrix as choice of Γ in Eq. (2.24). Hence it is the simplest quantity for which quark line disconnected diagrams are required. Therefore many lattice studies exist [26] on this topic and it is an ideal playground to test signal-to-noise improvement strategies for disconnected diagrams.
An alternative scheme to compute the relevant matrix elements is given by the Feyn-

man-Hellman theorem

$$\sigma_q = m_q \frac{\partial M_N}{\partial m_q} \,. \tag{2.37}$$

It was used in lattice studies like [27], and so one can cross-check the simulations on the lattice.
The σ-term can be used to constrain $m_N(m_q)$ and thus aid in the extrapolation of lattice results to physical quark masses. This was used in [28, 29] to determine $r_0 m_N$ and hence r_0 in physical units. Alternatively it can serve as a benchmark of the scale setting as outlined in [30].

2.4.2. Dirac and Pauli form factors

The electromagnetic form factors can be obtained from

$$\langle P' \mid \overline{\Psi}_q \gamma^\mu \Psi_q \mid P \rangle = \langle\langle \gamma^\mu \rangle\rangle \, F_1^q(t) + \frac{\mathrm{i}}{2m_N} \left\langle\left\langle \sigma_M^{\mu\nu} \right\rangle\right\rangle \Delta_\nu F_2^q(t) \,. \tag{2.38}$$

The relation to GPDs is given by

$$F_1^q(t) = \int_{-1}^{1} dx \, H^q(x,\xi,t) \,, \quad F_2^q(t) = \int_{-1}^{1} dx \, E^q(x,\xi,t) \,. \tag{2.39}$$

The electromagnetic current, where we again define electric charges in units of the elementary charge e, is given by

$$\mathcal{J}^\mu_{\mathrm{e/m}} = \frac{2}{3}\overline{u}\gamma^\mu u - \frac{1}{3}\overline{d}\gamma^\mu d \,, \tag{2.40}$$

and thus the Dirac form factor F_1 (no spin flip) and the Pauli form factor F_2 (spin flip) for the proton (when the nucleon in Eq. (2.38) is taken as a proton) are the linear combinations of

$$F_{1/2}(t) = \frac{2}{3} F^u_{1/2}(t) - \frac{1}{3} F^d_{1/2}(t) \,. \tag{2.41}$$

In the limit of $t \to 0$ they yield, after renormalization, the electric charge of the proton $g_V = F_1(0) = 1$ and $F_2(0) = \mu_p - 1$ where $\mu_p = 2.7928$ is the magnetic moment of the proton. Note that the vector coupling g_V corresponds to a conserved current and thus transition matrix elements would be zero. This means that on the lattice we expect to get flat plateaus. Excited state contributions could be present, but they would be suppressed by $e^{-\Delta m t_{\mathrm{sink}}}$, see Section 5.1.
A point particle would have t-independent form factors, so a non-trivial momentum

transfer dependence allows for insights on the structure of the nucleon like the spatial charge distribution. Lattice studies include [31].
The Dirac radius r_1 and the Pauli radius r_2 of the proton can indeed be computed from F_1/F_2 via

$$\langle r_i^2 \rangle = -6 \frac{\mathrm{d}F_i}{\mathrm{d}Q^2} \mid_{Q^2=0} , \qquad i = 1, 2 . \tag{2.42}$$

The linear combinations

$$G_E(t) = F_1(t) - \frac{t}{(2m_N)^2} F_2(t) \tag{2.43}$$

$$G_M(t) = F_1(t) + F_2(t) , \tag{2.44}$$

are the electric and magnetic Sachs form factors. The corresponding radii, computed in complete analogy to Eq. (2.42), are the magnetic and charge radius of the nucleon.
For the charge radius two contradicting experimental results [32] exist and there is an ongoing discussion in the literature [33]. Current lattice studies like [34] fail to resolve the discrepancy between them. In [34] the difference to the experimental results is attributed to the presence of excited state contributions.
In the iso-spin symmetric limit we have the identity [35]

$$\langle \text{proton} \mid \mathcal{J}^\mu_{\text{e/m}} \mid \text{proton} \rangle - \langle \text{neutron} \mid \mathcal{J}^\mu_{\text{e/m}} \mid \text{neutron} \rangle = \langle \text{proton} \mid \mathcal{J}^\mu_{\text{e/m};u-d} \mid \text{proton} \rangle \tag{2.45}$$

where we define the iso-vector (iv) current

$$\mathcal{J}^\mu_{\text{e/m};u-d} = \overline{u}\gamma^\mu u - \overline{d}\gamma^\mu d . \tag{2.46}$$

This current has the advantage that disconnected contributions for the light flavors cancel in this limit.
Another choice often found in the literature is the iso-scalar (is) form factor. For these two combinations of flavors we define

$$F^{iv}_{1/2}(t) = F^u_{1/2}(t) - F^d_{1/2}(t) , \quad F^{is}_{1/2}(t) = F^u_{1/2}(t) + F^d_{1/2}(t) . \tag{2.47}$$

2.4.3. Axial form factors

From the axial current we obtain

$$\langle P' \mid \overline{\Psi}_q \gamma^\mu \gamma_5 \Psi_q \mid P \rangle = \langle\langle \gamma^\mu \gamma_5 \rangle\rangle \, G^q_A(t) + \frac{\Delta^\mu}{2m_N} \langle\langle \gamma_5 \rangle\rangle \, G^q_P(t) , \tag{2.48}$$

where $G_A^q(t)$ is the axial form factor and $G_P^q(t)$ is the induced pseudoscalar form factor.

The axial coupling of the nucleon, which also parameterizes the strength of β-decay, is $g_A = G_A^u(0) - G_A^d(0)$.

In this combination the disconnected contributions to the matrix element cancel in the iso-spin limit. This simplifies the computation significantly and thus this quantity has been studied extensively on the lattice, see Section 4.1 for a review on recent results.

The pseudoscalar coupling constant is connected to the axial coupling [36] via the Goldberger-Treiman [37] relation, using PCAC,

$$\frac{m_\mu}{2m_N} G_P^{u-d}(t) \equiv g_P(t) = \frac{2m_\mu m_N}{m_\pi^2 + t} \tag{2.49}$$

This is a first order result and it can be compared to the experiment to test the accuracy of the PCAC prediction. For a recent review see [38].

The threshold for muon capture of the proton is $t = 0.88 m_\mu^2$ and hence one usually quotes $g_P = g_P(0.88 m_\mu^2)$. From Eq. (2.49) one would expect $g_P \approx 6.77 g_A$.

The GFFs of Eq. (2.48) are the first moments of $\widetilde{H}$ and $\widetilde{E}$:

$$G_A(t) = \int_{-1}^{1} dx \widetilde{H}(x,\xi,t)\,, \quad G_P(t) = \int_{-1}^{1} dx \widetilde{E}(x,\xi,t)\,. \tag{2.50}$$

By looking at the definition of the quark densities Eq. (2.16), using Eq. (2.30) and Eq. (2.50) we find

$$g_A = \int_{-1}^{1} dx\ (\Delta u(x) - \Delta d(x))\ , \tag{2.51}$$

which is the net-contribution to the longitudinally polarized spin of the proton by the up-quarks minus the down-quark contributions.

The proton spin crisis was initiated by the EMC [9] experiment measuring that the quark spin contributions are small and cannot account for the proton spin alone. The individual contributions of the partons to the hadron spin can be split up like this [11]

$$J = \frac{1}{2}\Delta\Sigma + L_q + J_G\,. \tag{2.52}$$

The orbital angular momentum terms of quarks is L_q and the total gluon spin contribution J_G. To compute them one needs also disconnected contributions and gluonic operator insertions. This was, e.g., done in [39].

The total quark spin contributions can be summed up[11]

$$\Delta\Sigma = \Delta u + \Delta d + \Delta s + \Delta\overline{u} + \Delta\overline{d} + \Delta\overline{s}\,. \tag{2.53}$$

The light quark part of the spin can be computed from the matrix elements of Eq. (2.48), where one also needs the disconnected diagrams.
The strange quark contributions to the nucleon spin stem from disconnected contributions to three-point functions. They can be evaluated in LQCD with the help of all-to-all propagators. This is e.g. done by the Regensburg group [40].
It is an ongoing debate whether one can define the individual contributions to the nucleon spin as [41]

$$J = \frac{1}{2}\Delta\Sigma + \tilde{L}_q + L_G + \Delta G\,, \tag{2.54}$$

in a gauge invariant way. As way to organize computations of ΔG it was suggested to split the gauge potential up in contributing and non-contributing parts in, e.g., [42], but the solution is not unique [43]. For an extensive overview article in this c.f. [44]. In [45] it is argued that the difference between the quark orbital angular momentum L_q in Eq. (2.52) and $\tilde{L}_q$ in Eq. (2.54) is due to final state interactions, after the quark has left the target in a deep inelastic scattering.

2.4.4. Tensor form factors

The tensor current with no derivatives yields

$$\begin{aligned}\langle P' \mid \overline{\Psi}_q \mathrm{i}\sigma^{\mu\nu}\Psi_q \mid P\rangle = \langle\langle \mathrm{i}\sigma^{\mu\nu}\rangle\rangle\, A_{T10}(t) + \left\langle\left\langle \gamma^{[\mu}\Delta^{\nu]}\right\rangle\right\rangle \frac{B_{T10}(t)}{2m_N} \\ + \langle\langle 1\rangle\rangle\, \overline{P}^{[\mu}\Delta^{\nu]}\frac{\tilde{A}_{T10}(t)}{m_N^2}\,.\end{aligned} \tag{2.55}$$

The form factors are the first moments of the tensorial GPDs:

$$\begin{aligned}A_{T10}(t) = \int_{-1}^{1} dx H_T(x,\xi,t)\,, \quad B_{T10}(t) = \int_{-1}^{1} dx E_T(x,\xi,t)\,, \\ \widetilde{A}_{T10}(t) = \int_{-1}^{1} dx \widetilde{H}_T(x,\xi,t)\,.\end{aligned} \tag{2.56}$$

The first moment of $\widetilde{E}_T(x,\xi,t)$ vanishes hence there are only three generalized form factors in Eq. (2.55), whereas there are four GPDs in the matrix element of the bilocal tensor operator Eq. (2.28).

[11] We neglect heavier sea quark flavors and imply $\Delta q = \int_0^1 \Delta q(x)\mathrm{d}x$.

The tensor coupling $g_T = A_{T10}^{u-d}(t)$ is similar to g_A as it is given (see Eq. (2.17), Eq. (2.31)) as

$$g_T = \int_{-1}^{1} dx\, \delta u(x) - \delta d(x)\,. \tag{2.57}$$

The non-relativistic quark model predicts $\Delta u = \delta u = \frac{4}{3}$ and $\Delta d = \delta d = -\frac{1}{3}$, viz $g_A = g_T$.

Lorentz-boosts in a relativistic theory single out the boost direction and thus break the rotational invariance of the proton, and introduce antiparticle contributions. Thus the difference of axial coupling and tensor coupling is a measure of these relativistic effects.

The tensor coupling is experimentally much harder to access than g_A as it cannot be measured in DIS. The transverse spin structure can only be probed in processes with a helicity flip of the struck quark.

Experimental extractions of g_T also use the Soffer bound [46]

$$q(x) + \Delta q(x) \geq 2 \mid \delta q(x) \mid, \tag{2.58}$$

to constrain their fits.

For a recent lattice result see [47].

2.4.5. Second moment of vector GPDs

The second moments of GPDs are generally obtained by matrix elements of operators with one derivative. In the vector current case this yields

$$\begin{aligned}\langle P' \mid \overline{\Psi}_q \gamma^{\{\mu} \overleftrightarrow{D}^{\nu\}} \Psi_q \mid P\rangle = S(\mu,\nu)\Big(&\langle\langle \gamma^\mu \rangle\rangle\, \overline{P}^\nu A_{20}(t) \\ &+ \langle\langle \mathrm{i}\sigma^{\mu\alpha} \rangle\rangle\, \frac{\Delta_\alpha \overline{P}^\nu}{2m_N} B_{20}(t) + \langle\langle 1 \rangle\rangle\, \frac{\Delta^\mu \Delta^\nu}{m_N} C_{20}(t)\Big)\,.\end{aligned} \tag{2.59}$$

Here we have to subtract the traces on both sides, see Appendix C.2.1. The indices μ, ν are symmetrized on both sides, indicated by the symmetrization function $S(\mu,\nu)$ and the curly brackets on the left side.

The first moments of the vector GPDs correspond to these linear combinations of GFFs:

$$\int_{-1}^{1} dx x H(x,\xi,t) = A_{20}(t) + (2\xi)^2 C_{20}(t)\,, \quad \int_{-1}^{1} dx x E(x,\xi,t) = B_{20}(t) - (2\xi)^2 C_{20}(t)\,. \tag{2.60}$$

At zero momentum transfer we get the quark momentum fraction

$$\int_{-1}^{1} dx\, xq(x) = A_{20}(0) = \langle x \rangle_q \,, \tag{2.61}$$

and the iso-vector momentum fraction $\langle x \rangle_{u-d}$ is often considered as a benchmark for GPD computations on the lattice. This quantity is experimentally accessible and disconnected contributions cancel in the computation. There is a long standing disagreement with the lattice predictions and the experimental results, see Section 4.2.
The contributions of the gluons to the nucleon momentum was estimated, e.g., in [48].

2.4.6. Second moment of axial GPDs

In the iso-spin symmetric limit we obtain

$$\langle P' \mid \overline{\Psi}_q \gamma^{\{\mu} \gamma_5 \overleftrightarrow{D}^{\nu\}} \Psi_q \mid P \rangle = S(\mu,\nu) \Big[\big\langle\big\langle \gamma^\mu \gamma^5 \big\rangle\big\rangle \overline{P}^\nu \tilde{A}_{20}(t) + \big\langle\big\langle \gamma^5 \big\rangle\big\rangle \frac{\Delta^\mu \overline{P}^\nu}{2m_N} \tilde{B}_{20}(t) \Big] \,. \tag{2.62}$$

for the matrix element of the axial current with one derivative. As above we have to subtract the traces on both sides, see Appendix C.2.1. The GFFs correspond to

$$\int_{-1}^{1} dx x \widetilde{H}(x,\xi,t) = \widetilde{A}_{20}(t) \,, \quad \int_{-1}^{1} dx x \widetilde{E}(x,\xi,t) = \widetilde{B}_{20}(t) \,. \tag{2.63}$$

The forward matrix element

$$\int_{-1}^{1} dx x \Delta q(x) = \tilde{A}_{20}(0) = \langle x \rangle_{\Delta q} \,, \tag{2.64}$$

is the quark helicity fraction. The iso-vector quantity can be written as $\langle x \rangle_{\Delta u - \Delta d}$. Since neither lattice calculations for g_A nor $\langle x \rangle_{u-d}$ agree with the experiment, results for this quantity are to be treated with caution.

2.4.7. Second moment of tensor GPDs

In the tensor case

$$\begin{aligned} \langle P' \mid \mathcal{O}_T^{\mu\nu\rho} \mid P \rangle = A(\mu,\nu) S(\nu,\rho) \Big(\big\langle\big\langle \mathrm{i}\sigma^{\mu\nu} \big\rangle\big\rangle \overline{P}^\rho A_{T20}(t) + \Big\langle\Big\langle \gamma^{[\mu} \Delta^{\nu]} \Big\rangle\Big\rangle \frac{\overline{P}^\rho}{2m_N} B_{T20}(t) \\ + \langle\langle 1 \rangle\rangle \frac{\overline{P}^{[\mu} \Delta^{\nu]}}{m_N^2} \overline{P}^\rho \tilde{A}_{T20}(t) + \Big\langle\Big\langle \gamma^{[\mu} \overline{P}^{\nu]} \Big\rangle\Big\rangle \frac{\Delta^\rho}{m_N} \tilde{B}_{T21}(t) \Big) \,. \end{aligned} \tag{2.65}$$

the subtraction of the traces on both sides is a bit more involved, see Appendix C.2.1. The function $A(\mu,\nu)$ antisymmetrizes the indices μ,ν. As there was no good agreement between the lattice data for $\langle x\rangle_{u-d}$ and the experiment, more effort was put into ameliorating this difference, then computing the tedious tensor GPD quantities. The tensor GPDs are nevertheless very interesting as they depend on the correlations of quark spin and nucleon spin in the transverse plane. See Fig. 2.6 for a pictorial representation.
The second moments of the tensor GPDs are

$$\begin{aligned}
\int_{-1}^{1} dx\, x H_T(x,\xi,t) =& A_{T20}(t)\,, \quad \int_{-1}^{1} dx\, x E_T(x,\xi,t) = B_{T20}(t)\,,\\
\int_{-1}^{1} dx\, x \widetilde{H}_T(x,\xi,t) =& \widetilde{A}_{T20}(t)\,, \quad \int_{-1}^{1} dx\, x \widetilde{E}_T(x,\xi,t) = -2\xi \widetilde{B}_{T21}(t)\,.
\end{aligned} \tag{2.66}$$

Note that $\widetilde{E}_T(x,\xi,t)$ is odd in ξ and hence its moments correspond to GFFs with only odd second indices [23].

3
Methods in lattice QCD

The most prominent feature of the theory of the strong interactions (QCD) is the gluon-gluon interaction, which makes the theory non-linear. As a direct consequence exact analytical computations are not feasible for most quantities of interest. Thus one uses effective theories (like chiral perturbation theory [49]). Asymptotic freedom [3] permits the use of perturbative QCD at high energies, which organizes calculations in expansions of small coupling. At low energies, however, one cannot use this approach. A way out for quantities that can be analytically continued to Euclidean spacetime is to perform a Monte Carlo evaluation of the discretized path integral to obtain the expectation value. This is called lattice QCD and there is a wealth of monographs on the subject, e.g., [50, 51, 52, 53, 54].
We present a short introduction of the key aspects needed for the calculations done in this work. First we will explain the computation of expectation values and the necessary definitions and algorithms to compute simple quantities. In Section 3.5 we will explain the measurement of energies and masses of hadrons. Three-point functions are needed to compute quantities related to the structure of the nucleon. Their interpretation will be displayed in Section 3.6 and in Section 3.7 we will show how to measure them on the lattice. A new algorithm to compute them is shown in Section 3.7.4. In Section 3.8 the method to extract generalized form factors out of measured three-point functions is explained, before we show how to relate the results to the experiment by renormalization (Section 3.9) and conversion to physical units (Section 3.10).

3.1. Expectation values in Euclidean QCD

To construct the Lagrangian of the quantum field theory of strong interactions (QCD) one demands Lorentz-invariance, the color $SU(3)$ gauge degrees of freedom, and the $U(1)$ gauge symmetry of electromagnetism (QED).
As the QED part is playing a small role in nucleon structure we drop it here.
From these principles one can construct the QCD-Lagrangian in Euclidean spacetime

by taking the terms with the lowest dimension that satisfy all symmetries:

$$\mathcal{L}[\psi,\overline{\psi},A](x)=\sum_{i=f}^{N_f}\left[\overline{\psi}_i(x)(D_\mu(x)\gamma_\mu+m_i)\psi_i(x)\right]-\frac{1}{4g^2}F_{\mu\nu}(x)F_{\mu\nu}(x)\;, \tag{3.1}$$

where $D_\mu(a)$ is a covariant derivative and the field strength tensor is $F_{\mu\nu}=-\mathrm{i}\,[D_\mu,D_\nu]$. This yields the following action

$$S_{QCD}[\psi,\overline{\psi},A]=\int_0^{L_t}\mathrm{d}x_4\int\mathrm{d}^3\vec{x}\mathcal{L}(x)\;, \tag{3.2}$$

where we have chosen L_t to denote the temporal extent of our spacetime. For zero temperature quantities one has to take the limit $L_t\to\infty$. In Euclidean spacetime, using the path integral formalism, the expectation value of an operator $\mathcal{O}$ is given by

$$\langle\mathcal{O}\left[\psi,\overline{\psi},A\right]\rangle=\frac{1}{Z}\int[\mathrm{d}\psi][\mathrm{d}\overline{\psi}][\mathrm{d}A]\mathcal{O}\left[\psi,\overline{\psi},A\right]\mathrm{e}^{-S_{QCD}} \tag{3.3}$$

$$Z=\int[\mathrm{d}\psi][\mathrm{d}\overline{\psi}][\mathrm{d}A]\mathrm{e}^{-S_{QCD}}\;, \tag{3.4}$$

where we abbreviate the integration measures as

$$\begin{aligned}[\mathrm{d}\psi]&=\prod_{f,c,\alpha}\prod_{x\in\mathbb{R}^4}\mathrm{d}\psi_{f(\alpha,c)}(x)\,,\\ [\mathrm{d}\overline{\psi}]&=\prod_{f,c,\alpha}\prod_{x\in\mathbb{R}^4}\mathrm{d}\overline{\psi}_{f(\alpha,c)}(x)\,,\\ [\mathrm{d}A]&=\prod_{a,\mu}\prod_{x\in\mathbb{R}^4}\mathrm{d}A^a_\mu(x)\,.\end{aligned} \tag{3.5}$$

In Eq. (3.5) $c\in1,2,3$ corresponds to color, $a\in1,2,\ldots,8$ labels the generators of $SU(3)$, $\alpha\in1,2,3,4$ enumerates the spin and $\mu\in1,2,\ldots,N_d$ is a Lorentz index[1]. We replace the fields A as fundamental degrees of freedom by gauge links U, see Section 3.2.2,

$$\langle\mathcal{O}\left[\psi,\overline{\psi},A\right]\rangle\mapsto\langle\mathcal{O}\left[\psi,\overline{\psi},U\right]\rangle\,. \tag{3.6}$$

We can perform the integral over the fermionic degrees of freedom using Graßmann calculus, e.g., following textbooks like [55]. This changes the weight of each configuration to the fermion determinant times the exponentiated negative gauge action; the observables reduce to functions of gauge links U and propagators G_{ψ_f}:

[1]Throughout this work we will assume a four-dimensional spacetime ($N_d=4$).

$$\frac{1}{Z}\int [\mathrm{d}\psi][\mathrm{d}\overline{\psi}][\mathrm{d}U]\mathcal{O}\left[\psi,\overline{\psi},U\right]\mathrm{e}^{-S_{QCD}} \mapsto \frac{1}{Z}\int [\mathrm{d}U]\prod_f \det\left(\mathcal{D}_f\right)\mathcal{O}\left[G_{\psi_f},U\right]\mathrm{e}^{-S_{\mathrm{gauge}}}, \tag{3.7}$$

where $\mathcal{D}_f$ is the discretized Dirac operator corresponding to flavor f.
Propagators are *Green's functions* of the discretized Dirac operator and thus matrices of size $12 \cdot 12V$ as they have an color and spin entry at each lattice point y for each color spin component on the source position x.
We can denote the propagators as[2]

$$G_{\psi_f}(x,y)^{ab}_{\alpha\beta}[U] \tag{3.8}$$

where we emphasize that the propagators are functions of the gauge links and we denote spin indices by Greek letters and Roman indices are used for color.
The form of Eq. (3.3) is very similar to expectation values in statistical physics (see [51] for a nice overview) and we can exploit that fact by evaluating them numerically using the Monte Carlo method [56].
We create a *Markov Chain* of gauge configurations which are distributed according to the fermion determinant times $\mathrm{e}^{-S_{\mathrm{gauge}}}$. To do this we start from a random gauge configuration and update it with an ergodic algorithm that guarantees that the set of created configurations is closer to the equilibrium ensemble with each new configuration. An efficient algorithm, which also reduces the autocorrelations in the Markov Chain, is hybrid Monte Carlo [57]. We obviously can start measuring only after the configurations are thermalized.
This yields

$$\langle\mathcal{O}\left[\psi,\overline{\psi},A\right]\rangle \approx \frac{1}{N}\sum_{n=1}^{N}\mathcal{O}\left[G_\psi[U_n],U_n\right] + \mathcal{O}(\frac{1}{\sqrt{N}}), \tag{3.9}$$

where N is the number of independent thermalized gauge configurations we have used to measure our observable.
Since our data stem from a Markov chain there is autocorrelation along the Monte Carlo trajectory. The autocorrelation time τ_{int} is generally hard to determine and a detailed explanation is beyond the scope of this section. Nevertheless it can estimated using various methods, e.g., outlined in [58]. When we do not choose to measure only on configurations which are sufficiently separated in Monte Carlo time (several τ_{int}) then we need to bin the data to obtain independent measurements. A typical bin size would

[2] When the notation is clear we sometimes abbreviate the propagators with the flavor of the propagating quark, e.g. for a down quark $G_d(x,y)^{ab}_{\alpha\beta} \equiv D(x,y)^{ab}_{\alpha\beta}$.

be $4\tau_{\mathrm{int}}$.

3.2. Discretization

3.2.1. Spacetime on the lattice

Lattice sites are defined by the components of a four-dimensional integer vector

$$n_l = \begin{pmatrix} 0 \leq n_1 < N_x \\ 0 \leq n_2 < N_y \\ 0 \leq n_3 < N_z \\ 0 \leq n_4 < N_t \end{pmatrix} . \tag{3.10}$$

The spatial volume of the lattice in physical units is $V_3 = L_x L_y L_z = a^3 N_x N_y N_z$, where a is the lattice spacing. Coordinates in continuum space can be constructed by multiplying the lattice coordinates by $a : x = an$ and a shift in direction μ is given as $x' = x + a\hat{\mu}$.

Symanzik improvement prescription [59] is a systematic way to improve the continuum limit of observables on the lattice. The discretization of an observable in the continuum is not unique and equivalent formulations can differ by the order of the corrections in the lattice spacing. Once we have defined an observable with the correct continuum limit we can add correction terms with matching coefficients in order to cancel the leading orders of discretization errors. This typically increases the number of lattice sites involved in an observable and the difficulty of this prescription lies in tuning the coefficient of the correction terms.

3.2.2. Gauge fields on the lattice

To define the discretized gauge covariant derivative one has to introduce gauge links (*gauge connectors*), members of the $SU(3)$-group, instead of the algebra valued gauge fields A as fundamental degrees of freedom. This enables us to preserve gauge symmetry exactly for quantities which correspond to closed paths.
These gauge links connect two lattice sites in μ direction

$$U(x, x+\hat{\mu}) \equiv U_\mu(x) = e^{\mathrm{i}aA_\mu(x)} . \tag{3.11}$$

The link in the other direction is given by

$$U(x, x-\hat{\mu}) \equiv U_{-\mu}(x) = e^{-\mathrm{i}aA_\mu(x)} = U^\dagger(x-\hat{\mu}, x) . \tag{3.12}$$

The discretized action for gauge fields proposed by Wilson [7] is defined by

$$S_G^W[U] = \beta \sum_x \sum_{\mu>\nu} \mathrm{tr}\{1 - \frac{1}{N_c} \mathrm{Re}\ U_{\mu\nu}(x)\}, \tag{3.13}$$

where the sum runs over all lattice sites x, $\beta \equiv \frac{2N_c}{g^2}$ is a common abbreviation and $U_{\mu\nu}(x)$ is a gauge invariant product of gauge links called plaquette:

$$U_{\mu\nu}(x) = \mathrm{tr} U_\mu(x) U_\nu(x+\hat{\mu}) U_{-\mu}(x+\hat{\nu}+\hat{\mu}) U_{-\nu}(x+\hat{\nu})\,. \tag{3.14}$$

This gauge action has discretization errors of $\mathcal{O}(a^2)$. Following the Symanzik prescription, the Lüscher-Weisz action [60] with 1-loop improved coefficients reduces the discretization effects to $\mathcal{O}(g^4a^2, a^4)$. As we will use a fermion action which is improved only to $\mathcal{O}(a^2)$, we will use the standard Wilson gauge action.

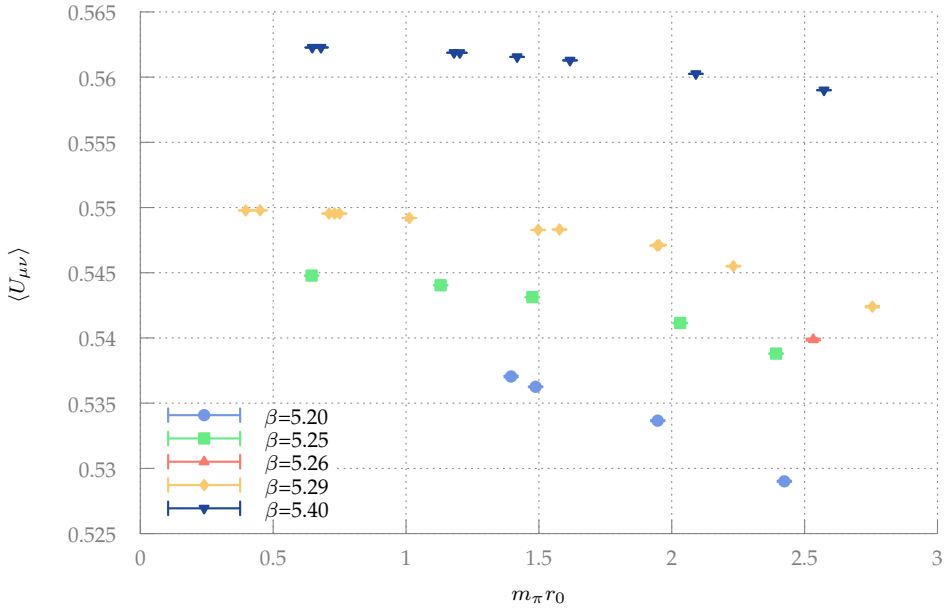

Figure 3.1.: Average plaquette versus the pion mass on $N_f = 2$ Wilson Clover configurations for various values for the gauge coupling. The dynamical quarks clearly change the gluonic observables.

3.2.3. Fermions on the lattice

The naive discretization of the Dirac operator $\mathcal{D}$

$$\mathcal{D}(x,y)^{ab}_{\alpha\beta} = \sum_{\mu=1}^{4} (\gamma_\mu)_{\alpha\beta} \frac{1}{2a} \left[U_\mu(x)_{ab} \delta_{x+\hat{\mu},y} - U_{-\mu}(x)_{ab} \delta_{x-\hat{\mu},y} \right] + m \delta_{\alpha\beta} \delta_{ab} \delta_{x,y} \,, \tag{3.15}$$

suffers from the doubling problem. To explain this we first note that the finite box size of our lattice induces a momentum cut-off and thus the dispersion relation is periodic on the lattice ($p^2 \to a^{-2} \sin^2(pa)$). Thus the massless propagator has additional (and unphysical) poles at the edges of the Brillouin zone. Poles in the propagator correspond to particles [61] and the unphysical ones are called doublers. They would cancel the axial anomaly [62] as shown in, e.g., [63]. To circumvent these doublers, Wilson suggested to add a mass-like term $(-\frac{a}{2}\partial_\mu\partial_\mu)$ with vanishing continuum limit to the action [7]. This explicitly breaks chiral symmetry on the lattice.
The Wilson Dirac operator is then

$$\mathcal{D}_W(x,y)^{ab}_{\alpha\beta} = \left(m_0 + \frac{4}{a} \right) \delta_{\alpha\beta} \delta_{ab} \delta_{x,y} - \frac{1}{2a} \sum_{\mu=\pm1}^{\pm4} (\mathbb{1} - \gamma_\mu)_{\alpha\beta} U_\mu(x)_{ab} \delta_{x+\hat{\mu},m} \,, \tag{3.16}$$

and m_0 undergoes additive renormalization.
We can rewrite the Wilson Dirac operator as

$$\mathcal{D}_W = C \left(\mathbb{1} - \kappa H \right) \,, \tag{3.17}$$

where $C = m_0 + 4/a$ is often absorbed in the quark field definitions, the hopping parameter $\kappa = (2(am_0 + 4))^{-1}$ and the hopping term H is the sum in Eq. (3.16). This is conventionally done when writing code for simulations and thus the parameter κ is commonly used to describe the quark mass parameter.
The Wilson Dirac operator is γ_5 hermitian[3], i.e.,

$$\mathcal{D}_W^\dagger = \gamma_5 \mathcal{D}_W \gamma_5 \,. \tag{3.18}$$

This property is inherited to propagators, i.e., the inverse of the Dirac operators

$$G_\psi^\dagger(y,x) = \gamma_5 G_\psi(x,y) \gamma_5 \,, \tag{3.19}$$

where the hermitian conjugation is meant in color, the spatial transposition was already explicitly written.
Following the Symanzik improvement [59] prescription one can add the so called *clover*

[3] There are also other discretizations of the Dirac operator with this property.

term

$$S_{sw} = c_{sw} \frac{\mathrm{i}}{4} a^5 \sum_x \overline{\psi}(x) \sigma_{\mu\nu} F_{\mu\nu} \psi(x) \,, \tag{3.20}$$

to the action to obtain the $\mathcal{O}(a^2)$ improved Sheikholeslami-Wohlert action [64]. The coefficient c_{sw} can be computed non-perturbatively using the Schrödinger-functional [65]. Note that the addition of this term implies a redefinition of the bare parameters m_0 and $\beta = 6/g^2$. This preserves γ_5 hermiticity.
In this work we consider the effect of the broken chiral symmetry on the lattice as acceptable for the quantities we are interested in and use clover Wilson fermions. There are however more expensive (in terms of computer time) actions available, which have a better chiral behavior [66] [67] [68].

3.3. Linear system solving

3.3.1. Algorithms

The Dirac operator is a sparse matrix, and its action on a vector is computationally cheap. The inverse of the Dirac operator is a full matrix of dimension $12V \times 12V$ and thus propagators from all points in the volume to all points in the volume are too big to fit into the memory of our systems for the lattices we typically use.
The way out is to construct only the action of the inverse matrix on a source vector. This can be done by iterative Krylov subspace [69] methods. A prominent example is the BiCGstab [70] algorithm, which works most of the times but sometimes does not converge. The conjugate gradient [71] has stable convergence properties and can thus be used for the truncated solver method (TSM) [72] or the all-mode averaging (AMA) [73] and it was used for our results when the BiCGstab failed.
Modern solvers employ multi-grid methods, e.g., [74] or domain decomposition with inexact deflation, which is explained in [75]. Both of these algorithms were used to generate the results for Chapter 5 and Chapter 7.

3.3.2. Point-to-all Propagators

The system we generally solve is

$$\sum_y \mathcal{D}^{ab}_{\alpha\beta}(x,y) \chi^b_\beta(y) = \eta^a_\alpha(x) \,. \tag{3.21}$$

To get the propagation from a point x to all other lattice points y we need to choose the source η as a (smeared) δ-source for each color spin combination separately. We can

then combine these twelve[4] solutions χ to form the propagator

$$G_\psi(x,y)^{ab}_{\alpha\beta}[U]\,, \tag{3.22}$$

where the flavor ψ is determined by the κ we have used in the discretized Dirac operator, so that propagators of different quark flavors are distinguished by the masses of the respective quarks.

3.3.3. All-to-all Propagators

In the computation of the (smeared) point-to-all propagator we have to invert separately for each of the twelve color/spin component to construct the full propagator. To do this for a large subset[5] of the lattice is impractical. Following the conventions of [76] we can estimate a projector to our subspace by seeding N white noise source vectors η, with the property

$$\frac{1}{N}\sum_{n=1}^{N}\eta_i^{(n)}\eta_j^{(n)\dagger} = \delta_{ij} + \mathcal{O}(\frac{1}{\sqrt{N}})\,, \tag{3.23}$$

on it. Here the indices i, j correspond to lattice site, color and spin on the subset. In [77] it was shown that $\mathbb{Z}_2 \times \mathrm{i}\mathbb{Z}_2$ source vectors $\eta_{\alpha,a}(x) = \frac{1}{\sqrt{2}}(v + \mathrm{i}w)$ with $v, w \in \pm 1$ are well suited for this purpose.
Solution vectors χ are obtained by solving Eq. (3.21):

$$\chi_i^{(n)} = \mathcal{D}^{-1}_{ij}\eta_j^{(n)}\,. \tag{3.24}$$

Now switching to an explicit index notation, we can reconstruct the propagator from

$$\frac{1}{N}\sum_{n=1}^{N}\chi_\beta^{(n),b}(z)\eta_\alpha^{(n)\dagger,a}(y) = G^{ba}_{\beta\alpha}(z,y)\left(\mathbb{1} + \mathcal{O}(\frac{1}{\sqrt{N}})\right)\,. \tag{3.25}$$

This estimation gets better if we use more and more source vectors, but we can hope that we need significantly less noise vectors than we have points (lattice-site, color, and spin combinations) in our subset.
Strategies to improve the signal-to-noise ratio include: dividing the subset into even smaller subsets and reconstructing each subsubset separately (dillution [78]) or reducing the number of contributing paths with the hopping parameter expansion [76, 79]. The former was tried in this work (see Section 6.1.2) without much success and the latter could not be used, as all path lengths were needed.

[4] One for each α, a.
[5] A subset could be, e.g., the whole lattice, or a single time-slice; it could be color and or spin diluted.

3.4. Smoothing techniques

3.4.1. Link smearing

The links on the lattice fluctuate wildly on short distances due to the ultraviolet degrees of freedom. Smearing procedures suppress these UV fluctuations while leaving the infrared sector intact. For long range quantities, like the topological charge or the heavy quark potential, that depend only on the infrared degrees of freedom one can use smearing techniques to improve the signal-to-noise ratio. If this is done in a gauge invariant way the links are still gauge connectors and can be used in a quark smearing algorithm (see Section 3.4.2). To keep the eigenvalues of the transfer matrix and thus the spectrum intact the link smearing can only be done on the spatial directions, if it is used as an input for the quark smearing.

A way to perform this link smearing was suggested in [80] and is named after the APE-collaboration[81] and was also described in [82]. Here we add staples

$$C_{\mu\nu}^{(n)}(x) = U_{\nu}^{(n)}(x)U_{\mu}^{(n)}(x+\hat{\nu})U_{-\nu}^{(n)}(x+\hat{\mu}+\hat{\nu}) + U_{-\nu}^{(n)}(x)U_{\mu}^{(n)}(x-\hat{\nu})U_{\nu}^{(n)}(x-\hat{\nu}+\hat{\mu}) \quad (3.26)$$

to an existing link in an iterative procedure

$$U_{\mu}^{(n+1)}(x) = \mathcal{P}_G \left\{ \alpha_{APE} U_{\mu}^{(n)}(x) + \sum_{\nu \neq \mu,\rho} C_{\mu\nu}^{(n)}(x) \right\} , \quad (3.27)$$

where we can specify a direction ρ in which we do not smear[6] and we leave the $SU(3)$ of the links and thus have to project back to it with $\mathcal{P}_G$. This projection is not unique and we choose

$$\mathcal{P}_G\{V\} = X \in SU(3) \mid \max \left\{ \mathrm{Re}\,\mathrm{tr}\left(\left[XV^{\dagger} \right] \right) \right\} . \quad (3.28)$$

The smearing parameter α_{APE} can be chosen freely and a way to fix it would be to determine at which value the plaquette drops the most after one smearing iteration. Throughout this work $\alpha_{APE} = 2.5$ was taken. An alternative to APE-smearing would be STOUT smearing [83] where the smearing is applied by multiplication and thus we do not leave the group. The iteration step is

$$U_{\mu}^{(n+1)}(x) = e^{\mathrm{i}Q_{\mu}^{(n)}(x)} U_{\mu}^{(n)}(x) , \quad (3.29)$$

[6] For spatial APE-smearing we would apply this procedure to $\mu \in 1, 2, 3$ and choose $\rho = 4$.

where

$$Q_\mu^{(n)}(x) = \frac{\mathrm{i}}{2}\left(\Omega^{(n)}(x)^\dagger - \Omega^{(n)}(x) - \frac{\mathbb{1}}{3}\mathrm{tr}\left[\Omega^{(n)}(x)^\dagger - \Omega^{(n)}(x)\right]\right), \tag{3.30}$$

$$\Omega^{(n)}(x) = \left(\sum_{\nu\neq\mu}\rho_{\mu\nu}C_{\mu\nu}^{(n)}(x)\right)U_\mu^{(n)}(x)^\dagger, \tag{3.31}$$

and the weight factors $\rho_{\mu\nu}$ are real.

3.4.2. Quark smearing

In Eq. (3.21) we have seen that we compute the propagator by inverting on a source vector. This can be for example a δ-source, meaning that we have only one non-zero color/spin component at a single lattice site. This makes the interpretation of the propagator straightforward as it is starting at a single site. When we consider an extended (*smeared*) spatial object in color space, centered at a lattice site with fixed spin, this interpretation still holds. As this would not change the quantum numbers of our interpolating operators, which we define in Section 3.5.4.1, this is a nice way to change their overlap with the physical states. Of course, smearing can also be applied to the sink of the propagator and also the sink vectors, as well as the source vectors after the inversion of an all-to-all propagator can be smeared.

An iterative procedure that produces a Gaussian shape in a gauge covariant way is Wuppertal smearing [84]:

$$\psi^{(n+1)}(x) = \frac{1}{1+2(d-2)\alpha_{Wup}}\left(\psi^{(n)}(x) + \alpha_{Wup}\sum_{j=\pm1}^{\pm3}U_j(x)\psi^{(n)}(x+\hat{j}a)\right). \tag{3.32}$$

A typical choice is $\alpha_{Wup} = 0.25$, which was used throughout this work. This smearing does not extend the source in the time direction and it is spin-diagonal. For δ-sources it only needs to be performed on the source time-slice and for each color entry. The spin-entries of the same color are the same and thus the result of the smearing can be re-used.

In this work we use APE-smeared gauge links for the gauge connectors in Eq. (3.32). As it was illustrated in [85] this smoothens the resulting shape of the quark source. Without such a link smearing short-range fluctuations can distort the resulting shape significantly [86].

3.5. Hadron spectroscopy

To study the energies of hadrons on the lattice one has to compute two-point functions, which are correlation functions of a creation and annihilation operator. The relation between these energies and the two-point functions will be clarified in Section 3.5.1. Baryons are slightly more complicated than mesons, as they require projection to definite parity and their parity partners will appear as backward propagating particles. This subtleties will be treated in Section 3.5.4.4. This chapter is meant to clarify the functional form of the excited state contributions that pollute the ground-state signal and the handles one can pull to reduce their effect. We will follow the line of argument found in [87].

3.5.1. Euclidean correlators

The correlator of two gauge invariant operators, e.g., local fields or fields connected by gauge transporters, is given by

$$\langle \mathcal{O}_1(t_1)\mathcal{O}_2(t_2)\rangle = \frac{1}{Z}\mathrm{tr}\left\{\mathrm{e}^{(L_t-t_1)\hat{H}}\mathcal{O}_1\mathrm{e}^{(t_1-t_2)\hat{H}}\mathcal{O}_2\mathrm{e}^{t_2\hat{H}}\right\} \tag{3.33}$$

where

- we set $t_1 > t_2$ to avoid writing the time ordered product in the definition,
- the discretized equivalent to the time evolution operator $e^{-\hat{H}a}$ with the Hamilton operator $\hat{H}$ is also called the transfer matrix $\hat{S}$,
- the partition function $Z = \mathrm{tr}\{\mathrm{e}^{L_t\hat{H}}\}$, yields, if we normalize our energies such that the ground state energy vanishes ($E_0 = 0$) and in the limit $L_t \to \infty : Z = 1$,
- and the operators $\mathcal{O}_i$ act in the Hilbert space and correspond to the fields $\mathcal{O}_i(t)$.

Since we do not distinguish any particular time-slice we need to define the temporal boundary conditions[7] here to make the formula valid for any t: We use periodic boundary conditions for bosons, in particular the gauge fields, and antiperiodic boundaries for fermionic fields [8] . Spatial boundaries are always periodic.
We normalize our lattice states such that

$$\mathbb{1} = \sum_n \mid n\rangle\langle n \mid \tag{3.34}$$

[7] Autocorrelation times increase rapidly with smaller lattice spacings [88]. A way out are open boundary conditions [89] in the temporal direction. Then one needs to stay away from the edges in t-direction for spectroscopy and for the sake of brevity we do not go into detail about this here.
[8] The implementation of this is clarified in Section 3.5.3

and the connection to the continuum states is given by

$$\mid 0\rangle_{\text{lattice}} = \mid 0\rangle_{\text{continuum}} \equiv \mid 0\rangle \tag{3.35}$$

$$\mid n\rangle_{\text{continuum}} \equiv \mid n\rangle_c = \sqrt{2V_3 E_n} \mid n\rangle, \qquad n \neq 0 \qquad \text{and} \qquad E_0 = 0. \tag{3.36}$$

This can be seen from the normalization conditions

$$_c\langle n(\vec{p}) \mid n(\vec{q})\rangle_c = 2E_n(\vec{p})\delta(\vec{p}-\vec{q}) \tag{3.37}$$

$$\langle n(\vec{p}) \mid n(\vec{q})\rangle = \delta_{\vec{p}-\vec{q}}, \tag{3.38}$$

and by integrating both equations over all momenta $\vec{q}$.

We can insert complete sets of lattice states into Eq. (3.33) to evaluate the trace:

$$\begin{aligned}\langle \mathcal{O}_1(t_1)\mathcal{O}_2(t_2)\rangle &= \sum_{\mu,\nu} \mathrm{e}^{-E_\mu(L_t-t_1)}\langle \mu \mid \mathcal{O}_1 \mid \nu\rangle \mathrm{e}^{-E_\nu(t_1-t_2)}\langle \nu \mid \mathcal{O}_2 \mid \mu\rangle \mathrm{e}^{-E_\mu t_2} \\ &= \sum_{\mu,\nu} \mathrm{e}^{-E_\mu(L_t-\Delta t)}\langle \mu \mid \mathcal{O}_1 \mid \nu\rangle \mathrm{e}^{-E_\nu \Delta t}\langle \nu \mid \mathcal{O}_2 \mid \mu\rangle \end{aligned} \tag{3.39}$$

where we see that the correlation function depends only on the separation in Euclidean time $\Delta t = t_1 - t_2$, thus we will in the following always set $t_2 = 0$ and denote $\Delta t \equiv t$.

The sum over all states includes states with different spin and to make this explicit we can write Eq. (3.39) as

$$\langle \mathcal{O}_1(t)\mathcal{O}_2(0)\rangle = \sum_{\mu,\nu}\sum_{\sigma,\sigma'} \mathrm{e}^{-E_\mu(L_t-t)}\langle \mu,\sigma \mid \mathcal{O}_1 \mid \nu,\sigma'\rangle \mathrm{e}^{-E_\nu t}\langle \nu,\sigma' \mid \mathcal{O}_2 \mid \mu,\sigma\rangle\,. \tag{3.40}$$

Note that the energies of states that differ only in their spin are degenerate and we will suppress the spin dependence of the states in the notation, wherever it is possible.

In this sum, if the states $\mu = \nu = 0$, we obtain a term proportional to

$$\langle 0 \mid \mathcal{O}_1 \mid 0\rangle\langle 0 \mid \mathcal{O}_2 \mid 0\rangle\,. \tag{3.41}$$

When we are interested in hadronic quantities we use $\mathcal{O}_i$ which create or annihilate a hadron and then those terms will be zero. Typically we consider matrix elements with

$$\mathcal{O}_2 = \mathcal{O}_1^\dagger \gamma_4 = \overline{\mathcal{O}_1}\,. \tag{3.42}$$

Ground state contributions will dominate those matrix elements for large t:

$$\sum_{\mu}\sum_{\nu}\langle\nu \mid \mathcal{O} \mid \mu\rangle\langle\mu \mid \overline{\mathcal{O}} \mid \nu\rangle \mathrm{e}^{-E_\mu t}\mathrm{e}^{-E_\nu(L_t-t)} \approx \sum_{\mu}\langle 0 \mid \mathcal{O} \mid \mu\rangle\langle\mu \mid \overline{\mathcal{O}} \mid 0\rangle \mathrm{e}^{-E_\mu t} + \sum_{\nu}\langle\nu \mid \mathcal{O} \mid 0\rangle\langle 0 \mid \overline{\mathcal{O}} \mid \nu\rangle \mathrm{e}^{-E_\nu(L_t-t)} \,. \tag{3.43}$$

3.5.2. Effective mass

As we have seen in the previous section the two-point function is measured on the lattice as a tower of states which all decay exponentially with increasing Euclidean time separation from the source. For sufficiently long distances in Euclidean time, the baryonic correlator decays like a single exponential, with the ground state energy in the exponent. To judge at which time-slice the single exponential can be reliably extracted from the data one defines the effective mass of baryons in lattice units as

$$am_{\mathrm{eff}}^{\mathrm{baryon}}(t/a+\frac{1}{2}) = \ln\left(\frac{C^{2pt}(t/a)}{C^{2pt}(t/a+1)}\right) . \tag{3.44}$$

This converges to a constant as higher energy states die out for increasing Euclidean time separations form the baryon source.
For mesons the correlator behaves like a hyperbolic cosine and one can define the effective mass for mesons accordingly by solving

$$\frac{C^{2pt}(t/a)}{C^{2pt}(t/a+1)} = \frac{\cosh\left(am_{\mathrm{eff}}^{\mathrm{meson}}\cdot(t/a-N_t/2)\right)}{\cosh\left(am_{\mathrm{eff}}^{\mathrm{meson}}\cdot(t/a+1-N_t/2)\right)} . \tag{3.45}$$

In the following, when we mention the effective mass of a particle, we use the appropriate formula.

3.5.3. Implementation of antiperiodic boundary conditions for fermions

Antiperiodic boundary conditions for fermions are usually implemented by multiplying the gauge links on the temporal boundary by -1 in the gauge field used to construct the discretized Dirac operator. This encodes the boundary conditions correctly in the propagators. When we now construct a meson – an object build out of two propagators – the sign change on the boundary cancels. For baryons (three propagators) it has to be corrected for, so we have to multiply the two-point function by -1 on the source-sink-separations that cross the boundary. For three-point functions of baryons we need to multiply by -1 if $t_{\mathrm{sink}} < t_{\mathrm{source}}$. For covariant derivatives on propagators we have to

correct it as well and the method of choice is to use the same gauge field that we have used to construct the discretized Dirac operator.

3.5.4. Nucleon spectroscopy

3.5.4.1. Interpolating operators

To study the nucleon on the lattice we have to use interpolating operators with the right quantum numbers. They have to be symmetric in $u \leftrightarrow u$ and antisymmetric in $u \leftrightarrow d$. Candidates for that are discussed in Section 7.1.2.1 and for the moment it is sufficient to assume[9]

$$\mathcal{N}_\alpha(x) = \varepsilon^{abc} u^a_\alpha(x) \left(u^{T,b}_\beta(x) (C\gamma_5)^{\beta\gamma} d^c_\gamma(x) \right) , \tag{3.46}$$

$$\overline{\mathcal{N}}_{\overline{\alpha}}(x) = \varepsilon^{\overline{a}\overline{b}\overline{c}} \left(\overline{u}^{T,\overline{b}}_{\overline{\beta}}(x) (C\gamma_5)^{\overline{\beta}\overline{\gamma}} \overline{d}^{\overline{c}}_{\overline{\gamma}}(x) \right) \overline{u}^{\overline{a}}_{\overline{\alpha}}(x) , \tag{3.47}$$

where the charge conjugation matrix is C, $\mathcal{N}$ is a nucleon-type annihilation operator and a $\overline{\mathcal{N}}$ nucleon-type creation operator.

The overlap factors of this operators with continuum and lattice states will be shown in Section 3.5.4.3. The operators have mass dimension[10] $3/2$, so that the quark fields have dimension $1/2$.

To get an overlap with only one definite momentum state we can define

$$\overline{\mathcal{N}}_\alpha(\vec{p}, t) = a^3 \sum_{\vec{x}} \overline{\mathcal{N}}_\alpha(\vec{x}, t) e^{-\mathrm{i}\vec{p}\cdot\vec{x}} . \tag{3.48}$$

The Wick contractions are performed as follows

$$\langle d^a_\alpha(x) u^b_\beta(x) u^c_\gamma(x) \overline{u}^{\overline{c}}_{\overline{\gamma}}(0) \overline{d}^{\overline{a}}_{\overline{\alpha}}(0) \overline{u}^{\overline{b}}_{\overline{\beta}}(0) \rangle \propto$$

$$D^{a\overline{a}}_{\alpha\overline{\alpha}}(x,0) \left(U^{b\overline{b}}_{\beta\overline{\beta}}(x,0) U^{c\overline{c}}_{\gamma\overline{\gamma}}(x,0) - U^{b\overline{c}}_{\beta\overline{\gamma}}(x,0) U^{c\overline{b}}_{\gamma\overline{\beta}}(x,0) \right) . \tag{3.49}$$

[9] Since we assume to be in Euclidean spacetime upper and lower indices are not distinguished.

[10] This is true in the standard Lagrangian formulation Eq. (3.1), if one works in the fermion action formulation Eq. (3.17) one often rescales the fields to absorb the constant C.

3.5.4.2. Projection operators to definite parity

Common choices for a projection operator $\mathcal{P}$ are the unpolarized projector with positive or negative parity

$$\mathcal{P}_{\text{Unpol.}\,\pm} \equiv \mathcal{P}^u_\pm = \frac{1}{2}\left(1 \pm \gamma_t\right) , \tag{3.50}$$

which averages over spin up and down and in the polarized projectors

$$\mathcal{P}_{\text{Pol}_x\,\pm} \equiv \mathcal{P}^x_\pm = \frac{1}{2}\left(1 \pm \gamma_t\right)\left(-\mathrm{i}\gamma_x\gamma_5\right) \tag{3.51}$$

$$\mathcal{P}_{\text{Pol}_y\,\pm} \equiv \mathcal{P}^y_\pm = \frac{1}{2}\left(1 \pm \gamma_t\right)\left(-\mathrm{i}\gamma_y\gamma_5\right) \tag{3.52}$$

$$\mathcal{P}_{\text{Pol}_z\,\pm} \equiv \mathcal{P}^z_\pm = \frac{1}{2}\left(1 \pm \gamma_t\right)\left(-\mathrm{i}\gamma_z\gamma_5\right) \tag{3.53}$$

which project to spin up along the projection axis minus spin down along the projection axis. A generic projector to positive parity will be abbreviated $\mathcal{P}_+$.

3.5.4.3. Overlap factors

The overlap with the physical nucleon on the lattice is given by[11]

$$\langle 0 \mid \mathcal{N}_\alpha(\vec{x}, 0) \mid N, \vec{p}, \sigma\rangle_c = e^{\mathrm{i}\omega}\sqrt{Z(\vec{p},\phi)}\, U_\alpha(N, \vec{p}, \sigma) e^{\mathrm{i}\vec{p}\cdot\vec{x}} \tag{3.54}$$

$${}_c\langle N, \vec{p}, \sigma \mid \overline{\mathcal{N}}_\alpha(\vec{x}, 0) \mid 0\rangle = e^{-\mathrm{i}\omega}\sqrt{Z(\vec{p},\phi)}\, \overline{U}_\alpha(N, \vec{p}, \sigma) e^{-\mathrm{i}\vec{p}\cdot\vec{x}} , \tag{3.55}$$

where U, $\overline{U}$ are the (anti-) particle solutions to the Dirac equation, see [90] p. 45 and following, and and the connection to the states on the lattice is following Eq. (3.36) given by

$$\mid N, \vec{p}, \sigma\rangle_c = \sqrt{2V_3 E_N(\vec{p})} \mid N, \vec{p}, \sigma\rangle_{\text{lattice}} \equiv \sqrt{2V_3 E_N(\vec{p})} \mid N, \vec{p}, \sigma\rangle , \tag{3.56}$$

where V_3 is the spatial volume of the lattice.
The phase ω is mostly irrelevant as the nucleon two-point function has a creation and annihilation operator and their phases cancel, thus we drop it in the following. The variable ϕ should indicate that the smearing of the single quark fields of the interpolating operator influences the overlap with the physical states. Due to the smearing we have to allow for a momentum dependence in our overlap factors.
Since a sum over the spin of the nucleon states in the continuum is always implied (see

[11] We follow notes by Meinulf Göckeler here for our conventions.

Eq. (3.40)) we note that the relation

$$\sum_{\sigma} U(\vec{p},\sigma)\overline{U}(\vec{p},\sigma) = -\mathrm{i}\not{p} + m \tag{3.57}$$

can be used. We find

$$\mathrm{tr}\left\{\mathcal{P}_{\mathrm{Unpol.}\,+} U(\vec{p},\sigma)\overline{U}(\vec{p},\sigma)\right\} = \frac{1}{2}\mathrm{tr}\{\mathbb{1}\}(E(\vec{p})+m) = 2(E(\vec{p})+m)\,. \tag{3.58}$$

3.5.4.4. Evaluation of the nucleon two-point function

The nucleon two-point function is given by

$$C^{2pt}_{\mathcal{P}_+}(\vec{p},t) = V_3 a^3 \sum_{\vec{x}\in V_3} e^{-\mathrm{i}\vec{p}\cdot\vec{x}}\mathrm{tr}\left\{\mathcal{P}_+^{\alpha\alpha'}\langle\mathcal{N}^{\alpha'}(\vec{x},t)\overline{\mathcal{N}}^{\alpha}(0,0)\rangle\right\}\,. \tag{3.59}$$

To evaluate this we need to insert two complete sets and we can use the approximation Eq. (3.43). This reduces the trace to

$$\begin{aligned}\mathrm{tr}\left\{\mathcal{P}_+^{\alpha\alpha'}\langle\mathcal{N}^{\alpha'}(\vec{x},t)\overline{\mathcal{N}}^{\alpha}(0)\rangle\right\} &= \sum_{\nu\alpha}\langle 0 \mid (\mathcal{P}_+\mathcal{N})_\alpha \mid \nu\rangle\langle\nu \mid \left(\mathcal{P}_+\overline{\mathcal{N}}\right)_\alpha \mid 0\rangle \mathrm{e}^{E_\nu t} \\ &+ \sum_{\nu\alpha}\langle\nu \mid (\mathcal{P}_+\mathcal{N})_\alpha \mid 0\rangle\langle 0 \mid \left(\mathcal{P}_+\overline{\mathcal{N}}\right)_\alpha \mid \nu\rangle \mathrm{e}^{E_\nu(L_t-t)}\,,\end{aligned} \tag{3.60}$$

where we have used $\mathcal{P}_+ = \mathcal{P}_+\mathcal{P}_+$. As we project to positive parity we obtain positive parity particles and antiparticles of particles with negative parity. To evaluate this term by term we note that

$$\langle\nu \mid \mathcal{P}_+\overline{\mathcal{N}} \mid 0\rangle \neq 0 \tag{3.61}$$

only if ν has positive parity and baryon number +1. The lowest state that fulfills this requirement is the nucleon[12], which in QCD has a mass of about 938 MeV [28]. Similarly, we need positive parity and baryon number -1 for

$$\langle\nu \mid \mathcal{P}_+\mathcal{N} \mid 0\rangle \neq 0\,. \tag{3.62}$$

We find that the lowest available state fulfilling that is the antiparticle of the N^*. The N^* is the parity partner of the nucleon and has a mass of around 1520MeV [91], which is heavier than the first excitation of the nucleon in nature, the so called Roper excitation (1440 MeV [91]).

[12] We neglect electromagnetism and isospin breaking and thus proton (938.27 MeV [91]) and neutron (939.57 MeV [91]) are considered the same.

Now we can write down Eq. (3.60) for the unpolarized nucleon in a nicer way, where we denote excitations by a prime

$$\begin{aligned}\frac{C^{2pt}_{\mathcal{P}^u_+}(\vec{p},t)}{V_3} &= Z_N(\vec{p},\phi)\frac{E_N+m_N}{E_N}\mathrm{e}^{-E_N t} + Z_{N'}(\vec{p},\phi)\frac{E_{N'}+m_{N'}}{E_{N'}}\mathrm{e}^{-E_{N'}t} + \dots \\ +Z_{N^*}(\vec{p},\phi)\frac{E_{N^*}+m_{N^*}}{E_{N^*}}\mathrm{e}^{-E_{N^*}(L_t-t)} &+ Z_{N^{*\prime}}(\vec{p},\phi)\frac{E_{N^{*\prime}}+m_{N^{*\prime}}}{E_{N^{*\prime}}}\mathrm{e}^{-E_{N^{*\prime}}(L_t-t)} + \dots ,\end{aligned} \tag{3.63}$$

where $Z_{N^*} = Z_{\overline{N}^*}$, $E_{N^*} = E_{\overline{N}^*}$, etc. and we assumed that we smear the sink and source in the same way. Otherwise we would have to replace

$$Z_N(\vec{p},\phi) \to e^{i(\omega_{\text{sink}}-\omega_{\text{source}})}\sqrt{Z_N(\vec{p},\phi_{\text{sink}})}\sqrt{Z_N(\vec{p},\phi_{\text{source}})}\,. \tag{3.64}$$

Eq. (3.63) is readily interpreted as the fact that particles propagate forward in time and antiparticles propagate backwards.

3.5.4.5. Signal to noise ratio

For large time extents L_t one can extract the particles for $t \ll L_t/2$ and can neglect the antiparticle contributions in this range. For $0 \ll t$ the ground state should dominate. The signal-to-noise ratio $S_{N_\nu}(t)$ for nucleon correlators decreases as [92]

$$S_{\mathcal{N}_\nu}(t) = \sqrt{N}e^{-\left(m_{N_\nu}-\frac{3}{2}m_\pi\right)t}\,. \tag{3.65}$$

For a pedagogical derivation of this see [53], section 9.3.2. Thus choosing an appropriate range of t to extract the ground state is an art of its own, due to the competing requirements of large (no excitations visible) and low (good signal) t_{start}. In Chapter 7 we will try to find methods to reduce the distance from the source in Euclidean time at which the ground state dominates.

3.5.5. Other baryons

The contractions for the octet follow the contractions for the nucleon. In [93] there is a very elegant way of organizing the contractions which we will follow here. First we define

$$\begin{aligned}B^{C\gamma_5}_{\mathcal{P}}(G_1,G_2,G_3) = \epsilon^{abc}\epsilon^{a'b'c'}\mathrm{tr}\big\{&\mathcal{P}G_1^{aa'}\mathrm{tr}_D[(C\gamma_5)^T G_3^{cc'T}(C\gamma_5)G_2^{bb'}] \\ &+ \mathcal{P}G_1^{aa'}(C\gamma_5)^T G_3^{cc'T}(C\gamma_5)G_2^{bb'}\big\}\end{aligned} \tag{3.66}$$

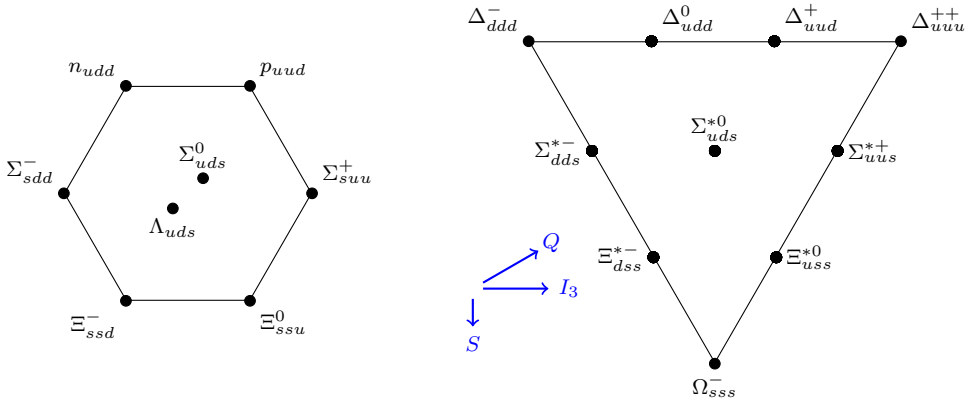

Figure 3.2.: The spin $\frac{1}{2}$ baryon octet and spin $\frac{3}{2}$ decuplet for the three lightest flavors. Q is the electrical charge, S is the strangeness and I_3 is the z-component of the iso-spin.

and a short comparison shows that with this the two-point function for the proton is given by

$$\begin{aligned} C^{\overline{N}N}_{\mathcal{P}}(\vec{p},t) &= V_3 a^3 \sum_{\vec{x}\in V_3} \mathrm{e}^{-\mathrm{i}\vec{p}\cdot\vec{x}} \mathcal{P}_{\overline{\gamma}\gamma} \langle N_\gamma(x) \overline{N}_{\overline{\gamma}(0)} \rangle \\ &= V_3 a^3 \sum_{\vec{x}\in V_3} \mathrm{e}^{-\mathrm{i}\vec{p}\cdot\vec{x}} B^{C\gamma_5}_{\mathcal{P}}(U(x,0), U(x,0), D(x,0)) \,. \end{aligned} \tag{3.67}$$

Here is a list of two-point functions in the octet:

$$C^{\overline{\Sigma}^+\Sigma^+}_{\mathcal{P}}(\vec{p},t) = V_3 a^3 \sum_{\vec{x}\in V_3} \mathrm{e}^{-\mathrm{i}\vec{p}\cdot\vec{x}} B^{C\gamma_5}_{\mathcal{P}}(U,U,S) \tag{3.68}$$

$$C^{\overline{\Xi}^0\Xi^0}_{\mathcal{P}}(\vec{p},t) = V_3 a^3 \sum_{\vec{x}\in V_3} \mathrm{e}^{-\mathrm{i}\vec{p}\cdot\vec{x}} B^{C\gamma_5}_{\mathcal{P}}(S,S,U) \tag{3.69}$$

$$C^{\overline{\Sigma}^0\Sigma^0}_{\mathcal{P}}(\vec{p},t) = V_3 a^3 \sum_{\vec{x}\in V_3} \mathrm{e}^{-\mathrm{i}\vec{p}\cdot\vec{x}} \{B^{C\gamma_5}_{\mathcal{P}}(D,U,S) + B^{C\gamma_5}_{\mathcal{P}}(U,D,S)\} \tag{3.70}$$

$$C_{\mathcal{P}}^{\overline{\Lambda}_8\Lambda_8}(\vec{p},t) = V_3 a^3 \sum_{\vec{x}\in V_3} \mathrm{e}^{-\mathrm{i}\vec{p}\cdot\vec{x}}\{2B_{\mathcal{P}}^{C\gamma_5}(S,D,U)+2B_{\mathcal{P}}^{C\gamma_5}(S,U,D) \\ +2B_{\mathcal{P}}^{C\gamma_5}(D,S,U)+2B_{\mathcal{P}}^{C\gamma_5}(U,S,D) \\ +B_{\mathcal{P}}^{C\gamma_5}(D,U,S)+B_{\mathcal{P}}^{C\gamma_5}(U,D,S)\} \tag{3.71}$$

3.6. Evaluation of three-point functions

Loosely formulated a three-point function is a two-point function with a current insertion. We consider currents of the form

$$\mathcal{J}(f_1,f_2,x,x_1,x_2,\vec{q},\mathcal{O}) = a^3 \sum_{\vec{x}\in V_3} \mathrm{e}^{\mathrm{i}\vec{q}\cdot\vec{x}}\overline{\Psi}_{f_1}{}^{a}_{\alpha}(x_1)\mathcal{O}^{ab}_{\alpha\beta}(x,x_1,x_2)\Psi_{f_2}{}^{b}_{\beta}(x_2)\,. \tag{3.72}$$

This is the most general form of currents, where we create a quark of flavor f_1 and destroy one of flavor f_2. The indices in color and Dirac space are fully contracted and the position of the insertion is summed over. This means that if the quarks are at different positions gauge transporters have to connect them, so that the currents are gauge invariant. Therefore we can set $x_1 = x_2 = x$ and write shifts as covariant derivatives in $\mathcal{O}$. Additionally, $\mathcal{O}$ can contain a product of γ-matrices. Flavor changing currents $f_1 \neq f_2$ are not considered in this work, and flavor neutral currents can produce disconnected contributions. In this work we will neglect them.

So the simplified expression for the current is

$$\mathcal{J}_\Psi(t,\vec{q},\mathcal{O}) = a^3 \sum_{\vec{x}\in V_3} \mathrm{e}^{\mathrm{i}\vec{q}\cdot\vec{x}}\,\overline{\Psi}^{a}_{\alpha}(x)\mathcal{O}^{ab}_{\alpha\beta}(x)\Psi^{b}_{\beta}(x)\,. \tag{3.73}$$

The definition of a three-point function reads

$$C_{\mathcal{P}}^{3pt}(t_{\mathrm{sink}},t_{\mathrm{ins}};\vec{p}_f,\vec{q};\mathcal{O},\Psi) = \mathrm{tr}\left\{\mathcal{P}\langle\mathcal{N}(\vec{p}_f,t_{\mathrm{sink}})\mathcal{J}_\Psi(t_{\mathrm{ins}},\vec{q},\mathcal{O})\overline{\mathcal{N}}(\vec{p}_i,0)\rangle\right\}\,, \tag{3.74}$$

where[13] $t_{\mathrm{source}} = 0 \leq t_{\mathrm{ins}} \leq t_{\mathrm{sink}}$ and momentum conservation means $\vec{p}_f = \vec{p}_i + \vec{q}$.

In similar fashion as in the two-point function case we can evaluate this expression by inserting complete sets of states. As we choose $t_{\mathrm{sink}} \ll L_t/2$ we can neglect any backward propagating contribution if we use a positive parity projector.

[13] We obtain the three-point function of the antiparticle of the N^* if this time ordering is not fulfilled.

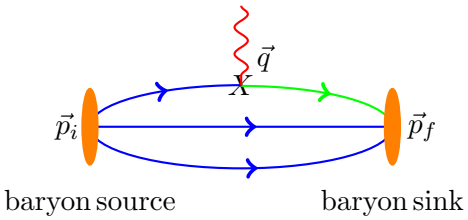

Figure 3.3.: Pictorial representation of the kinematics in a three-point function.

The result is

$$\begin{aligned} C^{3pt}_{\mathcal{P}_+}(t,\tau;\vec{p}_f,\vec{q};\mathcal{O},\Psi) &= V_3 a^6 \sum_{\vec{x},\vec{y}\in V_3} \mathrm{e}^{-\mathrm{i}\vec{p}\cdot\vec{x}+\mathrm{i}\vec{q}\cdot\vec{y}} \mathrm{tr}\left\{\mathcal{P}_+ \langle \mathcal{N}(\vec{x},t)\mathcal{J}_\Psi(\tau,\vec{y},\mathcal{O})\overline{\mathcal{N}}(0,0)\rangle\right\} \\ &= V_3 a^6 \sum_{\vec{x},\vec{y}\in V_3} \mathrm{e}^{-\mathrm{i}\vec{p}\cdot\vec{x}+\mathrm{i}\vec{q}\cdot\vec{y}} \mathrm{tr}\left\{\mathcal{P}_+ \langle \mathrm{e}^{-(L_t-t)\hat{H}}\mathcal{N}(\vec{x})\mathrm{e}^{-(t-\tau)\hat{H}}\mathcal{J}_\Psi(\vec{y},\mathcal{O})\mathrm{e}^{-\tau\hat{H}}\overline{\mathcal{N}}(0)\rangle\right\} \\ &= V_3 a^6 \sum_{\vec{x},\vec{y}\in V_3} \mathrm{e}^{-\mathrm{i}\vec{p}\cdot\vec{x}+\mathrm{i}\vec{q}\cdot\vec{y}} \sum_{\mu,\nu}\sum_{\sigma,\sigma'} \mathrm{tr}_D\big\{\mathcal{P}_+\langle 0 \mid \mathcal{N}(\vec{x}) \mid N_\mu,\vec{p}_f,\sigma\rangle \\ &\quad \langle N_\mu,\vec{p}_f,\sigma \mid \mathcal{J}_\Psi(\vec{y},\mathcal{O}) \mid N_\nu,\vec{p}_i,\sigma'\rangle\langle N_\nu,\vec{p}_i,\sigma' \mid \overline{\mathcal{N}}(0) \mid 0\rangle\big\}\mathrm{e}^{-E_\mu(\vec{p_f})\cdot(t-\tau)-E_\nu(\vec{p_i})\cdot\tau} + \dots \end{aligned} \tag{3.75}$$

We can use Lorentz invariance to connect the matrix element of our current in the continuum to a linear combination of γ-matrices and Lorentz vectors inside two spinors

$${}_c\langle N,\vec{p}_f,\sigma \mid \mathcal{J}_\Psi(0,\mathcal{O}) \mid N_\nu,\vec{p}_i,\sigma'\rangle_c = \overline{U}(N,\vec{p}_f,\sigma) M^{\mathcal{O}}_\Psi(\vec{p}_f,\vec{p}_i) U(N,\vec{p}_i,\sigma')\,. \tag{3.76}$$

Examples for this Lorentz decomposition were given in Section 2.4.
To use this expression we need to see

$$a^3 \sum_{\vec{y}\in V_3} \mathrm{e}^{\mathrm{i}\vec{q}\cdot\vec{y}} \langle N_\mu,\vec{p}_f,\sigma \mid \mathcal{J}_\Psi(\vec{y},\mathcal{O}) \mid N_\nu,\vec{p}_i,\sigma'\rangle = \frac{{}_c\langle N_\mu,\vec{p}_f,\sigma \mid \mathcal{J}_\Psi(0,\mathcal{O}) \mid N_\nu,\vec{p}_i,\sigma'\rangle_c}{2\sqrt{E(\vec{p}_f)E(\vec{p}_i)}} \tag{3.77}$$

plugging this in we obtain

$$\begin{aligned} C^{3pt}_{\mathcal{P}}(t,\tau;\vec{p}_f,\vec{q};\mathcal{O},\Psi) &= V_3 \sum_{\mu,\nu}\sum_{\sigma,\sigma'} \frac{\sqrt{Z_\mu(\vec{p}_f)Z_\nu(\vec{p}_i)}}{4E_\mu(\vec{p}_f)E_\nu(\vec{p}_i)} \mathrm{tr}_D\big\{\mathcal{P}U(N_\mu,\vec{p}_f,\sigma) \\ &\quad \overline{U}(N_\mu,\vec{p}_f,\sigma) M^{\mathcal{O}}_\Psi(\vec{p}_f,\vec{p}_i) U(N_\nu,\vec{p}_i,\sigma')\overline{U}(N_\nu,\vec{p}_i,\sigma')\big\}\mathrm{e}^{-E_\mu(\vec{p_f})\cdot(t-\tau)-E_\nu(\vec{p_i})\cdot\tau} + \dots \end{aligned} \tag{3.78}$$

Now we can use Eq. (3.57) to define the F-function

$$\begin{aligned} F(\mathcal{P}, M_\Psi^O, \mu, \nu) = \sum_{\sigma,\sigma'} & \frac{1}{4E_\mu(\vec{p}_f)E_\nu(\vec{p}_i)} \\ & \mathrm{tr}_D\left\{\mathcal{P}U(N_\mu,\vec{p}_f,\sigma)\overline{U}(N_\mu,\vec{p}_f,\sigma)M_\Psi^O(\vec{p}_f,\vec{p}_i)U(N_\nu,\vec{p}_i,\sigma')\overline{U}(N_\nu,\vec{p}_i,\sigma')\right\} \\ = & \frac{1}{4E_\mu(\vec{p}_f)E_\nu(\vec{p}_i)}\mathrm{tr}_D\left\{\mathcal{P}(-\mathrm{i}\not{p}_f(\mu)+m_\mu)M_\Psi^O(\vec{p}_f,\vec{p}_i)(-\mathrm{i}\not{p}_i(\nu)+m_\nu)\right\} \end{aligned} \tag{3.79}$$

so that we are left with

$$C_{\mathcal{P}}^{3pt}(t,\tau;\vec{p}_f,\vec{q};\mathcal{O},\Psi) = V_3\sum_{\mu,\nu}\sqrt{Z_\mu(\vec{p}_f)Z_\nu(\vec{p}_i)}F(\mathcal{P},M_\Psi^O,\mu,\nu)\mathrm{e}^{-E_\mu(\vec{p_f})\cdot(t-\tau)-E_\nu(\vec{p_i})\cdot\tau}+\cdots\,. \tag{3.80}$$

So far we have only neglected the contributions from antiparticles. When we restrict the sum over states to the ground state of the nucleon in two-point function

$$C_{\mathcal{P}_+^u}^{2pt}(\vec{p},t) = V_3 Z_N(\vec{p},\phi)\frac{E_N+m_N}{E_N}\mathrm{e}^{-E_N t}\,, \tag{3.81}$$

and three-point function and use the same smearing in both we find that the ratio

$$R_{\mathcal{P}}(t,\tau;\vec{p}_i,\vec{p}_f;\mathcal{O},\Psi) = \frac{C_{\mathcal{P}}^{3pt}(t,\tau;\vec{p}_f,\vec{p}_i;\mathcal{O},\Psi)}{C_{\mathcal{P}_u}^{2pt}(t,\vec{p}_f)}\left[\frac{C_{\mathcal{P}_u}^{2pt}(\tau,\vec{p}_f)C_{\mathcal{P}_u}^{2pt}(t,\vec{p}_f)C_{\mathcal{P}_u}^{2pt}(t-\tau,\vec{p}_i)}{C_{\mathcal{P}_u}^{2pt}(\tau,\vec{p}_i)C_{\mathcal{P}_u}^{2pt}(t,\vec{p}_i)C_{\mathcal{P}_u}^{2pt}(t-\tau,\vec{p}_f)}\right]^{\frac{1}{2}} \tag{3.82}$$

cancels Z factors and the exponentials. To see that, note that the logarithm of the terms in the square root, up to a normalization factor $\tilde{Z}$, is

$$\begin{aligned} \ln([\ldots]^{\frac{1}{2}}/\tilde{Z}) &= \frac{1}{2}\left(-E_{\vec{p}_f}\tau - E_{\vec{p}_f}t - E_{\vec{p}_i}(t-\tau) + E_{\vec{p}_i}\tau + E_{\vec{p}_i}t + E_{\vec{p}_f}(t-\tau)\right) \\ &= -\tau(E_{\vec{p}_f}-E_{\vec{p}_i})\,. \end{aligned} \tag{3.83}$$

So the remaining normalization is

$$R_{\mathcal{P}}(t,\tau;\vec{p}_i,\vec{p}_f;\mathcal{O},\Psi) = \sqrt{\frac{E_{\vec{p}_i}E_{\vec{p}_f}}{(E_{\vec{p}_i}+m)(E_{\vec{p}_f}+m)}}F(\mathcal{P},M_\Psi^O,\mu,\nu)+\ldots \tag{3.84}$$

3.7. Computation of three-point functions

Three-point functions are a little more involved than two-point functions as they contain one propagator more. This propagator does not start at a lattice point but at a whole time-slice with fixed separation from the hadron source. In this chapter we will restrict ourselves to nucleon three-point functions. The formulae for other baryons will be very similar and will be briefly mentioned at the end of the section. Meson three-point functions are a bit easier to compute as there are less propagators to insert a current in.

3.7.1. Contractions

As we assume iso-spin symmetry proton and neutron are mass degenerate and their two-point function is computed in the same way. In the three-point function we must specify the flavor of the current, and thus also if we insert it into a neutron or a proton. Generally we will choose that the doubly represented flavor is called u the singly represented flavor is d, and hence we take the nucleon to be a proton. For the sake of simplicity we compute the current insertion of a d-quark.

$$\begin{aligned}\mathcal{P}_{\gamma\overline{\gamma}}\langle N_\gamma(x)\overline{d}^d_{\overline{\delta}}(y)\mathcal{O}_{\overline{\delta}\delta}d^d_\delta(y)\overline{N}_{\overline{\gamma}}(0)\rangle \propto \mathcal{P}_{\overline{\gamma}\gamma}\varepsilon^{abc}\varepsilon^{\overline{a}\overline{b}\overline{c}}(C\gamma_5)^{\alpha\beta}(C\gamma_5)^{\overline{\alpha}\overline{\beta}}\mathcal{O}_{\overline{\delta}\delta}\times \\ \langle d^a_\alpha(x)u^b_\beta(x)u^c_\gamma(x)\overline{d}^d_{\overline{\delta}}(y)d^d_\delta(y)\overline{u}^{\overline{c}}_{\overline{\gamma}}(0)\overline{d}^{\overline{a}}_{\overline{\alpha}}(0)\overline{u}^{\overline{b}}_{\overline{\beta}}(0)\rangle\,. \end{aligned} \tag{3.85}$$

The contractions that lead to disconnected diagrams, i.e., ones that contain

$$\langle d^a_\alpha(x)u^b_\beta(x)u^c_\gamma(x)\overline{d}^d_{\overline{\delta}}(y)d^d_\delta(y)\overline{u}^{\overline{c}}_{\overline{\gamma}}(0)\overline{d}^{\overline{a}}_{\overline{\alpha}}(0)\overline{u}^{\overline{b}}_{\overline{\beta}}(0)\rangle\,, \tag{3.86}$$

yield the two-point function times the loop and is not part of our discussion here.
The other two contractions are

$$\begin{aligned}\langle d^a_\alpha(x)u^b_\beta(x)u^c_\gamma(x)\overline{d}^d_{\overline{\delta}}(y)d^d_\delta(y)\overline{u}^{\overline{c}}_{\overline{\gamma}}(0)\overline{d}^{\overline{a}}_{\overline{\alpha}}(0)\overline{u}^{\overline{b}}_{\overline{\beta}}(0)\rangle = \\ D^{ad}_{\alpha\overline{\delta}}(x,y)D^{d\overline{a}}_{\delta\overline{\alpha}}(y,0)\left(U^{b\overline{b}}_{\beta\overline{\beta}}(x,0)U^{c\overline{c}}_{\gamma\overline{\gamma}}(x,0)-U^{b\overline{c}}_{\beta\overline{\gamma}}(x,0)U^{c\overline{b}}_{\gamma\overline{\beta}}(x,0)\right)\,. \end{aligned} \tag{3.87}$$

3.7.2. Sequential source with fixed baryon sink

We follow the chapter 5.1 in [94]. To compute $D^{ad}_{\alpha\overline{\delta}}(x,y)$ in Eq. (3.87) we invert on a *sequential source* [95, 96] S which has all the information at x and no free indices.
Thus we get $\Sigma_{N,u,u}(\mathcal{P},t_{\text{sink}},\vec{p}_f,t,y)^{\overline{a}d}_{\overline{\alpha}\overline{\delta}}$ which contains two propagators to x and propagates away from the baryon sink, which only depends on the color spin combination at

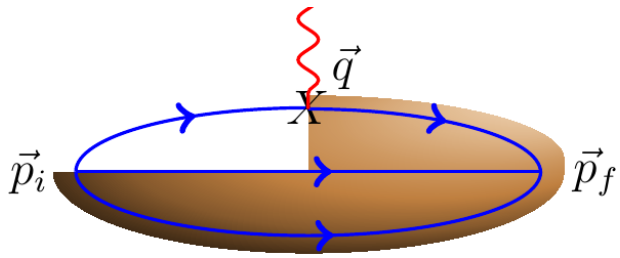

Figure 3.4.: A pictorial representation of the sequential propagator. All indices at the baryon sink are fixed.

the baryon source and the color, spin and position the propagation ends. This has the structure of a propagator:

$$\sum_y \mathcal{D}^{a\bar{a}}_{\alpha\bar{\alpha}}(x,y)\gamma_5\Sigma^{\dagger}_{N,u,u}(\mathcal{P},t_{sink},\vec{p}_f,t,y)^{\bar{a}d}_{\bar{\alpha}\delta} = \gamma_5 S^{\dagger}_{N,u,u}(\mathcal{P},\vec{p}_f,\vec{x},t')^{ad}_{\alpha\delta}\delta_{t't_{sink}} \tag{3.88}$$

where $\mathcal{D}$ is our discretized Dirac operator and we have used γ_5-hermiticity, Eq. (3.19) , to get the propagation to the baryon sink. By collecting said terms from 3.85 and 3.87 we find

$$\begin{aligned} S_{N,u,u}(\mathcal{P},\vec{p}_f,\vec{x},t)^{\bar{a}a}_{\bar{\alpha}\alpha} &= \mathrm{e}^{-\mathrm{i}\vec{p}_f\cdot\vec{x}}\mathcal{P}_{\bar{\gamma}\gamma}\varepsilon^{abc}\varepsilon^{\bar{a}\bar{b}\bar{c}}(C\gamma_5)^{\alpha\beta}(C\gamma_5)^{\bar{\alpha}\bar{\beta}} \\ &\quad \left(U^{b\bar{b}}_{\beta\bar{\beta}}(x,0)U^{c\bar{c}}_{\gamma\bar{\gamma}}(x,0) - U^{b\bar{c}}_{\beta\bar{\gamma}}(x,0)U^{c\bar{b}}_{\gamma\bar{\beta}}(x,0)\right) . \end{aligned} \tag{3.89}$$

which we can manipulate into a matrix product like this

$$\begin{aligned} S_{N,u,u}(\mathcal{P},\vec{p}_f,\vec{x},t)^{\bar{a}a}_{\bar{\alpha}\alpha} &= -\mathrm{e}^{-\mathrm{i}\vec{p}_f\cdot\vec{x}}\varepsilon^{abc}\varepsilon^{\bar{a}\bar{b}\bar{c}}\Big(\mathcal{P}_{\bar{\gamma}\gamma}U^{c\bar{c}}_{\gamma\bar{\beta}}(x,0)(C\gamma_5)^{T\bar{\beta}\bar{\alpha}}(C\gamma_5)^{\alpha\beta}U^{b\bar{b}}_{\beta\bar{\gamma}}(x,0) \\ &+ \left[U^{c\bar{c}}_{\gamma\bar{\gamma}}(x,0)\mathcal{P}_{\bar{\gamma}\gamma}(C\gamma_5)^{\alpha\beta}U^{b\bar{b}}_{\beta\bar{\beta}}(x,0)(C\gamma_5)^{T\bar{\beta}\bar{\alpha}}\right]^{T_D}\Big) \end{aligned} \tag{3.90}$$

The computation for a u-quark current is very similar and slightly more involved as there are two propagators where the current can be inserted. From this computation we see that we need to compute a new sequential source for each polarization $\mathcal{P}$, sink momentum $\vec{p}_f$ and flavor of the current. This means twelve additional inversions per sequential source to get the sequential propagator we need to compute the three-point function. A common trick to reduce this number of inversions is to use the non-relativistic projection of the nucleon. There one replaces $C\gamma_5$ with $\mathcal{P}^u_+ C\gamma_5$ and thus removes the antiparticle contributions in the nucleon-diquark. This makes the sequential source zero at two of the four spin components and thus reduces the number of inversions one needs to compute the sequential propagator to six per sequential source.

As this non-relativistic projection [97] is believed to work best for heavy quarks [98] it is not clear how light one can go in m_π until this is a bad approximation. We therefore have refrained from using this trick in computing physical quantities with light pion masses, but have used it to compare the sequential sink method with the three-point functions from stochastic estimation.

3.7.3. Sequential source with fixed current insertion

In [99] a method was described that fixes the insertion time-slice. This means new inversions for each operator in the current, but one is free to choose the baryon sink. This freedom can be used to vary the smearing and compute a generalized eigenvalue problem at the baryon sink. A recent computation of g_A utilizing this method is [100]. The downside to this approach is that it becomes very costly to compute many different currents and it is also less suited for off-forward matrix elements. To control the excited state contributions one has to choose the insertion time carefully and one has to optimize the baryon source for optimal ground state overlap before hand, as it is fixed throughout the analysis.

3.7.4. Stochastic estimation

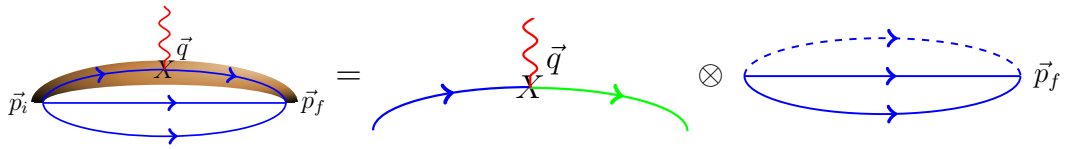

Figure 3.5.: The stochastic estimation of the propagator from the insertion to the baryon sink. The computation factorizes in a weight factor depending only on the current and a modified two-point function, so that the stochastic propagator can be used for arbitrary values of $\vec{p}_f$.

By comparing Eq. (3.87) with Eq. (3.49) we see that we can compute the three-point functions like two-point functions with one modified propagator.
In this section we will derive how we can compute this *inserted propagator*.
In formulas this is

$$G^{ab}_{\alpha\beta}(x,0)[\vec{q},\mathcal{O}] = \sum_{\vec{y}\in V_3} \mathrm{e}^{\mathrm{i}\vec{q}\cdot\vec{y}} G^{ab'}_{\alpha\beta'}(x,y)\mathcal{O}^{b'a'}_{\beta'\alpha'}(y)G^{a'b}_{\alpha'\beta}(y,0) \tag{3.91}$$

and we want to employ stochastic estimation for the propagator $G^{ab'}_{\alpha\beta'}(x,y)$. As we have seen in Section 3.3.3 the propagator is reconstructed from our $\mathbb{Z}_2 \times \mathrm{i}\mathbb{Z}_2$ noise sources, η,

and the corresponding solutions, χ, via

$$\frac{1}{N}\sum_{n=1}^{N}\chi^{(n)}_{\alpha,a}(x)\eta^{(n)\dagger}_{\beta',b'}(y) = G^{ab'}_{\alpha\beta'}(x,y)\left(\mathbb{1}+\mathcal{O}(\frac{1}{\sqrt{N}})\right). \tag{3.92}$$

3.7.4.1. Fixed insertion time

First we will fix the insertion time at y_4 by seeding η only at this time-slice. We can then perform the sum over y for each color spin component a, α to get a weight factor

$$W^{(n),b}_{I,\beta}(\mathcal{O},\vec{q},t_{\text{ins}}=y_4) = \sum_{\vec{y}\in V_3}\mathrm{e}^{\mathrm{i}\vec{q}\cdot\vec{y}}\eta^{(n)\dagger}_{\beta',b'}(y)\mathcal{O}^{b'a'}_{\beta'\alpha'}(y)G^{a'b}_{\alpha'\beta}(y,0) \tag{3.93}$$

where we have added the t_{ins}-dependence to make clear that this is the weight factor for a fixed insertion time.

Then we define

$$\tilde{\tilde{G}}^{(n)a\tilde{b}}_{I,\alpha\tilde{\beta}}(x,0,t_{\text{ins}}=y_4,b,\beta) = \chi^{(n)}_{\alpha,a}(x)\delta_{\tilde{b}b}\delta_{\tilde{\beta}\beta} \tag{3.94}$$

and plug this into the definition of the two-point function, where it replaces the propagator into which we want to insert the current. In the case of the d-quark in the proton this is

$$\tilde{C}^{(n),d}_{2pt,I}(t_{\text{sink}}=x_4,t_{\text{ins}}=y_4,\vec{p}_f)^b_\beta = \sum_{\vec{x}\in V_3}\mathrm{e}^{-\mathrm{i}\vec{p}_f\cdot\vec{x}}B^{C\gamma_5}_{\mathcal{P}}\left(U(x,0),U(x,0),\tilde{\tilde{G}}^{(n)}_I(x,0,t_{\text{ins}}=y_4,b,\beta)\right) \tag{3.95}$$

and we can recover the three-point function from

$$C^{3pt}_{\overline{N}N\mathcal{P}}(t_{\text{sink}},t_{\text{ins}};\vec{p}_f,\vec{q},O_d) = \frac{1}{N}\sum_{n=1}^{N}\sum_{b,\beta}\tilde{C}^{(n),d}_{2pt,I}(t_{\text{sink}}=x_4,t_{\text{ins}}=y_4,\vec{p}_f)^b_\beta W^{(n),b}_{I,\beta}(\mathcal{O},\vec{q},t_{\text{ins}}=y_4) \tag{3.96}$$

and expect a plateau for larger values of t_{sink}. With this trick we have split up the double sum into a product of two sums which speeds up the calculation greatly as now the current insertion is independent of the baryon sink.

For inserting a u-quark we have to define the $\tilde{C}_{2pt,I}$ in a similar way

$$\tilde{C}^{(n),u}_{2pt,I}(t_{\text{sink}} = x_4, t_{\text{ins}}, \vec{p}_f)^b_\beta = \sum_{\vec{x}\in V_3} \Big[\mathrm{e}^{-\mathrm{i}\vec{p}_f\cdot\vec{x}} B^{C\gamma_5}_{\mathcal{P}} \left(U(x,0), \tilde{\tilde{G}}^{(n)}_I(x,0,t_{\text{ins}},b,\beta), D(x,0) \right) + B^{C\gamma_5}_{\mathcal{P}} \left(\tilde{\tilde{G}}^{(n)}_I(x,0,t_{\text{ins}},b,\beta), U(x,0), D(x,0) \right) \Big] \tag{3.97}$$

and we can use the same weight factors as in the d-insertion case and thus the three-point function for u-quark insertions is recovered in complete analogy to Eq. (3.96).
This approach is very nice to study the t_{sink} dependence of local operators without derivatives. Its downside is that to be able to compute a current with a derivative in time direction seeding only one time-slice is not enough and thus already for second moments of GPDs this approach is cumbersome.

3.7.4.2. Fixed sink time

We can also fix the time-slice x_4 of the baryon sink, in complete analogy to traditional sequential source techniques. To do this we seed the stochastic noise at this time-slice and utilize γ_5-hermiticity

$$G^{ab}_{\alpha\beta}(x,y) = \gamma_5 [G^{ab}_{\alpha\beta}(y,x)]^\dagger \gamma_5 \,, \tag{3.98}$$

to revert the propagation direction. This modifies our weight to

$$W^{(n),b}_{S,\beta}(\mathcal{O}, \vec{q}, t_{\text{sink}} = x_4, t_{\text{ins}} = y_4) = \sum_{\vec{y}\in V_3} \mathrm{e}^{\mathrm{i}\vec{q}\cdot\vec{y}} \chi^{(n)\dagger}_{\beta',b'}(y) \gamma_5 \mathcal{O}^{b'a}_{\beta'\alpha}(y) G^{ab}_{\alpha\beta}(y,0) \tag{3.99}$$

and the modified propagator for the $\tilde{C}_{2pt,S}$ is

$$\tilde{\tilde{G}}^{(n)a\tilde{b}}_{S,\alpha\tilde{\beta}}(x,0,b,\beta) = \gamma_5 \eta^{(n)}_{\alpha,a}(x) \delta_{\tilde{b}b} \delta_{\tilde{\beta}\beta} \,. \tag{3.100}$$

The three-point function again is recovered by summing over the color/spin combinations of the weight and $\tilde{C}_{2pt,S}$ for each stochastic estimator. This method has the advantage that all derivatives needed are well defined and the data analysis is in complete analogy to the sequential source technique.
Both methods of fixing the insertion or baryon time-slice have additional freedoms compared to the respective sequential source method.
In Section 6.1.3 we will examine how many noise vectors we need to get a competitive signal-to-noise ratio compared to the sequential source method and study its applicability to nucleon form factors and moments of GPDs.

3.8. Extraction of nucleon form factors

3.8.1. Overdetermined systems of linear equations

As we have seen in Section 3.6 we can extract the matrix elements of local operators in nucleon ground states from nucleon three-point functions. These matrix elements can be decomposed via Lorentz invariance as indicated in Eq. (3.76).

We do not extract the right hand side of Eq. (3.76) directly in a three-point function on the lattice, but the trace over the Dirac indices times $\mathcal{P}$ and two additional spinors. This object was defined as F-function in Eq. (3.79). This yields a system of equations which looks like Eq. (3.84) for each value of Q^2 we have computed on the lattice. This can be solved by employing a *singular value decomposition* (SVD). The algorithm we use is explained in [101] and it decomposes a real matrix A into two orthogonal matrices U and V and a diagonal matrix w, which contains the singular values:

$$A = U \cdot w \cdot V^T \tag{3.101}$$

Now we can define

$$w_i^{-1} = \begin{cases} \frac{1}{w_i}, & \text{if } w_i > \epsilon; \\ 0, & \text{otherwise.} \end{cases} \tag{3.102}$$

where ϵ is a threshold we can choose in a reasonable interval, where the final result does not depend on its concrete value. It is chosen as a certain fraction of the biggest singular value of our matrix and it corresponds to the expected numerical round off errors. The motivation of this threshold is that otherwise equations which are not well constrained dominate the result.

With this definition we can pseudo-invert the matrix A via

$$A^{-1} = V \,\mathrm{diag}\,[w_i^{-1}] U^T \,. \tag{3.103}$$

For non-singular (so no inverse of a singular value has been set to zero) square matrices A this is exactly the inverse of the matrix. The advantage is that this definition also works for non-square and singular matrices.

Our system of equations can be written in matrix form as

$$A \cdot x = b \,, \tag{3.104}$$

where each line i corresponds to a combination of $\vec{p}_f, \vec{p}_i, \mathcal{P}, \mathcal{O}^{\mu_1 \cdots \mu_n}$ with $-(p_f - p_i)^2 =$

Q^2:

$$\sum_j A_{ij} x_j = b_i \tag{3.105}$$

and the A_{ij} are the F-functions multiplying the (generalized) form factors x_j and b_i are the measured ratios of three over two-point functions. If all the prefactors A_{ij} in a line i are zero[14] we exclude it from our equation system as it does not constrain the x_j.
The solution of this, utilizing the SVD, is

$$x = V \,\mathrm{diag}\,[w_i^{-1}] U^T b\,, \tag{3.106}$$

and this minimizes the squared residuals

$$r^2 = \sum_i \left(\sum_j A_{ij} x_j - b_i \right)^2 . \tag{3.107}$$

As we want to minimize

$$\chi^2 = \sum_i \frac{\left(\sum_j A_{ij} x_j - b_i \right)^2}{\sigma_i^2}\,, \tag{3.108}$$

where σ_i is the error on the plateau value b_i, we rescale $A_{ij} \to A_{ij}/\sigma_i$ and $b_i \to b_i/\sigma_i$ to achieve that.

3.8.2. Working example

This is best explained by considering an example. In Minkowski spacetime the electromagnetic form factors are defined, see Section 2.4.2 , by

$$\langle N, \vec{p}_f, \sigma' \mid \overline{\Psi}_q \gamma_M^\mu \Psi_q \mid N, \vec{p}_i, \sigma \rangle = \left\langle\left\langle \gamma_M^\mu \right\rangle\right\rangle F_1^q(Q^2) + \frac{\mathrm{i}}{2m_N} \left\langle\left\langle \sigma_M^{\mu\nu} \right\rangle\right\rangle (p_f - p_i)_\nu^M \, F_2^q(Q^2)\,. \tag{3.109}$$

This equation has to be converted to the convention in Euclidean spacetime, as described in Appendix C. We consider the iso-vector current, where disconnected contributions cancel.
For zero momentum transfer we have only one non-vanishing equation in this case and the term in front of F_2^q is zero. If we choose the smallest non-vanishing Q^2, where

[14] In practice this means smaller than our numerical precision.

one unit of lattice momentum is transfered, we have 6 choices where $\vec{p}_f{}^2 = (\frac{2\pi}{L_s})^2$ and $\vec{p}_i{}^2 = 0$, and additionally 6 choices where $\vec{p}_f^2 = 0$ and $\vec{p}_i^2 = (\frac{2\pi}{L_s})^2$.
Here we have 4 possibilities to choose the direction of the current, and 4 choices for a projector to positive parity $\mathcal{P}_+$. Of these 192 combinations 48 are non-zero.
The non-zero contributions are

- unpolarized Projector $\mathcal{P}_+^u$ and the current in t-direction: non-zero for each momentum combination $\rightarrow$ 12
- polarized projector $\mathcal{P}_+^l$ and current in m-direction: non-zero for if momentum is in the remaining spatial direction ($\varepsilon^{lmk}p_k$) $\rightarrow$ 24
- unpolarized Projector $\mathcal{P}_+^u$ and current in k-direction: non-zero for if momentum is parallel to the k-direction $\rightarrow$ 12

So A is a 48×2 matrix in this case. For higher momenta Q^2 the combinatorial possibilities to distribute the momenta can increase and also new terms, e.g., ones proportional to $\vec{p}_i \times \vec{p}_f$, can occur. So in general the system of equations is highly overdetermined. When working with sequential sources the cost is proportional to the number of sink momentum /polarization combinations that is computed. Thus oftentimes one restricts the calculation to a single sink momentum and computes less polarizations. This reduces the number of equations drastically, but leaves the equation system nevertheless overdetermined for $Q^2 > 0$.
In Fig. 3.6 we depict the solution of this example graphically for a range of fit-ranges. The fit start and end points are chosen symmetrically around $t_{\text{sink}}/2 = 7.5$. Our standard fit range corresponds to 5 to 10 and the dependence of the extracted form factors F_1 and F_2 on the fit-range is very mild. The fit-range 7 to 8 has only two-points and should not be trusted; it is just there for illustrative purposes. We have switched the sign on some equations to render the fit values to the ratio all positive. The ordering of the equations was first by value of the SVD prediction, then by magnitude of the initial momentum, where the directions are ordered by z,y,x and then by magnitude of the final momentum again with the directions ordered by z,y,x, and the final ordering criterion was the value of the ratio. For the three classes of equations in our example we find that the rotational invariance is only slightly broken and that we see no systematic dependence on the momentum being at the source or the sink of the baryon. This system was solved with a χ^2 per degree of freedom of slightly less than one.

3.9. Renormalization

All operators in the currents we use have to be renormalized. The general procedure is to compute the renormalization factor in the RGI-scheme, which only depends on the

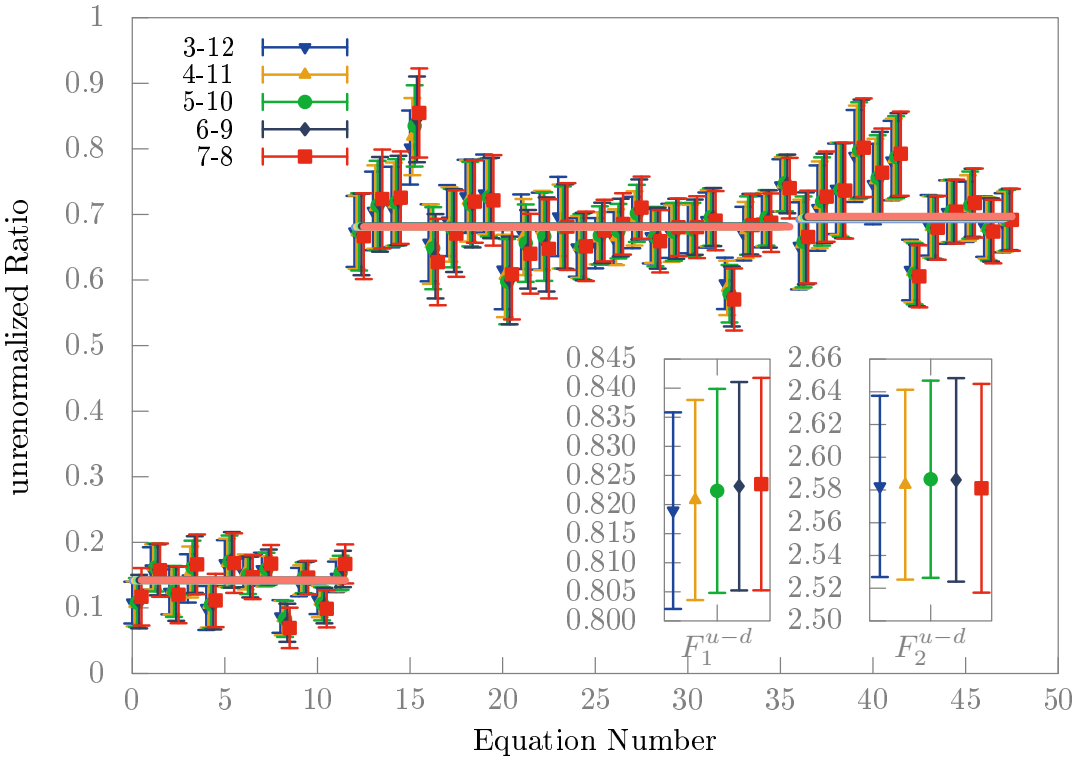

Figure 3.6.: The dependence on the fit-range used to extract the plateau of the ratio on the isovector electromagnetic form factor at the $N_f = 2 + 1$ symmetric point with 827 gauge configurations using 60 stochastic estimates. The momenta of the two-point functions were not averaged over equivalent directions.

coupling $g = \sqrt{6/\beta}$, and then perturbatively convert this number to the $\overline{MS}$-scheme at some scale μ:

$$\mathcal{O}_{\text{ren}} = Z_{RGI\to\overline{MS}}[\mu, \mathcal{O}] Z_{RGI}[\beta, \mathcal{O}] \left(1 + b[\mathcal{O}, \beta] a m_q + \cdots\right) \mathcal{O}_{\text{bare}} \tag{3.110}$$

The quark mass dependent corrections coming from the order a-improvement of the currents (the $1 + bam_q$-terms) depend on the gauge coupling $g^2 = 6/\beta$ and the critical value for the hopping parameter κ_{crit}, see Table 3.1. Their deviation from one is generally small.

The values for b_c depend on the current c and are computed via

$$b_c = 1 + w_c C_F g^2 \tag{3.111}$$

where w_c is a current dependent constant and the Casimir invariant of $SU(3)$ is $C_F =$

β	κ_{critical}
5.29	0.1364264(26)
5.40	0.13667925(76)

Table 3.1.: The values of the critical hopping parameter at a given gauge coupling parameter $\beta = 2N_c/g^2$. Values are taken from [102].

$4/3$.
The quark mass can be computed via

$$m_q a = \frac{1}{2\kappa} - \frac{1}{2\kappa_{\text{crit}}} \,. \tag{3.112}$$

The conversion to the $\overline{MS}$-scheme depends on the anomalous dimension of the operator. As non-singlet axial and vector currents do not have an anomalous dimension this is one in this case and also correct non-perturbatively.
The renormalization constants for the $N_f = 2$ data in this work were published in [103], table 3 and we use the value $r_0\Lambda_{\overline{MS}} = 0.789$. The conversion factors to the $\overline{MS}$-scheme are taken from [104].
For a sample table of renormalization constants used in this work see Table 5.2.

3.10. Setting the scale

To convert the results obtained on the lattice to physical units one has to determine the lattice spacing in fm. This process is called scale setting .
The scale depends on the action that one uses for the gauge fields and fermions and on the gauge coupling. Therefore one sets the lattice spacing only once for a family of lattices with the same coupling.
The approach one generally takes is to measure a quantity that is easily determined very precisely on every lattice, like w_0 [106], t_0 [105], Sommer parameter [107] r_0 or r_1 [108] and then fixing the continuum limit of another quantity, e.g., the nucleon mass or the heavy quark potential, to be in agreement with the experiment. The effects of the quark sea are usually interpolated to the physical point.
The scale setting with t_0 is shown in Fig. 3.7. Here t is the *flow time* and E is the action density. What is important is that $t^2\langle E\rangle$ is dimensionless and thus can be used to set the scale, and t_0 is defined as the value where this is 0.3.
In Table 3.2 we present the results for the gluonic quantities measured on each lattice. The scale setting is then done in [28] with the nucleon mass so that $r_0 = 0.501(10)(11)$ fm.

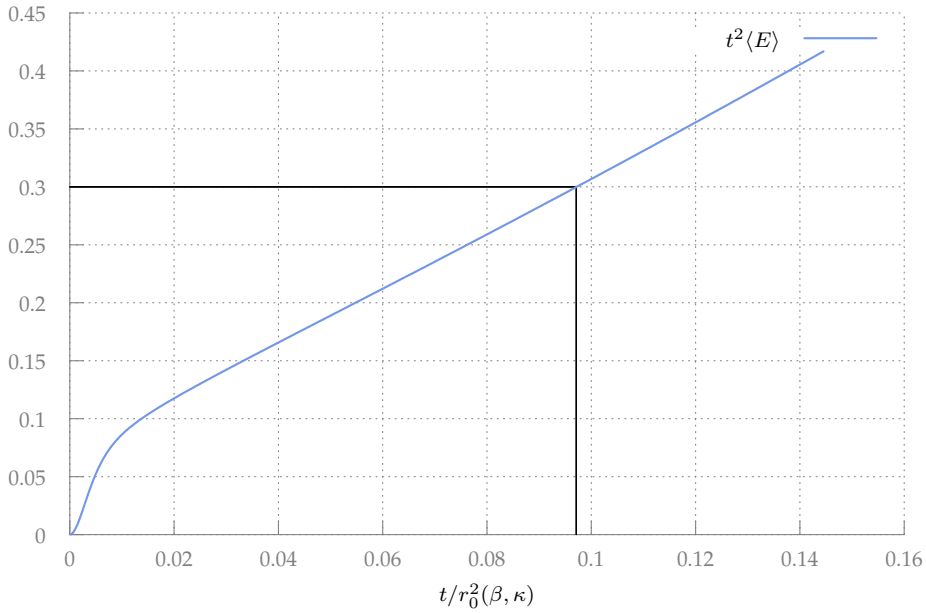

Figure 3.7.: Scale setting with t_0 at $\beta = 5.29$, $\kappa = 0.1364$ for a volume of 48^3x64. The data was taken for 218 configurations. This ensemble corresponds to $m_\pi \approx 157$MeV and a spatial lattice extend of $L_s \approx 3.45$fm. Plot design was taken from [105].

κ	vol	r_0	$\#(w_0)$	w_0	$\sqrt{8t_0}$
		β=5.20			
0.13420	16^3x32	4.145(26)	32	1.3504(80)	3.659(18)
0.13500	16^3x32	4.694(70)	22	1.5635(97)	4.194(20)
0.13550	16^3x32	5.117(100)	25	1.7414(99)	4.616(22)
0.13565	16^3x32	5.65(22)	35	1.850(12)	4.843(22)
		β=5.25			
0.13460	16^3x32	4.851(42)	36	1.597(11)	4.315(21)
0.13520	16^3x32	5.317(62)	22	1.738(15)	4.684(30)
0.13575	24^3x48	5.773(54)	37	1.9509(97)	5.154(16)

Table 3.2 Continued on next page.

κ	vol	r_0	$\#(w_0)$	w_0	$\sqrt{8t_0}$
0.13600	24^3x48	6.143(59)	32	2.095(12)	5.427(17)
0.13620	32^3x64	6.464(52)	34	2.224(11)	5.669(13)
		β=5.26			
0.13450	16^3x32	4.983(94)	26	1.585(10)	4.305(20)
		β=5.29			
0.13400	16^3x32	4.777(78)	25	1.580(10)	4.319(23)
0.13500	16^3x32	5.307(71)	28	1.813(13)	4.895(22)
0.13550	16^3x32	5.872(66)	30	1.944(16)	5.221(33)
0.13550	24^3x48	5.949(71)	25	1.9388(99)	5.196(17)
0.13590	16^3x32	6.27(11)	28	2.070(26)	5.487(45)
0.13590	24^3x48	6.252(56)	20	2.105(12)	5.565(22)
0.13620	24^3x48	6.526(67)	29	2.274(16)	5.886(22)
0.13632	24^3x48	6.740(48)	28	2.375(17)	6.059(25)
0.13632	32^3x64	6.830(45)	27	2.3540(82)	6.022(10)
0.13632	40^3x64	6.765(29)	30	2.3645(76)	6.042(10)
0.13640	40^3x64	6.826(44)	31	2.4192(75)	6.117(10)
0.13640	48^3x64	6.959(38)	218	2.4247(43)	6.1356(26)
0.13640	64^3x64	?	59	2.4216(43)	6.1316(44)
		β=5.40			
0.13500	24^3x48	6.384(48)	22	2.156(16)	5.867(29)
0.13560	24^3x48	6.695(67)	34	2.342(12)	6.279(19)
0.13610	24^3x48	7.323(83)	39	2.558(18)	6.718(30)
0.13625	24^3x48	7.455(74)	29	2.599(20)	6.830(32)
0.13640	24^3x48	7.82(13)	33	2.737(33)	7.063(44)
0.13640	32^3x64	7.847(62)	39	2.702(14)	7.003(21)
0.13660	32^3x64	8.043(71)	28	2.865(13)	7.270(16)
0.13660	48^3x64	8.123(45)	27	2.893(17)	7.296(20)

Table 3.2.: r_0, w_0 and t_0 scales and the number of measurements used to determine them. Table taken from [58].

4

Current status of the nucleon axial coupling and iso-vector quark momentum fraction in $N_f = 2$ Lattice QCD

This chapter contains an overview of the results for g_A and $\langle x \rangle_{u-d}$ obtained by the lattice community at $N_f = 2$. This is a selection of results and for results with a larger number of dynamical flavors and a more complete overview see [109].
The quantities discussed here display a large discrepancy with the experimental values. These observables are sensitive to a variety of systematic effects, such as excited state contributions and the non-physical quark masses[1] used in the simulations. As the contributions of excited states grow with decreasing pion mass, the extrapolation in m_π can also be improved by suppressing the excitations. Thus suppressing these excitations as much as possible is desirable to improve the reliability of the results. For an exploratory study on how to do that see Chapter 7.

4.1. Nucleon axial coupling g_A

In Fig. 4.1 we have compiled a comparison plot with the results of various collaborations for g_A. Large finite size effects are reducing the value, as can be seen for points at similar pion masses with different volumes. Thus to compare to the experimental value one would have to take appropriate corrections into account. This introduces an additional choice of the correction method and hence complicates the comparison of the results of different groups. For this reason we merely compare the finite volume renormalized data.
The data for large pion masses ($m_\pi > 500$ MeV) are flat and show no curvature upwards to the physical value. Older data that was not included in the plot shares this tendency. In the region below $m_\pi \approx 500$ MeV the data start to scatter and some choices of simulation parameters yield lower data points.

[1] too large m_π

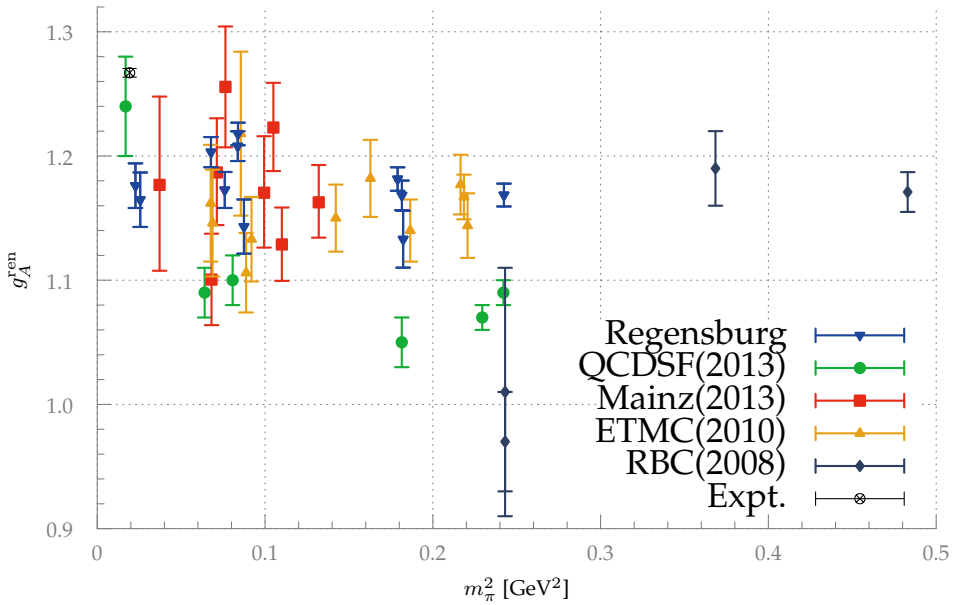

Figure 4.1.: The pion mass dependence of the axial coupling computed by various lattice groups. This is an update of the plot published in [110].

The scattering gets even more pronounced towards the lightest available pion masses of each collaboration and some of the points with large errors are compatible with the experimental value. The simulations generally become more expensive with smaller m_π and thus one is forced to choose the simulation parameters more aggressively. The volumes become smaller in terms of $m_\pi L$ and at the same time inversions are more costly if the quark mass is reduced.
There is no systematic tendency in the data towards the physical point and one has to perform a finite volume correction to the data before one can form a final verdict. A comprehensive analysis of the effect of the lattice spacing is still to be desired. An extrapolation using chiral perturbation theory is also needed to judge if the experimental point is in agreement with the data.
In the following we will discuss the treatment of excited states, finite volume effects, renormalization and discretization effects for each group.

The Mainz group [111] has created data for multiple $t_{\rm sink}$ and they have extrapolated the summed insertions to $t_{\rm sink} = \infty$. The resulting values lie above the ones from the plateau, but have bigger error bars. We have chosen to use the plateau data in the comparison plot. They have large volumes with box sizes up to $4^3 \times 8$ fm^4 and use only $m_\pi L \geq 4$, so finite volume effects are expected to be small. The data are non-

perturbatively renormalized [112]. The data does not display a systematic dependence on the lattice spacing and they use fine lattices between 0.079 and 0.05 fm.

The QCDSF collaboration [113] used a subset of the Wilson Clover configurations analyzed by the **Regensburg** group [110]. QCDSF have used a different smearing, than the Regensburg group except for the data point at the lightest pion mass. Apart from this point their values systematically lie below the Regensburg data, which is most likely due to excited state effects [110]. The Regensburg group has used an optimized Wuppertal smearing with APE smeared gauge links and a large number of smearing iterations. This renders the effective mass of the nucleon relatively flat, see Chapter 7. The volumes range from $Lm_\pi \approx 2.7$ to ≈ 4.9. QCDSF suggest to overcome the large finite size effects that are present in g_A and f_π by extrapolating the ratio g_A/f_π, where they partially cancel, to the infinite volume limit. The values of the pion mass have been extrapolated by QCDSF to the infinite volume limit, whereas the Regensburg group reports the pion masses without any volume corrections. Both groups employ non-perturbative renormalization [103]. Discretization effects were not observed, presumably due to the range of utilized lattice spacings being small (most data is for 0.07 fm and two lattices with 0.06 fm).

ETMC [114] has produced data for two flavor twisted mass fermions (TMF) [115]. In [116] they discuss reasons for the discrepancy with experiment and show that the plateaus of the three-point functions from which they extract g_A are very pronounced, i.e. the ratios of two- and three-point functions are very flat, so that excited state contributions are not seen at single t_{sink} studies.
The volumes used here range from $Lm_\pi = 3.27$ to 5.28. ETMC provide a chiral extrapolation with volume corrections according to [117] using one-loop heavy baryon chiral perturbation theory (HBχPT) in the small scale expansion (SSE) [118]. To facilitate the comparison of data we use the finite volume renormalized data. The renormalization was done non-perturbatively [119]. The lattice spacings in use vary between 0.056 and 0.089 fm and the data does not display a systematic lattice spacing dependence.

The RBC collaboration [120] produced $N_f = 2$ domain wall fermion (DWF) [121] data. DWF are chiral fermions which introduce a fifth dimension. In the limit of this additional dimension being large they fulfill the Ginsparg-Wilson [122] relation. Thus the RBC data should have less effects from chiral symmetry breaking than the Wilson-Clover and twisted mass fermions of the other collaborations. They have tried to estimate the effects of excited states by varying t_{sink} and the source/sink smearing. Two smearing radii of Gaussian smearing and a box source [123] were used. RBC see excited state contributions for g_A at the larger t_{sink} value and suspect that for the smaller t_{sink} value, which they use in the final results, these effects are also present. They use a

single spatial volume of $(1.9\ \text{fm})^3$. In [120] they employ a finite size correction strategy similar to [114] but we have again restricted ourselves to the un-corrected data. RBC renormalize g_A by taking the ratio g_A/g_V, assuming that the chiral symmetry breaking effects are strongly suppressed for DWF. Hence the associated renormalization constant cancel and $g_V^{\text{ren}} = 1$. The same reasoning would not work for Clover fermions or TMF as the chiral symmetry breaking yields different renormalization constants for axial and vector current. RBC use a single rather coarse lattice spacing of 0.116 fm and hence an analysis of discretization effects is not feasible.

4.2. Nucleon quark momentum fraction $\langle x \rangle_{u-d}$

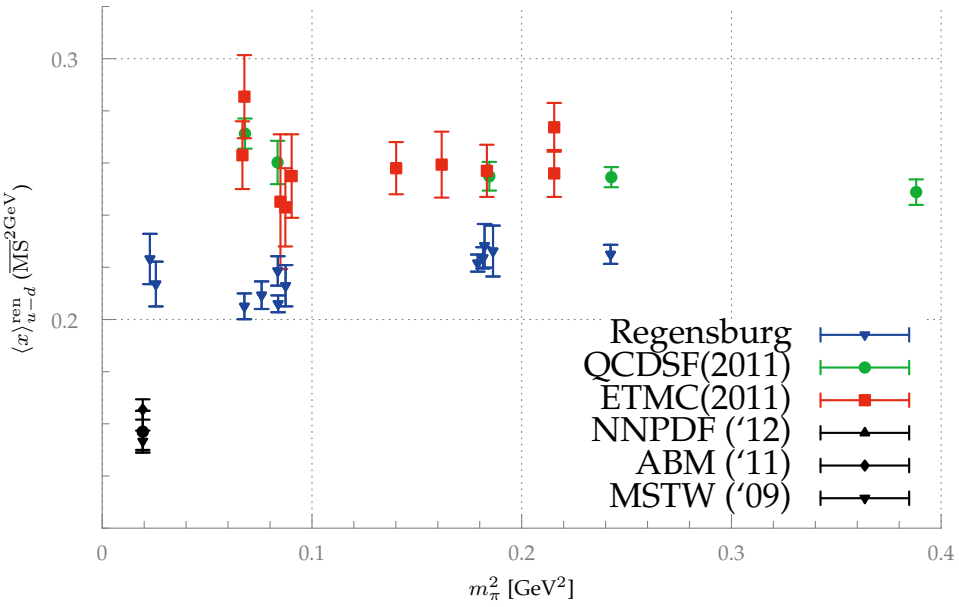

Figure 4.2.: The pion mass dependence of the quark momentum fraction computed by various lattice groups. This is an update of the plot published in [110].

In Fig. 4.2 we plot the results for the iso-vector quark momentum fraction in the nucleon of various collaborations and fits to experimental results from three groups (MSTW [124], ABM [125], NNPDF [126]). The lattice data are very flat throughout the whole range of m_π. The Regensburg data bend slightly downwards towards the physical point, but there is no indication that this bending is strong enough to reach the physical point at even lower pion masses. In fact the lowest data points are almost at the physical point and the experimental quark momentum fraction is missed by the lattice prediction, but

a chiral perturbation theory extrapolation has to be performed according to [127] to finalize this statement.
The difference between the QCDSF results and the Regensburg data is very pronounced and again can be attributed to excited state effects. In Section 2.4.5 and more explicitly in Eq. (5.23) we see that the matrix element of the excitation of the nucleon is enhanced by the mass of the excited state.

ETMC [128] computed the quark momentum fraction with two flavor twisted mass fermions. They observe a minor pion mass dependence, with decreasing values for smaller pion masses. In [116] they provide an update, where they also include results for more dynamical flavors($N_f = 2 + 1 + 1$) but do not find a systematic change of the data. They show the plateaus of the ratio of three- and two-point function, and some excited state contributions are visible. ETMC have used an optimized Gaussian smearing utilizing APE smeared gauge links, the same as for g_A [129]. To check for finite volume effects they used two volumes, one with $Lm_\pi = 3.3$ and one with $Lm_\pi = 4.3$, and found the results to be consistent. EMTC again employ non-perturbative renormalization and observe no significant cut-off effects.

QCDSF produced results on Jacobi smeared quark sources [130]. They display little m_π dependence of $\langle x \rangle_{u-d}$. QCDSF have employed chiral effective theory to fit the data and this fit misses the experimental value. This is due to the data not displaying enough curvature towards the physical point as a function of the pion mass. The finite size effects haven been checked, but there was no visible effect. Non-perturbative renormalization is applied and QCDSF finds the discretization effects to be small.

The Regensburg group has used the same set-up as for g_A in the analysis of $\langle x \rangle_{u-d}$. They differ from QCDSF in the choice of $r_0\Lambda_{\overline{MS}}$, which is used to convert the renormalized data from RGI to $\overline{MS}$. The Regensburg group uses $r_0\Lambda_{\overline{MS}} = 0.789$ and QCDSF uses $r_0\Lambda_{\overline{MS}} = 0.617$ [131].

The Mainz group has also computed $\langle x \rangle_{u-d}$, but they only have published un-renormalized results in [111]. Thus their results are not shown in the plot. Their ratios display excited state contributions and a strong dependence on the choice of t_{sink}. This hints that one has to perform an analysis either involving multiple t_{sink}, involving summed insertions or a combined fit analysis, see Chapter 5, or optimize the smearing significantly to render the exited state effects negligible. As they use very large lattices and fine lattice spacings finite volume or discretization effects are not expected.

5

Excited states in nucleon structure

As we have seen in Chapter 4 the excited state contributions to nucleon matrix elements may play a significant role in the disagreement with the experimental results. In this section we present a way to estimate these unwanted contributions. Parts of this chapter were published in [110].

5.1. Fit functions

We have seen in Eq. (3.84) that a ratio of three- and two-point functions can be used to extract the matrix elements of local operators, if both three- and two-point functions are dominated by the ground state. This ratio was formed to cancel the exponentials in the t_{ins} and t_{sink} dependence as well as the overlap factors $Z_\mu(\vec{p}, \phi)$ of the physical continuum states (μ) with the interpolating operators on the lattice.
A more general approach to compute matrix elements is presented in [132] and [133] . They perform a combined fit to the functional forms of two- and three-point function. This parameterization allows for different contributions from excited states. Then one can extract the matrix elements directly from the fit.
We parameterize Eq. (3.63) at zero momentum for times $t \ll N_t/2$ as

$$C_N(t) = A_1 e^{-m_1 t} + A_2 e^{-(m_1+\Delta m)t}\,, \tag{5.1}$$

where $m_1 = m_N$, and $\Delta m = m_{N'} - m_N > 0$ is the mass splitting of the ground state to the first excitation. To increase the numerical stability the amplitudes A_1 and A_2 were coded as exponential functions $A_i = \mathrm{e}^{a_i}$, where the a_i were the new fit parameters.
We can connect these amplitudes to physical parameters,

$$A_1 = V_3 Z_N \frac{E_N + m_N}{E_N} \overset{\vec{p}=0}{=} 2V_3 Z_N \qquad \text{and} \qquad A_2 = 2V_3 Z_{N'}\,. \tag{5.2}$$

For simplicity we take the source and the sink to have the same smearing ϕ and thus

can suppress the smearing dependence:

$$Z_\mu(\vec{p}=\vec{0},\phi) \equiv Z_\mu \,. \tag{5.3}$$

For $t_{\text{sink}} \ll L_t/2$ we can neglect antiparticle contributions and we have seen in Eq. (3.80) that the three-point function at rest and zero momentum transfer can be written as

$$\begin{aligned} C^{3pt}_{\mathcal{P}_+}(t_{\text{sink}}=t, t_{\text{ins}}=\tau;\vec{0},\vec{0};\mathcal{O},\Psi)/V_3 = {} & Z_N F(\mathcal{P}_+, M^O_\Psi, N, N)\mathrm{e}^{-m_N t} \\ & + \sqrt{Z_N Z_{N'}} F(\mathcal{P}_+, M^O_\Psi, N, N')\mathrm{e}^{-m_N(t-\tau)-m_{N'}\tau} \\ & + \sqrt{Z_{N'} Z_N} F(\mathcal{P}_+, M^O_\Psi, N', N)\mathrm{e}^{-m_{N'}(t-\tau)-m_N\tau} \\ & + Z_{N'} F(\mathcal{P}_+, M^O_\Psi, N', N')\mathrm{e}^{-m_{N'}t} + \cdots \,. \end{aligned} \tag{5.4}$$

We note that

$$F(\mathcal{P}_+, M^O_\Psi, N', N) = F(\mathcal{P}_+, M^O_\Psi, N, N') \tag{5.5}$$

and so we can fit the three-point function to

$$C^{3pt}_{\mathcal{P}_+}(t,\tau;\vec{0},\vec{0};\mathcal{O},\Psi) = A_1 e^{-m_1 t}\big(B_1 + \tilde{B}_2(e^{-\Delta m(t-\tau)} + e^{-\Delta m\tau}) + \tilde{B}_3 e^{-\Delta m t}\big) \,. \tag{5.6}$$

B_1, the quantity of our main interest, corresponds to

$$B_1 = 2F(\mathcal{P}_+, M^O_\Psi, N, N) \,. \tag{5.7}$$

Note that the normalization of the ratio R in Eq. (3.84) is such that it also corresponds to $R = 2F(\mathcal{P}_+, M^O_\Psi, N, N)$ and thus the ratio and B_1 should agree within errors if excited state contributions are negligible.

The corrections to this coming from t_{ins} dependent excited state contributions is parameterized by

$$\tilde{B}_2 = \sqrt{\frac{Z_{N'}}{Z_N}} 2F(\mathcal{P}_+, M^O_\Psi, N, N') \,. \tag{5.8}$$

To extract the transition matrix element of the first excited state and the ground state we define

$$B_2 = \tilde{B}_2 \sqrt{\frac{A_1}{A_2}} = 2F(\mathcal{P}_+, M^O_\Psi, N, N') \,. \tag{5.9}$$

$\tilde{B}_3$ describes the t_{sink}-dependent corrections from excited states; for only one value of

t_{sink} it cannot be extracted from the data. In formulas it is

$$\tilde{B}_3 = \frac{Z_{N'}}{Z_N} 2F(\mathcal{P}_+, M_\Psi^O, N', N')\,, \tag{5.10}$$

and we can extract the matrix element of the first excitation via

$$B_3 = \frac{A_1}{A_2}\tilde{B}_3 = 2F(\mathcal{P}_+, M_\Psi^O, N', N')\,. \tag{5.11}$$

5.2. Connection of the fit-parameters to physical quantities

In this section we will demonstrate how the fit parameters correspond to the charges and second moments of PDFs. The basis for that is the decomposition of nucleon matrix elements into Lorentz structures with the generalized form factors as their coefficients. This was outlined in Section 2.4.

5.2.1. Axial coupling

As can be seen from Section 2.4.3 the matrix element of the iso-vector axial current

$$\mathcal{J}^{u-d}_{\text{Axial},\mu} = \overline{u}\gamma_\mu\gamma_5 u - \overline{d}\gamma_\mu\gamma_5 d \tag{5.12}$$

for all momenta zero corresponds to

$$\left\langle \text{proton}(\vec{p}=\vec{0},\sigma) \,\middle|\, \mathcal{J}^{u-d}_{\text{Axial},\mu} \,\middle|\, \text{proton}(\vec{p}=\vec{0},\sigma') \right\rangle = G_A^{u-d}(0)\overline{U}(\vec{0},\sigma)\gamma_\mu\gamma_5 U(\vec{0},\sigma')\,, \tag{5.13}$$

and $g_A = G_A^{u-d}(0)$. The expectation value of this current at zero momenta is non-zero if the current is aligned with the polarization. Thus the system of equations yields three three-point functions that contribute (($\mathcal{P}_+^x, \gamma_x$) , ($\mathcal{P}_+^y, \gamma_y$), and ($\mathcal{P}_+^z, \gamma_z$)). We can average them since they have the same expectation value. Then our fit parameters are connected to the desired quantities via:

$$\begin{aligned} B_1 &= g_A 2F(\mathcal{P}_+^i, \gamma_i\gamma_5, N, N) = g_A 2\frac{1}{4m_N^2}\text{tr}_D\Big\{\frac{1}{2}\left(\mathbb{1}+\gamma_t\right)(-\text{i}\gamma_i\gamma_5)m_N\gamma_i\gamma_5 m_N\Big\} \\ &= g_A\frac{\text{i}}{4}\text{tr}_D\big\{\mathbb{1}\big\} = \text{i}g_A \qquad (5.14a) \\ B_2 &= g_A(N,N')2F(\mathcal{P}_+^i, \gamma_i\gamma_5, N, N') = \text{i}g_A(N,N') \qquad (5.14b) \\ B_3 &= g_A(N',N')2F(\mathcal{P}_+^i, \gamma_i\gamma_5, N', N') = \text{i}g_A(N',N')\,. \qquad (5.14c) \end{aligned}$$

5.2.2. Tensor coupling

The iso-vector tensor current

$$\mathcal{J}^{u-d}_{\text{Tensor},\mu\nu} = \overline{u}\mathrm{i}\sigma_{\mu\nu}\gamma_5 u - \overline{d}\mathrm{i}\sigma_{\mu\nu}\gamma_5 d \tag{5.15}$$

yields for vanishing momenta

$$\left\langle \text{proton}(\vec{p}=\vec{0},\sigma) \mid \mathcal{J}^{u-d}_{\text{Tensor},\mu\nu} \mid \text{proton}(\vec{p}=\vec{0},\sigma') \right\rangle = A^{u-d}_{T10}(0)\overline{U}(\vec{0},\sigma)\mathrm{i}\sigma_{\mu\nu}U(\vec{0},\sigma')\,, \tag{5.16}$$

and we denote $g_T^{u-d} = A_{T10}^{u-d}(0)$.
The three-point function of this current at zero momenta contributes to the determination of g_T^{u-d} if the current has two spatial indices $j \neq k$ which differ from the polarization direction i. In this case we can write $\mathrm{i}\sigma_{jk} = \gamma_k\gamma_j, j \neq k$.
We can now compute, similar to Eqs. (5.14a) to (5.14c), the interpretation of our fit parameters as

$$\begin{aligned} B_1 &= g_T^{u-d} 2F(\mathcal{P}^i_+, \mathrm{i}\sigma_{jk}, N, N) \overset{j\neq k}{=} g_T^{u-d} 2\frac{1}{4m_N^2}\mathrm{tr}_D\Big\{\frac{1}{2}\left(\mathbb{1}+\gamma_t\right)(-\mathrm{i}\gamma_i\gamma_5) m_N \gamma_k\gamma_j m_N\Big\} \\ &= g_T \frac{-\mathrm{i}}{4}\mathrm{tr}_D\left\{\gamma_t\gamma_i\gamma_x\gamma_y\gamma_z\gamma_t\gamma_k\gamma_j\right\} = \mathrm{i}\varepsilon^{ijk} g_T^{u-d} \qquad (5.17a) \\ B_2 &= g_T^{u-d}(N,N') 2F(\mathcal{P}^i_+, \mathrm{i}\sigma_{jk}, N, N') = \mathrm{i}\varepsilon^{ijk} g_T^{u-d}(N,N') \qquad (5.17b) \\ B_3 &= g_T^{u-d}(N',N') 2F(\mathcal{P}^i_+, \mathrm{i}\sigma_{jk}, N', N') = \mathrm{i}\varepsilon^{ijk} g_T^{u-d}(N',N')\,. \qquad (5.17c) \end{aligned}$$

We average the three-point functions over all all independent combinations of $\{i,j,k\}$ before we perform the fit. This reduces the statistical noise on each time-slice and facilitates the analysis.

5.2.3. Scalar matrix element

The forward matrix element of the iso-vector scalar current

$$\mathcal{J}^{u-d}_{\text{Scalar}} = \overline{u}u - \overline{d}d \tag{5.18}$$

is

$$\left\langle \text{proton}(\vec{p}=\vec{0},\sigma) \mid \mathcal{J}^{u-d}_{\text{Scalar},\mu\nu} \mid \text{proton}(\vec{p}=\vec{0},\sigma') \right\rangle = G_S^{u-d}(0)\overline{U}(\vec{0},\sigma)U(\vec{0},\sigma')\,, \tag{5.19}$$

and the scalar coupling is $g_S^{u-d} = G_S^{u-d}(0)$.
For this current we obtain a non-zero three-point function for an unpolarized projector

and we find

$$B_1 = g_S^{u-d} 2F(\mathcal{P}_+^u, \mathbb{1}, N, N) = g_S^{u-d} \tag{5.20a}$$
$$B_2 = g_S^{u-d}(N, N') 2F(\mathcal{P}_+^u, \mathbb{1}, N, N') = g_S^{u-d}(N, N') \tag{5.20b}$$
$$B_3 = g_S^{u-d}(N', N') 2F(\mathcal{P}_+^u, \mathbb{1}, N', N') = g_S^{u-d}(N', N')\,. \tag{5.20c}$$

5.2.4. Quark momentum fraction

The operators we insert here are of the type

$$\mathcal{O}^{u-d,\mu\nu}_{\text{VectorGPD}} = S(\mu,\nu)\left\{\overline{u}\gamma^\mu \overleftrightarrow{D}^\nu u - \overline{d}\gamma^\mu \overleftrightarrow{D}^\nu d\right\}\,. \tag{5.21}$$

The operators that contribute to twist two are traceless. After the subtraction of traces and setting all momenta to zero we find

$$\left\langle \text{proton}(\vec{p}=\vec{0},\sigma) \,\middle|\, \mathcal{O}_V^{44} - \frac{1}{3}\sum_i O_V^{ii} \,\middle|\, \text{proton}(\vec{p}=\vec{0},\sigma') \right\rangle = \mathrm{i}\overline{U}(\vec{0},\sigma)\overline{P}_t\gamma_t U(\vec{0},\sigma') A_{20}(t), \tag{5.22}$$

and we have defined $\overline{P}_t = \mathrm{i}(m_{\text{initial}} + m_{\text{final}})/2$. $v_{2b}^{u-d} = A_{20}^{u-d}(0)$ corresponds to the iso-vector quark momentum fraction $\langle x\rangle_{u-d}$ as it is the second Mellin moment of the unpolarized parton distribution function.
With similar calculations as in the previous subsections we can interpret our fit-parameters as

$$B_1 = v_{2b}^{u-d} 2F(\mathcal{P}_+^u, \mathrm{i}\overline{P}_t\gamma_t, N, N) = -m_N v_{2b}^{u-d} \tag{5.23a}$$
$$B_2 = v_{2b}^{u-d}(N, N') 2F(\mathcal{P}_+^u, \mathrm{i}\overline{P}_t\gamma_t, N, N') = -\frac{m_N + m_{N'}}{2} v_{2b}^{u-d}(N, N') \tag{5.23b}$$
$$B_3 = v_{2b}^{u-d}(N', N') 2F(\mathcal{P}_+^u, \mathrm{i}\overline{P}_t\gamma_t, N', N') = -m_{N'} v_{2b}^{u-d}(N', N')\,. \tag{5.23c}$$

5.3. Summed insertions

The method of summed insertions is a way to treat excited states in nucleon three-point functions. It is recommended in [134]. The idea was first presented for the special case of the scalar and γ_5 insertion [96]. The method was later generalized in [84]. We define $t_{\text{sink}} \equiv t$ and the insertion time $t_{\text{ins}} \equiv \tau$ the summed insertion as

$$S(t) = \sum_{\tau=\delta t}^{t-\delta t} R(\tau, t)\,, \tag{5.24}$$

where $R(\tau, t)$ is shorthand for the ratio of three-point to two-point function[1].
Using the functional forms of the two-point function Eq. (5.1) and three-point function Eq. (5.6) we can estimate the t-dependence of the ratio after summing over the insertion time τ from the start time δt to $t - \delta t$:

$$\begin{aligned} S(t) &= \sum_{\tau=\delta t}^{t-\delta t} \left(B_1 + \tilde{B}_2(\mathrm{e}^{-\Delta m(t-\tau)} + \mathrm{e}^{-\Delta m\tau}) + \tilde{B}_3\mathrm{e}^{-\Delta mt}\right)\left(1 + A\mathrm{e}^{\Delta mt}\right)^{-1} \\ &= \frac{t - 2\delta t + 1}{1 + A\mathrm{e}^{-\Delta mt}} B_1 + \frac{2\tilde{B}_2\mathrm{e}^{-\delta t\Delta m}}{1 + A\mathrm{e}^{-\Delta mt}} \sum_{\tau=0}^{t-2\delta t} \left(\mathrm{e}^{-\Delta m}\right)^{\tau} + \frac{t - 2\delta t + 1}{1 + A\mathrm{e}^{-\Delta mt}} \tilde{B}_3\mathrm{e}^{-\Delta mt} \end{aligned} \tag{5.25}$$

where $A = \frac{A_2}{A_1}$.
We can use the geometrical series

$$\sum_{k=0}^{n-1} x^k = \frac{1 - x^n}{1 - x} \qquad \text{for} \quad (x \neq 1)\,, \tag{5.26}$$

to evaluate

$$\sum_{\tau=0}^{t-2\delta t} \left(\mathrm{e}^{-\Delta m}\right)^{\tau} = \frac{1 - \mathrm{e}^{-\Delta m(t-2\delta t+1)}}{1 - e^{-\Delta m}}\,. \tag{5.27}$$

We can now collect the t-independent corrections in a constant C so that we can approximate Eq. (5.25) as

$$S(t) \approx tB_1 + C + \mathcal{O}(t\mathrm{e}^{-\Delta mt})\,. \tag{5.28}$$

By summing over the insertion times we were collecting all $t_{\text{ins}} = \tau$ dependent terms and are only left with corrections which are exponentially suppressed in t_{sink}. The price we have to pay for that is that we need multiple t_{sink}-values to extract B_1 as the slope of a straight line fit. The fitting window of the range of t_{sink} one uses has to be chosen with care, as the smallest t_{sink} needs to be big enough that the (exponential) suppression of the excited states is sufficient. The larger one goes in t_{sink} the lower the signal-to-noise ratio, so at some range of t_{sink} one cannot extract any additional information on B_1. This is why matrix elements extracted with summed insertions typically have larger error bars than values extracted directly from a fit to the plateau. Nevertheless the suppression of excited states is necessary and if they are present in the plateau data the result of a plateau fit is meaningless, and so small error bars are no help. This is why

[1] Which also have a momentum dependence which we have suppressed here.

t_{sink}[a]	N_{conf}	N_{sources}
7	2011	1
9	2011	1
11	2011	1
13	2011	2
15	2011	2
17	2011	2

Table 5.1.: Used statistics for the different values of t_{sink}.

this method is used by many groups [111, 135].

5.4. General considerations

5.4.1. Simulation details

We use an ensemble with $\beta = 5.29$, $\kappa = 0.13632$, and a volume $V = 32^3 \times 64$. This corresponds to a pion mass of $m_\pi = 294$ MeV, a lattice extend of $Lm_\pi = 3.4$ and a lattice spacing $a = 0.07$fm.

We have used 400 steps of Wuppertal smearing with 25 times APE smeared gauge links as quark smearing.

We vary t_{sink} in a range of 0.49 fm to 1.19 fm and the number of measurements for each value of t_{sink} can be found in Table 5.1. We have decided to increase the number of sources starting from $t_{\text{sink}} = 13a$ to counter the increase of the statistical noise with t_{sink}.

The currents have to be multiplicatively renormalized and the associated renormalization constants listed in Table 5.2. The renormalization is done using procedure outlined in Section 3.9.

The values for the coefficient w_c, defined in Eq. (3.111), of the quark mass dependent current correction for the scalar, axial, pseudoscalar and vector current can be found in Table 1 of [136]. Note that $b_s = -2b_m$. The correction for the tensor current is from Table V of [137]. We have computed the order a-correction to the for $v_2 b$ from the appendix table 10 of [138] for $c_2 = 0$.

In principle also $\mathcal{O}(g^2)$ corrections from the operator improvement, but we do not have the improved three-point functions available.

The three-point functions were multiplied by this constants before fitting such that the matrix elements we extract from the fit are renormalized.

Quantity	Z_{RGI}	$1 + bam$	$Z_{\mathrm{RGI}\to\overline{\mathrm{MS}}^{\mu=2\mathrm{GeV}}}$	total
g_A	0.7647(14)	1.0034	1	0.7673(14)
g_T	0.9137(48)	1.0033	0.9415	0.8631(45)
g_S	0.4585(61)	1.0035	1.35052	0.6214(83)
v_{2b}	1.509(23)	1.0033	0.74027	1.1208(17)

Table 5.2.: Renormalization constants for $\beta = 5.29$ and $\kappa = 0.13632$.

5.4.2. Fit setup

We performed several types of fits to our data, where we have varied the data-set, the fit-range and the definition of χ^2. We then chose the fit which yielded the most robust result with a reasonable goodness of the fit.

As the quantity $\langle x \rangle_{u-d}^{\overline{\mathrm{MS}}\,\mu=2\mathrm{GeV}}$ is later used to infer the effects of choosing a certain t_{sink} value on other ensembles the analysis for it is most crucial. We therefore show the plots that illustrate the choice of the optimal fit for this case and only report the results of this procedure for the other quantities.

5.4.2.1. Fit-ranges

As this is a combined fit we have several fit-ranges to vary. The three-point functions should have symmetric fit-rages centered around $t_{\mathrm{sink}}/2$, so we can define their fit-range to be Δt to $t_{\mathrm{sink}} - \Delta t$. We keep Δt fixed within a combined fit for all three-point functions, as the t_{ins}-dependent decay of the higher excited states is independent of t_{sink}, for a given the insertion operator.

In the combined fits where we simultaneously analyzed the three-point functions of different insertion operators we still kept Δt fixed, to reduce the overall number of fits to a tractable number. Since we use the Wilson-Clover action, there are artifacts on the time-slices next to the quark source, and thus our smallest choice is $\Delta t = 2$. For $\Delta t = 4$ we cannot use our smallest t_{sink} value and in addition the signal for excited states has mostly decayed already, so we do not go higher than $\Delta t = 3$.

The fit-range for the two-point function can be chosen independently and we scanned it with twelve different fit-ranges; t_{start} was chosen between 2, 3, 4 and t_{end} in 13, 17, 20 and 23.

In the plots, Figs. 5.4 to 5.7 , we present the different fits as the abscissa where we vary our fit-ranges from slow to fast indices: Δt, t_{start} to t_{end}.

5.4.2.2. Data sets

We have analyzed data for operators that correspond to g_A^{u-d}, g_T^{u-d}, g_S^{u-d} and $\langle x \rangle^{u-d}$. The fits were first performed for each channel individually (at the six different t_{sink} values and the two-point function). As the masses of nucleon ground and first excited state occur in all fit formulae a combined fit to the full data set was also performed. This is forcing the fit results to values where the mass of the excitation does not depend on the channel we look at, as the analytic computation predicts. We plot both kinds of fits for comparison in Figs. 5.4 to 5.7.

5.4.2.3. χ^2 definitions

We have binned our data to obtain N independent measurements. We label the different data-sets, e.g. three-point functions for different insertion operators, by the sub/superscripts $(d), (d')$. A data set consists of multiple points, labeled by Latin indices i, j. This points are for example taken at different time-slices.
The mean value at a given time-slice is then given by

$$\overline{x}_i^{(d)} = \frac{1}{N} \sum_{k=1}^{N} x_i^{(d)}(k) \tag{5.29}$$

where the index k enumerates the different data bins.
The fits were done by minimizing

$$\chi^2 = \sum_{d,d'} \sum_{i,j} \left(\overline{x}_i^{(d)} - f^{(d)}(i) \right) C^{-1}_{i(d)j(d')} \left(\overline{x}_j^{(d')} - f^{(d')}(j) \right) . \tag{5.30}$$

The minimization is performed by finding the appropriate fit parameters in the functions $f^{(d)}$. The "goodness of fit" interpretation of the minimal value of χ^2 per degree of freedom ($\chi^2_{\text{p.d.o.f}}$) tells us that a good fit (i.e. a fit function that is in full agreement with the data, and data with a good estimation of its error) is reached for values of $\chi^2_{\text{p.d.o.f}} \approx 1$.
A value much smaller than one would suggest that we overestimate the errors on the data, or that our fit function has too many free parameters that cannot be determined by the data. A value of much more than one would suggest that our data is not well described by the form of the fit function.
The variance-covariance matrix is

$$C_{i(d)j(d')} = \frac{1}{N-1} \sum_{k=1}^{N} \left(x_i^{(d)}(k) - \overline{x}_i^{(d)} \right) \left(x_j^{(d')}(k) - \overline{x}_j^{(d')} \right) . \tag{5.31}$$

It can be inverted using SVD, and we have varied the cut-off for the singular values in a range from the numerical precision, and from 10^{-8} to 10^{-6} times the biggest singular value. It is a very difficult task to find the best approximation to the inverse variance-covariance matrix since the errors of the matrix entries can be quite large. We find that our fully covariant fit using all data-sets is not very stable due to the uncertainty on the variance-covariance matrix. This can be seen from Figs. 5.4 to 5.7.
Another ansatz is to neglect the correlations, i.e. using a diagonal variance-covariance matrix. Then the definition of χ^2 reduces to

$$\chi^2 = \sum_d \sum_i \frac{\left(\overline{x}_i^{(d)} - f^{(d)}(i)\right)^2}{\sigma_i^2} \,. \tag{5.32}$$

This yields more stable fits and often is a better estimation of the inverse variance covariance matrix than the inverse of the full variance covariance matrix [139], when the errors on the correlations are too big. Unfortunately this definition of χ^2 does not allow for an interpretation of $\chi^2_{\text{p.d.o.f}}$ to indicate the "goodness of fit". This is due to the fact that we have correlated data, which will usually fluctuate much less around the fit function than the statistical errors imply.

5.5. Results

5.5.1. Extraction of the nucleon mass

We extracted the nucleon mass from the combined fit of the two-point function and three-point functions at all available values of t_{sink} with an insertion corresponding to v_{2b}^{u-d}. We obtain $m_N a = 0.3882(58)$ at $\beta = 5.29$, $\kappa = 0.13632$, $m_\pi = 294$ MeV, and a volume $V = 32^3 \times 64$ with a lattice spacing of $a = 0.07$fm , which corresponds to $m_N = 1.094(16)$ GeV in physical units. This results is used to extract the quark momentum fraction from the plateau value of the ratios and the slope of the fit to the summed insertions.

5.5.2. Summed insertion

The summed insertion method yields stable results and the t_{sink}-dependence is in good agreement with a straight line. The $\chi^2_{\text{p.d.o.f.}}$ of the fully correlated fit is below one in all channels except for the tensor charge. So we probably overestimate the errors on the sum and we ignore the results of the correlated fits in the following. Our best uncorrelated fit results for $\delta t = 2$ and all t_{sink} can be found in Table 5.3, where the second error is the systematic error estimated by varying δt and the t_{sink} values that were included in the fit. In the plots Fig. 5.1 we use statistical errors only. We can also

Observable	$N \to N$	$N \to N'$	$N' \to N'$	Sum. Insertion
$G_A(0)^{\mathrm{RGI}}_{u-d}$	$1.124(20)(^{+5}_{-2})$	$0.001(29)(^{+3}_{-12})$	$1.32(42)(^{+5}_{-12})$	$1.164(15)(^{+0}_{-12})$
$A_{T10}(0)^{\overline{\mathrm{MS}}^{\mu=2\mathrm{GeV}}}_{u-d}$	$1.010(26)(^{+6}_{-5})$	$0.195(26)(^{+3}_{-11})$	$1.82(44)(^{+15}_{-29})$	$1.054(12)(^{+15}_{-28})$
$G_S(0)^{\overline{\mathrm{MS}}^{\mu=2\mathrm{GeV}}}_{u-d}$	$0.861(98)(^{+16}_{-4})$	$-0.18(13)(^{+2}_{-6})$	$2.1(1.4)(^{+0.4}_{-0.1})$	$0.85(10)(^{+0}_{-2})$
$\langle x \rangle^{\overline{\mathrm{MS}}^{\mu=2\mathrm{GeV}}}_{u-d}$	$0.1971(73)(^{+62}_{-13})$	$0.054(11)(^{+2}_{-23})$	$0.197(66)(^{+94}_{-10})$	$0.2056(66)(^{+48}_{-37})$

Table 5.3.: Overview of the results of the combined fit to all observables.

use the results of the combined fit to all three-point functions for all insertions and the two-point function to compute the prediction for the sum over the insertions. This gives a systematically smaller absolute value. This may stem from the fact that we exclude excitations higher than the first one. Nevertheless the fit agrees within errors, and as we perform a combined fit over all data sets the agreement with the individual sub-data sets needs not to be as good as for the linear fit.

5.5.3. Fits to individual observables

We have also performed fits to individual observables (Single Obs), so the two-point function and the (averaged) three-point function corresponding to a single current, and contrast them to the results of the ratio. Since the three-point functions are evaluated at zero momenta the denominator of the ratio is a constant. We fit the two-point function permitting an excited state. We then divide the three-point function by the ground state two-point function ($A_1 \mathrm{e}^{-m_N t_{\mathrm{sink}}}$) at t_{sink}. Therefore the denominator is slightly smaller than in the ratio, since the first excited state is taken out. This is especially visible for small values of t_{sink}.
This amounts to the fact that by omitting excited state contributions in the formula for the ratio one overestimates both nominator and denominator, such that the effects cancel partially.
In Fig. 5.2 we plot the ratios and in Fig. 5.3 the results to the fit.

5.5.4. Combined fits

In Fig. 5.4 we see that the fits using the full covariance matrix clearly disagree with the ones using a diagonal one. This fit is pulled away from the data-points by using the full variance-covariance matrix, so that the fits are rendered unreliable. This is usually a unequivocal indication that the errors on the estimation of the covariance matrix are too big, so that only uncorrelated fits are supported by the data. This statement also holds true for other observables although this discrepancy is not as obvious as in the g_A case. The uncorrelated fits are stable within a wide variation of the fit-range.

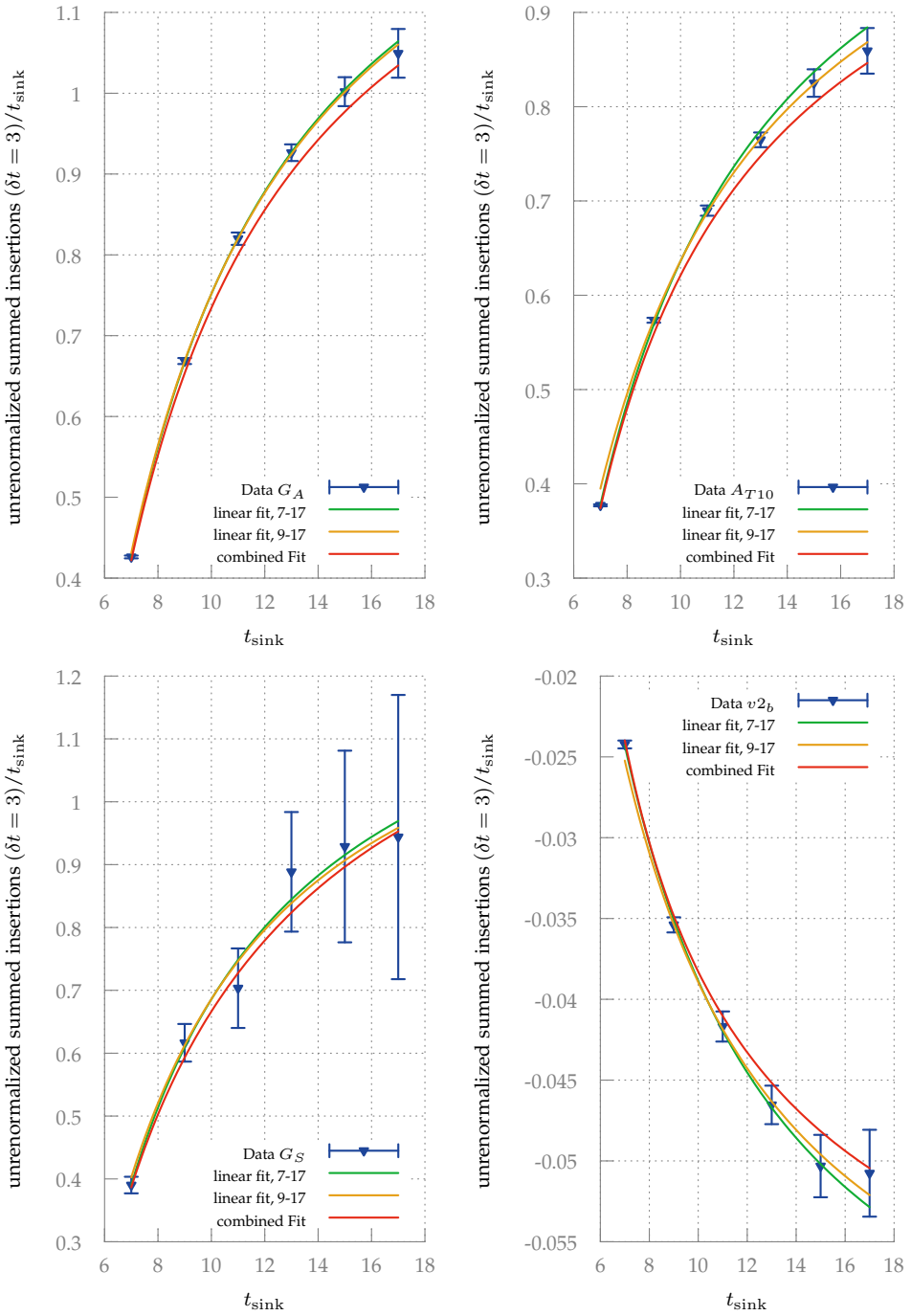

Figure 5.1.: Comparison of a linear fit to summed insertions and sum over the fit prediction coming from the combined fit over the same interval. We divide the data by t_{sink} for the plot, so that in the limit of large t_{sink} one obtains a constant.

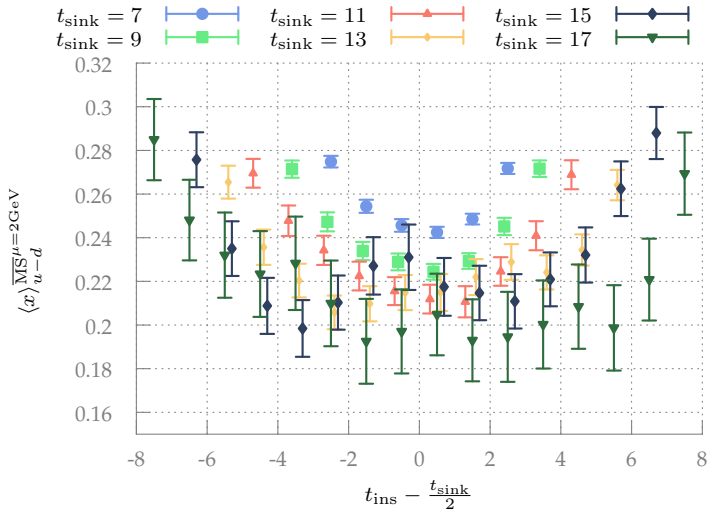

Figure 5.2.: Ratios of two and three-point function for $\langle x \rangle_{u-d}^{\overline{\text{MS}}, \mu=2\text{GeV}}$ at various t_{sink}.

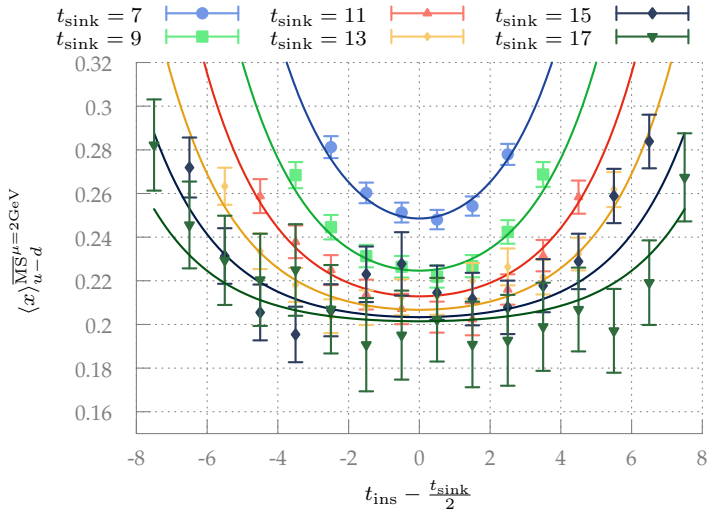

Figure 5.3.: Combined fit to the three-point function and two-point function for $\langle x \rangle_{u-d}^{\overline{\text{MS}}, \mu=2\text{GeV}}$ at various t_{sink}. We plot the ratios of two and three-point function as predicted by the fit. Note that the points are slightly shifted upwards compared to Fig. 5.2 due to the omission of the first excited state in the two-point function.

The systematic errors in Table 5.3 are given by the maximal change in the central value by choosing other fit ranges. As not all fits are of equivalent quality this probably overestimates the systematic errors, but as higher excitation have been neglected this conservative approach appears to be justified.
We now discuss the results of Table 5.3 for each quantity. The axial coupling is lower than predicted by the experiment, but is in agreement with the values observed by other collaborations at comparable pion mass, see Fig. 4.1.
Its transition matrix element from ground- to first excited state for g_A is comparable with zero, where as in the other channels it is clearly non-zero.
The axial coupling of excited state of the nucleon could not be determined with a precision comparable to the one we found for the ground state. Within its larger errorbars the value seems to be comparable with the one of the ground state.
This is also the case for $\langle x \rangle_{u-d}$. Here the ground state matrix element is rather low compared to the results of other studies at similar pion mass, see Fig. 4.2 , but still higher than the experimental value. Note that the excited state matrix element is enhanced by the mass of the excited state in the three-point function. This means that at a choice of too small t_{sink} the plateau value will yield a too big result for $\langle x \rangle_{u-d}$.
The tensor coupling seems to be larger for the excitation and its transition element is clearly visible in the data.
The scalar coupling of the first excitation of the nucleon could not be determined reliably as the data is very noisy. The scalar transition matrix element is the only negative transition element.
We find a good agreement between our combined fit results and the results from the summed insertion method.

5.5.5. Comparison of the different methods

In Fig. 5.8 we plot the results of the fits to plateaus at various t_{sink} for the four quantities in question. In addition we plot the results of the analysis of the same data with the summation method and a combined fit to the full data set with the formulae of Eq. (5.1) and Eq. (5.6).
We see that the analysis with the combined methods (summation and combined fit) does agree with the larger plateau values for $t_{\text{sink}} = 15, 17$, due to the fact that the errors are so big and thus the (small) differences are not significant. Since we plot statistical errors only, we note that by choosing fit-ranges differently this agreement of the plateau method and the combined fit can be enhanced. We did refrain from that and chose the best fits, but therefore the small differences may not be over interpreted.
The plateau value should approach the pure ground state contribution monotonously with increasing t_{sink} for infinite statistics. In the case of $\langle x \rangle_{u-d}$ the fact that it stays constant when going from $t_{\text{sink}} = 11a$ to $t_{\text{sink}} = 15a$ and then falls of at $t_{\text{sink}} = 17a$

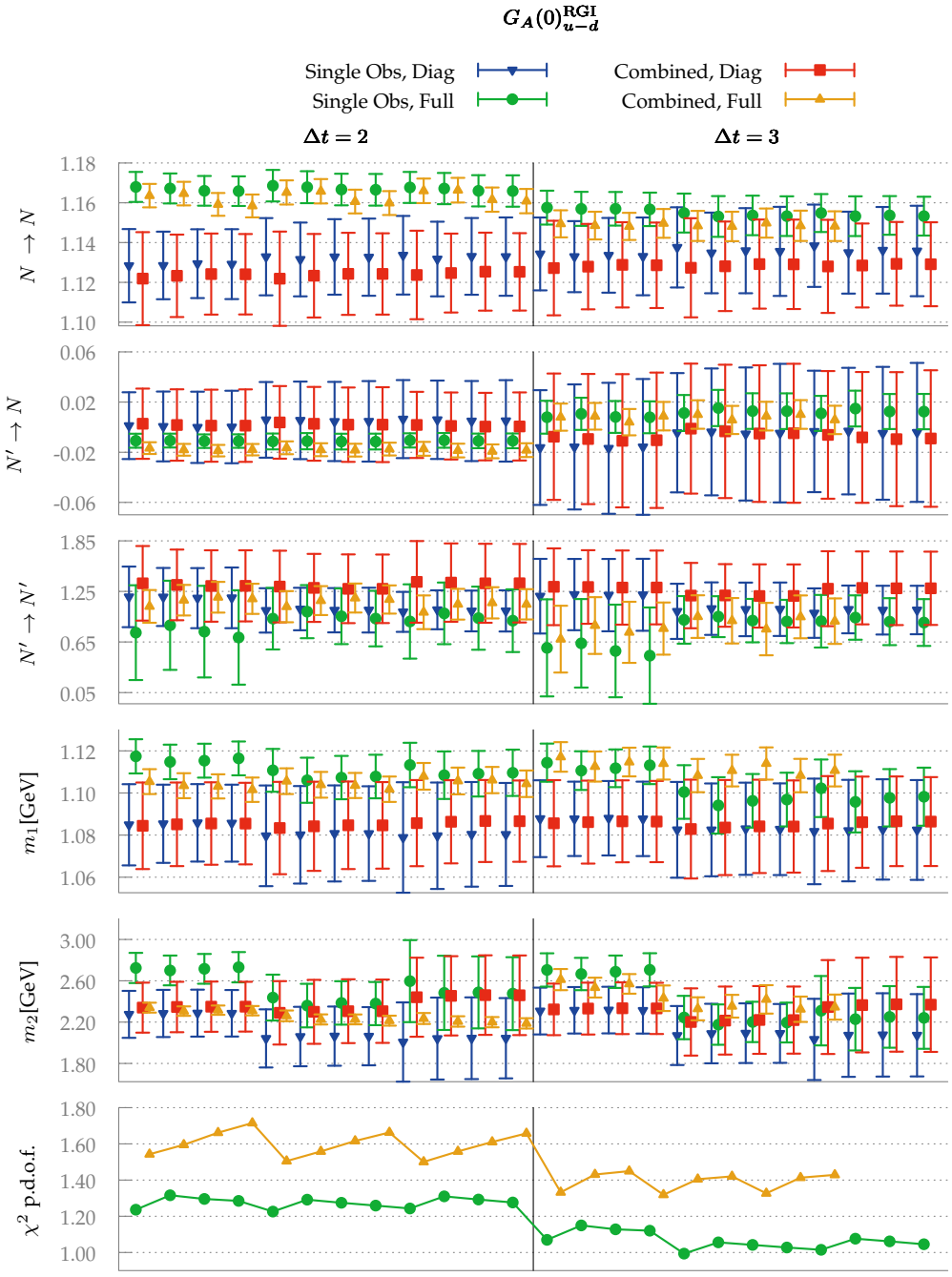

Figure 5.4.: Comparison of combined fits and single observable fits for $G_A(0)^{\mathrm{RGI}}_{u-d}$ at different fit ranges. We vary (slow to fast): Δt, t_{start} to t_{end}.

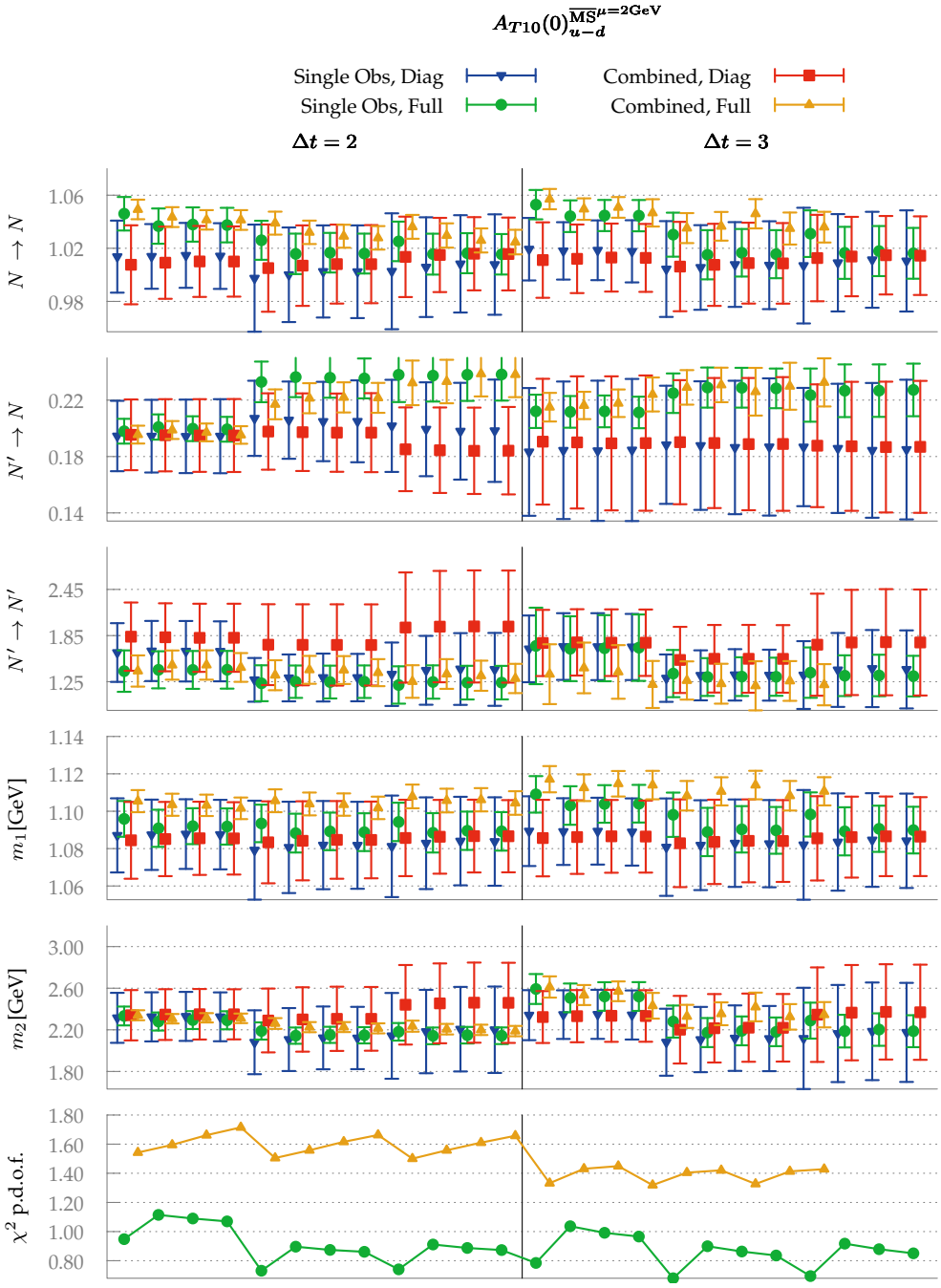

Figure 5.5.: Same as Fig. 5.4 but for $A_{T10}(0)_{u-d}^{\overline{\text{MS}}\,\mu=2\text{GeV}}$.

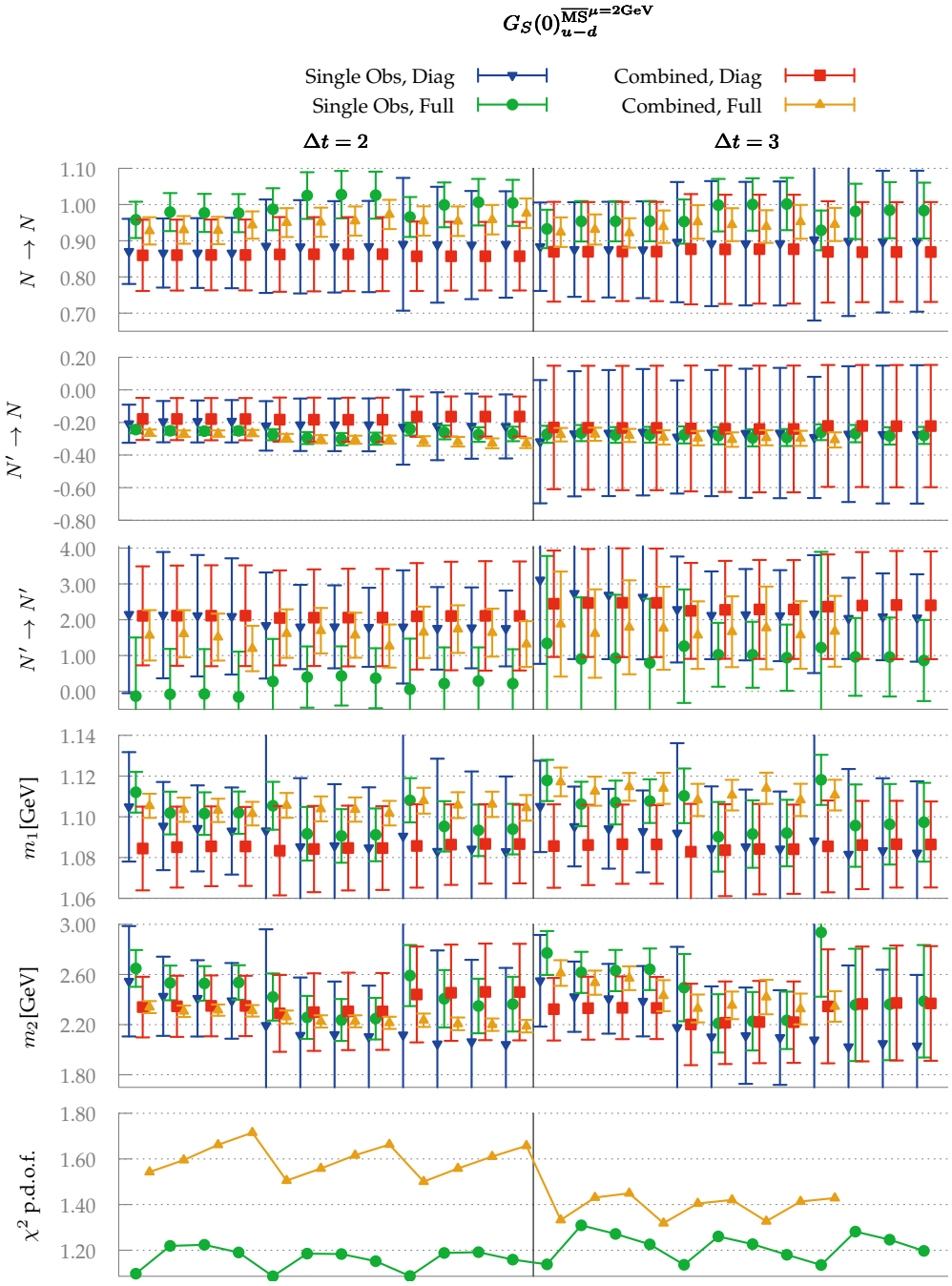

Figure 5.6.: Same as Fig. 5.4 but for $G_S(0)^{\overline{\rm MS}^{\mu=2\rm GeV}}_{u-d}$.

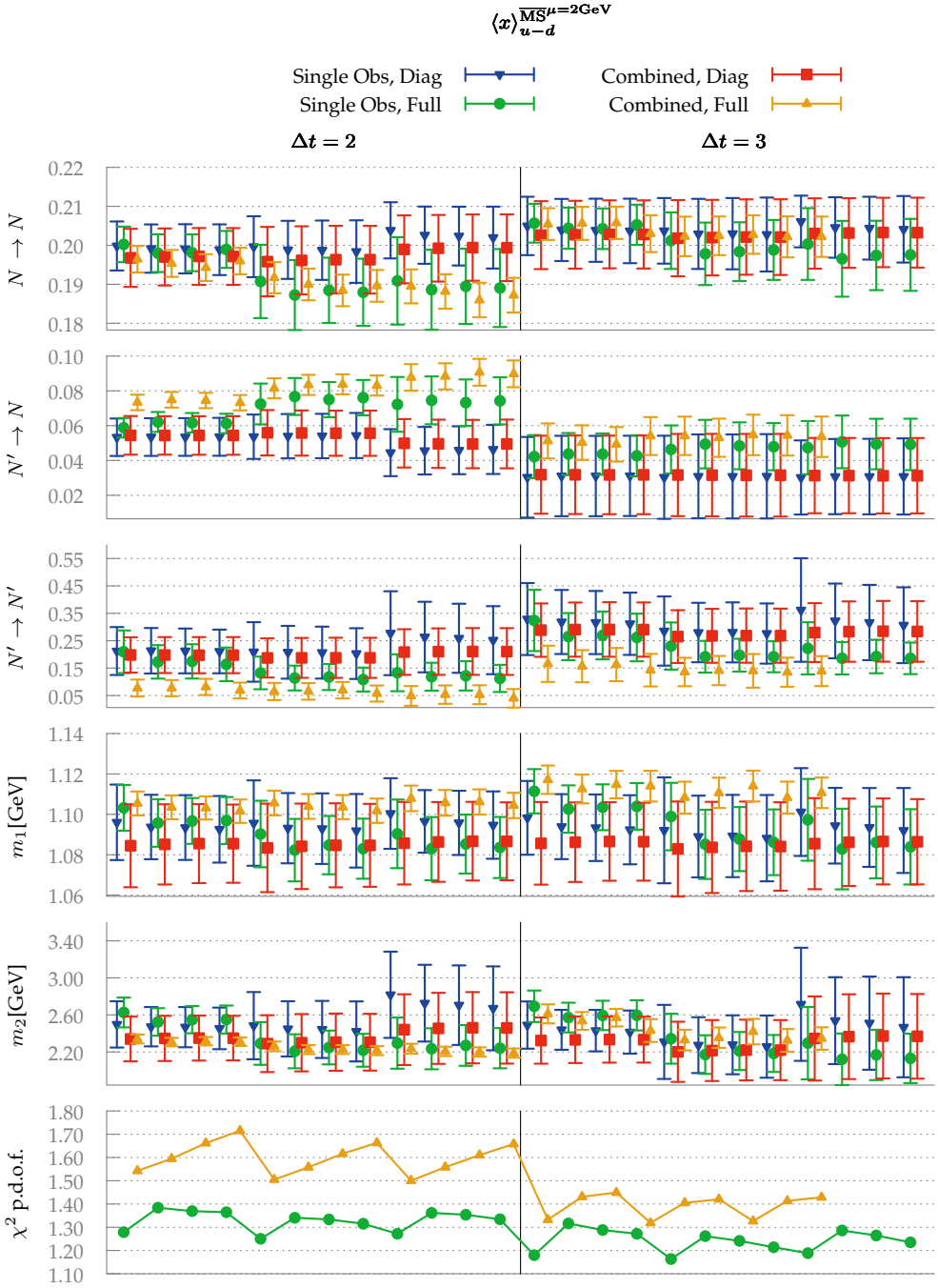

Figure 5.7.: Same as Fig. 5.4 but for $\langle x \rangle_{u-d}^{\overline{\text{MS}}\,\mu=2\text{GeV}}$.

means that statistical fluctuations due to finite statistics dominate the systematic effects stemming from the choice of t_{sink} in this channel.
Nevertheless when considering A_{T10} it becomes obvious that systematic effects due to the choice of t_{sink} can be sizable if the choice was made too small.

5.6. Estimation of systematic effects on a different lattice

In the previous sections we conducted an extensive analysis of the effects of excited states on nucleon matrix elements. The quark smearing was kept fixed to 400 steps of Wuppertal smearing on APE smeared links and t_{sink} was varied. On other lattices a similar study is impractical as oftentimes one wants to extract the quantities of interest with a single choice of t_{sink}.
At a bigger lattice volume of $48^3 \times 64$ sites and the same value of the gauge coupling $\beta = 5.29$, at a slightly lighter pion mass of ≈ 157 MeV ($\kappa = 0.13640$) we measured $\langle x \rangle_{u-d}$ at $t_{\text{sink}} = 15a$. This choice of parameters corresponds to the ensemble "b5p29kp13640-48x64". To estimate the systematic effects of this choice we parameterize the three-point function as

$$\begin{aligned} C^{3pt}_{v2_b} =& A_1 e^{-m_1 t}\big(-m_1 \overline{B}_1 \\ & -\sqrt{\frac{A_2}{A_1}}\frac{m_1+m_2}{2}\overline{B}_2(e^{-\Delta m(t-\tau)} + e^{-\Delta m \tau}) - m_2 \frac{A_2}{A_1}\overline{B}_3 e^{-\Delta m t}\big) \end{aligned} \tag{5.33}$$

so that the fit parameters $\overline{B}_i$ correspond to the matrix elements of the quark momentum fraction directly. We take $\overline{B}_2$ and $\overline{B}_3$ from the fit of the heavier lattice (with pion mass of 294 MeV, "b5p29kp13632-32x64") and fix their values in the constrained fit. This is our best guess for these values and as the quark momentum fraction seems to be stable over a wide range of pion masses, see Fig. 4.2, it is natural to assume that the excited state matrix elements are too.
In the free fit we fix $\overline{B}_3$ to zero and allow $\overline{B}_2$ to vary. Note that the free fit is not consistent in the number of permitted excited states in three- and two-point function and is just performed as a small consistency check.
In Fig. 5.9 we illustrate the stability of the constrained and the free-fit and show the result of the simple plateau fit. We see that there is good agreement between the fit methods, ranges and the standard analysis. So the systematical errors connected with the choice of $t_{\text{sink}} = 15$ can be assumed to be very small compared to the statistical errors.
To quantify that statement consider Table 5.4. For the smaller lattice "b5p29kp13632-32x64", with bigger m_π, we find that the plateau fit suggests a slightly higher value at $t_{\text{sink}} = 15a$ than the other fits, even though the difference is not significant. This is in agreement with Fig. 5.8 where the plateau value at $t_{\text{sink}} = 15a$ does not follow the

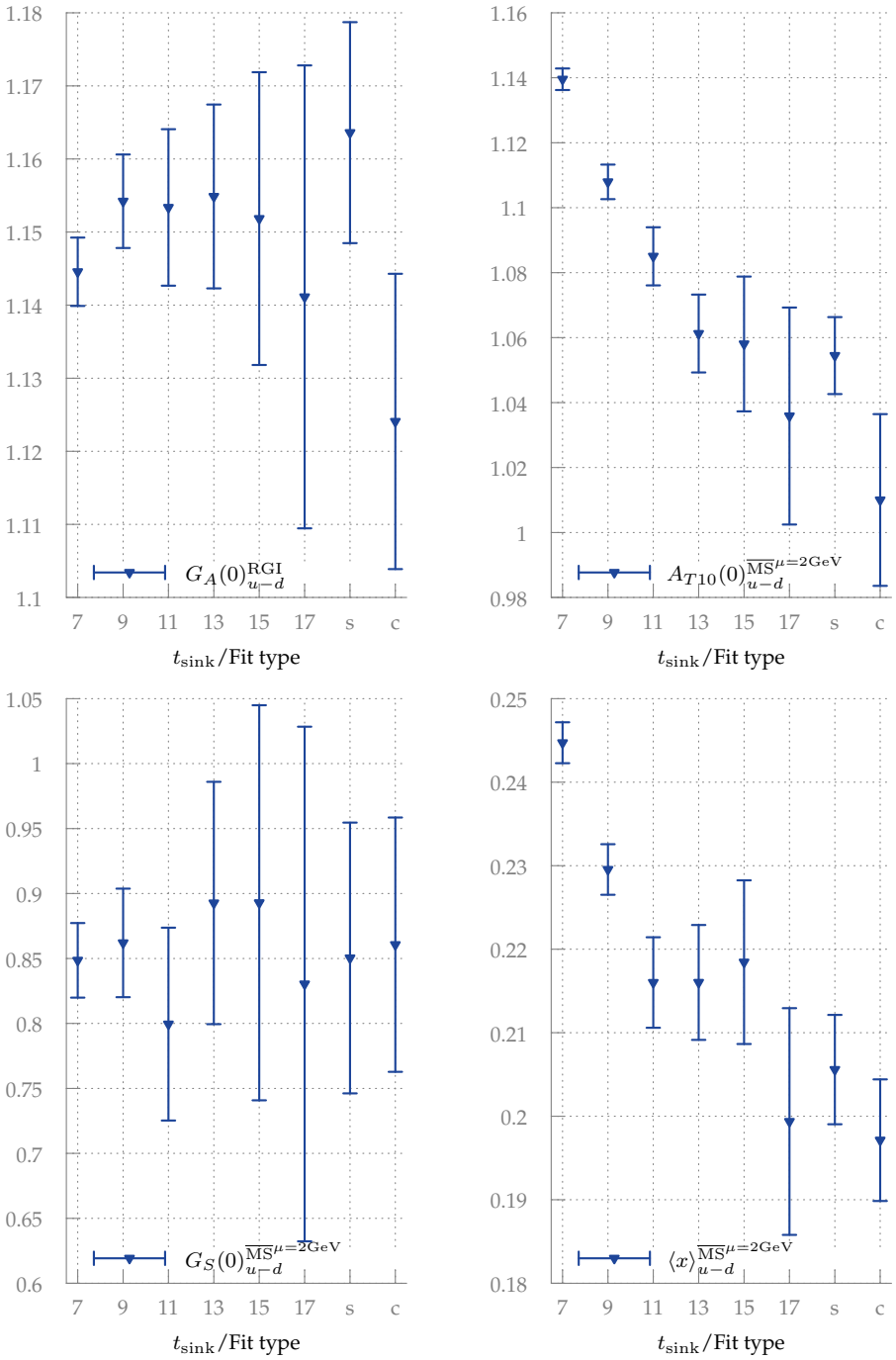

Figure 5.8.: Comparison of summed insertion (s), combined fit (c) and single plateau fit at given t_{sink}.

general downward trend with increasing t_{sink}. For the bigger lattice the constrained fit lies even higher than the plateau fit, but again the difference is not significant.

Lattice	Constrained Fit	Free Fit	Plateau Fit $t_{\text{sink}} = 15a$
b5p29kp13632-32x64	0.2053(81)	0.206(11)	0.216(11)
b5p29kp13640-48x64	0.2115(73)	0.202(10)	0.204(10)

Table 5.4.: The uncorrelated fit results to the different fit functions at two lattices.

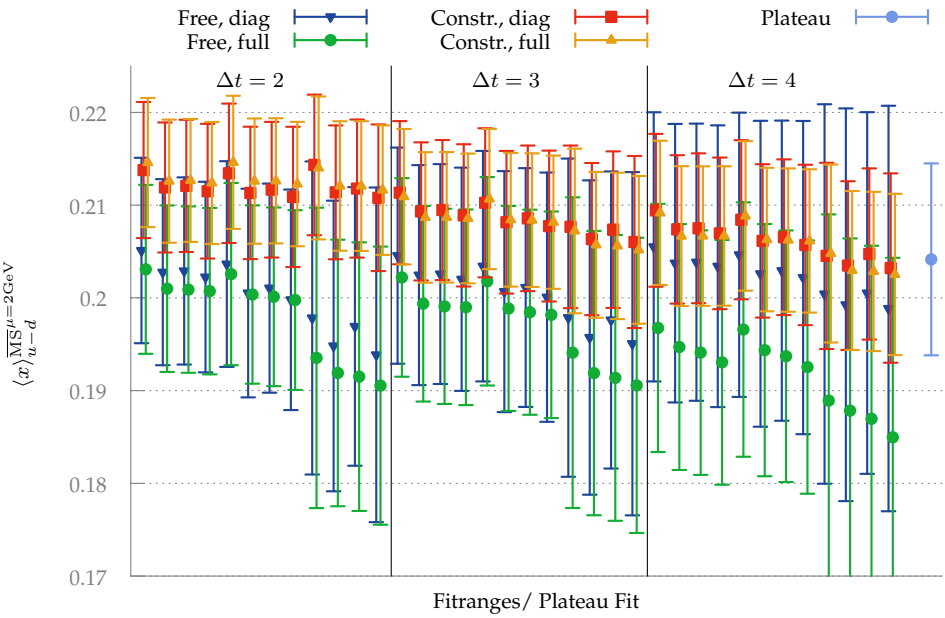

Figure 5.9.: Different fit ranges for the constrained (Constr.) and free fit in comparison with the result of the plateau fit at $\beta = 5.29$,$\kappa = 0.13640$, $48^3 \times 64$.

In Fig. 5.10 we show the fit curves of constrained and free fit and the standard ratio of two- and three-point function as in Eq. (3.82). The points in the plot are the measured three-point function divided by the fit to the ground state two-point function ($A_1 \mathrm{e}^{-m_N t_{\text{sink}}}$). The discrepancy between the ratio definition and those reconstructed ratio-points comes from the excited state contributions to the measured two-point function.

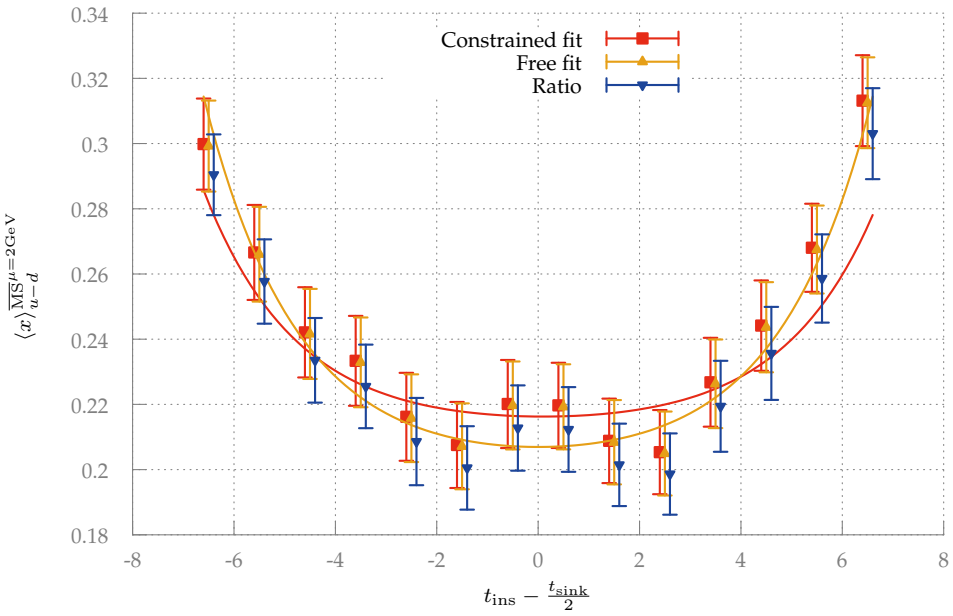

Figure 5.10.: The fits from Fig. 5.9 plotted as lines and for comparison with the standard ratio we add the measured three-point function divided by $A_1 \mathrm{e}^{-m_N t_{\mathrm{sink}}}$ of each fit.

6
Nucleon structure from stochastic estimates

In Section 3.7.4 we have seen that we can use all-to-all propagators to compute baryon three-point functions. The benefit of this method is that one can freely compute many sink momenta and polarizations of the nucleon. This could in theory outweigh the additional noise one gets on the signal as one can access many more momentum combinations, compare Table C.1 and Table C.2. To compare the stochastic method with fixed t_{sink} and the sequential sink method in terms of signal-to-noise ratio at fixed computer time we have first tried to optimize the performance of the stochastic estimation setup (Section 6.1) and then compared our findings to the sequential source method (Section 6.2).

6.1. Optimization of the computation setup

6.1.1. Parity partner averaging

Under time-reversal symmetry $t/a \to (N_t - t/a) \mod N_t \equiv -t/a$, $\gamma_4 \to -\gamma_4$ we see that $\mathcal{P}_+ \to \mathcal{P}_-$ and we obtain from Eq. (3.60) the N^* and the antiparticle of the nucleon. With a given point-to-all propagator we can compute the two-point functions of the nucleon using a positive parity projector $\mathcal{P}_+$ and a negative parity projector $\mathcal{P}_-$ separately at little additional cost.
Since particle and antiparticle have the same mass, the results prior the transformation can be averaged with the ones after time reversal. This improves the signal-to-noise ratio.
For the three-point function a similar procedure can be used. We need a three-point function at t_{sink} and another one at $-t_{\text{sink}}$. With the stochastic estimation we can seed the time-slices t_{sink} and $-t_{\text{sink}}$ simultaneously and then use the stochastic propagator to compute both three-point functions, see Fig. 6.2 and Fig. 6.3. The sum over lattice sites in the modified two-point function is then taken at the forward/backward baryon sink time-slice using the appropriate $\mathcal{P}$. As the contributions from the second time-slice

are not connected to this baryon sink time-slice there is no bias in the result. This was checked by comparing the result with the independent computation of the forward and backward going three-point function using stochastic sources at a single time-slice.

Since for the sequential source method the sink time-slice and parity projector $\mathcal{P}$ have to be chosen before the inversion for the sequential propagator, this trick requires additional inversions in this case. This is why it is not used there.

The disadvantage of seeding two time-slices is that it increases the stochastic noise on each configuration. Since we sample the gauge fields better by computing two three-point functions per configuration the overall noise can still decrease, see Section 6.1.3.

When considering ratios of two and three-point functions we average the ratios of forward going three-point function over forward going two-point function and the backward going equivalent. This keeps more of the correlations between two- and three-point function intact[1], decreasing the overall error of the ratio, see Fig. 6.1.

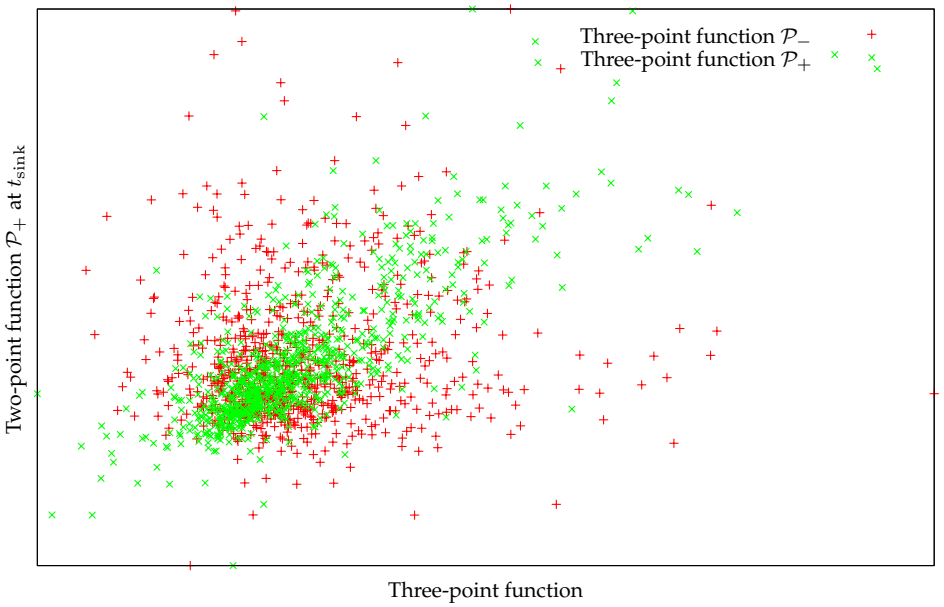

Figure 6.1.: Correlation of the two-point function and three-point functions with different $\mathcal{P}$, for γ_4 insertion at $t_{\mathrm{ins}} = 7$. The forward propagating three-point function is more correlated with the forward going two-point function.

The sign with which to average forward and backward ratio can be determined from

[1] This is meant in contrast to averaging two- and three-point functions individually with their t − *symmetry* conjugated equivalent prior to computing the ratio. The mean values of both methods, of course, agree within errors.

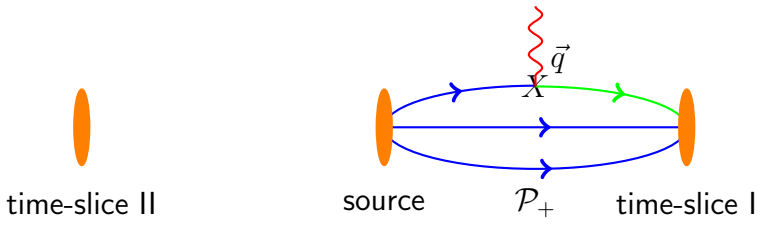

Figure 6.2.: The forward contribution of the double seeded stochastic three-point function.

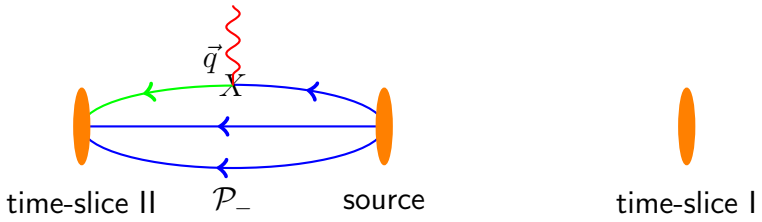

Figure 6.3.: The backward contribution of the double seeded stochastic three-point function.

the time reversal transformation of the

$$\begin{aligned}
\text{fields}: \quad & \Psi(\vec{x},t) \rightarrow \gamma_4\gamma_5\Psi(\vec{x},-t) \\
& \overline{\Psi}(\vec{x},t) \rightarrow \overline{\Psi}(\vec{x},-t)\gamma_4\gamma_5 \\
\text{interpolating operators}: \quad & \mathcal{N}^\alpha(\vec{x},t) \rightarrow \gamma_4\gamma_5\mathcal{N}^\alpha(\vec{x},-t) \\
\text{unpolarized projector}: \quad & \mathcal{P}^u_+ \rightarrow \mathcal{P}^u_- \\
\text{polarized projector}: \quad & \mathcal{P}^i_+ \rightarrow -\mathcal{P}^i_- \,.
\end{aligned} \tag{6.1}$$

In addition currents in three-point functions pick up a minus sign for each

$$D_t, \gamma_4, \gamma_5 \,. \tag{6.2}$$

To evaluate if this method works one has to look at how many estimators are necessary to get a certain signal-to-noise ratio. This is examined in Section 6.1.3.

6.1.2. Dilution

The Cyprus group reported success using color and spin dilution in stochastic estimators in nucleon three-point functions [140]. In meson three-point functions the Regensburg group observed no improvement [141]. Since neither of these investigations contained double seeding (having the source vector on two distant time-slices) we have

tried spin-dilution in this setup. We looked at two methods: One can seed the same spin component on both time-slices or one seeds spin $s \in \{0, 1, 2, 3\}$ on the first and $s' = 3 - s$ in the second time-slice of the source. This choice of dilution is motivated by the two different parity projectors one uses to compute the three-point functions.

Tests were performed on a $16^3 \times 32$ lattice at the symmetric point of the $N_f = 2+1$ Stout Link Non-perturbative Clover (SLiNC) configurations. We computed the three-point functions at $t_{\text{sink}} = 13a$ on two configurations with no dilution and the two schemes mentioned above. We then compared the stochastic error, i.e., the variation of the mean with respect to the different stochastic estimators, of each setup using 400 estimators. The mean values and errors agree quite accurately and therefore we have abandoned experimenting with dilution, as there was no indication of any improvement by using either method.

6.1.3. Optimal choice for N_{vec}

The stochastic estimation comes at the cost of an additional error on the three-point function that decreases like $\frac{1}{\sqrt{N_{\text{vec}}}}$. The two-point and three-point functions are correlated. This can be illustrated by the insertion of γ_4 in the unpolarized nucleon at $\vec{p}_f = \vec{p}_i = 0$ (Fig. 6.4).

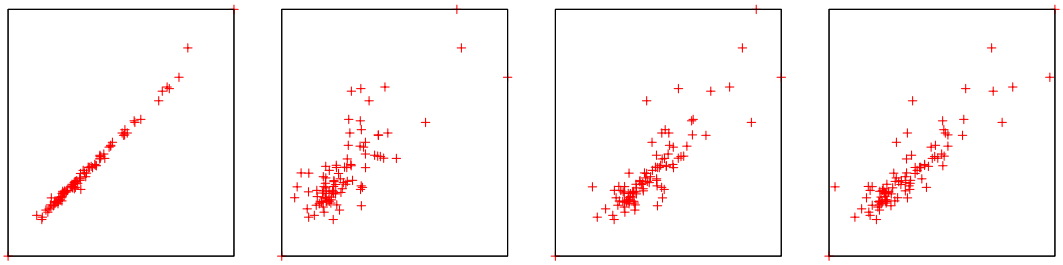

(a) sequential. (b) 12 estimates. (c) 32 estimates. (d) 52 estimates.

Figure 6.4.: Abcissa: unpolarized three-point function at $\vec{p}_f = \vec{p}_i = 0$ for γ_4 insertion, sequential or with increasing number of stochastic estimates, vs. unpolarized two-point function(ordinate).

This correlation decreases the error of the ratio of three-point function and two-point function. Thus we are actually interested in the total error on the ratio on a given set of gauge configurations. Therefore it is not enough to reproduce the three-point function within the gauge error, but one also has to recover the correlation with the two-point function, which increases the number of stochastic estimates that are required.

The relative error of the two-point function is given by

$$\frac{\Delta C_{2pt}^2}{C_{2pt}^2} = \frac{d_{2pt}}{N_{\text{configs}}}, \tag{6.3}$$

and the relative error of the three-point function is

$$\frac{\Delta C_{3pt}^2}{C_{3pt}^2} = \frac{1}{N_{\text{configs}}} \left(d_{3pt} + \frac{\Delta S}{N_{\text{vec}}} \right), \tag{6.4}$$

where ΔS is a constant connected to the stochastic error and the d_i are constants connected to the gauge error. The covariance between two- and three-point function can be written as $C_{23} \equiv d_{23}/N_{\text{configs}}$ which yields the relative error of the ratio

$$\frac{\Delta R^2}{R^2} = \frac{1}{N_{\text{configs}}} \left(d_{2pt} + d_{3pt} - 2d_{23} + \frac{\Delta \text{S}}{N_{\text{vec}}} \right). \tag{6.5}$$

So we can estimate the error reduction by increasing N_{vec} on a small set of configurations. On a sample of 97 $N_f = 2$ Clover QCDSF gauge configurations (volume=$16^3 \times 32$, pion mass 917 MeV), we measured the matrix element $\langle x \rangle_d^{\overline{\text{MS}}^{\mu=2\text{GeV}}}$ and the results are displayed in Fig. 6.5. The sequential point shows the forward going ratio between three- over two-point function. We refer to using random seeds at two time-slices and averaging the result with "two". The data labeled "one" has the source on one time-slice and we average the forward and backward going ratio. The number of estimates refers to the total number of inversions we use for the stochastic propagators. That means that for e.g. 24 we use 12 inversions for the forward and 12 for the backward going ratio in the case of "one".

The errors for "two" are smaller and thus it is preferable to do double seeding. The sequential error is slightly higher, which means that averaging forward and backward going ratio does (somewhat) compensate the stochastic error. Other observables yield similar plots.

Calculating the cost to produce these ratios we have to include the computer time for the contractions, the one-to-all propagator and the setup cost (like APE-smearing the gauge field for the Wuppertal smearing).

The volume and bare quark mass dependence of the number of estimates required was studied in [142].

To determine the optimal number of estimates one has to perform this check on each ensemble for a subset of configurations. Here and for our study at the larger volume ($32^3 \times 64$) of $N_f = 2 + 1$ SLiNC fermions we chose to use 60 estimates with double seeding, as this was most cost efficient.

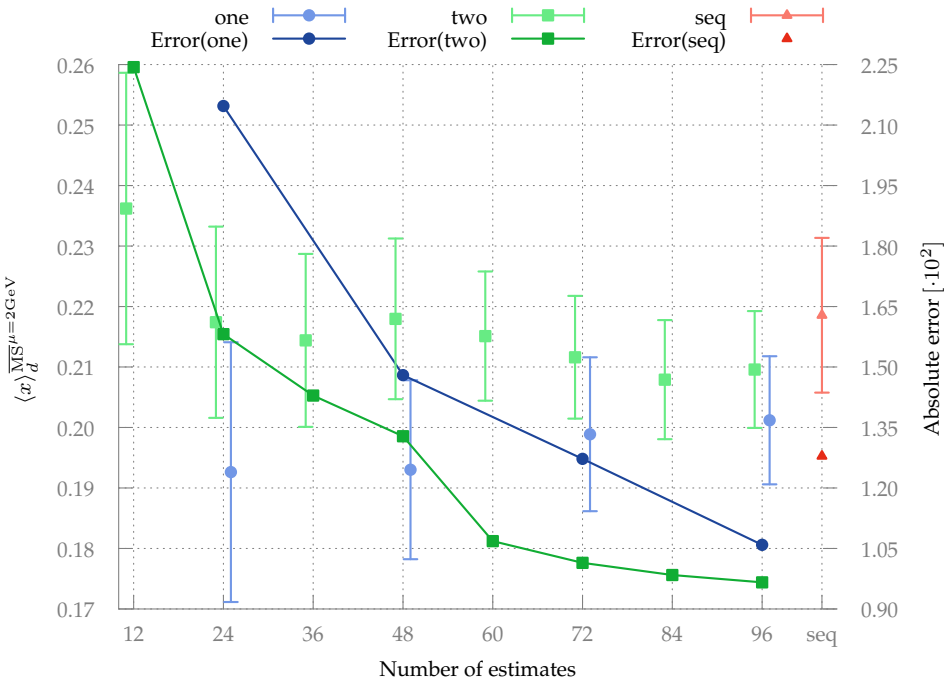

Figure 6.5.: Comparison of two stochastic estimation methods for measuring $\langle x \rangle_d^{\overline{\mathrm{MS}}^{\mu=2\mathrm{GeV}}}$.

6.2. Stochastic estimates for nucleon form factors

6.2.1. Motivation

The advantage of the stochastic method for evaluating nucleon form factors is that it provides many sink momenta and all nucleon polarizations simultaneously. This grants access to high momentum transfers with small momenta at source and sink, as the transfered momentum can be split between the baryon source and sink. Thus only two-point functions at small momenta are needed, whereas high momenta in the two-point function would be required in the sequential source analysis with fixed momentum at the baryon sink. Because the signal of two-point functions deteriorates fast with increasing momentum, this could potentially overcompensate the additional noise from the stochastic estimation, when comparing to the sequential method. To investigate that we performed the benchmark analysis of form factors with the stochastic method discussed in Section 6.2.4.

The error on the two-point function also determines the reliability of each equation of our overdetermined system of linear equations and thus the form factors. As a test of the systematics we compare two methods of forming the ratios of two- and three-point

functions. One is the "normal" method, where we use the same momenta in two- and three-point function. In the second method, called "average", we average two-point functions with the same $\vec{p}^2$ before using them in the ratio. This comparison is done in Section 6.2.3.

6.2.2. Setup

We used a $N_f = 2 + 1$, $32^3 \times 64$ SLiNC [143] QCDSF ensemble at the flavor symmetric point $m_s = m_u = m_d$ with a pion mass of 440 MeV. Quark smearing was done with 400 steps of Wuppertal smearing [84] on APE-smeared [80, 81, 82] gauge links.

The number of stochastic estimators was put to 60. The number of inversions necessary for the sequential method are 24 consisting of six per sequential source, and one needs two flavors, polarized and unpolarized to extract all the form factors and GPDs, that are measured here.

6.2.3. Comparison of momentum averaged and single momentum two-point functions in the ratio and choice of maximally permitted two-point function momentum

The relative error of the ratio, Eq. (3.82), of a three- and two-function at non-zero momentum transfer naively contains four times[2] the relative error of the two-point function. Thus the quality of the two-point function drastically influences the quality of the ratio. A possibility to reduce the error of the two-point function at fixed statistics is to average over equivalent momenta. But the reduced positive correlation between two- and three-point functions could also increase the error of the ratio. So the only objective method is to try both methods and compare.

In Fig. 6.6 we plot the equation system of the nucleon electro magnetic iso-vector form factors at full statistics once for the two-point function averaged over the equivalent momenta ("Averaged") and once for the standard choice of taking the two-point functions with the momenta $\vec{p}_f$/ $\vec{p}_i$ respectively ("Normal") for $\vec{p}_f{}^2 = 2(\frac{2\pi}{L_s})^2 = 2\vec{p}_i{}^2$ or $2\vec{p}_f{}^2 = \vec{p}_i{}^2 = 2(\frac{2\pi}{L_s})^2$ at $\vec{q}^2 = (\frac{2\pi}{L_s})^2$. We will abbreviate this choice of kinematics with $1 \leftrightarrows 2, 1$. In this case averaging the equivalent momenta is clearly advantageous. This is also evident when looking at the results for the form factors at this virtuality, where

[2] Naive means we assume that the relative error of the two-point function is constant overall time-slices and momenta. The relative error of a product is the sum of the relative errors. Thus we have six times the relative error on the fraction in the square root. Then the square root has three times the relative error of the two-point function. This yields four times the relative error of the two-point function plus the relative error of the three-point function.

we find

$$
\begin{aligned}
F_1^{u-d}[\text{average, bare}](1 \leftrightarrows 2, 1) &= 0.701(95) \\
F_1^{u-d}[\text{noaverage, bare}](1 \leftrightarrows 2, 1) &= 0.590(97) \\
F_2^{u-d}[\text{average, bare}](1 \leftrightarrows 2, 1) &= 1.48(28) \\
F_2^{u-d}[\text{noaverage, bare}](1 \leftrightarrows 2, 1) &= 0.93(31)\,.
\end{aligned} \tag{6.6}
$$

Here the different methods produce clearly different results, which is not surprising given that the equation system in Fig. 6.6 is very noisy for the un-averaged case.

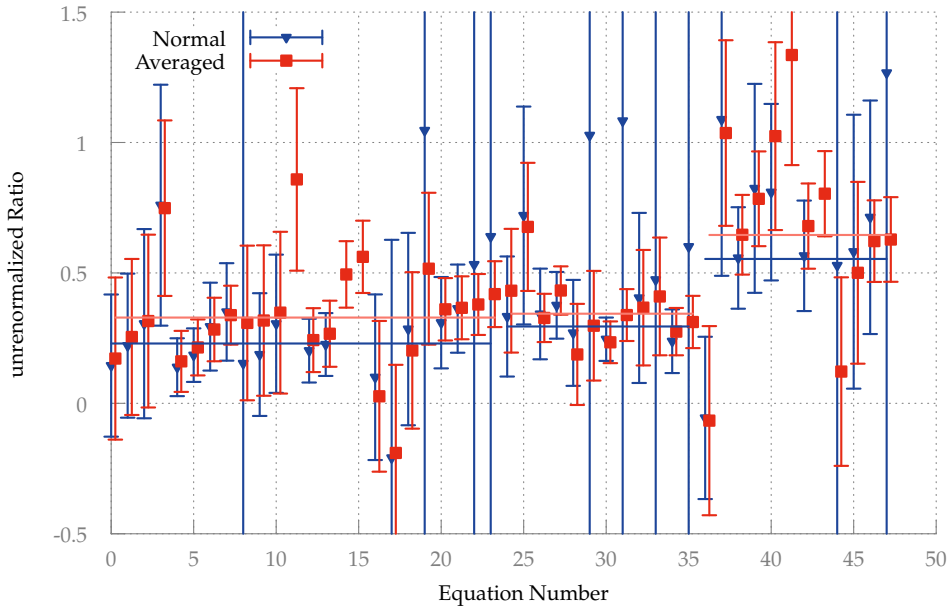

Figure 6.6.: Equation-System of the nucleon electro magnetic iso-vector form factors at $\vec{p}_f{}^{\,2} = 2(\frac{2\pi}{L_s})^2 = 2\vec{p}_i{}^{\,2}$ or $2\vec{p}_f{}^{\,2} = \vec{p}_i{}^{\,2} = 2(\frac{2\pi}{L_s})^2$ for averaged and not-averaged two-point function in the ratio. The straight lines are the prediction from the form factors for each equation. The equations are sorted as in Fig. 3.6.

As the energy-gap to the pion mass of the boosted nucleon increases with higher momenta the signal-to-noise ratio drops fast, c.f. Eq. (3.65). It is therefore necessary to exclude very high momenta in the two-point function from the analysis.
In Figs. 6.7 to 6.9 and Fig. 6.10 we plot the results for the nucleon electro magnetic iso-vector form factors at full statistics for various choices of the maximal two-point function momentum. It becomes clear that at some point three-point functions with higher $\vec{p}_f^{\,2}$ or $\vec{p}_i^{\,2}$ do not contribute a useful signal anymore. One has to introduce a cut-off for the relative error of the two-point function to produce meaningful results.

In this work we have fixed statistics and we assume that the relative error of the two-point function is rotationally invariant and thus this criterion is equivalent to a maximal two-point function momentum.
Averaging over equivalent momenta improves the signal-to-noise ratio of the two-point function at given statistics. By comparing Fig. 6.7 and Fig. 6.8 one can see that the averaged data is much more consistent between similar virtualities, i.e. the data lies on a somewhat smooth curve. Still the data for $\vec{p}^2 \leq 5$ remains systematically below the data containing only smaller momenta.
The comparison of Fig. 6.7 and Fig. 6.8 yields similar conclusions, although the agreement here seems to extend also to $\vec{p}^2 \leq 5$ in the case of momentum averaging.

6.2.4. Comparison of the errors on (generalized) form factors from sequential sources and stochastic estimation

We have performed measurements on a small sample of 103 configurations using the non-relativistic sequential source method and the fully relativistic stochastic method at fixed t_{sink}.
We have restricted the results to $Q^2 < 1$ GeV as we do not claim to have reliable data above that threshold. The two-point functions in this analysis were not momentum averaged, as the correlation between sequential source data and the two-point function with corresponding momentum might be higher than for the stochastic case. Thus the stochastic data was furthermore restricted to use only $\vec{p}_f^2, \vec{p}_i^2 \leq 2\frac{(2\pi)^2}{L^2}$. To compare the results of the small sample to a bigger set we have included the results for the stochastic method on 827 configurations. The inlays in the plots Figs. 6.11 and 6.12 show the results of the sequential and stochastic method for the small sample with their values shifted to a constant such that one can easily compare the error bars.
To analyze the GPD data we had to assume some values for the renormalization constants, as the operators corresponding to different representations of H_4 renormalize differently and we extract the values for the generalized form factors from a single system of equations. The values taken correspond to $N_f = 2$ Wilson-Clover fermions at $\beta = 5.29$. As there the renormalization constants in general are very similar for the two representations corresponding to the quantities in question, this is a reasonable approximation for the difference between the renormalization constants, but the values are still not meaningfully renormalized.
For the electromagnetic form factors F_1 (Dirac form factor), Fig. 6.11, we see that the sequential method is much better at low Q^2, but the higher number of ratios that can be evaluated with the stochastic method allows to better disentangle F_2 (Pauli form factor), Fig. 6.12, even at medium Q^2 . For other charge form factors, especially those with many contributions from polarized nucleons, the performance of the stochastic method is better at high Q^2. The signal for form factors with non-trivial kinematical

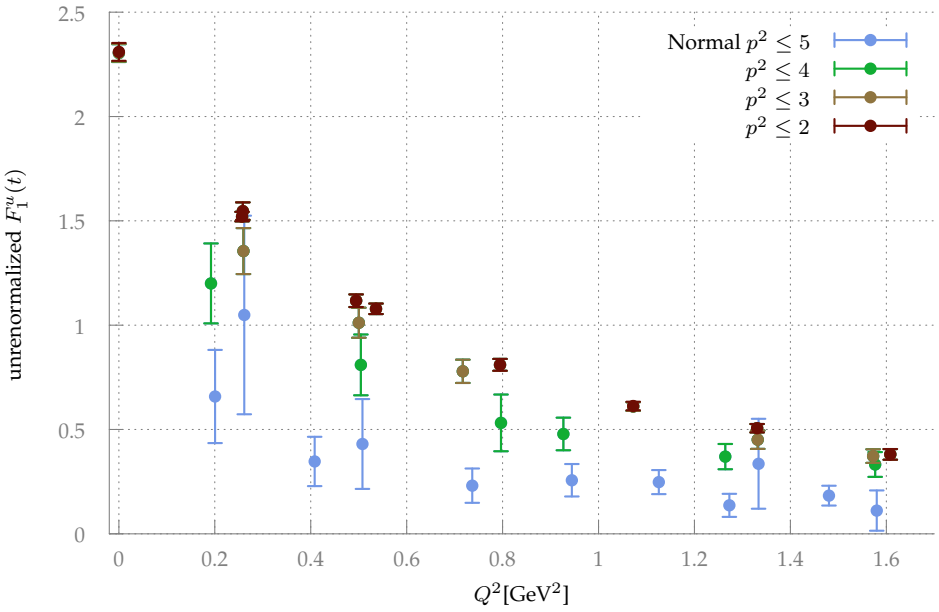

Figure 6.7.: Results for F_1^u at the flavor symmetric point of $N_f = 2 + 1$ SLiNC fermions at $m_\pi = 440$ MeV, 827 cfgs., with the two-point function in the ratio not averaged. Maximal allowed $\vec{p}^2$ for each data point is given in lattice units.

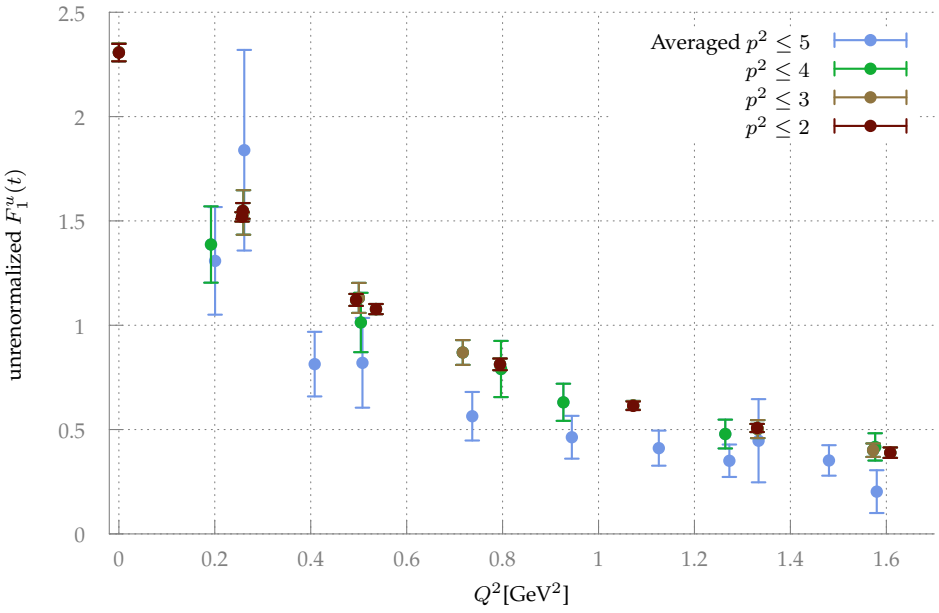

Figure 6.8.: Same as Fig. 6.7 but with averaging over momenta with the same $\vec{p}^2$.

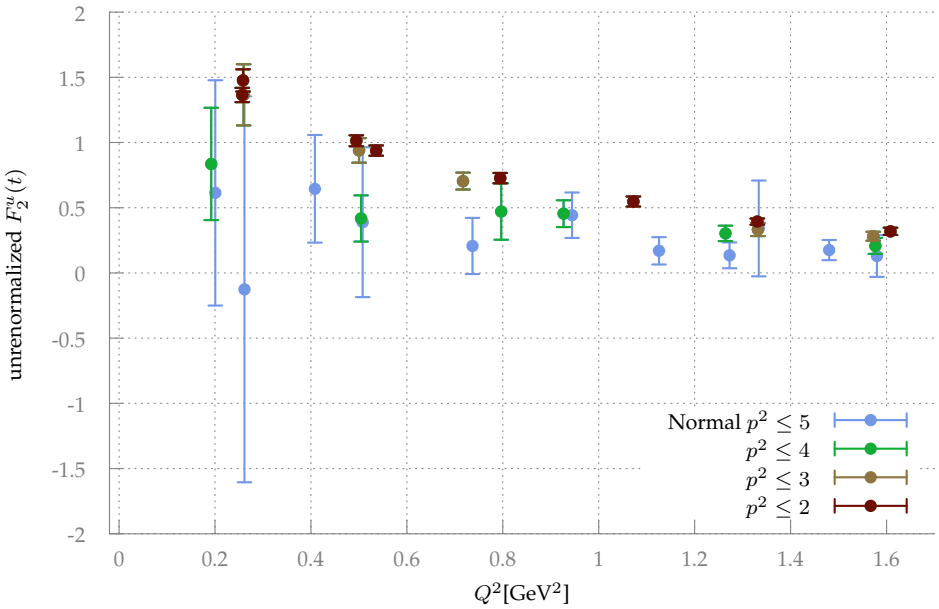

Figure 6.9.: As Fig. 6.7 but for F_2^u with the two-point function in the ratio not averaged.

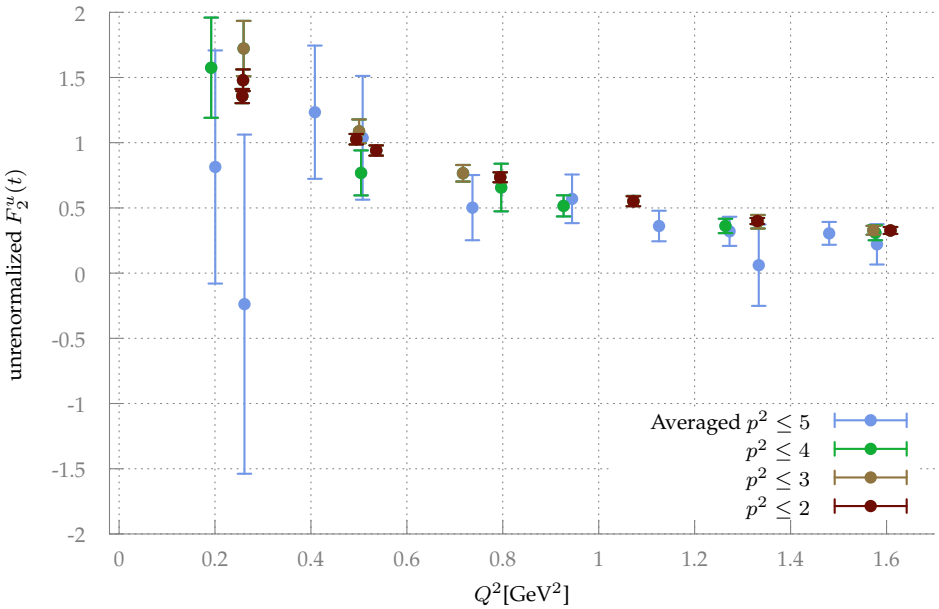

Figure 6.10.: Same as Fig. 6.9 but with momentum averaging.

prefactors, i.e. prefactors that vanish for $\vec{p}_i = \vec{p}_f = 0$, is improved by the presence of more kinematical combinations. Thus the errors of these form factors are significantly smaller for the stochastic method for the whole range of virtualities.
For the moments of GPDs the stochastic method performs clearly better than the sequential method. This is illustrated in Fig. 6.13 and Fig. 6.14 where the open symbols are for the sequential method and the full symbols are for the stochastic method. Additional plots can be found in Appendix B.

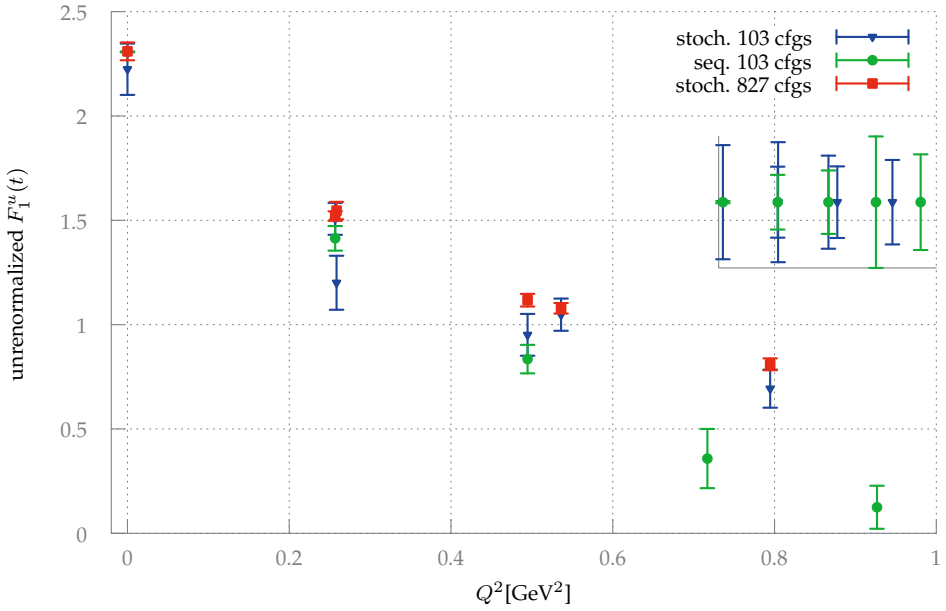

Figure 6.11.: Stochastic estimation vs. sequential source for the electromagnetic form factor F_1.

6.3. Further applications

The flexibility of the stochastic method allows one to compute multiple t_{sink} with the same stochastic propagator. One merely has to perform another point-to-all inversion at a different source time-slice and repeat all of the contractions. This was done and tested on a small test lattice ($16^3 \times 32$) for $N_f = 2 + 1$ SLiNC fermions at the symmetric point on 295 configurations and the results are shown in Fig. 6.15.
A similar idea was shown in [142] where the overall noise was reduced by averaging over the results for different spatial positions of the point-to-all source on the same time-slice. This means repeating the contractions but re-using the all-to-all propagator. For large volumes it was found that this reduces the noise significantly at acceptable

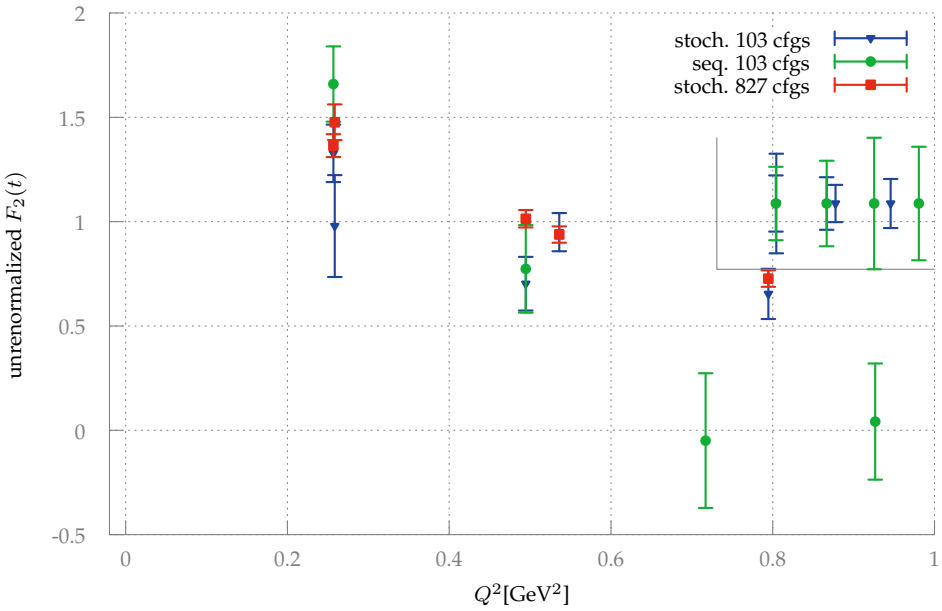

Figure 6.12.: Stochastic estimation vs. sequential source for the electromagnetic form factor F_2.

additional cost.
By varying not the source position but the smearing of source and sink one can perform an analysis using the variational method. This might be very attractive to extract ground states and the inversions for the stochastic propagator can also be re-used, but it is very expensive in terms of point-to-all inversions and contractions, as one needs a big enough basis to extract ground states reliably. A study using the variational method, similar to [100], would be facilitated by stochastic estimation.
A very promising application would be to compute transition form factors for different baryons of the octet and decuplet with the same all-to-all propagators. Here the amount of data created might be an obstacle in realizing the computation as it is possible to compute many sink/insertion momentum combinations for many different observables. Nevertheless studies like [144], [145] or [146] could be done with a much lower computational effort.

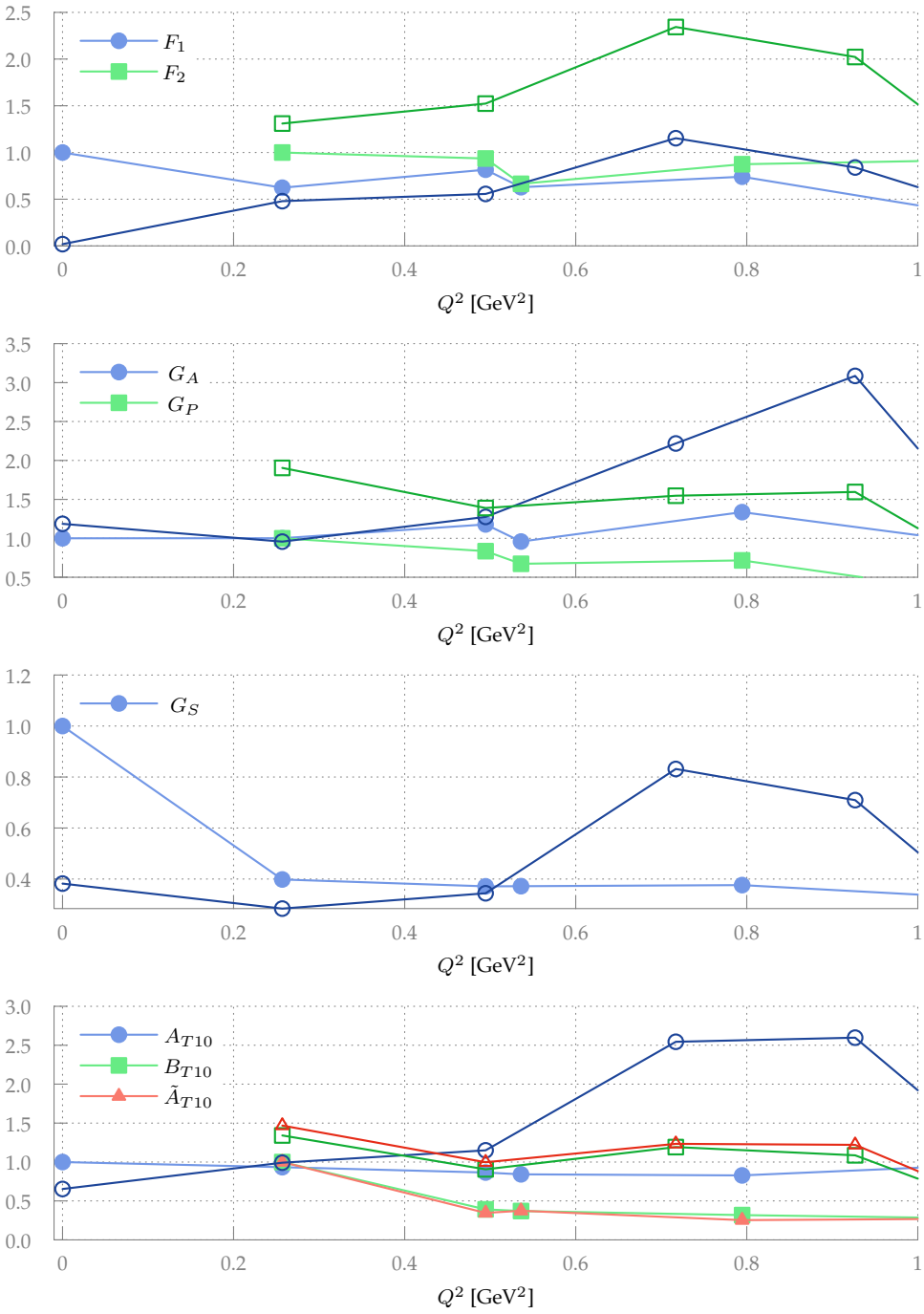

Figure 6.13.: Stochastic estimation error (full symbols) vs. sequential source error (open symbols) overview for the charge form factors. Stochastic estimation results with larger error at similar virtuality have been removed.

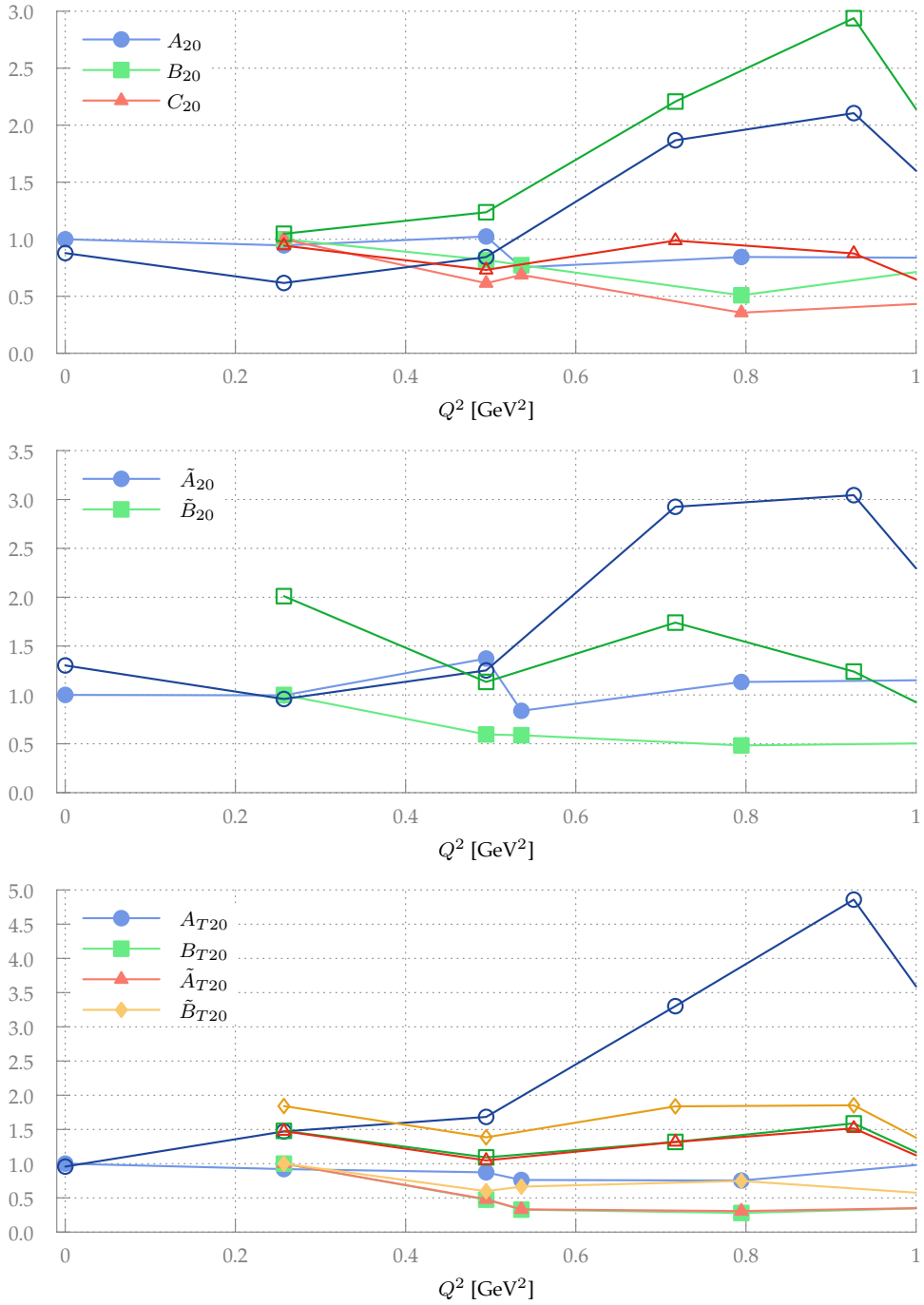

Figure 6.14.: Same as Fig. 6.13 for the second moments of generalized parton distributions.

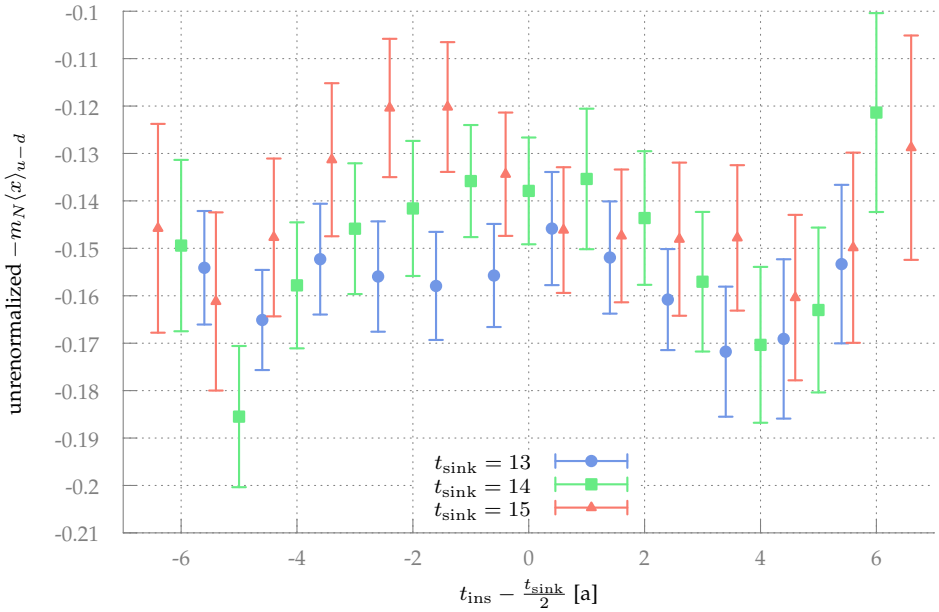

Figure 6.15.: Stochastic estimation of three-point functions corresponding to v_{2b} used to compute several values for t_{sink} with the same stochastic propagator. Data for $t_{\text{sink}} = 13a/\text{b}t_{\text{sink}} = 15a$ is shifted left/right in the plot to facilitate the comparison.

7

Improved interpolating operator to suppress excited states

To reliably extract quantities like masses of hadrons, or – even more delicate – matrix elements of currents in a hadron, excited state contributions have to be disentangled from the ground state signal. In Chapter 5 methods how to deal with this excitations were outlined.
In this chapter we present an approach how to suppress the contributions of excited states as much as possible without additional cost and with little overhead on the required tuning before the production run.
There are different smearing procedures on the market. Volume sources, like [123] require gauge fixing and allow to choose the form of the source freely. An early attempt for that is [147]. Gauge covariant quark field smearing methods contain iterative procedures as they need to connect the points of extended source by gauge links. Classical examples would be Jacobi smearing [148] or Wuppertal smearing outlined in Section 3.4.2.
The most obvious handle on excitations is to vary the smearing iteration count one uses in the quark propagator. One can compute the relevant hadron two-point functions for different smearings and see which number of smearings steps performs best. This was done for the study [110] and sufficiently suppressed the excitations on important observables.
To improve on that method we scan the available range of interpolators using the variational method in Section 7.1. It allows us to compare the goodness of the ground states we could extract from various basis of operators.
A two-by-two matrix of interpolators proved to be sufficient. To compute the mixing parameter between the two interpolators in the basis we have performed a fit to a parameterization of the cross-correlator matrix to a rotation matrix in Section 7.2.
The result was then used to construct an approximate mixing parameter for a superposition of the two Gaussian quark smearings in the basis in Section 7.4.
Then a new measurement on the same configurations was taken to judge the goodness of the combined smearing. The results are reported in Section 7.5.
We find that this method suppresses the excited states and reduces the statistical errors.

7.1. The variational method

7.1.1. General idea

In Quantum mechanics the variational method is used to find the ground state wave functions by using different trial wave functions and finding the linear combination with the minimal energy. Prominent examples are the Hartree-Fock method and the Reileigh method.
The variational method [149] used in lattice QCD is based on using different interpolating operators. This is a way to improve ground state signals of correlators and to extract excitations. One computes a whole $N \times N$ matrix of correlators, the *cross-correlation matrix* C_{ij} of different interpolators O_i such that

$$C_{ij}(t) = \langle O_i(t) O_j(0) \rangle \, . \tag{7.1}$$

The matrix C_{ij} is symmetric with infinite statistics and thus for practical purposes is symmetrized by hand. It is legitimate to choose $C_{ji} \equiv C_{ij}$, if C_{ij} has less statistical noise than C_{ji}, instead of $C_{ij}, C_{ji} \to (C_{ij} + C_{ji})/2$.
An eigenvalue λ_i of this matrix describes the energy and amplitude of the states i. The eigenvalues, ordered as $\lambda_0 > \lambda_1 > \cdots > \lambda_N$, are usually extracted by solving the generalized eigenvalue problem

$$C(t) w_n(t, t_0) = \lambda_n(t, t_0) C(t_0) w_n(t, t_0) \tag{7.2}$$

and they correspond to the lowest lying N physical states via

$$\lambda_n(t, t_0) = A_n e^{-m_n (t - t_0)} + \mathcal{O}(e^{-m_{N+1}(t-t_0)}) \tag{7.3}$$

for $t > t_0$. The presence of $C(t_0)$ in Eq. (7.2) has the benefit of being able to choose t_0 large enough so that most of the excitations have already died out[1].
Symmetric eigenvalue solvers are numerically more stable, and thus we solve

$$C^{-1/2}(t_0) C(t) C^{-1/2}(t_0) u_n(t, t_0) = \lambda_n(t, t_0) u_n(t, t_0) \, . \tag{7.4}$$

This leads to the same eigenvalues as Eq. (7.2) and the eigenvectors are connected by

$$C^{1/2}(t_0) w = u \, . \tag{7.5}$$

The standard eigenvalue problem

$$C(t) v_n(t) = \lambda_n(t) v_n(t) \, , \tag{7.6}$$

[1] In our calculation $t_0 = 2$ was sufficient; for $t_0 = 1$ we observed meta stable plateaus in some states that decayed into lighter states at larger Euclidean time distances.

cannot be transformed to the generalized eigenvalue problem if $C(t_0) \neq \mathbb{1}$.
The eigenvalues of Eq. (7.6) differ from the ones in Eq. (7.4) by the contribution of excited states and the amplitude normalization, but for large t they should display the same time dependence and thus one can use Eq. (7.4) to extract the spectrum.

7.1.2. Choice of Basis

7.1.2.1. Interpolators

Nucleons We use the following nucleon interpolators [150]

$$N^{(i)}_{\delta}(x) = \varepsilon^{abc}\Gamma^{\delta\alpha}_{1,(i)} u^a_\alpha(x)\left(u^{T,b}_\beta(x)\Gamma^{\beta\gamma}_{2,(i)} d^c_\gamma(x) - d^{T,b}_\beta(x)\Gamma^{\beta\gamma}_{2,(i)} u^c_\gamma(x)\right), \tag{7.7}$$

$$\overline{N}^{(i)}_{\bar{\delta}}(x) = \varepsilon^{\bar{a}\bar{b}\bar{c}}\left(\overline{u}^{T,\bar{b}}_{\bar{\beta}}(x)\Gamma^{\bar{\beta}\bar{\gamma}}_{2,(i)} \overline{d}^{\bar{c}}_{\bar{\gamma}}(x) - \overline{d}^{T,\bar{b}}_{\bar{\beta}}(x)\Gamma^{\bar{\beta}\bar{\gamma}}_{2,(i)} \overline{u}^{\bar{c}}_{\bar{\gamma}}(x)\right)\overline{u}^{\bar{a}}_{\bar{\alpha}}(x)\Gamma^{\bar{\alpha}\bar{\delta}}_{1,(i)}, \tag{7.8}$$

where we can choose[2]

$$(i, \Gamma_1, \Gamma_2) \in \{(1, \mathbb{1}, C\gamma_5), (2, \gamma_5, C), (3, \mathrm{i}\mathbb{1}, C\gamma_4\gamma_5)\}. \tag{7.9}$$

All choices for Γ_2 are antisymmetric, thus

$$u^{T,b}_\beta(x)\Gamma^{\beta\gamma}_{2,(i)} d^c_\gamma(x) = d^{T,c}_\beta(x)\Gamma^{\beta\gamma}_{2,(i)} u^b_\gamma(x) \tag{7.10}$$

and using the antisymmetry in color space we can simplify our interpolators significantly.

Mesons For mesons we use the interpolating operator

$$O_\Gamma = \overline{q}_{f_1}\Gamma q_{f_2}. \tag{7.11}$$

For $f_1 = f_2$ we would in principle have disconnected diagrams which we drop. This is justified as there is no mass difference between, e.g., $\pi^\pm$ and π^0 since we neglect electromagnetic effects and work with mass degenerate light quarks. Thus the meson correlation function is given by the choice matrices of the Clifford algebra, c.f. Table 7.1, at the meson source and sink. In this work we focus on the pseudo scalar (pions) and vector mesons (rhos).
For the rhos we choose the same γ_i at source and sink (there is no spin flip).

[2] For $i = 2$ we have the nucleon propagating to the left (from the source towards smaller t) and the N^* to the right, i.e. in the opposite direction as the other two operators.

Interpolator Name	Γ
π_1	γ_5
π_2	$\gamma_4\gamma_5$
ρ_1	γ_i
ρ_2	$\gamma_4\gamma_i$

Table 7.1.: Overview of the meson interpolators.

Number of smearing steps	RMS [a]
5	1.212040(13)
25	2.72813(31)
100	5.3151(27)
400	9.579(16)
combined	7.3065(45)

Table 7.2.: Overview of the root mean squared for different numbers of Wuppertal smearing iterations.

7.1.2.2. Variation of the smearing radius

For our Wuppertal smearing procedure we use 25 times APE-smeared links. We have varied the number of Wuppertal smearing steps of the quark smearing in the basis for the cross-correlation matrix. We measured the root mean squared (RMS) in lattice units of the each smeared quark source Ψ,

$$\mathrm{RMS} = \sqrt{\frac{\sum_{n\in\Lambda} n^2 \Psi(n)}{\sum_{n\in\Lambda} \Psi(n)}}\,, \tag{7.12}$$

where n is a site on the lattice Λ, on one coulomb gauge-fixed configuration at each time-slice. The results can be found in Table 7.2 and the errors correspond to the fluctuations between the time-slices.
The RMS scales approximately with the square root of the smearing sweep count. The Adelaide group has published their data in [151] and also their data starts to differ from square root scaling at around 200 sweeps. Nevertheless we can fit to our data and the RMS of our combined wave function, from Section 7.5, corresponds to ≈ 186 sweeps.

7.1.3. Results of the Variational method

Varying the interpolating operator at fixed quark field smearing did not yield an improvement for the ground state of the particles we looked at. This is illustrated on the

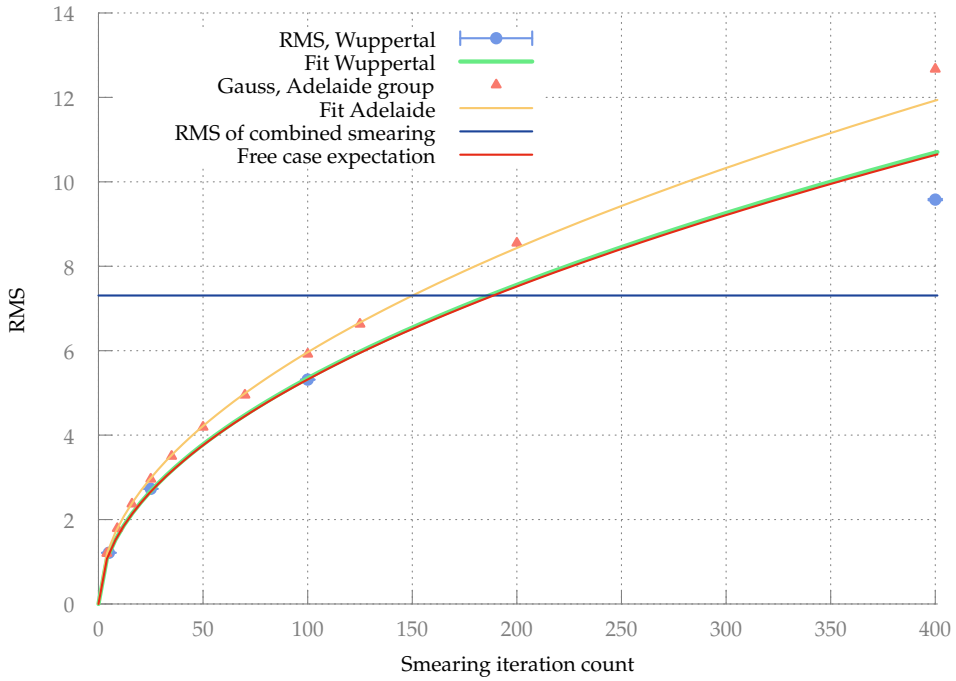

Figure 7.1.: Root mean squared versus the number of smearing interations on two different lattices by the Adelaide group and the author. We have enhanced the thickness of the curve of the fit to the Wuppertal data to make it visible, as it agrees very well with the free case expectation [152] of $|\Psi|(n) = \sqrt{\sqrt{2}n/(3+\frac{1}{2\alpha_{Wup}})}$, where we use $\alpha_{Wup} = 0.25$.

ground state of N^* in Fig. 7.2. We show lowest eigenvalue for various bases, and there is an improvement with respect to the individual operators if one varies the smearing, which the variation of the interpolating operator did not yield.

The first excited state of the N^* could also not be extracted with a 2×2-matrix of interpolating operators with fixed smearing, whereas in a 2×2 matrix with varying smearing it could. A 4×4-matrix with two interpolators and two smearings was also tried, but here the first two eigenvalues displayed an almost degenerate effective mass, so it was not able to disentangle the ground state and the first excited state of the N^*. At different lattices to extract the first excited state it is, however, advantageous to vary the interpolator [153].

We have therefore focused on the variation of the smearing radii in our cross correlator matrix.

It turned out that our flattest effective masses can be constructed form all cross-correlator matrices that contain the 100 and 400 steps of Wuppertal smearing, with the

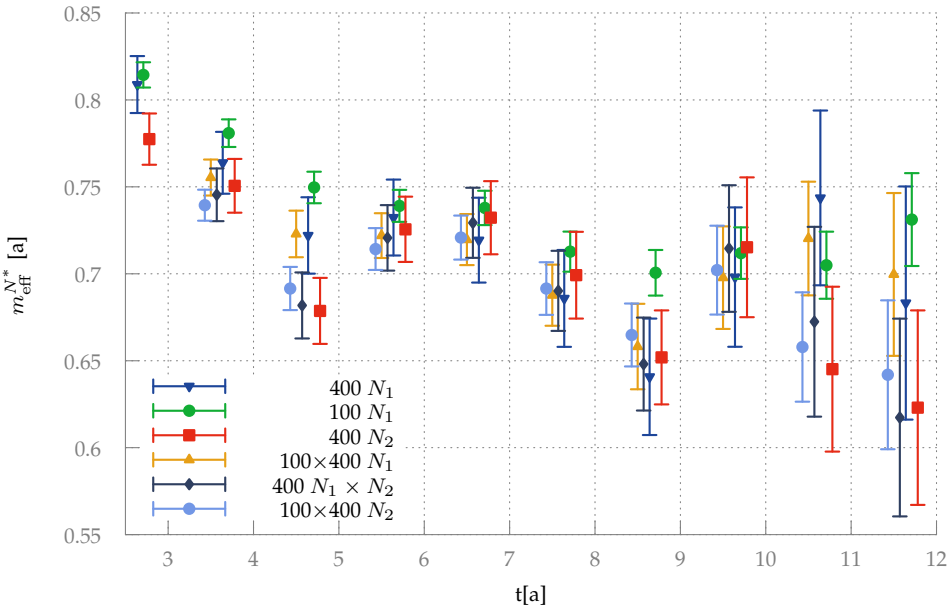

Figure 7.2.: Different basis used to construct the ground state of N^*.

additional smearings in the basis not having any influence what so ever, see Fig. 7.3. Eigenvalues of cross-correlator matrices that did not contain both of the two best correlators did have an effective mass, which plateaued later.

This can be understood from the plot of the point smeared correlators for the basic smearings, where the 400 comes from below – indicating a negative overlap with the first excited state – to the plateau value and the 100 comes from above, where all narrower smearings perform worse than the 100, see Figs. 7.4 and 7.5.

Therefore a linear combination of 100 and 400 steps of Wuppertal smearing can have a cancellation in the amplitude of the first excited state, while keeping the ground state overlap big. Had the ground state and first excitation overlap the same sign on both smearings any cancellation would have to be very finely tuned. The amplitudes would be subtracted in both states and the quality of the test wave function is determined by the ratio of the overlaps of ground and first excited state.

7.2. 2×2 Rotation Matrix parameterization

In the cross correlator matrix

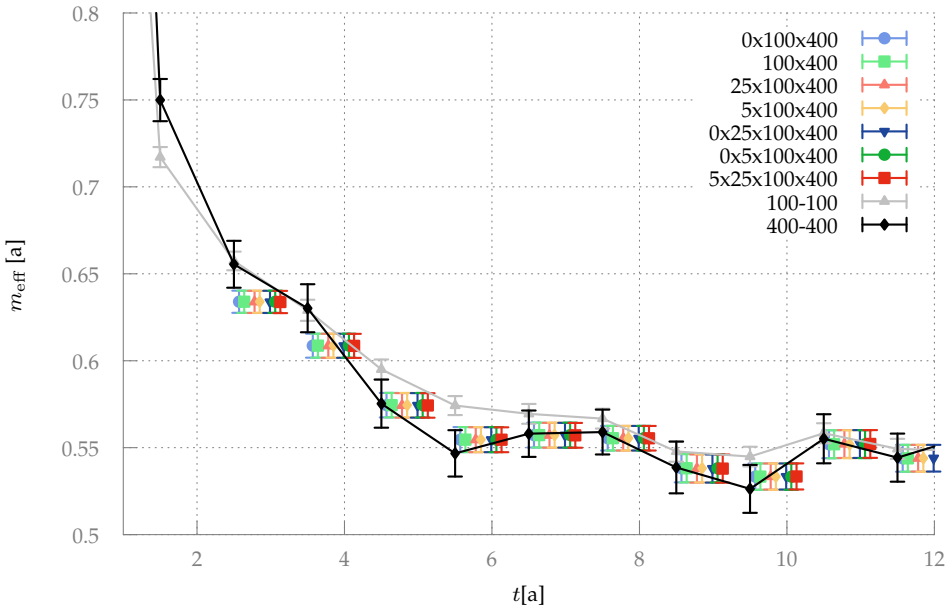

Figure 7.3.: The effective mass of the lowest eigenvalue obtained by diagonalizing various matrices of the nucleon (N_1) constructed by varying the smearing at source and sink, at $t_0 = 1$ and the best two diagonal correlators for reference.

$$C_{ij} = \langle O_j \mid O_i \rangle, \tag{7.13}$$

we take the interpolator O_i to be at the source and O_j is at the sink of our hadron. To specify the order of the O_i, when we vary the smearing, we assign indices such that the interpolator with the lesser amount of smearing steps corresponds to the smaller index. We now parameterize the cross correlator matrix as

$$\begin{aligned} C_{ij}(t) &= \begin{pmatrix} e^{a_1} & 0 \\ 0 & e^{a_2} \end{pmatrix} \begin{pmatrix} c_\theta & s_\theta \\ -s_\theta & c_\theta \end{pmatrix} \underbrace{\begin{pmatrix} e^{-m_2 t} & 0 \\ 0 & e^{-m_1 t} \end{pmatrix}}_{\text{Eigenvalues}} \underbrace{\begin{pmatrix} c_\theta & -s_\theta \\ s_\theta & c_\theta \end{pmatrix}}_{\text{Rotation}} \underbrace{\begin{pmatrix} e^{a_1} & 0 \\ 0 & e^{a_2} \end{pmatrix}}_{\text{Amplitude}} \Bigg|_{ij} \\ &= \begin{pmatrix} e^{2a_1}\left(c_\theta^2 e^{-m_2 t} + s_\theta^2 e^{-m_1 t}\right) & e^{a_1} e^{a_2} c_\theta s_\theta \left(e^{-m_1 t} - e^{-m_2 t}\right) \\ e^{a_1} e^{a_2} c_\theta s_\theta \left(e^{-m_1 t} - e^{-m_2 t}\right) & e^{2a_2}\left(s_\theta^2 e^{-m_2 t} + c_\theta^2 e^{-m_1 t}\right) \end{pmatrix} \Bigg|_{ij}, \end{aligned} \tag{7.14}$$

where we write $\cos(\theta) = c_\theta$ and $\sin(\theta) = s_\theta$. The eigenvectors are split up in an amplitude and the unit eigenvectors contained in the rotation matrix. This fit formula reduces the number of parameters one needs to get the two states as the eigenvectors

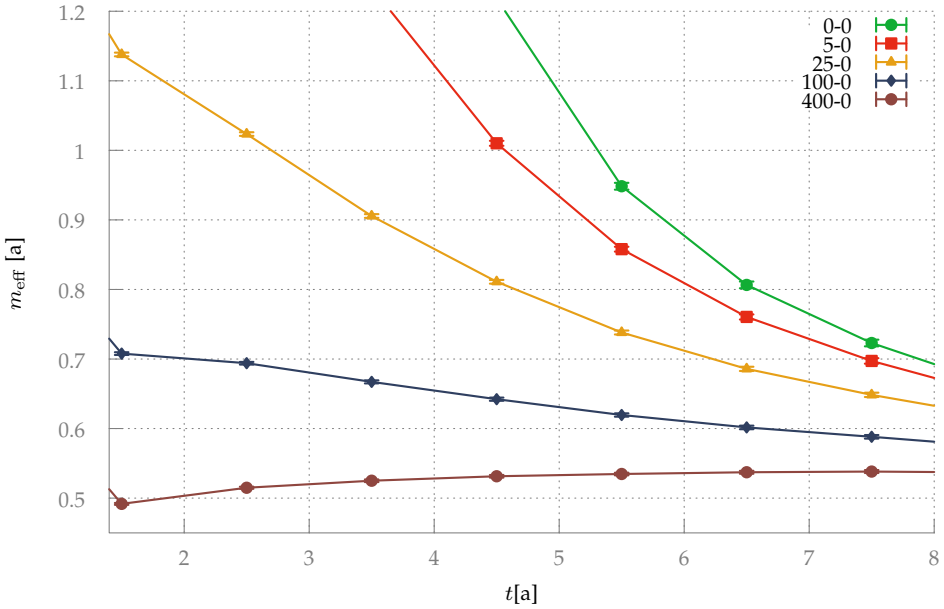

Figure 7.4.: Effective masses for the nucleon interpolator N_1 for various source smearings and point sink.

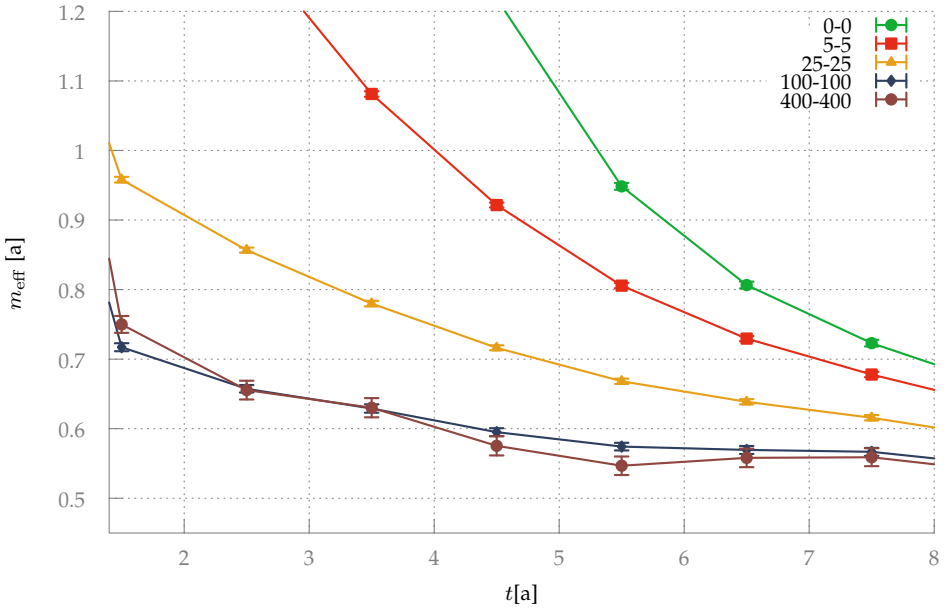

Figure 7.5.: Effective masses for the nucleon interpolator N_1 for various source/sink smearings.

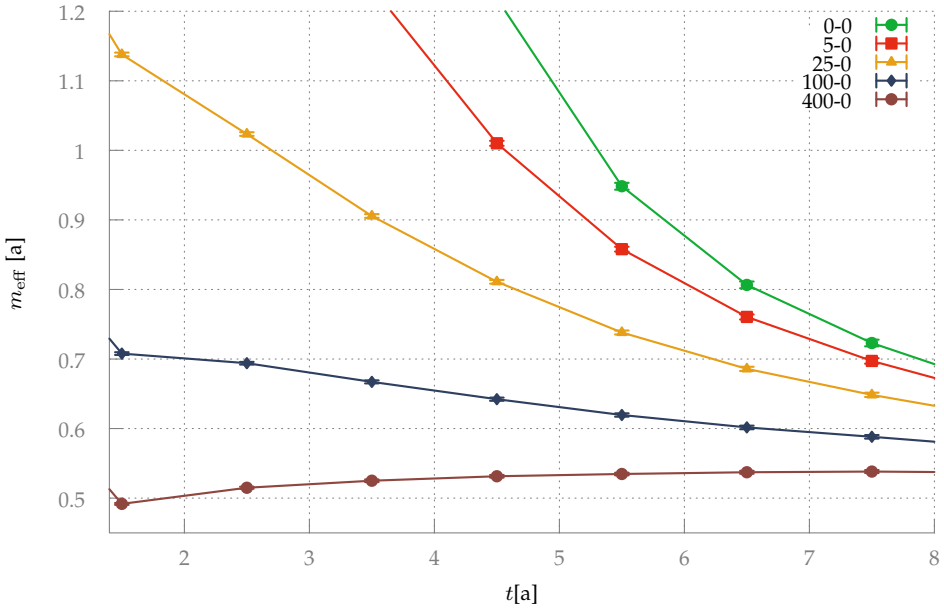

Figure 7.6.: Effective masses for the nucleon interpolator N_3 for various source smearings and point sink.

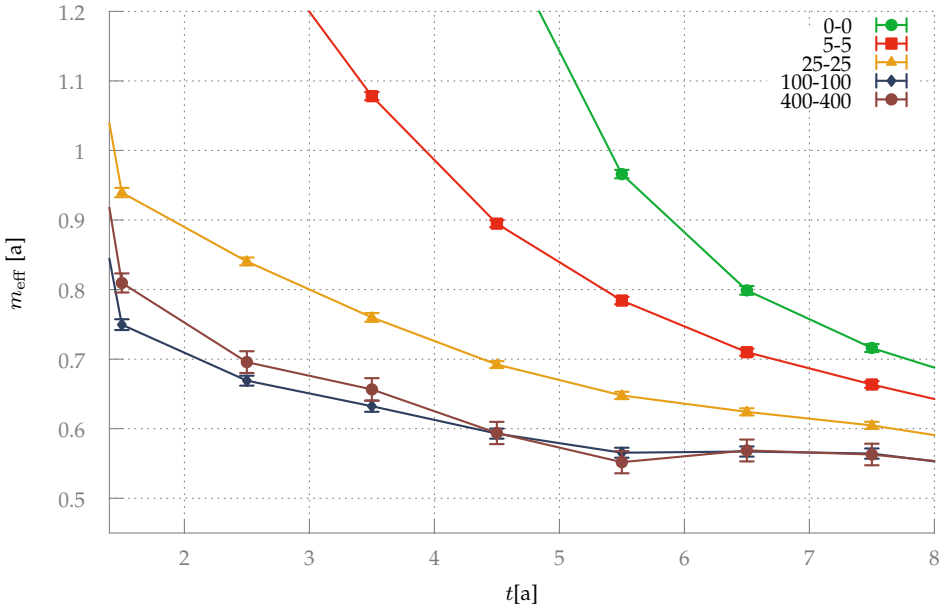

Figure 7.7.: Effective masses for the nucleon interpolator N_3 for various source/sink smearings.

are constant in time in contrast to Eq. (7.6).
Note that there is a symmetry that under $\theta = \frac{\pi}{2} - \theta' \rightarrow m_1 \leftrightarrow m_2$. We have to keep this in mind when fitting the results and forcing $m_1 < m_2$, because if the fitter finds the degenerate minimum with the masses switched we have to modify θ accordingly.
When we solve for our ground state this equation is modified in this way ($C_{12} \stackrel{!}{=} C_{21}$):

$$\begin{aligned} e^{-m_1 t} &= \begin{pmatrix} s_\theta & c_\theta \end{pmatrix} \begin{pmatrix} c_\theta & s_\theta \\ -s_\theta & c_\theta \end{pmatrix} \begin{pmatrix} e^{-m_2 t} & 0 \\ 0 & e^{-m_1 t} \end{pmatrix} \begin{pmatrix} c_\theta & -s_\theta \\ s_\theta & c_\theta \end{pmatrix} \begin{pmatrix} s_\theta \\ c_\theta \end{pmatrix} \\ &= \begin{pmatrix} s_\theta & c_\theta \end{pmatrix} \begin{pmatrix} e^{-a_1} & 0 \\ 0 & e^{-a_2} \end{pmatrix} \begin{pmatrix} C_{11} & C_{21} \\ C_{21} & C_{22} \end{pmatrix} \begin{pmatrix} e^{-a_1} & 0 \\ 0 & e^{-a_2} \end{pmatrix} \begin{pmatrix} s_\theta \\ c_\theta \end{pmatrix} \\ &= \begin{pmatrix} s_\theta & c_\theta \end{pmatrix} \begin{pmatrix} C_{11} e^{-2a_1} & C_{21} e^{-a_1 - a_2} \\ C_{21} e^{-a_1 - a_2} & C_{22} e^{-2a_2} \end{pmatrix} \begin{pmatrix} s_\theta \\ c_\theta \end{pmatrix} \\ &= s_\theta^2 e^{-2a_1} C_{11} + 2 c_\theta s_\theta e^{-a_1 - a_2} C_{21} + c_\theta^2 e^{-2a_2} C_{22} \end{aligned} \tag{7.15}$$

This means that we would expect an improved effective mass for the interpolator

$$\langle O \mid = s_\theta e^{-a_1} \langle O_1 \mid + c_\theta e^{-a_2} \langle O_2 \mid \ . \tag{7.16}$$

As the overall normalization is irrelevant we define a relative weight R

$$R = \tan(\theta) e^{a_2 - a_1} \ , \tag{7.17}$$

and use the interpolator

$$\langle O \mid = R \langle O_1 \mid + \langle O_2 \mid \ . \tag{7.18}$$

The interpolator Eq. (7.18) has a smaller statistical uncertainty than Eq. (7.16) as the fit parameters are correlated.
Note that the linear combination of interpolators is not the linear combination of smearings and that the conversion is non-trivial as we will explain in the next section.

7.3. Optimizing the quark smearing

We have shown ways to optimize a linear combination of interpolators with respect to the parameter R. For a simulation the most convenient way to optimize the smearing would be on the quark level. Recently efforts were made to use non-Gaussian shapes. They require either gauge fixing or some reshaping of a Gaussian source [86], or they are a superposition of gauge invariant source smearings at the same point. A natural candidate for a non-Gaussian gauge invariant smearing is a combination of two Gaus-

sian sources. So we can define a smearing

$$\phi = \phi_1 + r\phi_2 \tag{7.19}$$

for , e.g., $\phi_1 = \phi^{100}_{\text{Wupp}}$ and $\phi_2 = \phi^{400}_{\text{Wupp}}$.
Then the propagator constructed with this smearing at sink and source is a linear combination of the propagators with the individual smearing functions:

$$P = P_{11} + rP_{21} + rP_{12} + r^2 P_{22}\,, \tag{7.20}$$

where the indices correspond to the source and sink smearing.
When we use this propagator to construct correlators we obtain 16 terms

$$\begin{aligned} C[t] = C(P,P)[t] =& C(P_{11},P_{11})[t] + \\ & rC(P_{12},P_{11})[t] + \cdots + r^4 C(P_{22},P_{22})[t] \end{aligned} \tag{7.21}$$

for mesons[3] 64 terms

$$\begin{aligned} C(r)[t] =& C(P,P,P)(r)[t] = C(P_{11},P_{11},P_{11})[t] \\ & + rC(P_{12},P_{11},P_{11})[t] + \cdots + r^6 C(P_{22},P_{22},P_{22})[t] \end{aligned} \tag{7.22}$$

for baryons. To make this an function were we can scan the range of r we would need to compute these terms individually.
Then the correlator can be plugged into some functional which defines an optimal condition for r.
One could use [154]

$$M(r, t_{\text{start}}, t_{\text{end}}) = \sum_{t=t_{\text{start}}}^{t_{\text{end}}} \left(m_{\text{eff}}(r,t) - m_{\text{eff,plateau}}(t)\right)^2\,, \tag{7.23}$$

where $m_{\text{eff}}(r, t+0.5) = \ln\frac{C(r)[t]}{C(r)[t+1]}$, which we can minimize with respect to r in our "fitrange". This should yield a maximally flat effective mass.
The amount of computation is much higher than what is needed to do the variational method and in this work it we did not implement it. This might be the way to go if one wants a highly optimized smearing and also if one wants to investigate the merits of

[3] For mesons correlators the smearing operator can be transfered from one propagator sink/source to the sink/source of the other propagator. Therefore once could perform this analysis with a point-to-point propagator and three (narrow + narrow , narrow + wide, wide + wide) times three smeared-to-smeared propagators. As this would be more expensive in terms of inversions we do not recommend this approach.

using more then two different smearings in the linear combination (then r would be a vector of weights).

7.4. Optimal smearing combination

The variational method (Section 7.1) and the Euler angle fits (Section 7.2) find the ground state as some linear combination of interpolating operators governed by the ratio R. In our case each interpolating operator has the same smearing on all quarks. In the language of the linear combination of quark fields (Section 7.3) the correlator is then given for mesons as

$$C[t] = C(P_{11}, P_{11})[t] + r^2 C(P_{12}, P_{12})[t] + r^2 C(P_{21}, P_{21})[t] + r^4 C(P_{22}, P_{22})[t] \tag{7.24}$$

and for baryons as

$$\begin{aligned} C(r)[t] =& C(P_{11}, P_{11}, P_{11})[t] + r^3 C(P_{12}, P_{12}, P_{12})[t] \\ &+ r^3 C(P_{21}, P_{21}, P_{21})[t] + r^6 C(P_{22}, P_{22}, P_{22})[t]\,. \end{aligned} \tag{7.25}$$

Thus, as a rule of thumb, we could use

$$r = \sqrt[3]{R} \text{ for baryons} \qquad\qquad r = \sqrt[2]{R} \text{ for mesons}\,. \tag{7.26}$$

This is motivated because the terms in Eq. (7.21) and Eq. (7.22) have to be of the same order of magnitude to make any cancellations of excited states possible. Therefore the optimal choice for four of the 16 (in the meson case)/64 (for baryons) terms has to be in the right ballpark. The optimal choice is hard to determine very precisely, but it is not so crucial to get it exactly right. The smearing combination comes at no extra cost compared to the higher smearing iteration count that is used, so any kind of improvement is very welcome.
Applying this rule of thumb to estimate the optimal smearing parameter we obtain very similar results for the nucleon, the N^* and the meson interpolators at the heavy quark mass. This result seems to be stable for the baryon interpolators at the lighter flavors but seems to be a little too high for the mesons at this quark mass, see Fig. 7.8.

7.5. Results of the combined smearing

We have taken the result of the guess in Section 7.4 for the nucleon at the heavier quark mass and rerun the hadron spectrum at the same configurations. In the following we discuss our findings.

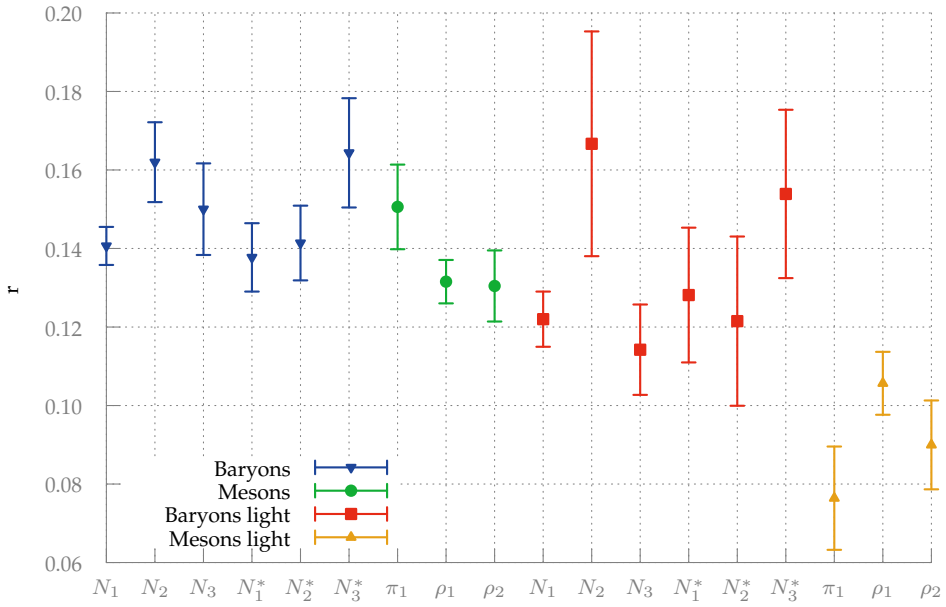

Figure 7.8.: Optimal choice for the parameter r in the linear combination of the quark smearings.

7.5.1. The wave function

To visualize the wave function, see Fig. 7.10, we have fixed a configuration to coulomb gauge, and then we performed the APE smearing [80] on it, and used the resulting gauge field to Wuppertal smear [84] a point source.
Wuppertal smearing generates a Gaussian wave function, but we expect systematic deviations for small distances. The way we have computed the wave function as a function of the direction did not incorporate the effects of the periodic boundary conditions. For points with a separation from the origin along an axis the effects of periodicity are more pronounced than for points with a similar distance which lie off axis (see Fig. 7.9). Therefore we can only fit in a range where the lattice artifacts are small (say $d = 3a$) and finite size effects are negligible (say $d \leq 10a$). To compare the shape of the wave functions we have normalized the wave function on the origin to one. In Fig. 7.10 we plot that and we fit each measured wave function to a Gaussian ϕ. The combined wave function was then fit to a linear combination of the normalized constituent Gaussians

$$WF_{\text{combined,normalized}} = c\phi(100) + (1-c)\phi(400)\,, \tag{7.27}$$

where the fit yields $c \approx 0.7$ so that the smearing with 100 steps has a bigger relative weight. This is not surprising as the broader smearing will always dominate the larger distances and to change the shape of the wave function significantly the narrower

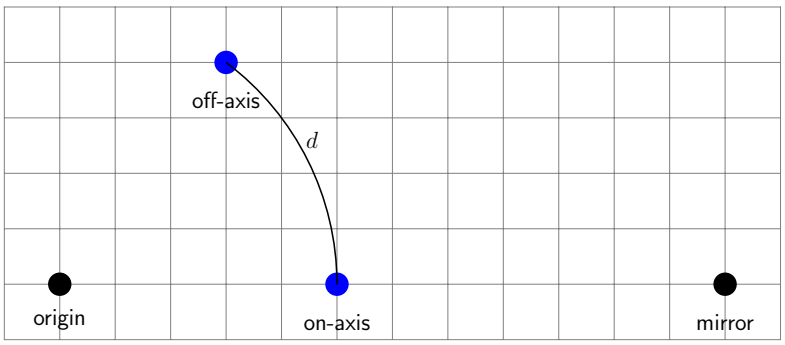

Figure 7.9.: The distance to the mirror of the origin is smaller for on-axis points than for other points with the same distance d to the origin. Thus the finite size effects, due to the periodic boundary conditions are bigger on the on-axis points.

smearing has to be coming with a bigger weight.
This fit describes the wave form better than a single Gaussian and the deviation from that for large distances can be clearly seen in Fig. 7.10.

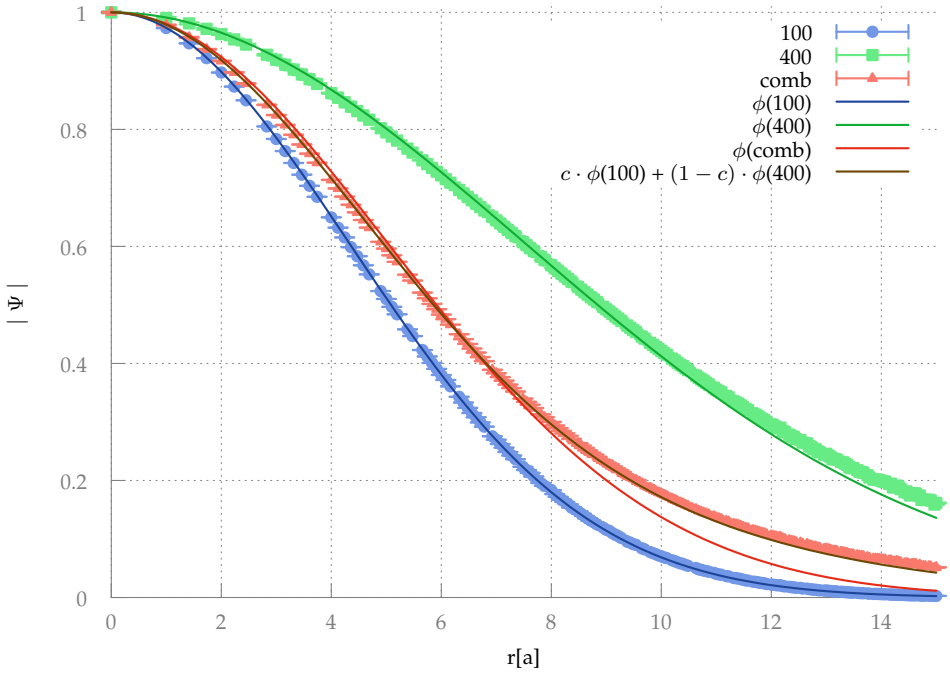

Figure 7.10.: Wave forms of the combined smearing and the constituent smearings for comparison. The single Gaussian fit to the combined smearing clearly misses the flatter tail.

In Fig. 7.10 we see that the combined wave function has a flatter tail than a Gaussian. This hints on the physical wave function of a quark in a nucleon ground state, but this is a qualitative statement which has to be taken with great caution.

7.5.2. Effective masses of the linear combination

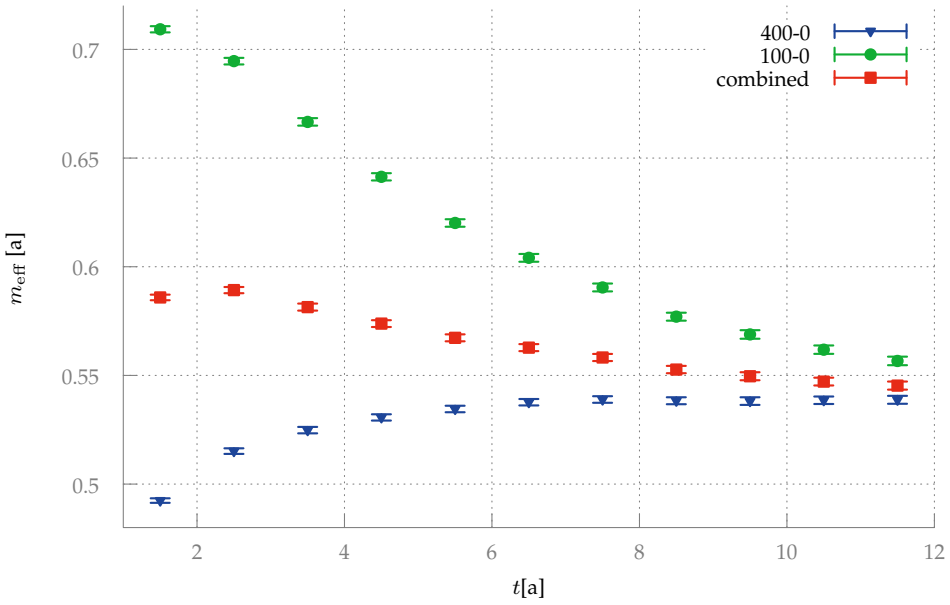

Figure 7.11.: Effect of the combined smearing in the effective mass of the point-smeared correlators.

We can see that the linear combination of smearings nicely cancels most of the overlap with the first excitation in the point-smeared effective mass of the nucleon, see Fig. 7.11. The smeared-smeared effective mass of the nucleon is also improved, as it is a little flatter than the 400 smearing steps alone and has smaller error bars, see Fig. 7.12.
The error of the effective mass of the nucleon N_1 was reduced by[4] $\approx 40\%$ when comparing ϕ_{400} with the combined smearing. This corresponds to a factor of $\approx$ two in computer time for the same signal-to-noise ratio. This means that optimizing the smearing is a crucial part of running a large scale simulation.
A similar analysis was performed for all the available interpolating operators of our basis. The correlators for them were either using propagators corresponding to the strange quark on this ensemble or propagators corresponding to the light flavor, i.e.,

[4] $\frac{m_{\mathrm{eff}}(\phi_4 00)}{m_{\mathrm{eff}}(c\cdot\phi_1 00+\phi_4 00)} \approx 1.4$

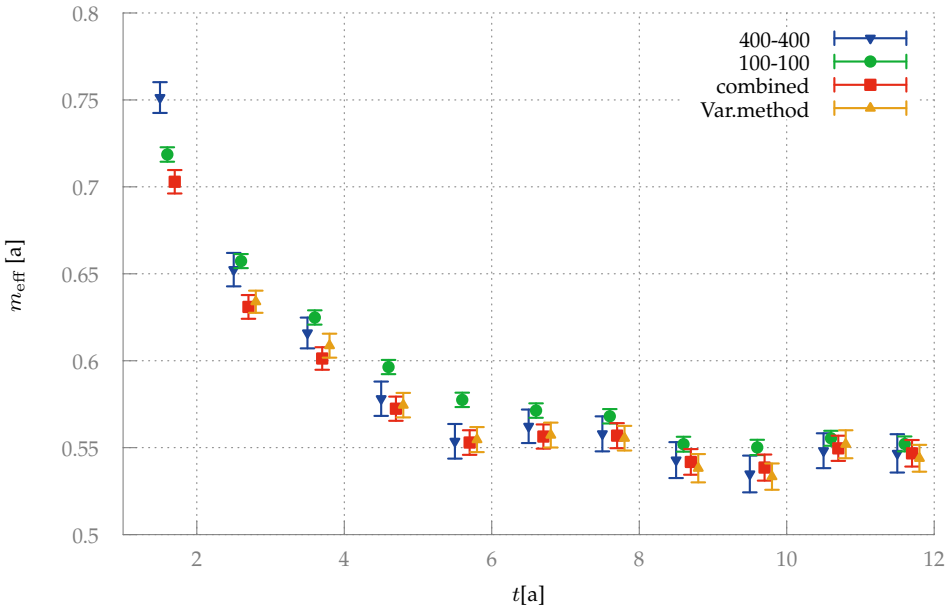

Figure 7.12.: Effect of the combined smearing in the effective mass.

no particles with quarks having different masses were analyzed. For all of them the combined smearing performed better than the 400 steps of Wuppertal smearing. For some interpolating operators, namely N_2, π_2 and ρ_2, the 100 steps of Wuppertal where better than the 400 steps, and thus the combined smearing was worse than the 100 steps.
The analysis was also done at non-zero momentum ($\vec{p} = (1,0,0) \cdot \frac{2\pi}{L}$) and all findings were confirmed.
The fact that other interpolators are also improved by this combined smearing is a very non-trivial observation. It implies that the optimal parameter r is not needed to extreme precision to improve our wave-function.
So one can estimate the optimal smearing parameter on a subset of the configurations one wants to analyze and then do the large scale computation with better signal-to-noise ratio and potentially less excited state effects. It would be very interesting to test this smearing on three-point functions, where the excited state contributions are naturally hard to get rid of, and often times much more expensive approaches are taken to cope with them. As a nice side effect this method is very cheap in terms of computation time and for example the combined smearing can be used in a multiple t_{sink}-study.

8 Summary

This thesis focused on methods to numerically access the internal structure of the nucleon. There are two aspects to a successful computation: one has to choose efficient algorithms and suitable parameter choices to obtain the correct results at acceptable computer time cost.

To address these points this thesis contains a study of excited state contributions in baryonic two- and three-point functions as well as a new algorithm to compute three-point functions. These studies were performed using Wilson-Clover fermions with two or three dynamical flavors.

In Chapter 2 we presented the physical motivation for the quantities we are interested in here: generalized form factors and forward matrix elements. They parameterize, e.g., the spatial distribution of charge and magnetization, or the individual contributions of the partons to the total momentum or spin.

Furthermore, we have presented the methods to compute them in lattice QCD in Chapter 3. We have outlined the data analysis procedure and have shown where parameter choices may introduce systematic effects. We have also introduced an alternative approach to compute the connected three-point functions with stochastic estimators.

In Chapter 6 we have then compared this method to the established sequential source method. We have shown that computing forward and backward going three-point functions improves the signal-to-noise ratio at fixed inversions. We have found that the stochastic estimation of three-point functions is competitive to the sequential source method at medium momentum transfers and that it produces more reliable results at large momentum transfers. Thus the stochastic estimation method for baryon three-point functions is advantageous. For projects where the broken flavor $SU(3)$ effects on three-point functions in the baryon octet are of interest the stochastic method is clearly the method of choice.

The lattice community has struggled to reproduce experimental results on generalized form factors and forward matrix elements. The results of different collaborations on g_A and $\langle x \rangle_{u-d}$ have been compared in Chapter 4. The common explanation for the tension of lattice QCD predictions with experimental observations is the presence of excited state contributions.

To compute three-point functions with fixed t_{sink} has some advantages, but the choice of t_{sink} can influence the excited state contributions to the the final results. We have shown an extensive analysis of this in Chapter 5, where we have compared and extended the available models for the t_{sink}-dependence. We have found that our choice of quark smearing sufficiently suppresses excited state contributions such that our choice of t_{sink} on other ensembles is safe.
Having acknowledged the importance of excited state suppression we introduce a novel approach to perform a gauge invariant optimized quark smearing in Chapter 7. We have found that a linear combination of two Gaussian quark smearings improves the ground state overlap with the additional benefit of drastically reducing the statistical noise. This noise suppression is equivalent to a factor of two in computational cost.

Outlook

With the methods outlined in this thesis it is possible to conduct a large scale study of baryon properties. Systematic effects from the choice of t_{sink} were checked and for similar pion masses and lattice spacing they are under control. Excited state contributions can be suppressed by applying the combined smearing and checking the t_{sink}-dependence without compromising the signal-to-noise ratio. The stochastic estimation method for three-point functions increases the reliability of form factors, especially those which are not accessible in the forward limit ($\vec{p}_i = \vec{p}_f = 0$), and results at high momentum transfers. It unfolds its full potential in a study of multiple baryons and transition elements between them, for example in a complete study of the baryon octet. Furthermore, once the tension with the experiment for established benchmark quantities is sufficiently released, lattice QCD with controlled systematics might clarify long-standing puzzles like the correct proton charge radius and the proton spin crisis.

A
Conventions and Resources

A.1. Units and conventions

Throughout this work natural units i. e. $\hbar = c = 1 = k_B$ are assumed in formulae. SI units can be recovered with the help of the identity [155]

$$1 = \hbar c = 197.3269718(44)\text{MeV fm}\,. \tag{A.1}$$

γ-matrices in Euclidean spacetime are sometimes written with their associated directions as indices:

$$\gamma_1 \equiv \gamma_x\,, \qquad \gamma_2 \equiv \gamma_y\,, \qquad \gamma_3 \equiv \gamma_z \qquad \gamma_4 \equiv \gamma_t\,. \tag{A.2}$$

This is meant to clarify the notation, but the two naming schemes are interchangeable. The Einstein sum conventions is always used. The lattice time-slices sometimes are referred to as integer numbers, then they can be converted to physical distances with the lattice spacing. Errors of secondary quantities, i.e., functions of the mean, where computed with the Jackknife method [156].

A.2. Programs and computer resources used in this work

All generation of two- and three-point functions was done using the Chroma library [157]. The generation of gauge configurations was done, e.g. on QPACE [158], and are for the most part available on the ILDG [159]. The minimization of χ^2 in fitting was done using Minuit [160]. Matrix algebra was coded using the GSL library [161] and Armadillo [162]. Simulations were performed on the Linux cluster and SuperMUC [163] at the Leibnitz Rechenzentum (LRZ) Munich, the idataCool cluster [164], the Linux Cluster of the theoretical physics department and athene in Regensburg, and the JUROPA in Julich [165].
The color scheme for the plots was done according to [166], which was downloaded from [167].

B

Additional plots for the comparison of sequential source and stochastic estimator form factors

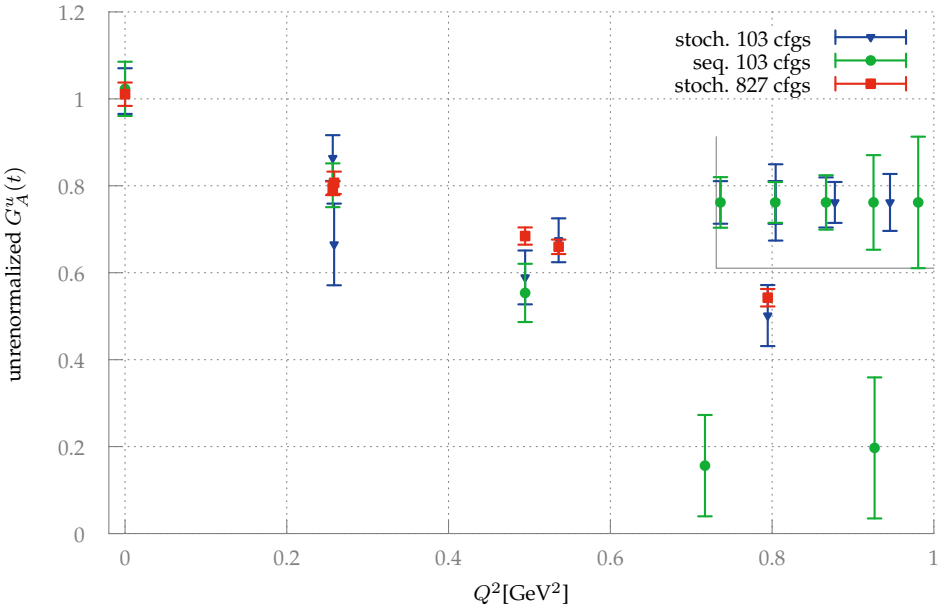

Figure B.1.: Stochastic estimation vs. sequential source for the axial form factor G_A^u. To compare the errors of both methods the inlay displays the data-points shifted to a constant. See Section 6.2.4 for details.

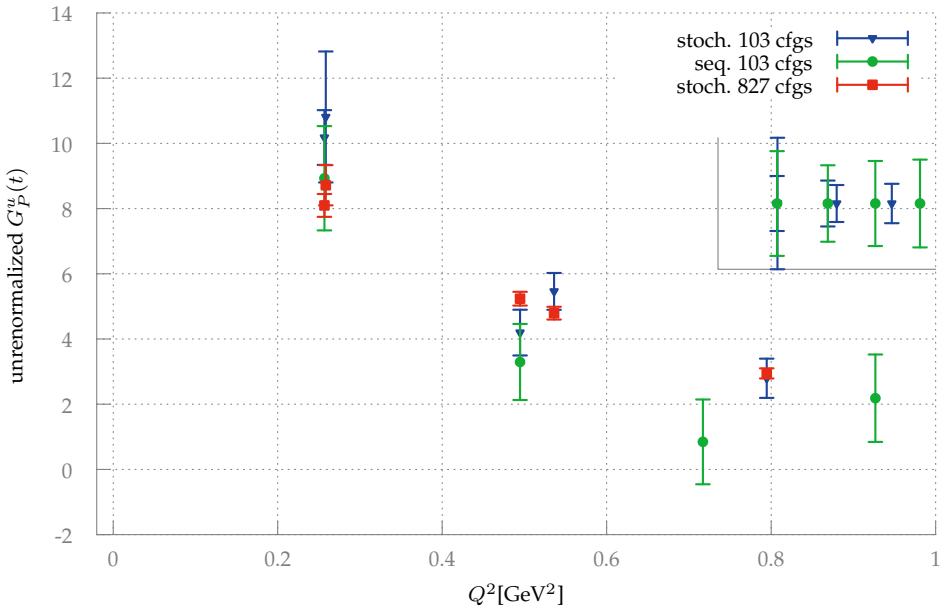

Figure B.2.: As Fig. B.1 for the induced pseudoscalar form factor G_P^u.

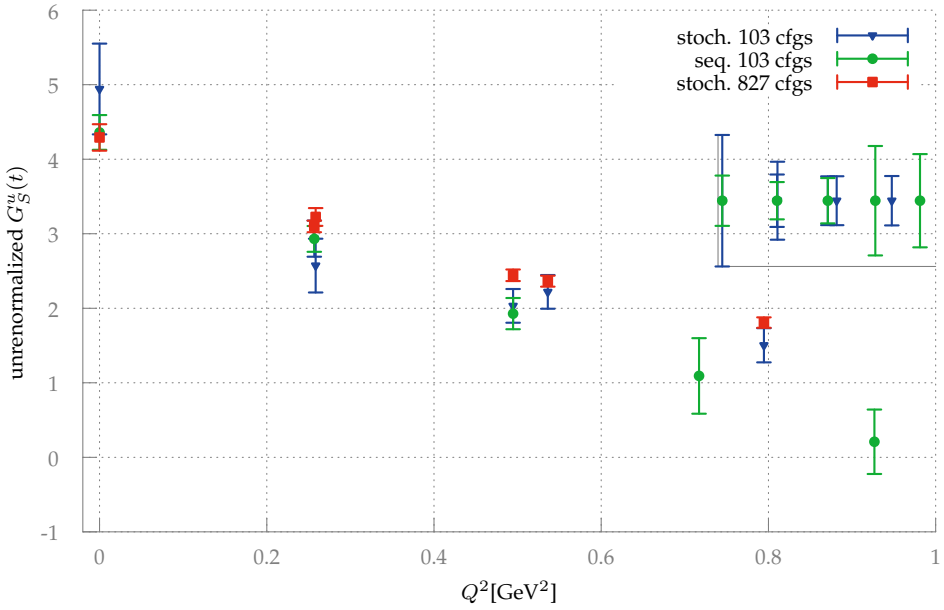

Figure B.3.: As Fig. B.1 for the scalar form factor G_S^u.

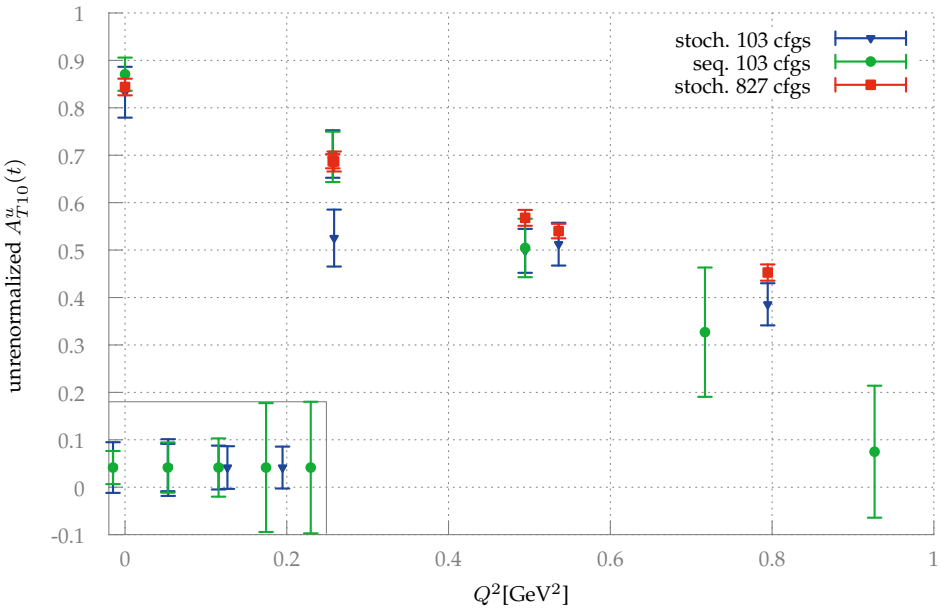

Figure B.4.: As Fig. B.1 for for the tensor form factor A^u_{T10}.

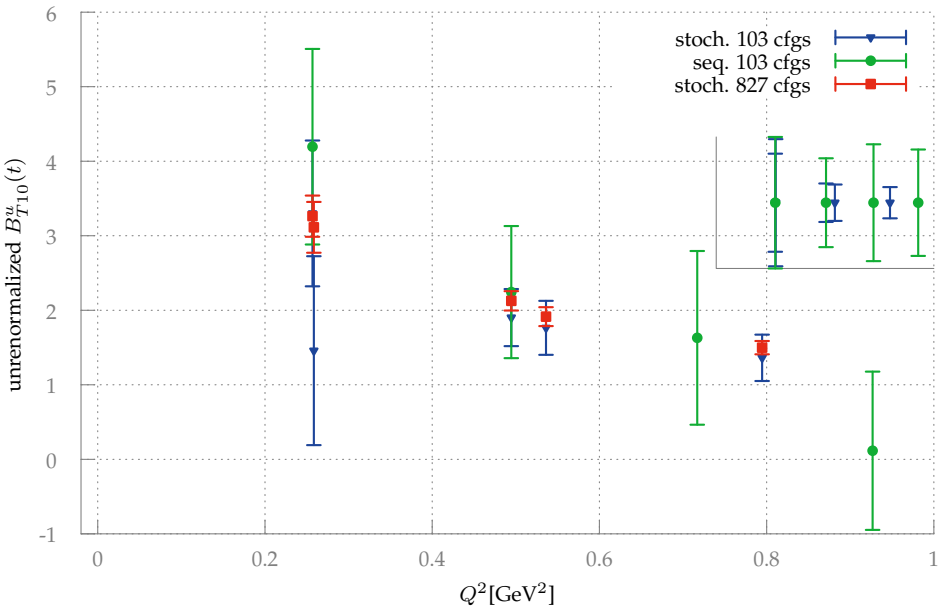

Figure B.5.: As Fig. B.1 for the tensor form factor B^u_{T10}.

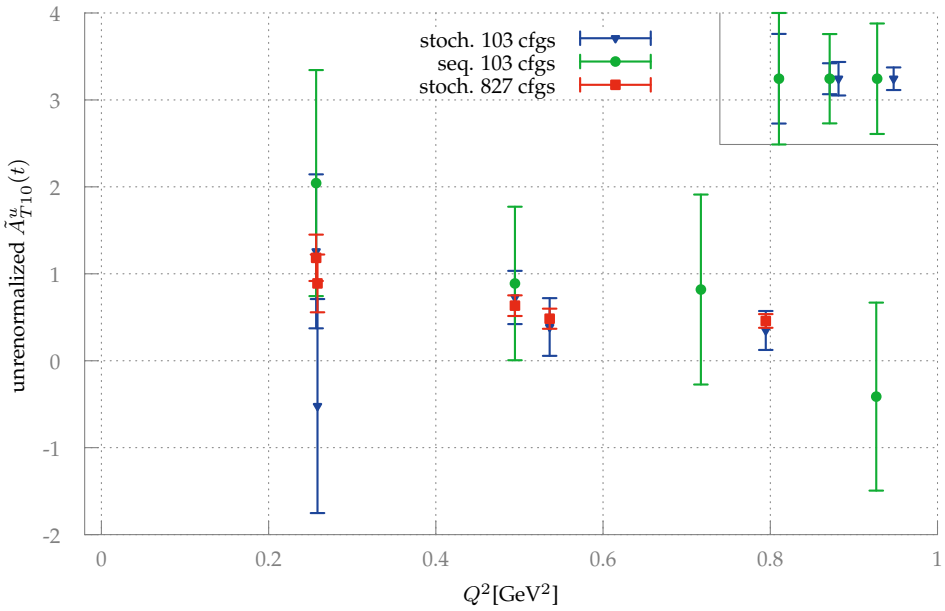

Figure B.6.: As Fig. B.1 for the tensor form factor $\tilde{A}^u_{T10}$.

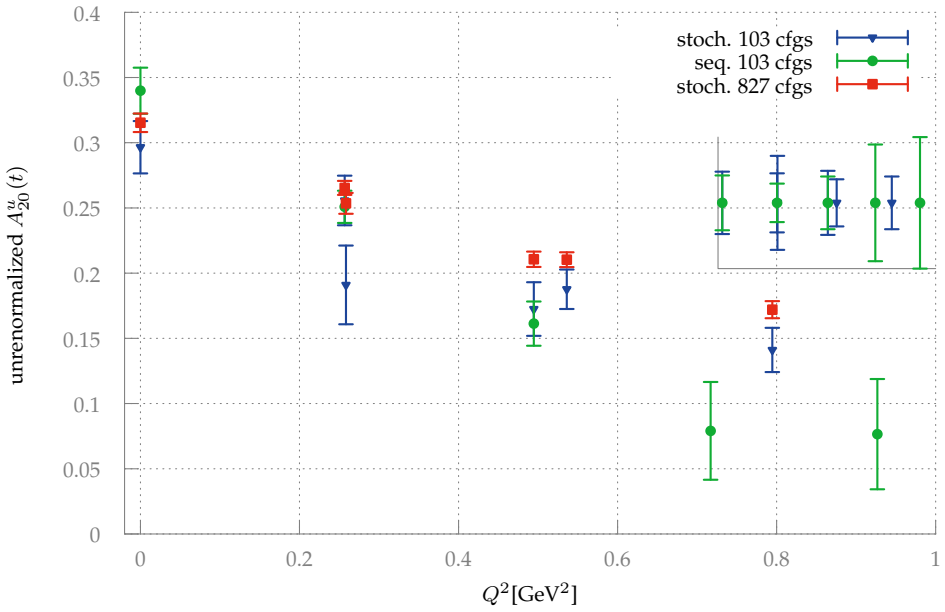

Figure B.7.: As Fig. B.1 for the vector GFF A^u_{20}.

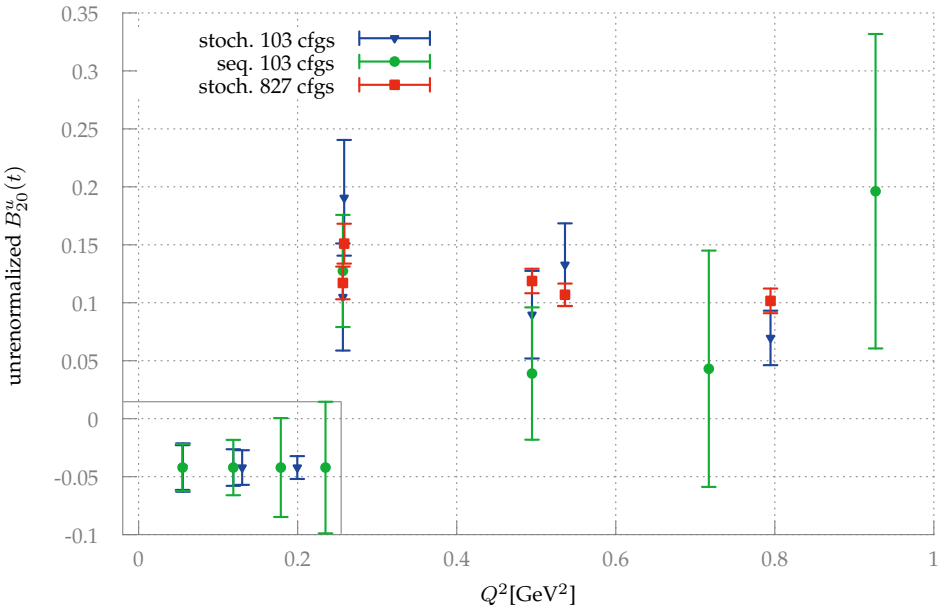

Figure B.8.: As Fig. B.1 for the vector GFF B^u_{20}.

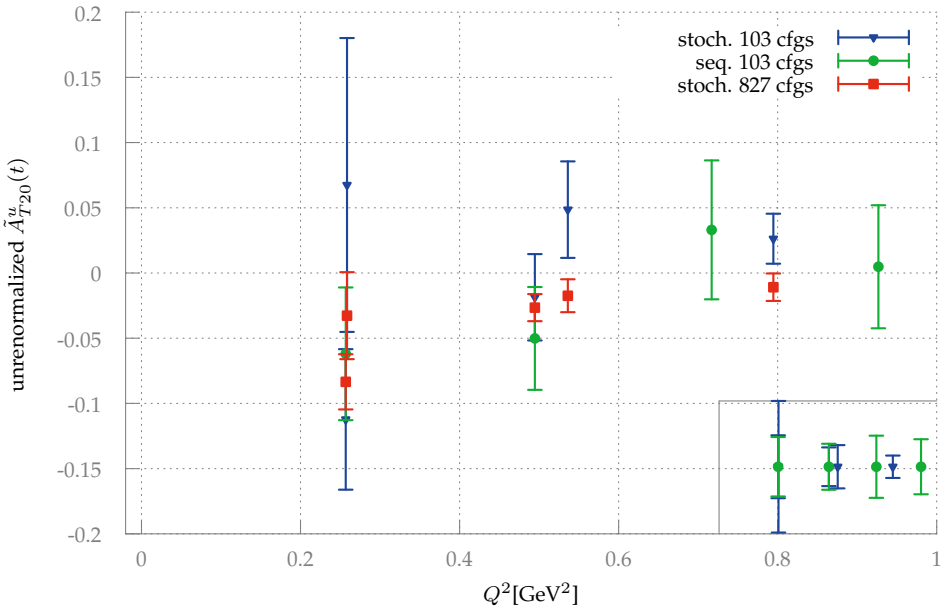

Figure B.9.: As Fig. B.1 for the vector GFF C^u_{20}.

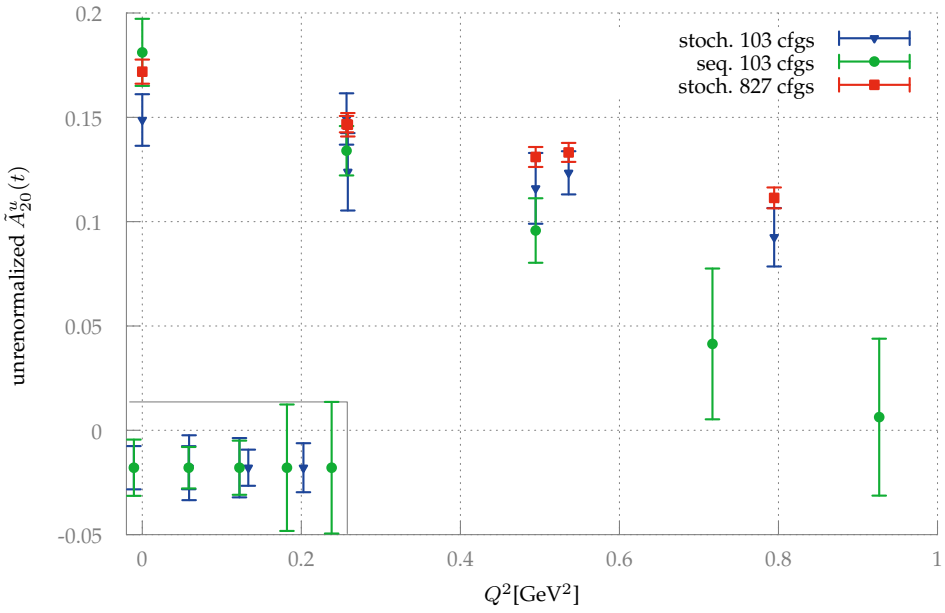

Figure B.10.: As Fig. B.1 for the axial GFF $\tilde{A}_{20}$

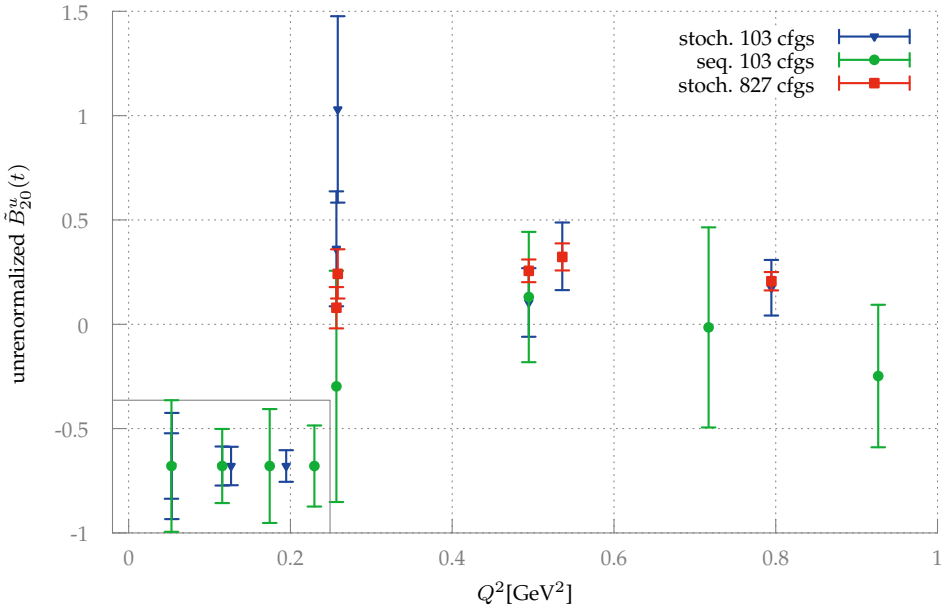

Figure B.11.: As Fig. B.1 for the axial GFF $\tilde{B}^u_{20}$.

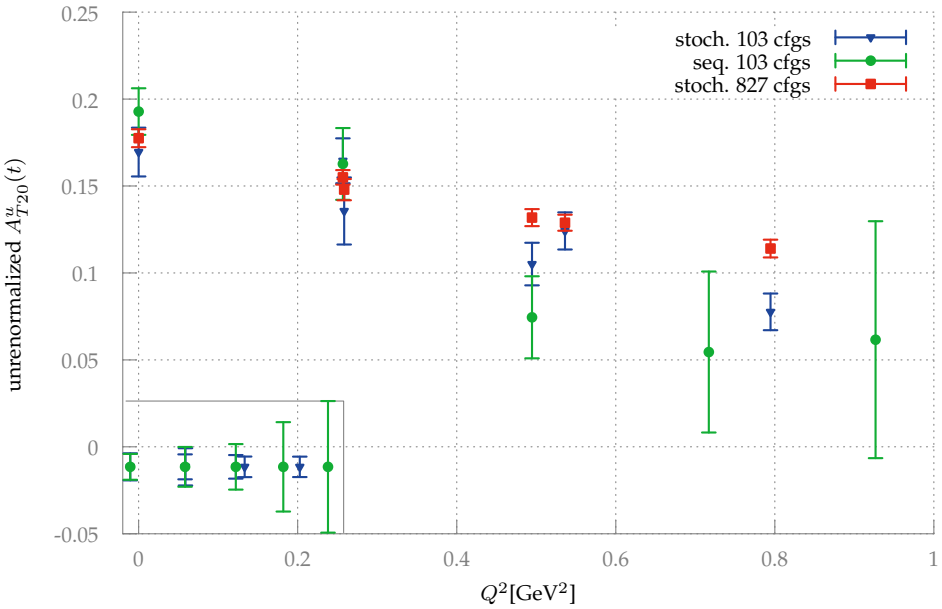

Figure B.12.: As Fig. B.1 the tensor GFF A^u_{T20}.

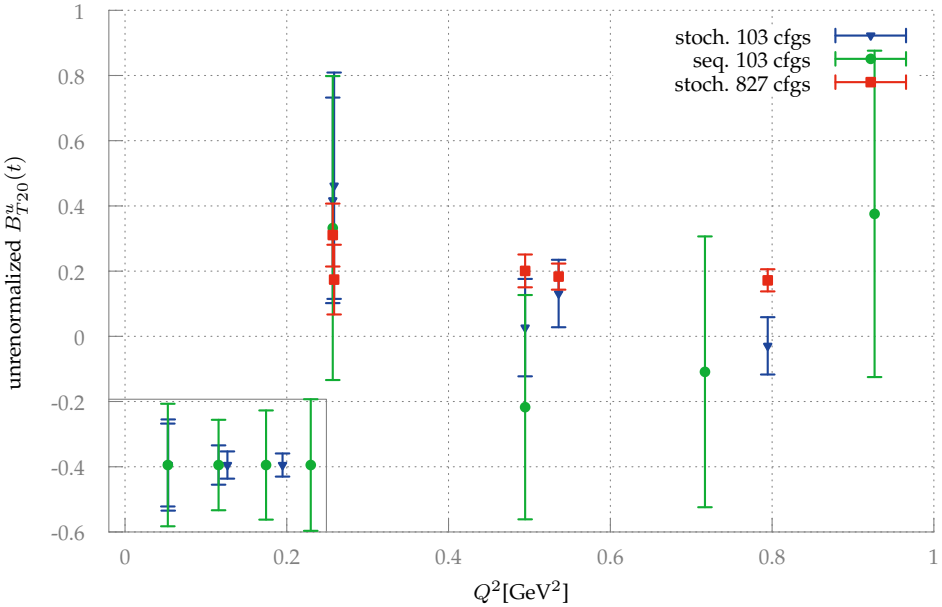

Figure B.13.: As Fig. B.1 the tensor GFF B^u_{T20}.

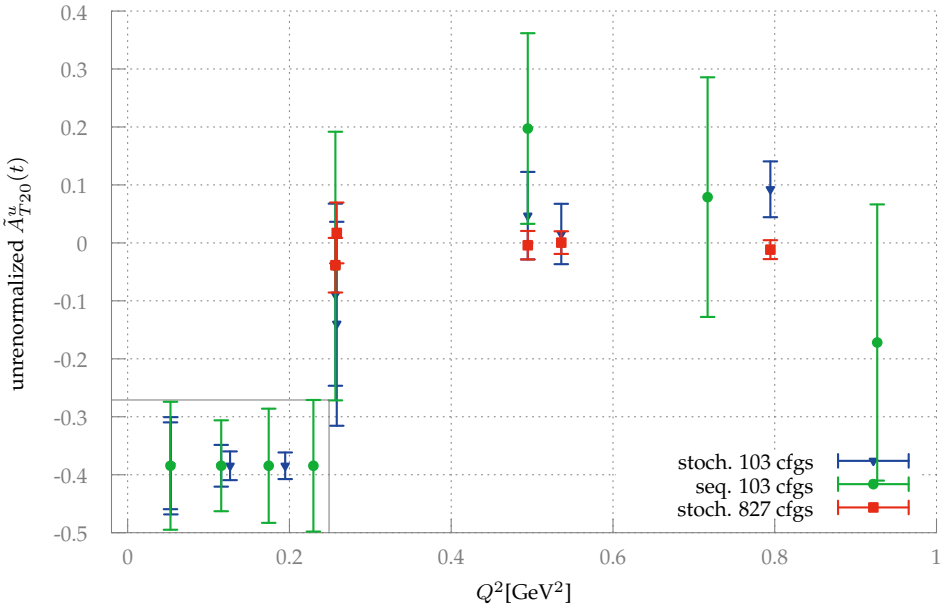

Figure B.14.: As Fig. B.1 the tensor GFF $\tilde{A}^u_{T20}$.

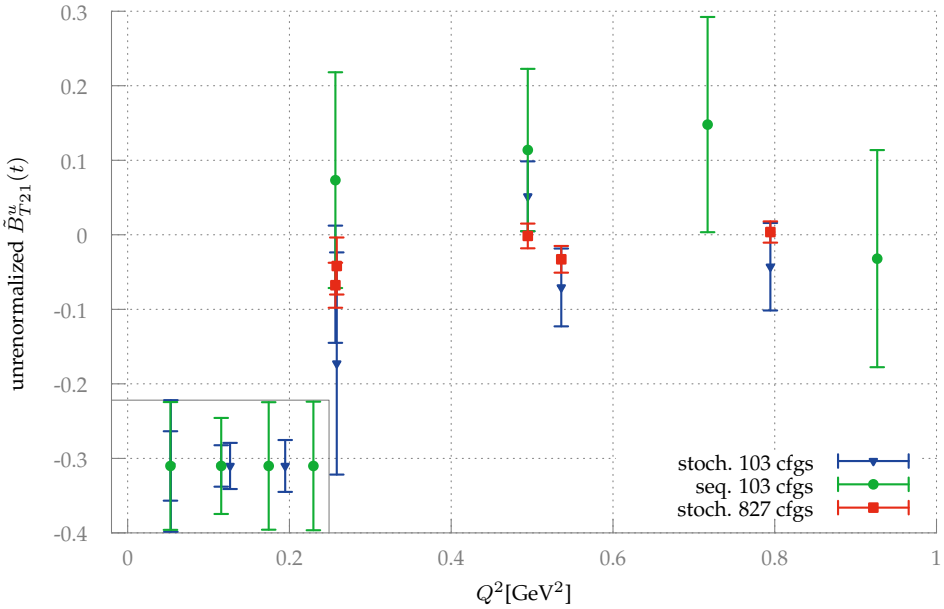

Figure B.15.: As Fig. B.1 the tensor GFF $\tilde{B}^u_{T21}$.

C

Form factors and GPDs in euclidean spacetime

We follow [168] and our conventions agree with [169][1]. On the lattice we use a wick rotated time direction. The coordinates, derivatives and γ-matrices in Minkowski spacetime (denoted by sub- or superscript M) are converted as follows to Euclidean spacetime:

$$\gamma_M^0 = \gamma_4\,, \qquad \gamma_M^j = \mathrm{i}\gamma_j \tag{C.1}$$

$$x_M^0 = x_0^M = -\mathrm{i}x_4\,, \qquad x_M^j = -x_j^M = x_j D_M^0 = D_0^M = \mathrm{i}D_4\,, \qquad D_M^j = -D_j^M = -D_j \tag{C.2}$$

We have implied that the covariant derivative transforms like the partial derivative when going from Minkowski to Euclidean spacetime, hence our gauge fields A_μ^M transform such that the link variables do not change their form ($U_\mu = U_M^\mu$).
The conventions leave the "slash" intact and up to a factor of i invariant:

$$\begin{aligned} \not{D}_M &= \gamma_M^\mu D_\mu^M = \gamma_M^0 D_0^M + \sum_{j=1}^{3} \gamma_M^j D_j^M \\ &= \gamma_4 \mathrm{i}D_4 + \sum_{j=1}^{3} \mathrm{i}\gamma^j D_j = \mathrm{i}\gamma_\mu D_\mu = \mathrm{i}\not{D}\,. \end{aligned} \tag{C.3}$$

γ_5 changes its sign:

$$\begin{aligned} \gamma_5^M &= \mathrm{i}\gamma_M^0\gamma_M^1\gamma_M^2\gamma_M^3 \\ \gamma_5 &= \gamma^1\gamma^2\gamma^3\gamma^4 = -\gamma_5^M\,. \end{aligned} \tag{C.4}$$

[1] The inclined reader can find a very good overview in Table 10.1 p.206 in the first edition of this reference.

We use the standard definition

$$\sigma_M^{\mu\nu} = \frac{\mathrm{i}}{2}\left[\gamma_M^\mu, \gamma_M^\nu\right] \tag{C.5}$$

and choose

$$\sigma^{\mu\nu} = \frac{\mathrm{i}}{2}\left[\gamma^\mu, \gamma^\nu\right] . \tag{C.6}$$

This gives the translation prescription

$$\sigma_M^{0j} = \mathrm{i}\gamma_M^0\gamma_M^j = \mathrm{i}\gamma_4\mathrm{i}\gamma_j = \mathrm{i}\frac{\mathrm{i}}{2}\left[\gamma_4, \gamma_j\right] = \mathrm{i}\sigma_{4j} , \tag{C.7}$$

$$\sigma_M^{jk} = \mathrm{i}\gamma_M^j\gamma_M^k = \mathrm{i}(\mathrm{i}\gamma_j)(\mathrm{i}\gamma_k) = -\mathrm{i}\gamma_j\gamma_k = \frac{-\mathrm{i}}{2}\left[\gamma_j, \gamma_k\right] = -\sigma_{jk} . \tag{C.8}$$

As useful abbreviations we use

$$\overline{P}_M = \frac{P_\mu'^M + P_\mu^M}{2} , \qquad \Delta_\mu^M = P_\mu'^M - P_\mu^M , \qquad t = \Delta_M^\mu\Delta_\mu^M , \tag{C.9}$$

and we note that

$$-\Delta_j^M = \Delta_M^j = \left(\vec{P}' - \vec{P}\right)_j \equiv \Delta_j , \qquad \Delta_4 = \mathrm{i}\left(E(\vec{p'}) - E(\vec{p})\right) = \mathrm{i}\Delta_0^M . \tag{C.10}$$

We define

$$\langle\langle O\rangle\rangle = \overline{U}(P', \sigma')\, O\, U(P, \sigma) . \tag{C.11}$$

We note here that the spinors $U(P, \sigma)$ only depend on $\vec{p}$ and $\vec{s}$, which are identical in Minkowski and Euklidean spacetime; hence the spinors do not change.
Symmetrization and antisymmetrization is abbreviated by putting the respective indices in brackets, and the following expansion is implied:

$$A^{\{\mu}B^{\nu\}} = \frac{1}{2}\left(A^\mu B^\nu + A^\nu B^\mu\right) \tag{C.12}$$

$$A^{[\mu}B^{\nu]} = \left(A^\mu B^\nu - A^\nu B^\mu\right) . \tag{C.13}$$

C.1. Form factors

C.1.1. Scalar form factor

$$\langle P' \mid \overline{\Psi}_q\Psi_q \mid P\rangle = \langle\langle \mathbb{1}\rangle\rangle\, G_S(t) \tag{C.14}$$

As there are no open indices this is the same in Euclidean spacetime.

C.1.2. Electromagnetic form factor

In Minkowski spacetime the electromagnetic form factors are defined by

$$\langle P' \mid \overline{\Psi}_q \gamma_M^\mu \Psi_q \mid P \rangle = \left\langle\left\langle \gamma_M^\mu \right\rangle\right\rangle F_1(t) + \frac{\mathrm{i}}{2m_N} \left\langle\left\langle \sigma_M^{\mu\nu} \right\rangle\right\rangle \Delta_\nu^M F_2(t)\,. \tag{C.15}$$

Applying the definitions above we get for the time direction

$$\begin{aligned}
\langle P' \mid \overline{\Psi}_q \gamma_4 \Psi_q \mid P \rangle &= \langle P' \mid \overline{\Psi}_q \gamma_M^0 \Psi_q \mid P \rangle \\
&= \left\langle\left\langle \gamma_M^0 \right\rangle\right\rangle F_1(t) + \frac{\mathrm{i}}{2m_N} \sum_{j=1}^{3} \left\langle\left\langle \sigma_M^{0j} \right\rangle\right\rangle \Delta_j^M F_2(t) \\
&= \left\langle\left\langle \gamma_4 \right\rangle\right\rangle F_1(t) + \frac{\mathrm{i}}{2m_N} \sum_{j=1}^{3} \left\langle\left\langle \mathrm{i}\sigma^{4j} \right\rangle\right\rangle (-\Delta_j) F_2(t) \\
&= \left\langle\left\langle \gamma_4 \right\rangle\right\rangle F_1(t) + \frac{1}{2m_N} \sum_{j=1}^{3} \left\langle\left\langle \sigma^{4j} \right\rangle\right\rangle \Delta_j F_2(t)
\end{aligned} \tag{C.16}$$

and for the spatial directions

$$\begin{aligned}
\langle P' \mid \overline{\Psi}_q \gamma_j \Psi_q \mid P \rangle &= -\mathrm{i} \langle P' \mid \overline{\Psi}_q \gamma_M^j \Psi_q \mid P \rangle \\
&= -\mathrm{i} \left\langle\left\langle \gamma_M^j \right\rangle\right\rangle F_1(t) + \frac{1}{2m_N} \left\{ \left\langle\left\langle \sigma_M^{j0} \right\rangle\right\rangle \Delta_0^M + \sum_{k=1}^{3} \left\langle\left\langle \sigma_M^{jk} \right\rangle\right\rangle \Delta_k^M \right\} F_2(t) \\
&= \left\langle\left\langle \gamma_j \right\rangle\right\rangle F_1(t) + \frac{1}{2m_N} \left\{ \left\langle\left\langle \mathrm{i}\sigma^{j4} \right\rangle\right\rangle (-\mathrm{i}\Delta_4) + \sum_{k=1}^{3} \left\langle\left\langle (-\sigma^{jk}) \right\rangle\right\rangle (-\Delta_k) \right\} F_2(t) \\
&= \left\langle\left\langle \gamma_j \right\rangle\right\rangle F_1(t) + \frac{1}{2m_N} \left\langle\left\langle \sigma^{j\alpha} \right\rangle\right\rangle \Delta_\alpha F_2(t)
\end{aligned} \tag{C.17}$$

and thus we get

$$\langle P' \mid \overline{\Psi}_q \gamma^\mu \Psi_q \mid P \rangle = \left\langle\left\langle \gamma^\mu \right\rangle\right\rangle F_1(t) + \frac{1}{2m_N} \left\langle\left\langle \sigma^{\mu\nu} \right\rangle\right\rangle \Delta_\nu F_2(t)\,. \tag{C.18}$$

C.1.3. Axial form factor

In Minkowski spacetime the iso-spin axial form factors between protons are defined by

$$\langle P' \mid \overline{\Psi}_q \gamma_M^\mu \gamma_5^M \Psi_q \mid P \rangle = \left\langle\left\langle \gamma_M^\mu \gamma_5^M \right\rangle\right\rangle G_A(t) + \frac{\Delta_M^\mu}{2m_N} \left\langle\left\langle \gamma_5^M \right\rangle\right\rangle G_P(t) \tag{C.19}$$

Splitting the conversion to Euclidean spacetime again in time and spatial components we get

$$\begin{aligned}
\langle P' \mid \overline{\Psi}_q \gamma_4 \gamma_5 \Psi_q \mid P \rangle &= \langle P' \mid \overline{\Psi}_q \gamma_M^0 (-1) \gamma_5^M \Psi_q \mid P \rangle \\
&= \left\langle\left\langle \gamma_M^0 (-1) \gamma_5^M \right\rangle\right\rangle G_A(t) + \frac{\Delta_M^0}{2m_N} \left\langle\left\langle (-1) \gamma_5^M \right\rangle\right\rangle G_P(t) \\
&= \langle\langle \gamma_4 \gamma_5 \rangle\rangle G_A(t) + \frac{-\mathrm{i}\Delta_4}{2m_N} \langle\langle \gamma_5 \rangle\rangle G_P(t)
\end{aligned} \tag{C.20}$$

and

$$\begin{aligned}
\langle P' \mid \overline{\Psi}_q \gamma_j \gamma_5 \Psi_q \mid P \rangle &= \mathrm{i} \langle P' \mid \overline{\Psi}_q \gamma_M^j \gamma_5^M \Psi_q \mid P \rangle \\
&= \mathrm{i} \left\langle\left\langle \gamma_M^j \gamma_5^M \right\rangle\right\rangle G_A(t) + \frac{\mathrm{i}\Delta_M^j}{2m_N} \left\langle\left\langle \gamma_5^M \right\rangle\right\rangle G_P(t) \\
&= \mathrm{i} \langle\langle \mathrm{i} \gamma_j (-1) \gamma_5 \rangle\rangle G_A(t) + \frac{\mathrm{i}\Delta_j}{2m_N} \langle\langle (-1) \gamma_5 \rangle\rangle G_P(t) \\
&= \langle\langle \gamma_j \gamma_5 \rangle\rangle G_A(t) + \frac{-\mathrm{i}\Delta_j}{2m_N} \langle\langle \gamma_5 \rangle\rangle G_P(t)
\end{aligned} \tag{C.21}$$

so combined we get

$$\langle P' \mid \overline{\Psi}_q \gamma_\mu \gamma_5 \Psi_q \mid P \rangle = \langle\langle \gamma_\mu \gamma_5 \rangle\rangle G_A(t) - \frac{\mathrm{i}\Delta_\mu}{2m_N} \langle\langle \gamma_5 \rangle\rangle G_P(t) \tag{C.22}$$

C.1.4. Tensor form factor

In Minkowski spacetime the tensor form factors are defined by

$$\begin{aligned}
\langle P' \mid \overline{\Psi}_q \mathrm{i}\sigma_M^{\mu\nu} \Psi_q \mid P \rangle = \left\langle\left\langle \mathrm{i}\sigma_M^{\mu\nu} \right\rangle\right\rangle A_{T10}(t) + \left\langle\left\langle \gamma_M^{[\mu} \Delta_M^{\nu]} \right\rangle\right\rangle \frac{B_{T10}(t)}{2m_N} \\
+ \langle\langle 1 \rangle\rangle \overline{P}_M^{[\mu} \Delta_M^{\nu]} \frac{\tilde{A}_{T10}(t)}{m_N^2}
\end{aligned} \tag{C.23}$$

So we get

$$\begin{aligned}
\langle P' \mid \overline{\Psi}_q \mathrm{i}\sigma_{4j} \Psi_q \mid P\rangle =& -\mathrm{i}\langle P' \mid \overline{\Psi}_q \mathrm{i}\sigma^{0j}_M \Psi_q \mid P\rangle \\
=& -\mathrm{i}\left\langle\left\langle \mathrm{i}\sigma^{0j}_M \right\rangle\right\rangle A_{T10}(t) - \mathrm{i}\left\langle\left\langle \gamma^0_M \Delta^j_M - \gamma^j_M \Delta^0_M \right\rangle\right\rangle \frac{B_{T10}(t)}{4m_N} \\
& -\mathrm{i}\left\langle\left\langle \overline{P}^0_M \Delta^j_M - \overline{P}^j_M \Delta^0_M \right\rangle\right\rangle \frac{\tilde{A}_{T10}(t)}{2m_N^2} \\
=& -\mathrm{i}\left\langle\langle -\sigma_{4j}\rangle\right\rangle A_{T10}(t) - \mathrm{i}\left\langle\langle \gamma_4 \Delta_j - \mathrm{i}\gamma_j(-\mathrm{i})\Delta_4\rangle\right\rangle \frac{B_{T10}(t)}{4m_N} \\
& -\mathrm{i}\left\langle\left\langle -\mathrm{i}\overline{P}_4 \Delta_j - \overline{P}_j(-\mathrm{i})\Delta_4 \right\rangle\right\rangle \frac{\tilde{A}_{T10}(t)}{2m_N^2} \\
=& \mathrm{i}\left\langle\langle \sigma_{4j}\rangle\right\rangle A_{T10}(t) - \mathrm{i}\left\langle\left\langle \gamma_{[4}\Delta_{j]} \right\rangle\right\rangle \frac{B_{T10}(t)}{2m_N} \\
& -\left\langle\left\langle \overline{P}_{[4}\Delta_{j]} \right\rangle\right\rangle \frac{\tilde{A}_{T10}(t)}{m_N^2}
\end{aligned} \tag{C.24}$$

and

$$\begin{aligned}
\langle P' \mid \overline{\Psi}_q \mathrm{i}\sigma_{ij} \Psi_q \mid P\rangle =& -\langle P' \mid \overline{\Psi}_q \mathrm{i}\sigma^{ij}_M \Psi_q \mid P\rangle = \\
& -\left\langle\left\langle \mathrm{i}\sigma^{ij}_M \right\rangle\right\rangle A_{T10}(t) - \left\langle\left\langle \gamma^{[i}_M \Delta^{j]}_M \right\rangle\right\rangle \frac{B_{T10}(t)}{2m_N} \\
& -\left\langle\left\langle \overline{P}^{[i}_M \Delta^{j]}_M \right\rangle\right\rangle \frac{\tilde{A}_{T10}(t)}{m_N^2} \\
=& \left\langle\langle \mathrm{i}\sigma_{ij}\rangle\right\rangle A_{T10}(t) - \left\langle\left\langle \mathrm{i}\gamma_{[i}\Delta_{j]} \right\rangle\right\rangle \frac{B_{T10}(t)}{2m_N} \\
& -\left\langle\left\langle \overline{P}_{[i}\Delta_{j]} \right\rangle\right\rangle \frac{\tilde{A}_{T10}(t)}{m_N^2}
\end{aligned} \tag{C.25}$$

This yields

$$\langle P' \mid \overline{\Psi}_q \mathrm{i}\sigma_{\mu\nu} \Psi_q \mid P\rangle = \left\langle\langle \mathrm{i}\sigma_{\mu\nu}\rangle\right\rangle A_{T10}(t) - \mathrm{i}\left\langle\left\langle \gamma_{[\mu}\Delta_{\nu]} \right\rangle\right\rangle \frac{B_{T10}(t)}{2m_N} - \left\langle\langle 1\rangle\right\rangle \overline{P}_{[\mu}\Delta_{\nu]} \frac{\tilde{A}_{T10}(t)}{m_N^2}\,. \tag{C.26}$$

C.2. GPDs

Moments of GPDs are described with the use of a tower of twist two operators with different Dirac structures:

$$\begin{aligned}
\mathcal{O}_{V,M}^{\mu_1\mu_2\cdots\mu_n} &= S(\mu_1,\ldots,\mu_n)\mathrm{i}^{n-1}\overline{\Psi}_q\gamma_M^{\mu_1}\overleftrightarrow{D}_M^{\mu_2}\cdots\overleftrightarrow{D}_M^{\mu_n}\Psi_q - \text{traces}\\
\mathcal{O}_{A,M}^{\mu_1\mu_2\cdots\mu_n} &= S(\mu_1,\ldots,\mu_n)\mathrm{i}^{n-1}\overline{\Psi}_q\gamma_M^{\mu_1}\gamma_M^5\overleftrightarrow{D}_M^{\mu_2}\cdots\overleftrightarrow{D}_M^{\mu_n}\Psi_q - \text{traces}\\
\mathcal{O}_{T,M}^{\mu\nu\mu_1\cdots\mu_n} &= A(\mu,\nu)S(\nu,\mu_1,\ldots,\mu_n)\mathrm{i}^n\overline{\Psi}_q\mathrm{i}\sigma_M^{\mu\nu}\overleftrightarrow{D}_M^{\mu_1}\cdots\overleftrightarrow{D}_M^{\mu_n}\Psi_q - \text{traces}
\end{aligned} \tag{C.27}$$

where

$$\overleftrightarrow{D}_\mu = \frac{1}{2}\left(\overrightarrow{D}_\mu - \overleftarrow{D}_\mu\right). \tag{C.28}$$

The functions A and S anti-/ symmetrize the indices in their arguments. As an example we have

$$A(\mu,\nu)S(\nu,\rho)T^{\mu\nu\rho} = A(\mu,\nu)\frac{1}{2}\left(T^{\mu\nu\rho}+T^{\mu\rho\nu}\right) = \frac{1}{4}\left(T^{\mu\nu\rho}+T^{\mu\rho\nu}-T^{\nu\mu\rho}-T^{\nu\rho\mu}\right) \tag{C.29}$$

for any tensor T or more concrete

$$\begin{aligned}
A(\mu,\nu)S(\nu,\rho)\sigma_{\mu\nu}\overleftrightarrow{D}^\rho &= A(\mu,\nu)\frac{1}{2}\left(\sigma_{\mu\nu}\overleftrightarrow{D}^\rho + \sigma_{\mu\rho}\overleftrightarrow{D}^\nu\right)\\
&= \frac{1}{2}\left(\sigma_{\mu\nu}\overleftrightarrow{D}^\rho + \frac{1}{2}\left(\sigma_{\mu\rho}\overleftrightarrow{D}^\nu - \sigma_{\nu\rho}\overleftrightarrow{D}^\mu\right)\right),
\end{aligned} \tag{C.30}$$

where we have used that $A(\mu,\nu)\sigma_{\mu\nu} = \sigma_{\mu\nu}$.

The traces need to be subtracted because these terms would correspond to higher twist, and we are interested in leading twist (two) operators from the OPE.

In Euclidean spacetime we define our operators as

$$\begin{aligned}
\mathcal{O}_{V}^{\mu_1\mu_2\cdots\mu_n} &= S(\mu_1,\ldots,\mu_n)\overline{\Psi}_q\gamma^{\mu_1}\overleftrightarrow{D}^{\mu_2}\cdots\overleftrightarrow{D}^{\mu_n}\Psi_q - \text{traces}\,,\\
\mathcal{O}_{A}^{\mu_1\mu_2\cdots\mu_n} &= S(\mu_1,\ldots,\mu_n)\overline{\Psi}_q\gamma^{\mu_1}\gamma_5\overleftrightarrow{D}^{\mu_2}\cdots\overleftrightarrow{D}^{\mu_n}\Psi_q - \text{traces}\,,\\
\mathcal{O}_{T}^{\mu\nu\mu_1\cdots\mu_n} &= A(\mu,\nu)S(\nu,\mu_1,\ldots,\mu_n)\overline{\Psi}_q\mathrm{i}\sigma^{\mu\nu}\overleftrightarrow{D}^{\mu_1}\cdots\overleftrightarrow{D}^{\mu_n}\Psi_q - \text{traces}\,.
\end{aligned} \tag{C.31}$$

Now we have to clarify what subtracting the traces means in this case. We have to take a traceless linear combination of the operators in question and take the same linear combination in the decomposition into Lorentz structures. In the following sections on the decomposition of matrix elements into Lorentz structures the subtraction of traces on both sides of the equations is implicitly understood.

C.2.1. Subtraction of traces

C.2.1.1. Trace subtraction for operators with two indices

The operators with two indices have the following trace-subtracted form

$$\mathcal{O}_{\mu\nu} - \text{traces} = \mathcal{O}_{\mu\nu} - \frac{1}{4}\sum_{\lambda} \mathcal{O}_{\lambda\lambda}\delta_{\mu\nu} \tag{C.32}$$

as a prominent example we can look at

$$\mathcal{O}_V^{44} - \text{traces} = \mathcal{O}_V^{44} - \frac{1}{4}\mathcal{O}_V^{44} - \frac{1}{4}\sum_i \mathcal{O}_V^{ii} = \frac{3}{4}\left(\mathcal{O}_V^{44} - \frac{1}{3}\sum_i \mathcal{O}_V^{ii}\right) = \frac{3}{4}\mathcal{O}_{v_2,b}\,. \tag{C.33}$$

This operator is connected to the expectation value of the momentum fraction carried by a quark $\langle x \rangle$, and it is widely used to extract it from a single ratio. It is symmetric in all the spatial directions. The overall factor is irrelevant as it on the right and left hand side of the equation.

For a system of equations a different set of operators is used. The symmetrization reduces the number of independent index combinations for the operators on the left hand side from 4×4 to 10, and the condition that the operators are traceless further reduces this number to 9.

Upon discretizing spacetime the 9 independent index combinations correspond to two different representations of the hyper-cubic group, one six-dimensional $\tau_3^{(6)}$ ($\mathcal{O}_{v_2,a}$ type: O_V^{12}, O_V^{13}, O_V^{14}, O_V^{23}, O_V^{24} and O_V^{34}) and one three-dimensional $\tau_1^{(3)}$ ($\mathcal{O}_{v_2,b}$ type: $\frac{1}{2}(O_V^{11} + O_V^{22} - O_V^{33} - O_V^{44})$, $\frac{1}{\sqrt{2}}(O_V^{33} - O_V^{44})$ and $\frac{1}{\sqrt{2}}(O_V^{11} - O_V^{22})$) [170].

For the axial GPDs the operators look the "same" but have an additional γ_5 and the representations of the hyper-cubic group can be constructed by multiplying the ones of the vector GPDs by $\tau_4^{(1)}$ and the results are are $\tau_4^{(6)}$($\mathcal{O}_{r_2,a}$ type) and $\tau_4^{(3)}$ ($\mathcal{O}_{r_2,b}$ type).

Furthermore we get different lattice artifacts and renormalization constants for the two representations on the lattice. When we decide to ignore the lattice artifacts we still have to consider the (empirically) small difference between the renormalization constants when solving the whole equation system.

C.2.1.2. Trace subtraction for operators with three indices

First we have to clarify how we can check whether a combination is traceless. We can check that a operator is traceless by contracting it with a Kronecker $\delta_{\mu\nu}$ for each index combination and then demanding they all are individually zero.

A traceless construction of the tensor operators is given by

$$M_{\mu\nu\rho} = \mathcal{O}^T_{\mu\{\nu\rho\}} - \mathcal{O}^T_{\nu\{\mu\rho\}} + \frac{1}{2}\delta_{\mu\rho}\mathcal{O}^T_{\nu\lambda\lambda} - \frac{1}{2}\delta_{\nu\rho}\mathcal{O}^T_{\mu\lambda\lambda}\,. \tag{C.34}$$

This is explicitely antisymmetric in μ and ν and we can see that

$$\begin{aligned} M_{\mu\rho\rho} &= \mathcal{O}^T_{\mu\rho\rho} - \mathcal{O}^T_{\rho\{\mu\rho\}} + \frac{1}{2}\mathcal{O}^T_{\mu\rho\rho} - 2\frac{1}{2}\mathcal{O}^T_{\mu\rho\rho} \\ &= -\frac{1}{2}\mathcal{O}^T_{\mu\rho\rho} - \frac{1}{2}\left(\mathcal{O}^T_{\rho\mu\rho} + \mathcal{O}^T_{\rho\rho\mu}\right) \\ &= -\frac{1}{2}\mathcal{O}^T_{\mu\rho\rho} - \frac{1}{2}\left(-\mathcal{O}^T_{\mu\rho\rho} + 0\right) = 0 \end{aligned} \tag{C.35}$$

and similarly for $M_{\rho\nu\rho}$.

We get 16 independent traceless linear combinations of the tensor GPD operators. They are in the representations $\tau_2^{(8)}$ and $\tau_1^{(8)}$. We take linear combinations of Eq. (C.62) for this index combinations. They then enter the overdetermined system of equations (OSE).

The solution of the OSE depends on the relative weights of these equations. Thus we need to normalize them appropriately, and we use the condition that the coefficient vector has norm 1.

The linear combination

$$2\mathcal{O}^T_{\mu\{\nu\rho\}} + \mathcal{O}^T_{\nu\{\mu\rho\}}\,, \mu < \nu < \rho \tag{C.36}$$

is traceless and can be rewritten as

$$\begin{aligned} 2\mathcal{O}^T_{\mu\{\nu\rho\}} + \mathcal{O}^T_{\nu\{\mu\rho\}} &= \mathcal{O}^T_{\mu\nu\rho} + \mathcal{O}^T_{\mu\rho\nu} + \frac{1}{2}\mathcal{O}^T_{\nu\mu\rho} + \frac{1}{2}\mathcal{O}^T_{\nu\rho\mu} \\ &= \mathcal{O}^T_{\mu\rho\nu} + \frac{1}{2}\mathcal{O}^T_{\mu\nu\rho} + \frac{1}{2}\mathcal{O}^T_{\nu\rho\mu} \end{aligned} \tag{C.37}$$

and thus the correct norm is given by $\sqrt{\frac{2}{3}}$.

We have chosen the following operator combinations:

#	Linear combination	irrep.
0	$\sqrt{\frac{2}{3}}\left(\mathcal{O}^T_{132}+\frac{1}{2}\mathcal{O}^T_{123}+\frac{1}{2}\mathcal{O}^T_{231}\right)$	$\tau_3^{(8)}$
1	$\sqrt{\frac{2}{3}}\left(\mathcal{O}^T_{142}+\frac{1}{2}\mathcal{O}^T_{124}+\frac{1}{2}\mathcal{O}^T_{241}\right)$	$\tau_3^{(8)}$
2	$\sqrt{\frac{2}{3}}\left(\mathcal{O}^T_{143}+\frac{1}{2}\mathcal{O}^T_{134}+\frac{1}{2}\mathcal{O}^T_{341}\right)$	$\tau_3^{(8)}$
3	$\sqrt{\frac{2}{3}}\left(\mathcal{O}^T_{243}+\frac{1}{2}\mathcal{O}^T_{234}+\frac{1}{2}\mathcal{O}^T_{342}\right)$	$\tau_3^{(8)}$
4	$\sqrt{2}\mathcal{O}^T_{2\{13\}}$	$\tau_3^{(8)}$
5	$\sqrt{2}\mathcal{O}^T_{2\{14\}}$	$\tau_3^{(8)}$
6	$\sqrt{2}\mathcal{O}^T_{3\{14\}}$	$\tau_3^{(8)}$
7	$\sqrt{2}\mathcal{O}^T_{3\{24\}}$	$\tau_3^{(8)}$
8	$\sqrt{\frac{1}{2}}\left(\mathcal{O}^T_{122}-\mathcal{O}^T_{133}\right)$	$\tau_1^{(8)}$
9	$\sqrt{\frac{1}{2}}\left(\mathcal{O}^T_{211}-\mathcal{O}^T_{233}\right)$	$\tau_1^{(8)}$
10	$\sqrt{\frac{1}{2}}\left(\mathcal{O}^T_{311}-\mathcal{O}^T_{322}\right)$	$\tau_1^{(8)}$
11	$\sqrt{\frac{1}{2}}\left(\mathcal{O}^T_{411}-\mathcal{O}^T_{422}\right)$	$\tau_1^{(8)}$
12	$\sqrt{\frac{1}{6}}\left(\mathcal{O}^T_{122}+\mathcal{O}^T_{133}-2\mathcal{O}^T_{144}\right)$	$\tau_1^{(8)}$
13	$\sqrt{\frac{1}{6}}\left(\mathcal{O}^T_{211}+\mathcal{O}^T_{233}-2\mathcal{O}^T_{244}\right)$	$\tau_1^{(8)}$
14	$\sqrt{\frac{1}{6}}\left(\mathcal{O}^T_{311}+\mathcal{O}^T_{322}-2\mathcal{O}^T_{344}\right)$	$\tau_1^{(8)}$
15	$\sqrt{\frac{1}{6}}\left(\mathcal{O}^T_{411}+\mathcal{O}^T_{422}-2\mathcal{O}^T_{433}\right)$	$\tau_1^{(8)}$

C.2.2. First moment of the vector GPDs

The first moments of the vector GPDs are given by

$$\begin{aligned}\langle P' \mid \mathcal{O}^{\mu\nu}_{V,M} \mid P\rangle = S(\mu,\nu)\Big(&\left\langle\left\langle\gamma^\mu_M\right\rangle\right\rangle \overline{P}^\nu_M A_{20}(t)\\ &+\left\langle\left\langle \mathrm{i}\sigma^{\mu\alpha}_M\right\rangle\right\rangle \frac{\Delta^M_\alpha \overline{P}^\nu_M}{2m_N} B_{20}(t) + \langle\langle 1\rangle\rangle \frac{\Delta^\mu_M \Delta^\nu_M}{m_N} C_{20}(t)\Big)\end{aligned} \tag{C.38}$$

To describe this in Euclidean spacetime we need to transform our operators

$$\mathcal{O}^{00}_{V,M} = \overline{\Psi}_q \gamma^0_M \mathrm{i}\overleftrightarrow{D}^0_M \Psi_q = -\overline{\Psi}_q \gamma_4 \overleftrightarrow{D}_4 \Psi_q = -\mathcal{O}^{44}_V \tag{C.39}$$

$$\mathcal{O}^{0j}_{V,M} = S(0,j)\overline{\Psi}_q \gamma^0_M \mathrm{i}\overleftrightarrow{D}^j_M \Psi_q = S(4,j)\overline{\Psi}_q \gamma_4 (-\mathrm{i})\overleftrightarrow{D}_j \Psi_q = -\mathrm{i}\mathcal{O}^{4j}_V \tag{C.40}$$

$$\mathcal{O}^{ij}_{V,M} = S(i,j)\overline{\Psi}_q \gamma^i_M \mathrm{i}\overleftrightarrow{D}^j_M \Psi_q = S(i,j)\overline{\Psi}_q \mathrm{i}\gamma_i (-\mathrm{i})\overleftrightarrow{D}_j \Psi_q = \mathcal{O}^{ij}_V \tag{C.41}$$

Plugging this in

$$\begin{aligned}
&\langle P' \mid \mathcal{O}_V^{44} \mid P\rangle = -\langle P' \mid \mathcal{O}_{V,M}^{00} \mid P\rangle = -\Big(\big\langle\big\langle \gamma_M^0 \big\rangle\big\rangle \overline{P}_M^0 A_{20}(t) \\
&+ \big\langle\big\langle \mathrm{i}\sigma_M^{0\alpha} \big\rangle\big\rangle \Delta_\alpha^M \overline{P}_M^0 \frac{B_{20}(t)}{2m_N} + \langle\langle 1\rangle\rangle \frac{\Delta_M^0 \Delta_M^0}{m_N} C_{20}(t)\Big) \\
&= -\langle\langle \gamma_4\rangle\rangle (-\mathrm{i})\overline{P}_4 A_{20}(t) - \langle\langle -\sigma_{0\alpha}\rangle\rangle (-1)\Delta_\alpha (-\mathrm{i})\overline{P}_4 \frac{B_{20}(t)}{2m_N} + \langle\langle 1\rangle\rangle \frac{\Delta_4\Delta_4}{m_N} C_{20}(t) \\
&= \mathrm{i}\langle\langle \gamma_4\rangle\rangle \overline{P}_4 A_{20}(t) + \mathrm{i}\langle\langle \sigma_{0\alpha}\rangle\rangle \Delta_\alpha \overline{P}_4 \frac{B_{20}(t)}{2m_N} + \langle\langle 1\rangle\rangle \frac{\Delta_4\Delta_4}{m_N} C_{20}(t)
\end{aligned} \tag{C.42}$$

$$\begin{aligned}
&\langle P' \mid \mathcal{O}_V^{4j} \mid P\rangle = \mathrm{i}\langle P' \mid \mathcal{O}_{V,M}^{0j} \mid P\rangle = \mathrm{i}S(0,j)\Big(\big\langle\big\langle \gamma_M^0 \big\rangle\big\rangle \overline{P}_M^j A_{20}(t) \\
&+ \big\langle\big\langle \mathrm{i}\sigma_M^{0\alpha} \big\rangle\big\rangle \Delta_\alpha^M \overline{P}_M^j \frac{B_{20}(t)}{2m_N} + \langle\langle 1\rangle\rangle \frac{\Delta_M^0 \Delta_M^j}{m_N} C_{20}(t)\Big) \\
&= \mathrm{i}S(4,j)\Big(\langle\langle \gamma_4\rangle\rangle \overline{P}_j A_{20}(t) \\
&+ \langle\langle (-1)\sigma_{4\alpha}\rangle\rangle (-1)\Delta_\alpha \overline{P}^j \frac{B_{20}(t)}{2m_N} + \langle\langle 1\rangle\rangle \frac{-\mathrm{i}\Delta_4\Delta_j}{m_N} C_{20}(t)\Big) \\
&= S(4,j)\Big(\mathrm{i}\langle\langle \gamma_4\rangle\rangle \overline{P}_j A_{20}(t) + \mathrm{i}\langle\langle \sigma_{4\alpha}\rangle\rangle \Delta_\alpha \overline{P}^j \frac{B_{20}(t)}{2m_N} + \langle\langle 1\rangle\rangle \frac{\Delta_4\Delta_j}{m_N} C_{20}(t)\Big)
\end{aligned} \tag{C.43}$$

$$\begin{aligned}
&\langle P' \mid \mathcal{O}_V^{ij} \mid P\rangle = \langle P' \mid \mathcal{O}_{V,M}^{ij} \mid P\rangle = S(i,j)\Big(\big\langle\big\langle \gamma_M^i \big\rangle\big\rangle \overline{P}_M^j A_{20}(t) \\
&+ \big\langle\big\langle \mathrm{i}\sigma_M^{i\alpha} \big\rangle\big\rangle \Delta_\alpha^M \overline{P}_M^j \frac{B_{20}(t)}{2m_N} + \langle\langle 1\rangle\rangle \frac{\Delta_M^i \Delta_M^j}{m_N} C_{20}(t)\Big) \\
&= S(i,j)\Big(\langle\langle \mathrm{i}\gamma_i\rangle\rangle \overline{P}_j A_{20}(t) + \Big\{\sum_{a=1}^{3} \langle\langle -\mathrm{i}\sigma_{ia}\rangle\rangle (-1)\Delta_a \\
&+ \big\langle\big\langle -\sigma^{i4} \big\rangle\big\rangle (-\mathrm{i})\Delta_4\Big\}\overline{P}_j \frac{B_{20}(t)}{2m_N} + \langle\langle 1\rangle\rangle \frac{\Delta_i\Delta_j}{m_N} C_{20}(t)\Big) \\
&= S(i,j)\Big(\mathrm{i}\langle\langle \gamma_i\rangle\rangle \overline{P}_j A_{20}(t) + \mathrm{i}\langle\langle \sigma_{i\alpha}\rangle\rangle \Delta_\alpha \overline{P}_j \frac{B_{20}(t)}{2m_N} + \langle\langle 1\rangle\rangle \frac{\Delta_i\Delta_j}{m_N} C_{20}(t)\Big)
\end{aligned} \tag{C.44}$$

In total this gives

$$\begin{aligned}
\langle P' \mid \mathcal{O}_V^{\mu\nu} \mid P\rangle = S(\mu,\nu)\Big(&\mathrm{i}\langle\langle \gamma_\mu\rangle\rangle \overline{P}_\nu A_{20}(t) \\
&+ \mathrm{i}\langle\langle \sigma_{\mu\alpha}\rangle\rangle \Delta_\alpha \overline{P}_\nu \frac{B_{20}(t)}{2m_N} + \langle\langle 1\rangle\rangle \frac{\Delta_\mu\Delta_\nu}{m_N} C_{20}(t)\Big)
\end{aligned} \tag{C.45}$$

We have successfully computed the expressions for continuum Euclidean spacetime.

C.2.3. First moment of the axial vector GPDs

The first moments of the axial vector GPDs are given by

$$\langle P' \mid \mathcal{O}^{\mu\nu}_{A,M} \mid P\rangle = S(\mu,\nu)\Big(\big\langle\big\langle\gamma^\mu_M\gamma^5_M\big\rangle\big\rangle\,\overline{P}^\nu_M\tilde{A}_{20}(t) + \big\langle\big\langle\gamma^5_M\big\rangle\big\rangle\,\frac{\Delta^\mu_M\overline{P}^\nu_M}{2m_N}\tilde{B}_{20}(t)\Big)\,. \tag{C.46}$$

To describe this in Euclidean spacetime we need to transform our operators

$$\mathcal{O}^{00}_{A,M} = \overline{\Psi}_q\gamma^0_M\gamma^M_5\mathrm{i}\overleftrightarrow{D}^0_M\Psi_q = \overline{\Psi}_q\gamma_4(-1)\gamma_5\mathrm{i}\mathrm{i}\overleftrightarrow{D}_4\Psi_q = \mathcal{O}^{44}_A \tag{C.47}$$

$$\mathcal{O}^{0j}_{A,M} = S(0,j)\overline{\Psi}_q\gamma^0_M\gamma^M_5\mathrm{i}\overleftrightarrow{D}^j_M\Psi_q = S(4,j)\overline{\Psi}_q\gamma_4(-1)\gamma_5(-\mathrm{i})\overleftrightarrow{D}_j\Psi_q = \mathrm{i}\mathcal{O}^{4j}_A \tag{C.48}$$

$$\mathcal{O}^{ij}_{A,M} = S(i,j)\overline{\Psi}_q\gamma^i_M\gamma^M_5\mathrm{i}\overleftrightarrow{D}^j_M\Psi_q = S(i,j)\overline{\Psi}_q\mathrm{i}\gamma_i(-1)\gamma_5(-\mathrm{i})\overleftrightarrow{D}_j\Psi_q = -\mathcal{O}^{ij}_A \tag{C.49}$$

Now we can write down the three different equations:

$$\begin{aligned}
&\langle P' \mid \mathcal{O}^{44}_A \mid P\rangle = \langle P' \mid \mathcal{O}^{00}_{A,M} \mid P\rangle = \big\langle\big\langle\gamma^0_M\gamma^5_M\big\rangle\big\rangle\,\overline{P}^0_M\tilde{A}_{20}(t) + \big\langle\big\langle\gamma^5_M\big\rangle\big\rangle\,\frac{\Delta^0_M\overline{P}^0_M}{2m_N}\tilde{B}_{20}(t)\\
&= \big\langle\big\langle\gamma_4(-1)\gamma_5\big\rangle\big\rangle\,(-\mathrm{i})\overline{P}_4\tilde{A}_{20}(t) + (-1)\,\big\langle\big\langle\gamma_5\big\rangle\big\rangle\,\frac{(-\mathrm{i})\Delta_4(-\mathrm{i})\overline{P}_4}{2m_N}\tilde{B}_{20}(t)\\
&= \mathrm{i}\,\big\langle\big\langle\gamma_4\gamma_5\big\rangle\big\rangle\,\overline{P}_4\tilde{A}_{20}(t) + \big\langle\big\langle\gamma_5\big\rangle\big\rangle\,\frac{\Delta_4\overline{P}_4}{2m_N}\tilde{B}_{20}(t)
\end{aligned} \tag{C.50}$$

$$\begin{aligned}
&\langle P' \mid \mathcal{O}^{4j}_A \mid P\rangle = -\mathrm{i}\langle P' \mid \mathcal{O}^{0j}_{A,M} \mid P\rangle\\
&= -\mathrm{i}S(0,j)\Big(\big\langle\big\langle\gamma^0_M\gamma^5_M\big\rangle\big\rangle\,\overline{P}^j_M\tilde{A}_{20}(t) + \big\langle\big\langle\gamma^5_M\big\rangle\big\rangle\,\frac{\Delta^0_M\overline{P}^j_M}{2m_N}\tilde{B}_{20}(t)\Big)\\
&= -\mathrm{i}S(4,j)\Big(\big\langle\big\langle\gamma_4(-1)\gamma_5\big\rangle\big\rangle\,\overline{P}_j\tilde{A}_{20}(t) + (-1)\,\big\langle\big\langle\gamma_5\big\rangle\big\rangle\,\frac{(-\mathrm{i})\Delta_4\overline{P}_j}{2m_N}\tilde{B}_{20}(t)\Big)\\
&= S(4,j)\Big(\mathrm{i}\,\big\langle\big\langle\gamma_4\gamma_5\big\rangle\big\rangle\,\overline{P}_j\tilde{A}_{20}(t) + \big\langle\big\langle\gamma_5\big\rangle\big\rangle\,\frac{\Delta_4\overline{P}_4}{2m_N}\tilde{B}_{20}(t)\Big)
\end{aligned} \tag{C.51}$$

$$\begin{aligned}
&\langle P' \mid \mathcal{O}^{ij}_A \mid P\rangle = -\langle P' \mid \mathcal{O}^{ij}_{A,M} \mid P\rangle\\
&= -S(i,j)\Big(\big\langle\big\langle\gamma^i_M\gamma^5_M\big\rangle\big\rangle\,\overline{P}^j_M\tilde{A}_{20}(t) + \big\langle\big\langle\gamma^5_M\big\rangle\big\rangle\,\frac{\Delta^i_M\overline{P}^j_M}{2m_N}\tilde{B}_{20}(t)\Big)\\
&= -S(i,j)\Big(\big\langle\big\langle\mathrm{i}\gamma_j(-1)\gamma_5\big\rangle\big\rangle\,\overline{P}_j\tilde{A}_{20}(t) + (-1)\,\big\langle\big\langle\gamma_5\big\rangle\big\rangle\,\frac{\Delta_j\overline{P}_j}{2m_N}\tilde{B}_{20}(t)\Big)\\
&= S(i,j)\Big(\mathrm{i}\,\big\langle\big\langle\gamma_4\gamma_5\big\rangle\big\rangle\,\overline{P}_j\tilde{A}_{20}(t) + \big\langle\big\langle\gamma_5\big\rangle\big\rangle\,\frac{\Delta_4\overline{P}_4}{2m_N}\tilde{B}_{20}(t)\Big)
\end{aligned} \tag{C.52}$$

So we finally arrive at

$$\langle P' \mid \mathcal{O}_A^{\mu\nu} \mid P\rangle = S(\mu,\nu)\Big(\mathrm{i}\,\langle\langle\gamma_\mu\gamma_5\rangle\rangle\,\overline{P}_\nu\tilde{A}_{20}(t) + \langle\langle\gamma_5\rangle\rangle\,\frac{\Delta_\mu\overline{P}_\nu}{2m_N}\tilde{B}_{20}(t)\Big) \tag{C.53}$$

C.2.4. First moment of the tensor GPDs

The first moments of the tensor vector GPDs in Minkowski spacetime are given by

$$\begin{aligned}\langle P' \mid \mathcal{O}_{T,M}^{\mu\nu\rho} \mid P\rangle = A(\mu,\nu)S(\nu,\rho)\Big(&\big\langle\big\langle\mathrm{i}\sigma_M^{\mu\nu}\big\rangle\big\rangle\,\overline{P}_M^\rho A_{T20}(t) + \Big\langle\Big\langle\gamma_M^{[\mu}\Delta_M^{\nu]}\Big\rangle\Big\rangle\,\frac{\overline{P}_M^\rho}{2m_N}B_{T20}(t)\\ &+ \langle\langle 1\rangle\rangle\,\frac{\overline{P}_M^{[\mu}\Delta_M^{\nu]}}{m_N^2}\overline{P}_M^\rho\tilde{A}_{T20}(t) + \Big\langle\Big\langle\gamma_M^{[\mu}\overline{P}_M^{\nu]}\Big\rangle\Big\rangle\,\frac{\Delta_M^\rho}{m_N}\tilde{B}_{T21}(t)\Big).\end{aligned} \tag{C.54}$$

To describe this in Euclidean spacetime we need to transform our operators

$$\begin{aligned}\mathcal{O}_{T,M}^{0j0} &= A(0,j)S(j,0)\overline{\Psi}_q\mathrm{i}\sigma_M^{0j}\mathrm{i}\overleftrightarrow{D}_M^0\Psi_q = A(4,j)S(j,4)\overline{\Psi}_q\mathrm{ii}\sigma_{4j}\mathrm{i}\overleftrightarrow{D}_4\Psi_q\\ &= A(4,j)S(j,4)\overline{\Psi}_q\sigma_{4j}\overleftrightarrow{D}_4\Psi_q = -\mathrm{i}\mathcal{O}_T^{0j0} &\text{(C.55)}\\ \mathcal{O}_{T,M}^{0ij} &= A(0,j)S(i,j)\overline{\Psi}_q\mathrm{i}\sigma_M^{0i}\mathrm{i}\overleftrightarrow{D}_M^j\Psi_q = A(4,i)S(i,j)\overline{\Psi}_q\mathrm{ii}\sigma_{4i}\mathrm{i}(-1)\overleftrightarrow{D}_j\Psi_q\\ &= A(4,i)S(i,j)\overline{\Psi}_q\mathrm{i}\sigma_{4i}\overleftrightarrow{D}_j\Psi_q = \mathcal{O}_T^{0ij} &\text{(C.56)}\\ \mathcal{O}_{T,M}^{ij0} &= A(i,j)S(j,0)\overline{\Psi}_q\mathrm{i}\sigma_M^{ij}\mathrm{i}\overleftrightarrow{D}_M^0\Psi_q = A(i,j)S(j,4)\overline{\Psi}_q\mathrm{i}(-1)\sigma_{ij}\mathrm{ii}\overleftrightarrow{D}_4\Psi_q\\ &= \mathcal{O}_T^{ij0} &\text{(C.57)}\\ \mathcal{O}_{T,M}^{ijk} &= A(i,j)S(j,k)\overline{\Psi}_q\mathrm{i}\sigma_M^{ij}\mathrm{i}\overleftrightarrow{D}_M^k\Psi_q = A(i,j)S(j,k)\overline{\Psi}_q\mathrm{i}(-1)\sigma_{ij}\mathrm{i}(-1)\overleftrightarrow{D}_k\Psi_q\\ &= \mathrm{i}\mathcal{O}_T^{ijk} &\text{(C.58)}\end{aligned}$$

We split the terms for easier readability:

$$\begin{aligned}\mathrm{i}\sigma_M^{0j}\overline{P}_M^0 &= \mathrm{ii}\sigma_{4j}(-\mathrm{i})\overline{P}_0 = \mathrm{i}\sigma_{4j}\overline{P}_0 & \mathrm{i}\sigma_M^{0i}\overline{P}_M^j &= \mathrm{ii}\sigma_{4j}\overline{P}_j = -\sigma_{4j}\overline{P}_0\\ \mathrm{i}\sigma_M^{ij}\overline{P}_M^0 &= \mathrm{i}(-1)\sigma_{ij}(-\mathrm{i})\overline{P}_0 = -\sigma_{ij}\overline{P}_0 & \mathrm{i}\sigma_M^{ij}\overline{P}_M^k &= \mathrm{i}(-1)\sigma_{ij}\overline{P}_j = -\mathrm{i}\sigma_{ij}\overline{P}_j\end{aligned} \tag{C.59}$$

Compared to the transformations of the operators this yields a factor of -1.

$$\begin{aligned}\gamma_M^{[0}\Delta_M^{j]}\overline{P}_M^0 &= \gamma_{[4}\Delta_{j]}(-\mathrm{i})\overline{P}_0 = -\mathrm{i}\gamma_{[4}\Delta_{j]}\overline{P}_0 & \gamma_M^{[0}\Delta_M^{j]}\overline{P}_M^j &= \gamma_{[4}\Delta_{j]}\overline{P}_j\\ \gamma_M^{[i}\Delta_M^{j]}\overline{P}_M^0 &= \mathrm{i}\gamma_{[i}\Delta_{j]}(-\mathrm{i})\overline{P}_0 = \gamma_{[i}\Delta_{j]}\overline{P}_0 & \gamma_M^{[i}\Delta_M^{j]}\overline{P}_M^k &= \mathrm{i}\gamma_{[i}\Delta_{j]}\overline{P}_j\end{aligned} \tag{C.60}$$

Compared to the transformations of the operators this yields a factor of 1.

$$\overline{P}^{[0}_M \Delta^{j]}_M \overline{P}^0_M = (-\mathrm{i})\overline{P}_{[4}\Delta_{j]}(-\mathrm{i})\overline{P}_4 = -\overline{P}_{[4}\Delta_{j]}\overline{P}_4 \qquad \overline{P}^{[0}_M \Delta^{j]}_M \overline{P}^j_M = -\mathrm{i}\overline{P}_{[4}\Delta_{j]}\overline{P}_j$$
$$\overline{P}^{[i}_M \Delta^{j]}_M \overline{P}^0_M = \overline{P}_{[i}\Delta_{j]}(-\mathrm{i})\overline{P}_4 = -\mathrm{i}\overline{P}_{[i}\Delta_{j]}\overline{P}_4 \qquad \overline{P}^{[i}_M \Delta^{j]}_M \overline{P}^k_M = \overline{P}_{[i}\Delta_{j]}\overline{P}_k \tag{C.61}$$

Compared to the transformations of the operators this yields a factor of $-\mathrm{i}$.
The fourth term in Eq. (C.54) transforms like the second term. So all in all we obtain:

$$\begin{aligned}\langle P' \mid \mathcal{O}^{\mu\nu\rho}_T \mid P\rangle = A(\mu,\nu)S(\nu,\rho)\Big(&-\langle\langle\sigma_{\mu\nu}\rangle\rangle\,\overline{P}_\rho A_{T20}(t) + \left\langle\left\langle\gamma_{[\mu}\Delta_{\nu]}\right\rangle\right\rangle \frac{\overline{P}^\rho}{2m_N} B_{T20}(t)\\ &-\mathrm{i}\,\langle\langle 1\rangle\rangle\,\frac{\overline{P}_{[\mu}\Delta_{\nu]}}{m_N^2}\overline{P}_\rho \tilde{A}_{T20}(t) + \left\langle\left\langle\gamma_{[\mu}\overline{P}_{\nu]}\right\rangle\right\rangle \frac{\Delta_\rho}{m_N}\tilde{B}_{T21}(t)\Big)\,.\end{aligned} \tag{C.62}$$

C.3. Equation system size for different (generalized) form factors

The number of equations we have available to extract the form factors at a given virtuality depends on the number of insertion and sink momenta we compute. As the stochastic estimation method allows to compute more sink momenta and polarizations at fixed cost, we compare the number of equations we have available at the parameters we have used in Section 6.2.3 there with what one would get in a typical sequential source analysis, e.g., performed in Section 6.2.4 for comparison with the stochastic method.
In Table C.1 and Table C.2 we abbreviate the different types of form factors with the type of operator we insert. The kinematics were abbreviated with the squared three-momenta in lattice units.
In our example we find that for the stochastic method in each channel at least 25 times more ratios can be analyzed.

$\vec{p}_i^{\,2} \leftrightarrows \vec{p}_f^{\,2}\,,\,\vec{q}^{\,2}$	$\mathbb{1}$	γ_μ	$\gamma_\mu\gamma_5$	$\sigma_{\mu\nu}$	$\overleftrightarrow{D}_\mu\gamma_\nu$	$\overleftrightarrow{D}_\mu\gamma_\nu\gamma_5$	$\overleftrightarrow{D}_\mu\sigma_{\nu\rho}$
$0 \leftrightarrows 0\,,0$	1	1	1	1	2	1	2
$1 \leftrightarrows 0\,,1$	6	16	8	16	30	12	40
$2 \leftrightarrows 0\,,2$	12	52	28	60	104	60	160

Table C.1 Continued on next page.

$\vec{p}_i^{\,2} \leftrightarrows \vec{p}_f^{\,2}$, $\vec{q}^{\,2}$	$\mathbb{1}$	γ_μ	$\gamma_\mu\gamma_5$	$\sigma_{\mu\nu}$	$\overleftrightarrow{D}_\mu\gamma_\nu$	$\overleftrightarrow{D}_\mu\gamma_\nu\gamma_5$	$\overleftrightarrow{D}_\mu\sigma_{\nu\rho}$
$3 \leftrightarrows 0$,3	8	48	32	64	104	64	184
$4 \leftrightarrows 0$,4	6	16	8	16	30	12	40
$5 \leftrightarrows 0$,5	24	104	56	120	224	120	328
$6 \leftrightarrows 0$,6	24	144	96	192	344	208	592
total	81	381	229	469	838	477	1346

Table C.1.: Number of equations for generalized form factors, $\mathcal{P}^u_+$ and $\mathcal{P}^z_+$, $\vec{p}_f^{\,2} = 0$, $\vec{q}^{\,2} \leq 6 \cdot (\frac{2\pi}{L})^2$.

$\vec{p}_i^{\,2} \leftrightarrows \vec{p}_f^{\,2}$, $\vec{q}^{\,2}$	$\mathbb{1}$	γ_μ	$\gamma_\mu\gamma_5$	$\sigma_{\mu\nu}$	$\overleftrightarrow{D}_\mu\gamma_\nu$	$\overleftrightarrow{D}_\mu\gamma_\nu\gamma_5$	$\overleftrightarrow{D}_\mu\sigma_{\nu\rho}$
$[0-4] \leftrightarrows [0-4]$, 0	33	93	231	291	178	479	774
$1 \leftrightarrows 4$, 1	12	48	48	72	92	88	172
$0 \leftrightarrows 1$, 1	12	48	48	72	92	88	172
$1 \leftrightarrows 2$, 1	96	384	384	576	864	864	1536
$2 \leftrightarrows 3$, 1	144	672	672	1056	1584	1584	2912
$0 \leftrightarrows 2$, 2	24	168	168	264	384	360	704
$1 \leftrightarrows 3$, 2	144	672	672	1056	1584	1584	2912
$2 \leftrightarrows 4$, 2	96	384	384	576	864	864	1536
$2 \leftrightarrows 2$, 2	240	960	912	1344	2080	2128	3664
$0 \leftrightarrows 3$, 3	16	160	192	288	432	416	832
$1 \leftrightarrows 2$, 3	144	672	672	1056	1584	1584	2912
$3 \leftrightarrows 4$, 3	144	672	672	1056	1584	1584	2912
$0 \leftrightarrows 4$, 4	12	48	48	72	92	88	172
$3 \leftrightarrows 3$, 4	126	354	354	480	692	706	1154
$1 \leftrightarrows 4$, 5	96	384	384	576	864	864	1536
$2 \leftrightarrows 3$, 5	384	1440	1344	2304	3360	3328	6096
$1 \leftrightarrows 3$, 6	144	672	672	1056	1488	1488	2912
$2 \leftrightarrows 4$, 6	144	672	672	1056	1584	1584	2912
$2 \leftrightarrows 2$, 6	192	672	672	1152	1600	1568	2912
total	2299	9559	9585	14979	21770	21953	40268

Table C.2.: Number of equations for generalized form factors, all polarizations, $\vec{p}_i^{\,2}, \vec{p}_f^{\,2} \leq 4 \cdot (\frac{2\pi}{L})^2$, $\vec{q}^{\,2} \leq 6 \cdot (\frac{2\pi}{L})^2$.

D
Bibliography

[1] S. Glashow, "Partial Symmetries of Weak Interactions," *Nucl.Phys.* **22** (1961) 579–588.

S. Weinberg, "A Model of Leptons," *Phys.Rev.Lett.* **19** (1967) 1264–1266.

A. Salam, "Weak and Electromagnetic Interactions," *Conf.Proc.* **C680519** (1968) 367–377.

[2] M. Gell-Mann, "A Schematic Model of Baryons and Mesons," *Phys.Lett.* **8** (1964) 214–215.

G. Zweig, "An SU(3) model for strong interaction symmetry and its breaking. Version 1,".

H. Fritzsch, M. Gell-Mann, and H. Leutwyler, "Advantages of the Color Octet Gluon Picture," *Phys.Lett.* **B47** (1973) 365–368.

[3] D. J. Gross and F. Wilczek, "Ultraviolet Behavior of Nonabelian Gauge Theories," *Phys.Rev.Lett.* **30** (1973) 1343–1346.

H. D. Politzer, "Reliable Perturbative Results for Strong Interactions?," *Phys.Rev.Lett.* **30** (1973) 1346–1349.

[4] G. 't Hooft, "Renormalizable Lagrangians for Massive Yang-Mills Fields," *Nucl.Phys.* **B35** (1971) 167–188.

[5] J. Ellis and T. You, "Updated Global Analysis of Higgs Couplings," 1303.3879.

[6] L. B. Okun, "The theory of weak interaction," in *1962 International Conference on High-Energy Physics at CERN*, J. Prentki, ed., p. 845. 1962.

[7] K. G. Wilson, "Confinement of Quarks," *Phys.Rev.* **D10** (1974) 2445–2459.

[8] S. Dürr, Z. Fodor, J. Frison, C. Hoelbling, R. Hoffmann, S. D. Katz, S. Krieg, T. Kurth, L. Lellouch, T. Lippert, K. K. Szabo, and G. Vulvert, "Ab-initio Determination of Light Hadron Masses," *Science* **322:1224-1227,2008** (June, 2009) 0906.3599.

[9] **European Muon Collaboration** Collaboration, J. Ashman *et al.*, "A Measurement of the Spin Asymmetry and Determination of the Structure Function g(1) in Deep Inelastic Muon-Proton Scattering," *Phys.Lett.* **B206** (1988) 364.

European Muon Collaboration Collaboration, J. Ashman *et al.*, "An Investigation of the Spin Structure of the Proton in Deep Inelastic Scattering of Polarized Muons on Polarized Protons," *Nucl.Phys.* **B328** (1989) 1.

[10] A. V. Belitsky and A. V. Radyushkin, "Unraveling hadron structure with generalized parton distributions," *Phys.Rept.* **418:1-387,2005** (Phys.Rept.418:1-387,2005) hep-ph/0504030.

[11] X. Ji, "Off-Forward Parton Distributions," *J.Phys.G* **24:1181-1205,1998** (J.Phys.G24:1181-1205,1998) hep-ph/9807358.

[12] **HERMES collaboration** Collaboration, A. Airapetian *et al.*, "Separation of contributions from deeply virtual Compton scattering and its interference with the Bethe-Heitler process in measurements on a hydrogen target," *JHEP* **0911** (2009) 083, 0909.3587.

[13] J. I. Friedman, H. W. Kendall, and R. E. Taylor, "Deep inelastic scattering: Acknowledgments," *Rev. Mod. Phys.* **63** (Jul, 1991) 629–629.

[14] A. V. Manohar, "An Introduction to Spin Dependent Deep Inelastic Scattering," hep-ph/9204208.

[15] T. Muta, *Foundations of Quantum Chromodynamics: An Introduction to Perturbative Methods in Gauge Theories*. World Scientific lecture notes in physics. World Scientific, 2010.

[16] D. J. Gross and F. Wilczek, "Asymptotically Free Gauge Theories. I," *Phys. Rev. D* **8** (1973) 3633–3652.

D. J. Gross and F. Wilczek, "Asymptotically free gauge theories. II," *Phys. Rev. D* **9** (1974) 980–993.

[17] N. Christ, B. Hasslacher, and A. H. Mueller, "Light-Cone Behavior of Perturbation Theory," *Phys. Rev. D* **6** (Dec, 1972) 3543–3562.

[18] R. Jaffe and X.-D. Ji, "Chiral odd parton distributions and polarized Drell-Yan," *Phys.Rev.Lett.* **67** (1991) 552–555.

[19] J. D. Bjorken, "Asymptotic Sum Rules at Infinite Momentum," *Phys. Rev.* **179** (Mar, 1969) 1547–1553.

[20] J. C. Collins, "Fragmentation of transversely polarized quarks probed in transverse momentum distributions," *Nucl.Phys.* **B396** (1993) 161–182, hep-ph/9208213.

[21] C. A. Aidala, S. D. Bass, D. Hasch, and G. K. Mallot, "The Spin Structure of the Nucleon," *Rev.Mod.Phys.* **85** (2013) 655–691, 1209.2803.

[22] P. Hägler, "Hadron structure from lattice quantum chromodynamics," 0912.5483.

[23] P. Hägler, "Form factor decomposition of generalized parton distributions at leading twist," *Phys.Lett. B* **594** (2004) 164–170, hep-ph/0404138.

[24] M. Diehl and P. Hägler, "Spin densities in the transverse plane and generalized transversity distributions," *Eur.Phys.J.C* **44:87-101,2005** (Eur.Phys.J.C44:87-101,2005) hep-ph/0504175.

[25] J. Ellis, K. A. Olive, and P. Sandick, "Update on the Direct Detection of Dark Matter in MSSM Models with Non-Universal Higgs Masses," *New J. Phys.* **11** (2009) 105015, 0905.0107.

[26] G. S. Bali, S. Collins, M. Göckeler, R. Horsley, Y. Nakamura, A. Nobile, D. Pleiter, P. E. L. Rakow, A. Schäfer, G. Schierholz, A. Sternbeck, and J. M. Zanotti, "The strange and light quark contributions to the nucleon mass from Lattice QCD," *Phys. Rev. D* **85** (Nov., 2011) 054502, 1111.1600.

[27] P. Junnarkar and A. Walker-Loud, "The Scalar Strange Content of the Nucleon from Lattice QCD," 1301.1114.

[28] G. Bali, P. Bruns, S. Collins, M. Deka, B. Gläßle, *et al.*, "Nucleon mass and sigma term from lattice QCD with two light fermion flavors," *Nucl.Phys.* **B866** (2013) 1, 1206.7034.

[29] G. Bali, S. Collins, B. Gläßle, M. Göckeler, J. Najjar, *et al.*, "Nucleon generalized form factors and sigma term from lattice QCD near the physical quark mass," 1312.0828.

[30] P. E. Shanahan, A. W. Thomas, and R. D. Young, "Scale setting, sigma terms and the Feynman-Hellman theorem," *PoS LATTICE* **2012** (Jan., 2013) 165, 1301.3231.

[31] S. Collins, M. Göckeler, P. Hägler, R. Horsley, Y. Nakamura, A. Nobile, D. Pleiter, P. E. L. Rakow, A. Schäfer, G. Schierholz, W. Schroers, H. Stüben, F. Winter, and J. M. Zanotti, "Dirac and Pauli form factors from lattice QCD," 1106.3580.

[32] A. Antognini, F. Nez, K. Schuhmann, F. D. Amaro, F. Biraben, *et al.*, "Proton Structure from the Measurement of $2S - 2P$ Transition Frequencies of Muonic Hydrogen," *Science* **339** (2013) 417–420.

J. C. Bernauer, P. Achenbach, C. A. Gayoso, R. Böhm, D. Bosnar, L. Debenjak, M. O. Distler, L. Doria, A. Esser, H. Fonvieille, J. M. Friedrich, J. Friedrich, M. G. R. de la Paz, M. Makek, H. Merkel, D. G. Middleton, U. Müller, L. Nungesser, J. Pochodzalla, M. Potokar, S. S. Majos, B. S. Schlimme, S. Širca, T. Walcher, and M. Weinriefer, "High-precision determination of the electric and magnetic form factors of the proton," *Phys.Rev.Lett.* **105:242001,2010** (July, 2010) 1007.5076.

[33] S. G. Karshenboim, "Recent progress in determination of fundamental constants and fundamental physics at low energies," *Annalen Phys.* **525** (2013), no. 7, 472–483.

[34] M. Lin, "Nucleon Form Factors with 2+1 Flavors of Domain Wall Fermions and All-Mode-Averaging," *PoS LATTICE* **2013,** (Jan., 2014) 275, 1401.1476.

[35] **QCDSF collaboration** Collaboration, M. Göckeler, T. R. Hemmert, R. Horsley, D. Pleiter, P. E. L. Rakow, A. Schäfer, and G. Schierholz, "Nucleon electromagnetic form factors on the lattice and in chiral effective field theory," *Phys. Rev. D* **71** (2005) 034508.

[36] J. V. Steele, H. Yamagishi, and I. Zahed, "The Pion-Nucleon Sigma Term and the Goldberger-Treiman Discrepancy," hep-ph/9512233.

[37] M. L. Goldberger and S. B. Treiman, "Form Factors in β Decay and μ Capture," *Phys. Rev.* **111** (Jul, 1958) 354–361.

[38] T. Gorringe and H. W. Fearing, "Induced pseudoscalar coupling of the proton weak interaction," *Rev.Mod.Phys.* **76:31-91,2004** (Rev.Mod.Phys.76:31-91,2004) nucl-th/0206039.

[39] M. Deka, T. Doi, Y. Yang, B. Chakraborty, S. Dong, *et al.*, "A Lattice Study of Quark and Glue Momenta and Angular Momenta in the Nucleon," 1312.4816.

[40] **QCDSF Collaboration** Collaboration, G. S. Bali *et al.*, "Strangeness Contribution to the Proton Spin from Lattice QCD," *Phys.Rev.Lett.* **108** (2012) 222001, 1112.3354.

QCDSF Collaboration Collaboration, G. Bali *et al.*, "A lattice study of the strangeness content of the nucleon," *Prog.Part.Nucl.Phys.* **67** (2012) 467–472, 1112.0024.

QCDSF Collaboration Collaboration, G. Bali, S. Collins, and A. Schäfer, "Strangeness and charm content of the nucleon," *PoS* **LAT2009** (2009) 149, 0911.2407.

G. Bali, S. Collins, and A. Schäfer, "Hunting for the strangeness content of the nucleon," *PoS* **LATTICE2008** (2008) 161, 0811.0807.

[41] R. Jaffe and A. Manohar, "The G(1) Problem: Fact and Fantasy on the Spin of the Proton," *Nucl.Phys.* **B337** (1990) 509–546.

[42] X. Ji, J.-H. Zhang, and Y. Zhao, "Physics of Gluon Helicity Contribution to Proton Spin," *Phys.Rev.Lett.* **111,** (Apr., 2013) 112002, 1304.6708.

[43] C. Lorcé, "The nucleon spin decomposition: news and experimental implications," 1401.3954.

[44] E. Leader and C. Lorcé, "The angular momentum controversy: What's it all about and does it matter?," 1309.4235.

[45] M. Burkardt, "The Nucleon Spin Sum Rule," 1304.0281.

[46] J. Soffer, "Positivity Constraints for Spin-Dependent Parton Distributions," *Phys.Rev.Lett.* **74:1292-1294,1995** (Phys.Rev.Lett.74:1292-1294,1995) hep-ph/9409254.

[47] C. Alexandrou, M. Constantinou, K. Jansen, G. Koutsou, and H. Panagopoulos, "Nucleon transversity generalized form factors with twisted mass fermions," 1311.4670.

[48] **QCDSF Collaboration, UKQCD Collaboration** Collaboration, R. Horsley *et al.*, "A Lattice Study of the Glue in the Nucleon," *Phys.Lett.* **B714** (2012) 312–316, 1205.6410.

[49] J. Gasser and H. Leutwyler, "Chiral perturbation theory to one loop," *Ann. Phys.* **158** (1984) 142.

[50] M. Creutz, *Quarks, Gluons and Lattices (Cambridge Monographs on Mathematical Physics)*. Cambridge University Press, 1985.

I. Montvay and G. Münster, *Quantum Fields on a Lattice (Cambridge Monographs on Mathematical Physics)*. Cambridge University Press, 1997.

[51] R. Gupta, "Introduction to lattice QCD," hep-lat/9807028.

[52] H. J. Rothe, *Lattice Gauge Theories: An Introduction (World Scientific Lecture Notes in Physics)*. World Scientific Publishing Company, 2005.

[53] T. Degrand and C. DeTar, *Lattice Methods for Quantum Chromodynamics*. World Scientific Publishing Company, 2006.

[54] C. Gattringer and C. B. Lang, *Quantum Chromodynamics on the Lattice*. Springer Series: Lecture Notes in Physics , Vol. 788, 2010.

[55] T.-P. Cheng and L.-F. Li, *Gauge Theory of elementary particle physics*. Oxford University Press, USA, 1988.

[56] N. Metropolis and S. Ulam, "The Monte Carlo Method," *Journal of the American Statistical Association* **44** (1949), no. 247, 335.

[57] **QCDSF** Collaboration, A. Ali Khan *et al.*, "Accelerating the hybrid Monte Carlo algorithm," *Phys. Lett.* **B564** (2003) 235, hep-lat/0303026.

[58] G. Bali and J. Najjar, "Gluonic observables in $N_f = 2$ lattice QCD: topology, r_0 and w_0 (in preparation)," *unpublished* (2014).

[59] K. Symanzik, "Continuum Limit and Improved Action in Lattice Theories. 1. Principles and phi**4 Theory," *Nucl. Phys.* **B226** (1983) 187.

[60] M. Lüscher and P. Weisz, "On-Shell Improved Lattice Gauge Theories," *Commun.Math.Phys.* **97** (1985) 59.

[61] H. Lehmann, "On the Properties of propagation functions and renormalization contants of quantized fields," *Nuovo Cim.* **11** (1954) 342.

[62] S. L. Adler, "Axial vector vertex in spinor electrodynamics," *Phys. Rev.* **177** (1969) 2426.

J. S. Bell and R. Jackiw, "A PCAC puzzle: pi0 $\to$ gamma gamma in the sigma model," *Nuovo Cim.* **A60** (1969) 47.

[63] L. H. Karsten and J. Smit, "Lattice Fermions: Species Doubling, Chiral Invariance, and the Triangle Anomaly," *Nucl. Phys.* **B183** (1981) 103.

[64] B. Sheikholeslami and R. Wohlert, "Improved Continuum Limit Lattice Action for QCD with Wilson Fermions," *Nucl. Phys.* **B259** (1985) 572.

[65] K. Jansen and R. Sommer, "O(a) improvement of lattice QCD with two flavors of Wilson quarks," *Nucl.Phys. B* **530** (1998) 185–203;Erratum–ibid.B643(2002)517–518, hep-lat/9803017.

[66] C. Gattringer, I. Hip, and C. B. Lang, "Approximate Ginsparg-Wilson fermions: A first test," *Nucl.Phys. B* **597** (2001) 451, hep-lat/0007042.

C. Gattringer, "A new approach to Ginsparg-Wilson fermions," *Phys.Rev. D* **63** (2001) 114501, hep-lat/0003005.

[67] J. Callan, Curtis G. and J. A. Harvey, "Anomalies and Fermion Zero Modes on Strings and Domain Walls," *Nucl. Phys.* **B250** (1985) 427.

D. B. Kaplan, "Chiral fermions on the lattice," *Nucl. Phys. Proc. Suppl.* **30** (1993) 597.

[68] R. Narayanan and H. Neuberger, "Chiral fermions on the lattice," *Phys. Rev. Lett.* **71** (1993) 3251, hep-lat/9308011.

R. Narayanan and H. Neuberger, "Chiral determinant as an overlap of two vacua," *Nucl. Phys.* **B412** (1994) 574, hep-lat/9307006.

R. Narayanan and H. Neuberger, "A Construction of lattice chiral gauge theories," *Nucl. Phys.* **B443** (1995) 305, hep-th/9411108.

[69] A. N. Krylov, "On the numerical solution of the equation by which in technical questions frequencies of small oscillations of material systems are determined," *Izv. Adad. Nauk SSSR otd. Mat. Estest.* (1931) 491–539.

[70] H. A. van der Vorst, "Bi-CGSTAB: A Fast and Smoothly Converging Variant of Bi-CG for the Solution of Nonsymmetric Linear Systems," *SIAM Journal on Scientific and Statistical Computing* **13** (1992), no. 2, 631.

[71] M. R. Hestenes and E. Stiefel, "Methods of Conjugate Gradients for Solving Linear Systems," *Journal of Research of the National Bureau of Standards* **49** (1952), no. 6, 409–436.

[72] G. S. Bali, S. Collins, and A. Schäfer, "Effective noise reduction techniques for disconnected loops in Lattice QCD," *Comput.Phys.Commun.* **181** (2010) 1570, 0910.3970.

[73] T. Blum, T. Izubuchi, and E. Shintani, "A new class of variance reduction techniques using lattice symmetries," 1208.4349.

[74] A. Frommer, K. Kahl, S. Krieg, B. Leder, and M. Rottmann, "Adaptive Aggregation Based Domain Decomposition Multigrid for the Lattice Wilson Dirac Operator," 1303.1377.

A. Frommer, K. Kahl, S. Krieg, B. Leder, and M. Rottmann, "An adaptive aggregation based domain decomposition multilevel method for the lattice wilson dirac operator: multilevel results," 1307.6101.

[75] M. Lüscher, "Computational Strategies in Lattice QCD," 1002.4232.

[76] **SESAM** Collaboration, G. S. Bali, H. Neff, T. Düssel, T. Lippert, and K. Schilling, "Observation of string breaking in QCD," *Phys. Rev.* **D71** (2005) 114513, hep-lat/0505012.

[77] S.-J. Dong and K.-F. Liu, "Stochastic estimation with Z(2) noise," *Phys. Lett.* **B328** (1994) 130, hep-lat/9308015.

[78] A. O. Cais, K. J. Juge, M. J. Peardon, S. M. Ryan, and J.-I. Skullerud, "Improving Algorithms to Compute All Elements of the Lattice Quark Propagator," hep-lat/0409069.

S. Bernardson, P. McCarty, and C. Thron, "Monte Carlo methods for estimating linear combinations of inverse matrix entries in lattice QCD," *Comput. Phys. Commun.* **78** (1993) 256.

[79] C. Thron, S. J. Dong, K. F. Liu, and H. P. Ying, "Pade-Z(2) estimator of determinants," *Phys. Rev.* **D57** (1998) 1642, hep-lat/9707001.

[80] M. Falcioni, M. Paciello, G. Parisi, and B. Taglienti, "Again On $SU(3)$ Glueball Mass," *Nucl.Phys.* **B251** (1985) 624.

[81] **APE** Collaboration, M. Albanese *et al.*, "Glueball Masses and String Tension in Lattice QCD," *Phys. Lett.* **B192** (1987) 163.

[82] M. Teper, "An Improved Method for Lattice Glueball Calculations," *Phys. Lett.* **B183** (1987) 345.

[83] C. Morningstar and M. J. Peardon, "Analytic smearing of SU(3) link variables in lattice QCD," *Phys. Rev.* **D69** (2004) 054501, hep-lat/0311018.

[84] S. Güsken *et al.*, "Nonsinglet Axial Vector Couplings Of The Baryon Octet In Lattice Qcd.," *Phys. Lett.* **B227** (1989) 266.

[85] C. Ehmann, "A lattice QCD calculation of the charmonium spectrum," Juli, 2010.

[86] G. M. von Hippel, B. Jäger, T. D. Rae, and H. Wittig, "The Shape of Covariantly Smeared Sources in Lattice QCD," *JHEP* **09** (June, 2013) 014, 1306.1440.

[87] M. Göckeler, "Hadron Structure from Lattice QCD," in *Dubna International Advanced School of Theoretical Physics Helmholtz International School*. September 5 - 17, 2011.

[88] M. Lüscher and S. Schaefer, "Non-renormalizability of the HMC algorithm," *JHEP* **1104** (2011) 104, 1103.1810.

[89] M. Lüscher and S. Schaefer, "Lattice QCD without topology barriers," *JHEP* **1107** (2011) 036, 1105.4749.

M. Lüscher and S. Schaefer, "Lattice QCD with open boundary conditions and twisted-mass reweighting," *Comput.Phys.Commun.* **184** (2013) 519–528, 1206.2809.

[90] M. E. Peskin and D. V. Schroeder, "An Introduction to quantum field theory,". Reading, USA: Addison-Wesley (1995) 842 p.

[91] **Particle Data Group** Collaboration, J. Beringer *et al.*, "Review of Particle Physics," *Phys. Rev. D* **86** (2012) 010001.

[92] H. Hamber, E. Marinari, G. Parisi, and C. Rebbi, "Considerations on numerical analysis of {QCD}," *Nuclear Physics B* **225** (1983), no. 4, 475 – 496.

[93] D. B. Leinweber, R. M. Woloshyn, and T. Draper, "Electromagnetic structure of octet baryons," *Phys. Rev.* **D43** (1991) 1659.

[94] R. Horsley, *The Hadronic Structure of Matter - a lattice approach*. Habilitationsschrift, Humbolt Universitaet Berlin, 1999.

[95] G. Martinelli and C. T. Sachrajda, "A Lattice Study of Nucleon Structure," *Nucl.Phys.* **B316** (1989) 355.

[96] L. Maiani, G. Martinelli, M. Paciello, and B. Taglienti, "Scalar Densities and Baryon Masses Differences in Lattice QCD with Wilson Fermions," *Nucl.Phys.* **B293** (1987) 420.

[97] A. Billoire, E. Marinari, and R. Petronzio, "Kogut-Susskind and Wilson Fermions in the Quenched Approximation: A Monte Carlo Simulation," *Nucl.Phys.* **B251** (1985) 141.

[98] M. Göckeler, R. Horsley, M. Ilgenfritz, H. Perlt, P. Rakow, G. Schierholz, and A. Schiller, "Towards a Lattice Calculation of the Nucleon Structure Functions," *Nucl. Phys. Proc. Suppl.* **42** (1995) 337, hep-lat/9412055.

[99] S. Dinter, C. Alexandrou, M. Constantinou, V. Drach, K. Jansen, *et al.*, "Precision Study of Excited State Effects in Nucleon Matrix Elements," *Phys.Lett.* **B704** (2011) 89, 1108.1076.

[100] B. J. Owen, J. Dragos, W. Kamleh, D. B. Leinweber, M. S. Mahbub, B. J. Menadue, and J. M. Zanotti, "Variational Approach to the Calculation of gA," *Phys.Lett.B* **723** (2012) 217, 1212.4668.

[101] W. H. Press, S. A. Teukolsky, W. T. Vetterling, and B. P. Flannery, *Numerical recipes : the art of scientific computing*. Cambridge University Press, 3 ed., 2007.

[102] G. Bali, "critical Kappas for $\beta = 5.29$ and $\beta = 5.40$, private communication.".

[103] M. Constantinou, M. Costa, M. Göckeler, R. Horsley, H. Panagopoulos, H. Perlt, P. E. L. Rakow, G. Schierholz, and A. Schiller, "Perturbatively improving RI-MOM renormalization constants," 1303.6776.

[104] M. Göckeler, "Conversion factors from RGI to $\overline{MS}$, private communication.".

[105] M. Lüscher, "Properties and uses of the Wilson flow in lattice QCD," 1006.4518.

[106] S. Borsanyi, S. Dürr, Z. Fodor, C. Hoelbling, S. D. Katz, S. Krieg, T. Kurth, L. Lellouch, T. Lippert, C. McNeile, and K. K. Szabo, "High-precision scale setting in lattice QCD," 1203.4469.

[107] R. Sommer, "A New Way to Set the Energy Scale in Lattice Gauge Theories and its Application to the Static Force and α_s in SU(2) Yang–Mills Theory," *Nucl.Phys. B* **411** (1994) 839, hep-lat/9310022.

[108] C. Bernard, T. Burch, K. Orginos, D. Toussaint, T. A. DeGrand, C. E. DeTar, S. Gottlieb, U. M. Heller, J. E. Hetrick, and R. L. Sugar, "The static quark potential in three flavor QCD," *Phys.Rev. D* **62** (2000) 034503, hep-lat/0002028.

[109] S. Syritsyn, "Hadron Structure Review," in *Lattice 2013, pleanry talk*. 2013.

[110] G. S. Bali, S. Collins, B. Gläßle, M. Göckeler, J. Najjar, R. Rödl, A. Schäfer, R. Schiel, A. Sternbeck, and W. Söldner, "Moments of structure functions for $N_f = 2$ near the physical point," 1311.7041.

[111] B. Jäger, T. D. Rae, S. Capitani, M. D. Morte, D. Djukanovic, G. von Hippel, B. Knippschild, H. B. Meyer, and H. Wittig, "A high-statistics study of the nucleon EM form factors, axial charge and quark momentum fraction," 1311.5804.

[112] M. D. Morte, R. Sommer, and S. Takeda, "On cutoff effects in lattice QCD from short to long distances," *Phys.Lett.B* **672:407-412,2009** (July, 2008) 0807.1120.

[113] R. Horsley, Y. Nakamura, A. Nobile, P. E. L. Rakow, G. Schierholz, and J. M. Zanotti, "Nucleon axial charge and pion decay constant from two-flavor lattice QCD," 1302.2233.

[114] C. Alexandrou, M. Brinet, J. Carbonell, M. Constantinou, P. A. Harraud, P. Guichon, K. Jansen, T. Korzec, and M. Papinutto, "Axial Nucleon form factors from lattice QCD," *Phys.Rev.D* **83:045010,2011** (Dec., 2010) 1012.0857.

[115] R. Frezzotti, P. A. Grassi, S. Sint, and P. Weisz, "Lattice QCD with a chirally twisted mass term," *JHEP* **0108:058,2001** (JHEP 0108:058,2001) hep-lat/0101001.

[116] C. Alexandrou, M. Constantinou, V. Drach, K. Hatziyiannakou, K. Jansen, C. Kallidonis, G. Koutsou, T. Leontiou, and A. Vaquero, "Nucleon Structure using lattice QCD," 1303.6818.

[117] A. A. Khan, M. Göckeler, P. Hägler, T. R. Hemmert, R. Horsley, D. Pleiter, P. E. L. Rakow, A. Schäfer, G. Schierholz, T. Wollenweber, and J. M. Zanotti, "Axial coupling constant of the nucleon for two flavours of dynamical quarks in finite and infinite volume," *Phys.Rev.D* **74:094508,2006** (Phys.Rev.D74:094508,2006) hep-lat/0603028.

[118] T. R. Hemmert, M. Procura, and W. Weise, "Quark mass dependence of the nucleon axial-vector coupling constant," *Phys.Rev.D* **68:075009,2003** (Phys.Rev.D68:075009,2003) hep-lat/0303002.

[119] C. Alexandrou, M. Constantinou, T. Korzec, H. Panagopoulos, and F. Stylianou, "Renormalization constants for 2-twist operators in twisted mass QCD," *Phys.Rev.D* **83:014503,2011** (June, 2010) 1006.1920.

[120] H.-W. Lin, T. Blum, S. Ohta, S. Sasaki, and T. Yamazaki, "Nucleon structure with two flavors of dynamical domain-wall fermions," *Phys.Rev.D* **78:014505,2008** (Feb., 2008) 0802.0863.

[121] Y. Shamir, "Chiral Fermions from Lattice Boundaries," *Nucl.Phys. B* **406** (1993) 90–106, hep-lat/9303005.

D. B. Kaplan, "A Method for Simulating Chiral Fermions on the Lattice," *Phys.Lett.B* **288:342-347,1992** (Phys.Lett.B288:342-347,1992) hep-lat/9206013.

V. Furman and Y. Shamir, "Axial symmetries in lattice QCD with Kaplan fermions," *Nucl.Phys. B* **439** (1995) 54–78, hep-lat/9405004.

[122] P. H. Ginsparg and K. G. Wilson, "A Remnant of Chiral Symmetry on the Lattice," *Phys. Rev.* **D25** (1982) 2649.

[123] **Ape Collaboration** Collaboration, P. Bacilieri *et al.*, "The Hadronic Mass Spectrum in Quenched Lattice QCD: Beta = 5.7," *Nucl.Phys.* **B317** (1989) 509–525.

[124] A. D. Martin, W. J. Stirling, R. S. Thorne, and G. Watt, "Uncertainties on α_S in global PDF analyses and implications for predicted hadronic cross sections," *Eur.Phys.J.C* **64:653-680,2009** (May, 2009) 0905.3531.

[125] S. Alekhin, J. Blumlein, and S. Moch, "Parton distribution functions and benchmark cross sections at NNLO," 1202.2281.

[126] T. N. Collaboration, R. D. Ball, V. Bertone, F. Cerutti, L. D. Debbio, S. Forte, A. Guffanti, J. I. Latorre, J. Rojo, and M. Ubiali, "Unbiased global determination of parton distributions and their uncertainties at NNLO and at LO," 1107.2652.

[127] P. Wein, P. C. Bruns, and A. Schäfer, "The first moments of nucleon generalized parton distributions in chiral perturbation theory at full one-loop order," 1402.4979.

[128] C. Alexandrou, J. Carbonell, M. Constantinou, P. A. Harraud, P. Guichon, K. Jansen, C. Kallidonis, T. Korzec, and M. Papinutto, "Moments of nucleon generalized parton distributions from lattice QCD," *Phys.Rev.D* **83:114513,2011** (Apr., 2011) 1104.1600.

[129] C. Alexandrou, "Hadron Structure and Form Factors," *PoS* **LATTICE2010** (2010) 001, 1011.3660.

[130] A. Sternbeck, M. Göckeler, P. Hägler, R. Horsley, Y. Nakamura, *et al.*, "First moments of the nucleon generalized parton distributions from lattice QCD," *PoS* **LATTICE2011** (2011) 177, 1203.6579.

S. Collins, M. Göckeler, P. Hägler, T. Hemmert, R. Horsley, Y. Nakamura, A. Nobile, H. Perlt, D. Pleiter, P. E. L. Rakow, A. Schäfer, G. Schierholz, A. Sternbeck, H. Stüben, F. Winter, and J. M. Zanotti, "Nucleon form factors and structure functions," 1101.2326.

[131] M. Göckeler, R. Horsley, Y. Nakamura, H. Perlt, D. Pleiter, P. E. L. Rakow, A. Schäfer, G. Schierholz, A. Schiller, H. Stüben, and J. M. Zanotti, "Perturbative and Nonperturbative Renormalization in Lattice QCD," *Phys.Rev.D* **82:114511,2010** (Mar., 2010) 1003.5756.

[132] J. Green, S. Krieg, J. Negele, A. Pochinsky, and S. Syritsyn, "Excited state contamination in nucleon structure calculations," 1111.0255.

[133] T. Bhattacharya, S. D. Cohen, R. Gupta, A. Joseph, and H.-W. Lin, "Nucleon Charges and Electromagnetic Form Factors from 2+1+1-Flavor Lattice QCD," 1306.5435.

[134] B. Brandt, S. Capitani, M. Della Morte, D. Djukanovic, J. Gegelia, *et al.*, "Form factors in lattice QCD," *Eur.Phys.J.ST* **198** (2011) 79, 1106.1554.

[135] J. R. Green, M. Engelhardt, S. Krieg, J. W. Negele, A. V. Pochinsky, and S. N. Syritsyn, "Nucleon Structure from Lattice QCD Using a Nearly Physical Pion Mass," 1209.1687.

C. Alexandrou, M. Constantinou, V. Drach, K. Jansen, C. Kallidonis, and G. Koutsou, "Nucleon generalized form factors with twisted mass fermions," 1312.2874.

J. Green, M. Engelhardt, S. Krieg, S. Meinel, J. Negele, A. Pochinsky, and S. Syritsyn, "Nucleon form factors with light Wilson quarks," 1310.7043.

[136] S. Sint and P. Weisz, "Further results on O(a) improved lattice QCD to one-loop order of perturbation theory," *Nucl.Phys. B* **502** (1997) 251, hep-lat/9704001.

[137] Y. Taniguchi and A. Ukawa, "Perturbative calculation of improvement coefficients to O(g^2a) for bilinear quark operators in lattice QCD," *Phys.Rev. D* **58** (1998) 114503, hep-lat/9806015.

[138] S. Capitani, M. Göckeler, R. Horsley, H. Perlt, P. E. L. Rakow, G. Schierholz, and A. Schiller, "Renormalisation and off-shell improvement in lattice perturbation theory," *Nucl.Phys.B* **593:183-228,2001** (Nucl.Phys.B593:183-228,2001) hep-lat/0007004.

[139] A. Pelissetto, "Monte Carlo Methods in Statistical Physics," *The STRONGnet 2013 fellow's workshop* **talk** (24-27 June 2013).

[140] C. Alexandrou, S. Dinter, V. Drach, K. Hadjiyiannakou, K. Jansen, and D. B. Renner, "A Stochastic Method for Computing Hadronic Matrix Elements," 1302.2608.

[141] R. Evans, G. Bali, and S. Collins, "Improved Semileptonic Form Factor Calculations in Lattice QCD," *Phys. Rev.* **D82** (2010) 094501, 1008.3293.

[142] S. Dinter, *Nucleon structure from lattice QCD*. PhD thesis, 2012.

[143] R. Horsley, H. Perlt, P. E. L. Rakow, G. Schierholz, and A. Schiller, "Perturbative determination of c_{SW} for plaquette and Symanzik gauge action and stout link clover fermions," *Phys. Rev.* **D78** (2008) 0807.0345.

R. Horsley, P. E. L. Rakow, H. Perlt, G. Schierholz, and A. Schiller, "Clover improvement for stout-smeared 2+1 flavour SLiNC fermions: perturbative results," *PoS LATTICE* **164** (2008) 0809.4769.

[144] G. Erkol, M. Oka, and T. T. Takahashi, "Axial Charges of Octet Baryons in Two-flavor Lattice QCD," *Phys.Lett.B* **686:36-40,2010** (Nov., 2009) 0911.2447.

[145] A. Cooke, R. Horsley, Y. Nakamura, D. Pleiter, P. Rakow, *et al.*, "SU(3) flavour breaking and baryon structure," *PoS* **LATTICE 2013** (2013) 278, 1311.4916.

[146] P. E. Shanahan, A. W. Thomas, R. D. Young, J. M. Zanotti, R. Horsley, Y. Nakamura, D. Pleiter, P. E. L. Rakow, G. Schierholz, and H. Stüben, "Magnetic form factors of the octet baryons from lattice QCD and chiral extrapolation," 1401.5862.

[147] T. A. DeGrand and R. D. Loft, "Wave function tests for lattice QCD spectroscopy," *Comput.Phys.Commun.* **65** (1991) 84–91.

[148] null UKQCD Collaboration, "Gauge-Invariant Smearing and Matrix Correlators using Wilson Fermions at beta=6.2," *Phys.Rev.D* **47:5128-5137,1993** (Phys.Rev.D47:5128-5137,1993) hep-lat/9303009.

[149] M. Lüscher and U. Wolff, "How to calculate the elastic scattering matrix in two-dimensional quantum field theories by numerical simulation.," *Nucl. Phys.* **B339** (1990) 222.

C. Michael, "Adjoint Sources in Lattice Gauge Theory," *Nucl. Phys.* **B259** (1985) 58.

[150] T. Burch, C. Gattringer, L. Y. Glozman, C. Hagen, D. Hierl, C. B. Lang, and A. Schäfer, "Excited hadrons on the lattice: Baryons," *Phys.Rev. D* **74** (2006) 014504, hep-lat/0604019.

[151] M. S. Mahbub, W. Kamleh, D. B. Leinweber, P. J. Moran, and A. G. Williams, "Roper Resonance in 2+1 Flavor QCD," *Phys.Lett.B* **707** (Nov., 2010) 389–393, 1011.5724.

[152] G. Bali, "Private communication.".

[153] V. Braun and R. Schiel, "In preparation.,".

[154] S.-W. Mages, "Private communication.".

[155] P. J. Mohr, B. N. Taylor, and D. B. Newell, "CODATA Recommended Values of the Fundamental Physical Constants: 2010," *Rev. Mod. Phys.* **84,** (Mar., 2012) 1527–1605, 1203.5425.

[156] B. Efron, "Bootstrap methods: another look at the jackknife," *Ann. Statist.* **7** (1979), no. 1, 1–26.

[157] R. G. Edwards and B. Joó, "The Chroma Software System for Lattice QCD," *Nucl.Phys.Proc.Suppl.* **140:832** (2005) hep-lat/0409003.

[158] H. Baier, H. Boettiger, M. Drochner, N. Eicker, U. Fischer, *et al.*, "QPACE: A QCD parallel computer based on Cell processors," *PoS* **LAT2009** (2009) 001, 0911.2174.

H. Baier, H. Boettiger, M. Drochner, N. Eicker, U. Fischer, *et al.*, "Status of the QPACE Project," *PoS* **LATTICE2008** (2008) 039, 0810.1559.

F. Belletti, G. Bilardi, M. Drochner, N. Eicker, Z. Fodor, *et al.*, "QCD on the Cell Broadband Engine," *PoS* **LAT2007** (2007) 039, 0710.2442.

[159] G. Beckett, P. Coddington, N. Ishii, B. Joo, D. Melkumyan, R. Ostrowski, D. Pleiter, M. Sato, J. Simone, C. Watson, and S. Zhang, "Towards an interoperable International Lattice Datagrid," *PoSLAT* **2007:044,2007** (Nov., 2007) 0711.4852.

P. Coddington, B. Joo, C. M. Maynard, D. Pleiter, and T. Yoshie, "Marking up lattice QCD configurations and ensembles," *PoSLAT* **2007:048,2007** (Oct., 2007) 0710.0230.

T. Yoshie, "Making use of the International Lattice Data Grid," *PoS LATTICE* **2008:019,2008** (Dec., 2008) 0812.0849.

G. Beckett, B. Joo, C. M. Maynard, D. Pleiter, O. Tatebe, and T. Yoshie, "Building the International Lattice Data Grid," *Comput.Phys.Commun.* **182:1208-1214,2011** (Oct., 2009) 0910.1692.

[160] F. James and M. Roos, "Minuit: A System for Function Minimization and Analysis of the Parameter Errors and Correlations," *Comput.Phys.Commun.* **10** (1975) 343–367.

[161] M. Galassi, J. Davies, J. Theiler, B. Gough, G. Jungman, M. Booth, and F. Rossi, *Gnu Scientific Library: Reference Manual*. Network Theory Ltd., Feb., 2003.

[162] C. Sanderson, "Armadillo: An Open Source C++ Linear Algebra Library for Fast Prototyping and Computationally Intensive Experiments," tech. rep., NICTA, Sept., 2010.

[163] W. Eckhardt, A. Heinecke, R. Bader, M. Brehm, N. Hammer, H. Huber, H.-G. Kleinhenz, J. Vrabec, H. Hasse, M. Horsch, M. Bernreuther, C. Glass, C. Niethammer, A. Bode, and H.-J. Bungartz, "591 TFLOPS Multi-trillion Particles Simulation on SuperMUC," in *Supercomputing*, J. Kunkel, T. Ludwig, and H. Meuer, eds., vol. 7905 of *Lecture Notes in Computer Science*, pp. 1–12. Springer Berlin Heidelberg, 2013.

[164] N. Meyer, M. Ries, S. Solbrig, and T. Wettig, "iDataCool: HPC with Hot-Water Cooling and Energy Reuse," *Lecture Notes in Computer Science* **7905** (Sept., 2013) 383, 1309.4887.

[165] U. Detert and K. Wolkersdorfer, "JUROPA - Jülich Research on Petaflop Architectures," *Innovatives Supercomputing in Deutschland: inSiDE* **7** (2009) 64 – 65.

[166] K. Moreland, "Diverging Color Maps for Scientific Visualization," in *Advances in Visual Computing*, G. Bebis, R. Boyle, B. Parvin, D. Koracin, Y. Kuno, J. Wang, R. Pajarola, P. Lindstrom, A. Hinkenjann, M. Encarnação, C. Silva, and

D. Coming, eds., vol. 5876 of *Lecture Notes in Computer Science*, pp. 92–103. Springer Berlin Heidelberg.

[167] H. Wierstorf, "http://www.gnuplotting.org/," February, 2014.

B. Rieck, "http://bastian.rieck.ru/blog/posts/2012/gnuplot_better_colour_palettes/," February, 2014.

[168] M. Göckeler, "Notes, private communication.".

[169] C.-Y. Wong, *Introduction to high-energy heavy-ion collisions*. World Scientific Publishing Company Incorporated, 1994.

[170] M. Göckeler, R. Horsley, E.-M. Ilgenfritz, H. Perlt, P. E. Rakow, *et al.*, "Lattice operators for moments of the structure functions and their transformation under the hypercubic group," *Phys.Rev.* **D54** (1996) 5705–5714, hep-lat/9602029.

[171] "http://bar.wikipedia.org/wiki/Woiperdinger."

[172] "git@rqcd.ur.de:johannes_najjar/woiperdinger.git."

Acknowledgements

Tiger got to hunt, bird got to fly
Man got to sit and wonder, 'Why, why, why?'
Tiger got to sleep, bird got to land
Man got to tell himself he understand

by Kurt Vonnegut from Cat's Cradle (1963)

It is a pleasure to thank those who made this thesis possible.
First of all I want to thank my advisor Prof. Dr. Gunnar Bali for providing me with the opportunity to do this thesis with him. He was always patient and supportive when I was struggling and always had creative ideas to overcome problems. He has made his support available in a number of ways and made it possible for me to go on courses, conferences and research visits whenever I so felt.
Dr. Sara Collins was so involved in all my projects that I feel like I had two advisors. Without her guidance and persistent help this thesis would not have been possible.
I would particularly like to thank PD Meinulf Göckeler and Prof. Dr. Andreas Schäfer who patiently answered all my countless physics questions.
The good souls of our Department Heidi Decock and Monika Maschek deserve all praise for keeping the show running!
I am indebted to the following for their hospitality in research stays and helpful discussions: Prof. Dr. Thomas DeGrand (University of Colorado), Prof. Dr. Joan Soto (University de Barcelona), Dr. James Zanotti and Dr. habil. Roger Horsley (University of Edinburgh), and Prof. Dr. Nilmani Mathur (TIFR Mumbai). It was a very nice experience working with you all.
I acknowledge the funding provided by ISAP/DAAD, HPCC2-Europa, Elitenetzwerk Bayern and SFB-TR55(Hadron Physics from Lattice QCD) and the EU ITN STRONGnet (238353).
I want to thank all my colleagues and collaborators for creating a pleasant work environment and helping me where ever they could.
My fellow SysAdmins and the Woiperdinger [171, 172] development team made working fun and educational at the same time.
Special thanks goes to Alessio Burello: You have always amazed me with your quick wits and how you solve physics puzzles with great intuition. "It's impressive" how you handle the hardest problems!
Last but not least I want to thank my family and friends!